

# THÈSE

présentée devant  
L'ÉCOLE CENTRALE DE LYON

pour obtenir  
le titre de DOCTEUR  
SPÉCIALITÉ ACOUSTIQUE

par

Mélanie PIELLARD

## A hybrid method for Computational AeroAcoustics applied to confined geometries

Soutenue le 27 novembre 2008 devant la Commission d'Examen

### JURY

Examineurs : M. C. BAILLY  
M. H. CLESSE  
M. A. HIRSCHBERG (Rapporteur)  
M. D. JUVÉ (Président)  
M. P. LAFON  
M. S. LÉWY (Rapporteur)



# A hybrid method for Computational AeroAcoustics applied to confined flows

This PhD work deals with the development of a Computational Aeroacoustics (CAA) method for industrial applications. The constraints linked to this context impose the choice of a hybrid method based on the use of commercial computing codes adapted to turbulent low velocity flows. This approach is based on Lighthill's Acoustic Analogy, and its application involves two steps. In the first step, the unsteady turbulent flow is computed to determine acoustic source terms, the latter being then propagated in a second step to produce the radiated acoustic field. The implementation is a variational formulation of Lighthill's Acoustic Analogy with the coupling of Fluent CFD code and Actran/LA acoustic code. It is well adapted to the industry since complex geometries are easily handled in both finite volumes (Fluent) and finite elements (Actran/LA) methods.

Two academic configurations are considered. The acoustic radiation produced by two corotating vortices with and without mean flow is first studied for validation. In particular, the goal is to show the necessity to take the local mean flow field into account when computing the source term. A Direct Numerical Simulation (DNS) is therefore performed within Fluent to yield a reference solution; this also reveals the rotating quadrupole nature of the acoustic source. The hybrid method is then applied with success: the source terms are computed from the velocity fields of the DNS, and then propagated to the far field in the spectral domain within Actran/LA. A second verification, in addition to the comparison with DNS results, consists in the analytical resolution of Lighthill's equation using the Lighthill's tensor obtained from the DNS. Another important conclusion of this study is that the presence of a mean flow field in both the propagation and source regions only acts on the acoustic waves refraction; however, it is not required to account for it in the source term determination. The second academic study concerns the handling of outgoing turbulent structures from the computing domain. These indeed produce a spurious dipolar acoustic radiation, of numeric nature purely, and with levels high enough to perturb the whole solution. This issue is modeled here with the convection of a perfect vortex through a virtual boundary. Several spatial filters are tested to smooth source terms down to zero at the boundary; the optimal filter tuning depends on the size and convection velocity of the structures to be dissipated.

Finally, a real application is considered, the ducted diaphragm at low Mach number. A first Large Eddy Simulation (LES) is performed on a reduced geometry consisting of 10% of the total span. In spite of the model limitations, mainly due to the span reduction preventing a correct three-dimensional development of turbulence, the associated two-dimensional acoustic computation yields consistent results. The full scale 3D flow field is then studied, with similarly a LES in which aerodynamic features conform well with the reference DNS. In order to reduce the acoustic model size, source terms are decimated through spatial interpolation. After propagation, the acoustic results suffer from this approximation that would require a more thorough validation.



# Vers une méthode hybride de calcul aéroacoustique appliquée à des écoulements confinés

Ce travail de thèse concerne le développement d'une méthode de calcul du bruit aéroacoustique pour des applications industrielles. Les contraintes liées à ce contexte imposent de choisir une méthode hybride basée sur l'utilisation de codes de calcul commerciaux, adaptée aux écoulements turbulents basse vitesse. Cette approche repose sur l'analogie de Lighthill, et son application fait intervenir deux étapes. Dans la première, l'écoulement turbulent instationnaire est calculé et permet de déterminer les termes sources acoustiques, lesquels sont ensuite propagés dans une seconde étape afin d'obtenir le champ acoustique rayonné. L'implémentation choisie, à savoir le couplage entre les codes Fluent (CFD) et Actran/LA (acoustique) dans une formulation variationnelle, est particulièrement bien adaptée pour l'industrie puisque la complexité des géométries est facilement prise en compte dans les méthodes aux volumes finis (Fluent) et éléments finis (Actran/LA).

On considère plusieurs configurations académiques. Le rayonnement acoustique de deux tourbillons corotatifs avec et sans écoulement moyen est d'abord étudié pour valider la méthode; en particulier, on souhaite démontrer la nécessité de prendre en compte l'écoulement moyen local dans le calcul du terme source. Pour ce faire, une simulation numérique directe (DNS) est effectuée avec Fluent pour obtenir une solution de référence, ce qui met en évidence la nature de quadrupôle tournant de la source acoustique. La méthode hybride est ensuite mise en oeuvre avec succès: les termes sources sont calculés à partir des champs de vitesse obtenus dans le calcul DNS, puis ils sont propagés en champ lointain dans le domaine spectral avec Actran/LA. Une deuxième vérification, complémentaire à la comparaison au calcul direct, consiste à résoudre de manière analytique l'équation de Lighthill en utilisant le tenseur de Lighthill calculé par DNS. On retrouve par ailleurs que la présence d'un écoulement moyen à la fois dans les zones de propagation acoustique et de sources a seulement une influence sur la réfraction des ondes acoustiques; en revanche, il n'est pas nécessaire d'en tenir compte dans la détermination du terme source. La deuxième étude académique porte sur la gestion de la sortie de structures turbulentes du domaine de calcul. Ceci produit un rayonnement dipolaire parasite, d'origine purement numérique, et dont les niveaux sont suffisamment élevés pour perturber la solution. On choisit ici de modéliser le problème par la convection d'un tourbillon parfait à travers une frontière fictive. Divers filtres spatiaux sont testés pour ramener les termes sources à zéro à la traversée de la frontière; le réglage optimal de ces filtres dépend de la taille de la structure à dissiper ainsi que de sa vitesse de convection.

Enfin, une application réelle est considérée, le diaphragme en conduit à faible nombre de Mach. Une première simulation des grandes échelles (LES) est effectuée sur un modèle réduit de la géométrie puisque l'envergure est tronquée à 10% de sa valeur totale. Malgré les limitations de cette approche, en particulier du fait que la trop petite extension du domaine selon l'envergure empêche un développement tridimensionnel correct de la turbulence, le calcul acoustique bidimensionnel associé produit des résultats consistants. Le modèle 3D complet est ensuite étudié, avec, de la même manière, une LES qui met en évidence des caractéristiques aérodynamiques cette fois tout à fait conformes à la DNS de référence. Une décimation des termes sources par interpolation spatiale est nécessaire pour réduire la taille du modèle acoustique 3D; les résultats après propagation souffrent donc de cette approximation qui nécessite une plus ample validation.



# Remerciements

Ce travail a été réalisé au Luxembourg dans la société Delphi, division systèmes thermiques (Delphi Thermal Systems). Il a été financé par le Fonds National de la Recherche du Luxembourg.

Je tiens d'abord à remercier mes directeurs de thèse, Christophe Bailly & Daniel Juvé pour m'avoir fait confiance durant ces presque quatre années. Christophe Bailly m'a beaucoup appris, son exigence a été indispensable dans ce travail de recherche. Son soutien constant et sa disponibilité m'ont été d'une aide précieuse.

Je remercie vivement Mico Hirschberg et Serge Léwy pour avoir accepté d'être les rapporteurs de mon mémoire de thèse; leurs commentaires pertinents et constructifs m'ont permis de voir plus loin. Merci également à Philippe Lafon, membre du jury, d'avoir jugé mon travail et de m'avoir fait partager son expérience.

Je tiens à remercier chaleureusement Henri Clesse pour m'avoir accueillie au sein de son équipe, et également pour m'avoir constamment soutenue dans mon travail. La pleine liberté d'action qu'il m'a laissée m'a permis de travailler dans de très bonnes conditions. Tous mes collègues sont également remerciés pour m'avoir encouragée et pour avoir rendu très agréable l'ambiance de travail au quotidien.

Merci également à toute l'équipe de Free Field Technologies pour son aide et ses conseils avisés à chaque fois que j'en ai eu besoin.

Une pensée à toute l'équipe du LMFA et aux thésards qui m'ont chaleureusement reçue à chacune de mes visites.

Je ne saurais terminer sans exprimer ma reconnaissance à ma famille et mes proches pour leur soutien. Enfin, mes plus profonds remerciements vont à Benoît qui me soutient depuis le début de cette aventure.



# Contents

---

<b>1</b>	<b>Introduction</b>	<b>1</b>
1.1	Context of this study . . . . .	1
1.2	Objectives of the present study . . . . .	5
1.3	Different CAA strategies . . . . .	6
1.3.1	Direct Noise Computation (DNC) . . . . .	7
1.3.2	Hybrid methods of noise computation . . . . .	10
1.3.3	Using CAA in complex configurations of internal flows . . . . .	22
1.4	Organization of the manuscript . . . . .	23
<b>2</b>	<b>Theoretical foundations of the computational method</b>	<b>25</b>
2.1	Lighthill's Acoustic Analogy applied in a spectral finite element framework . . . . .	26
2.1.1	Variational formulation of Lighthill's Acoustic Analogy . . . . .	26
2.1.2	Spectral formulation . . . . .	27
2.1.3	Discretization . . . . .	29
2.1.4	Boundary conditions . . . . .	31
2.1.5	Solver . . . . .	38
2.2	Modeling the noise sources . . . . .	39
2.2.1	Large Eddy Simulation . . . . .	39
2.2.2	Numeric aspects within Fluent . . . . .	42
2.3	Practical application of the method . . . . .	47
2.3.1	General overview . . . . .	47
2.3.2	Source interpolation: from the CFD mesh to the acoustic mesh . . . . .	47
2.3.3	Transformation in the spectral domain . . . . .	48
2.4	Potential issues associated with the method . . . . .	50
2.4.1	Accuracy of the computed noise sources . . . . .	50
2.4.2	Spatial truncation of convected noise sources . . . . .	50
2.4.3	Mesh interpolation . . . . .	51

2.5	Conclusion . . . . .	52
<b>3</b>	<b>Assessment of the hybrid method</b>	<b>53</b>
3.1	General validation: corotating vortices study . . . . .	54
3.1.1	Analytical resolution of Lighthill's Acoustic Analogy . . . . .	55
3.1.2	Two corotating vortices in a medium at rest . . . . .	56
3.1.3	Two corotating vortices placed in a shear layer . . . . .	67
3.1.4	Conclusion . . . . .	72
3.2	Exit of turbulent structures from the CFD domain . . . . .	73
3.2.1	Convection of a vortex through a virtual boundary: presentation . . .	73
3.2.2	Study on the filter shape . . . . .	74
3.2.3	Study on the filter length . . . . .	76
3.2.4	Conclusion . . . . .	76
3.3	Conclusion . . . . .	77
<b>4</b>	<b>Diaphragm study</b>	<b>79</b>
4.1	Introduction . . . . .	80
4.1.1	Geometry . . . . .	80
4.1.2	Previous studies on similar geometries . . . . .	80
4.2	Numerical study on a slice of the domain . . . . .	83
4.2.1	Configuration and parameters of the CFD simulation . . . . .	83
4.2.2	Aerodynamic results . . . . .	85
4.2.3	Acoustic simulation . . . . .	94
4.3	Numerical study on the complete 3D domain . . . . .	103
4.3.1	Mesh and numerical parameters for CFD . . . . .	103
4.3.2	Aerodynamic results . . . . .	104
4.3.3	Analysis and filtering of the source terms $S_i$ . . . . .	119
4.3.4	Acoustic simulation . . . . .	126
4.4	Conclusion . . . . .	136
	<b>Conclusion</b>	<b>137</b>
	<b>A Study of the diaphragm: two-dimensional case</b>	<b>141</b>
	<b>Bibliography</b>	<b>145</b>

# 1.

## Introduction

---

*T* HIS WORK is oriented toward the development of a Computational AeroAcoustics methodology applied to internal flows in complex geometries at low Mach numbers. The context, motivations and objectives of the study are firstly given. A non exhaustive description of different Computational AeroAcoustics strategies is then proposed, followed by a discussion on the applicability of these methods in the context of this study. The organization of the manuscript is finally outlined.

### 1.1 Context of this study

In the automotive industry, noise comfort is a growing concern to satisfy customer's demand. As great progresses have been made in decreasing the noise radiated by the engine, other types of noise are emerging inside the vehicle: the external aerodynamic noise at high speeds, the road-tire noise at moderate speeds and the ventilation noise at low speeds. Ventilation noise is particularly annoying for city driving or when weather conditions impose severe operating conditions (either fast cooling/heating of the car cabin or deicing/defogging of the windows).

In the late 90's, the automotive industry adopted Computational Fluid Dynamics (CFD) to predict the mean features of the flow field thanks to Reynolds Averaged Navier-Stokes (RANS) modeling. RANS computations, based on turbulence modeling, enable to tackle complex problems involving large and detailed geometries. These steady mean flow simulations provide a very useful insight on turbulent flows of practical interest at a relatively low cost, and enable to significantly reduce development times by simulating the statistical mean behavior of a turbulent flow instead of measuring it. A new step is being achieved at

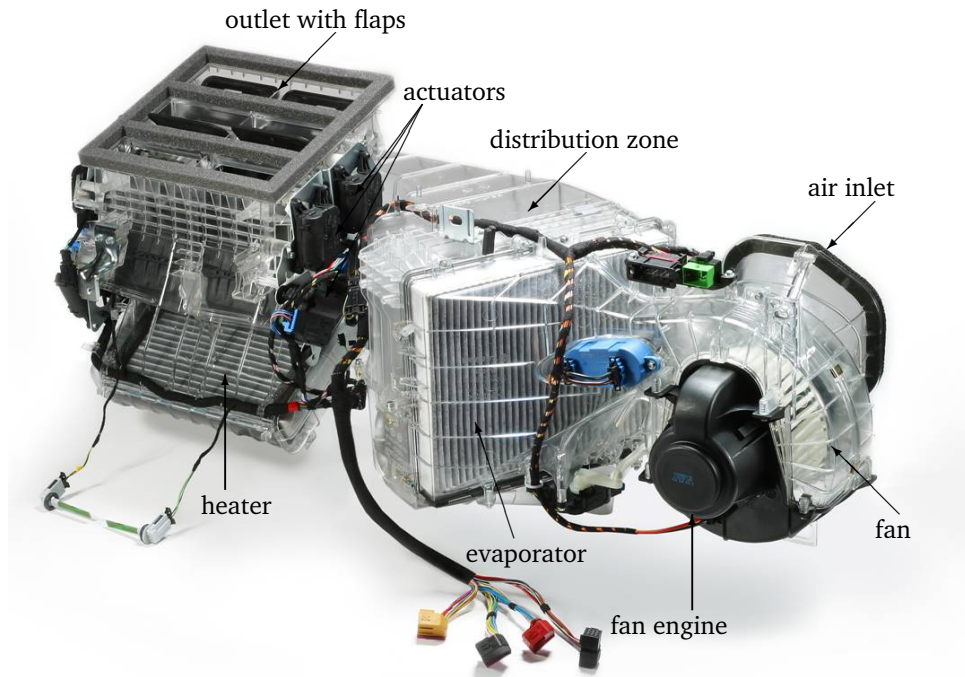


**Figure 1.1** – Typical Heating, Ventilating and Air Conditioning module, with main elements marked.

the present time with the standardization of unsteady simulations of fine-scale structures in the vicinity of a car, thanks to Large Eddy Simulations. Next step is to develop and use such CFD results to compute the noise generated aerodynamically and radiated in the far field. Considering the exterior problems such as noise generated by the aerodynamic flow around a vehicle, the main limitation nowadays is the computing power and time needed to accurately resolve such a huge flow domain, but some methods have been proposed for particular elements of the car, such as the side-view mirror<sup>84</sup> and the open sunroof<sup>88</sup> for instance. Besides, the aeroacoustic noise generated internally has gained less interest due to its complexity and to the fact that the industry did not see this issue as a major one in the past. However, ventilation is a typical example of internal aeroacoustic noise that has emerged in the car cabin thanks to the decrease of engine and external noise.

A photography of a typical Heating, Ventilating and Air Conditioning (HVAC) module is presented in Figure 1.1; this is a complex box of 40 to 50 liters internal volume, when duct are not considered. This product has the following functions: bring the airflow at specific mass flow and temperature to the desired locations in the car (in front of driver and passenger, at the feet, in the rear, at the defrost outlets), as specified by the user on the control board. The mechanism principle is the following: a fan drives the air into a duct at a very low velocity, most often less than 20 m/s, where it is first dried out and cooled down through an evaporator; part of the air is then heated through a heater, and a mixing between warm and cold air provides the desired temperature. The air is finally

conducted to the desired outlets. The temperature mixing phase in particular involves a series of obstacles in the airflow, such as flaps, valves and rigid walls; the internal airflow presents thus a great complexity, and the resulting acoustic field has many origins. Indeed, apart from the aeroacoustic problem, the physics involve vibro-acoustics, noise of electrical engines (fan and actuators) and mechanical noise (shifting of the flaps for instance); the noise may also have its origin in the refrigerant system.

Delphi, as a supplier of thermal comfort products, among others, for the automotive industry, has to find technical answers to achieve customer's requirements. All aerodynamic development is driven by Reynolds Averaged Navier-Stokes simulation, regarding the mass-flow repartition, temperature mixing as well as pressure drop management. As an example, temperature and velocity obtained by simulation are presented in Figure 1.2; the system complexity is clear, even if only a two-dimensional cut view is displayed. The conventional approach to achieve the acoustic specifications is mainly based on engineering background and on experimental tests; thus, simple laws relating pressure and mass-flow for instance give indications on the expected noise. In addition, the analysis of RANS results in terms of turbulent energy levels enable to localize the most probable acoustic source regions; the vibration analysis and the acoustic propagation of pure sources finally reveals the acoustic and structural modes present in the system. However, the market drives a reduction of vehicles development times, and while the time-consuming and costly experimental work is becoming hardly adequate, the mean flow field simulations are not accurate enough to lead the aeroacoustic developments. New methods have to be developed in order to understand earlier in the development process the physics of sound generation by the flow. With the increase of computing power, the aeroacoustic simulation starts to become affordable, even within an industrial context.

Regarding the aeroacoustic problem in an HVAC module, it can be split into three major parts: the heat exchangers noise, the centrifugal fan noise, and the internal aeroacoustic noise. To our knowledge, the heat exchangers noise has been little studied; the only available work<sup>60</sup> is experimental and concerns the drying machines industry. The fan noise has gathered much more attention, with the early developments of similarity laws for centrifugal or axial fans (Neise and Barsikow<sup>75</sup>, Guédel<sup>57</sup>) and of formulas for calculation of rotating blade noise (see the review of Farassat<sup>39</sup>). The most recent developments of Rozenberg<sup>89</sup> involve the use of CFD steady-state results to feed analytical formulas of fan noise radiation. The specific problem of centrifugal fan noise has been recently addressed by different teams, with the commune objective of developing a prediction method based on the use of acoustic analogies together with Computational Fluid Dynamics (cf. Tournour *et al.*<sup>106</sup> and Dubief *et al.*<sup>34</sup>, and Read *et al.*<sup>87</sup>, Caro *et al.*<sup>21</sup> and Sandbodge *et al.*<sup>92</sup>).

This study will focus on the third part of the problem, the prediction of aeroacoustic noise generation and radiation in a confined flow meeting obstacles. Confined flows have been studied experimentally by van Herpe *et al.*<sup>111</sup> and numerically by Lafon<sup>63</sup> and

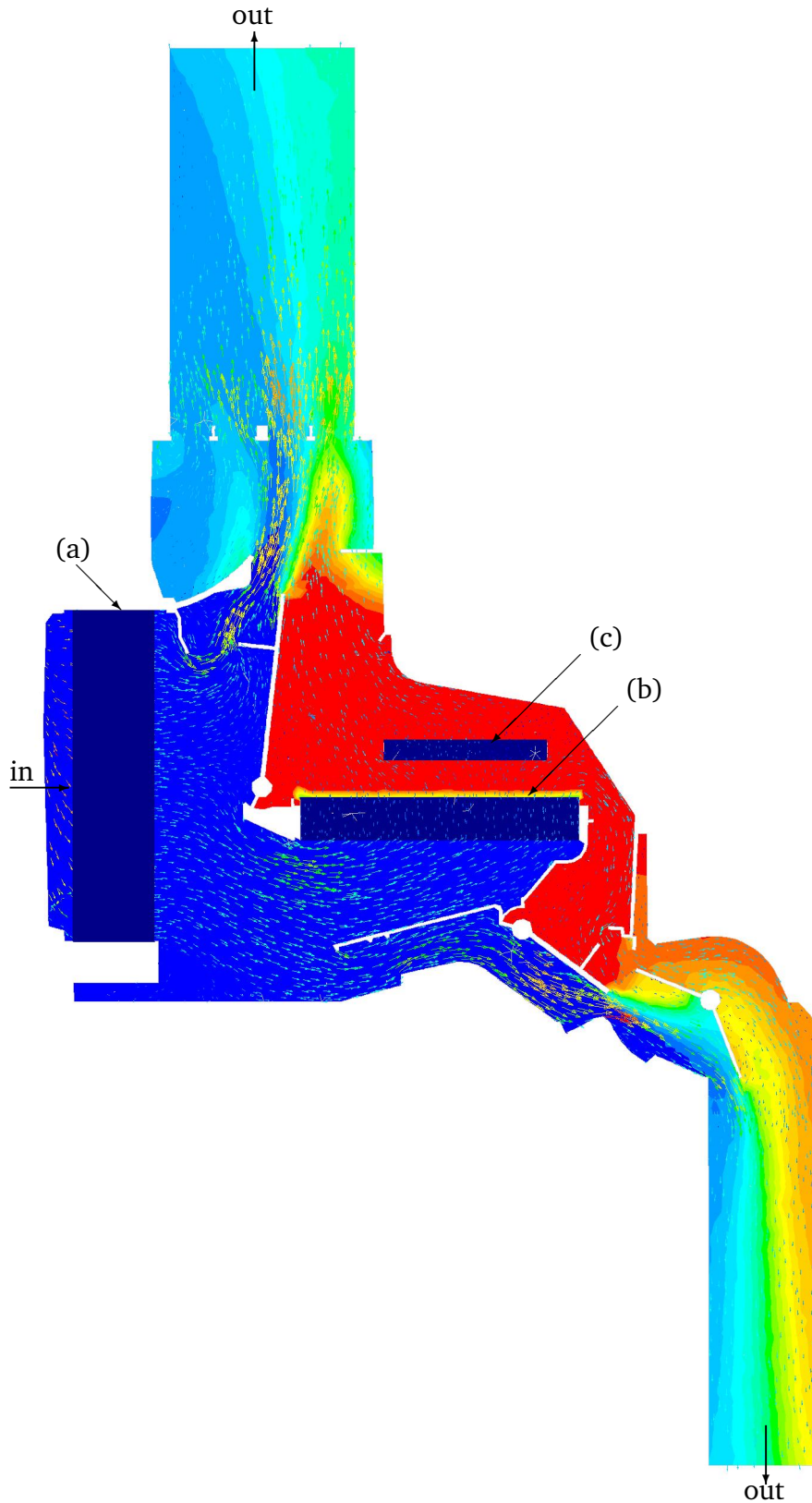


**Figure 1.2** – Typical HVAC simulation: velocity vectors superimposed on temperature contours; cut view. The inlet is coming on the left, two outlets are visible on top and bottom. Dark blue rectangles represent the location of heat exchangers, respectively (a): evaporator, (b): heater, and (c): electrical heater.

Longatte<sup>67</sup> for the case of a two-dimensional duct obstructed by a diaphragm. The prediction method proposed in these works is to solve the Linearized Euler Equations using a source term defined with stochastic space-time turbulent quantities from a steady-state CFD simulation: this model is called SNGR (Stochastic Noise Generation & Radiation). More recently, Gloerfelt *et al.*<sup>54</sup> continued this work from another point of view, with a Direct Noise Computation. Other researches conducted in the frame of confined subsonic flows aim at using acoustic analogies; thus Ayar *et al.*<sup>6</sup> apply Ffowcs Williams & Hawkings analogy in a boundary element framework, and Mendonça *et al.*<sup>72</sup> apply Lighthill's Acoustic Analogy in a finite element framework; Brotz *et al.*<sup>18</sup> present a first step toward aeroacoustic prediction consisting in predicting the near-field acoustic spectra computed directly from CFD; and de Guillebon *et al.*<sup>31</sup> propose an original acoustic model specifically derived for HVAC systems.

## 1.2 Objectives of the present study

The general scope of this work is to develop and validate a numerical tool for aeroacoustic noise prediction applicable to confined, low Mach number flows ( $M < 0.1$ ) in complex geometries, see Figure 1.2; as mentioned previously, the numerical prediction of heat exchanger noise and centrifugal fan noise is not treated here. Additional constraints linked to the industrial context where the tool will be used are imposed. Although very severe, the following criteria have been defined to assess the accuracy and performance of the simulation method:

- ★ the total simulation time for one prediction should not exceed one week;
- ★ the simulation tools have to be chosen amongst available commercial software;
- ★ the developed method has to be general enough to be directly applicable to any HVAC geometry without fine tuning;
- ★ in terms of frequency, the computed acoustic spectra should range from 50 Hz to 4000 Hz, where most of the acoustic energy is located for an HVAC system;
- ★ in the comparison of acoustic results to experiments, two accuracy criteria are considered: the simulated broadband noise should lie within the experimental broadband envelope within 3 dB, and on an A to B comparison, the shift between calculated noise levels on two different designs should not exceed 10% of the corresponding shift in experimental noise levels;
- ★ the computed error should always go in the same sense with respect to experiments;

- ★ all tonal noise observed by experiment should be captured by simulation and identified.

At the conclusion of the study, it will be assessed if the previous objectives are realistic in the present industrial context, taken the difficulties not expected at the beginning. The missing steps leading to the aeroacoustic prediction for HVAC will also be detailed.

### 1.3 Different CAA strategies

Computational AeroAcoustics (CAA) generally aims at predicting the sound produced by a turbulent flow. Implicitly, sound prediction will be used in most cases to reduce the noise generated by a specific device. The complexity of this problem is linked to the very wide range of associated issues: turbulence and deterministic phenomena are the starting point for noise generation; length scales and time scales involved in the fluid and in the acoustic problems differ from several orders of magnitude, and are difficult to be resolved in a single computation; the geometries considered can be very complex; additional physical phenomena can occur, such as shock waves, multiphase flow or vibrating structure.

This complexity can be broken into simpler problems<sup>27</sup> easier to address separately. As such, we may distinguish the following sub-problems:

- ★ the development of accurate and robust computational methods to solve flow equations (development of Direct Numerical Simulation and Large Eddy Simulation solvers for instance);
- ★ the use of these computations to investigate fundamental mechanisms of sound generation, in conjunction with experiments (application of Direct Noise Computation and confrontation to experimental results);
- ★ the use of computation, in conjunction with experiments and theory, to derive simpler models of turbulence or sound generation processes (development of hybrid methods of noise computation based on acoustic analogies or specific computational strategies);
- ★ the integration of theory, models and computation into predictive tools that can be used for engineering design, optimization and noise reduction strategies (choose a combination of previous items to solve a specific aeroacoustic problem).

This research work stands in the last item. In the following, we present different CAA strategies and explain in which context they are used. The emphasis is put on the general spirit and the applicability of each method to our particular aeroacoustic problem. A more complete review can be found in Colonius and Lele<sup>28</sup>.

### 1.3.1 Direct Noise Computation (DNC)

Direct calculation of noise radiation consists in determining the acoustic field directly from unsteady compressible fluid mechanics equations. The aerodynamic field and the acoustic field generated by turbulence are computed simultaneously. In this approach, all physical phenomena responsible for noise generation and propagation are taken into account *a priori*, as no acoustic model nor simplifying assumptions are used. In particular, all interactions between the velocity field and acoustic waves (such as refraction effects for instance) are computed.

In order to obtain an acoustic field clean and directly workable, it is necessary to introduce numerical techniques adapted to acoustic waves in simulations. The computing algorithm should indeed be able to compute acoustic fluctuations of very small amplitude with respect to those of the aerodynamic field (usually, acoustic fluctuations are three to four orders of magnitude lower than aerodynamic fluctuations). Acoustic waves have also to be propagated on long distances without excessive dissipation, damping or refraction. In addition, boundary conditions are to be treated cautiously in order to minimize spurious reflections on domain borders and to avoid the generation of non-physical acoustic waves by the outflow of turbulent structures; indeed, the amplitude of these waves may be superior to the physical acoustic waves amplitude. The use of sponge zones, where the mesh is slowly stretched, toward downstream boundaries usually improves the efficiency of boundary conditions.

Among different Direct Noise Computation methods, we give in the following some key features and examples for the solving of Navier-Stokes equations by direct methods (Direct Numerical Simulation or Large Eddy Simulation), in which the pressure field is explicitly solved.

#### 1.3.1.1 Direct Numerical Simulation (DNS)

Direct Numerical Simulation consists in solving compressible Navier-Stokes equations for all relevant scales of the true fluid motion. Only first principles are used to derive the Navier-Stokes equations, and numerical analysis is used to guarantee that the numerical solution is close enough to the true continuous solution; this is called the *verification* of the numerical solution. The *validation* ensures that all assumptions taken for a problem (boundary conditions, initial conditions, simplifications) are valid by comparing the results to a related experiment.

The smallest scale constitutive of the turbulent kinetic energy spectrum is called the Kolmogorov scale  $\eta$  and is characteristic of the structures dissipating energy. For a homogeneous and isotropic turbulence, a simple dimensional law (cf. Bailly *et al.*<sup>7</sup>) links

Kolmogorov scale  $\eta$  to the flow integral scale  $L$ :

$$\frac{L}{\eta} \sim Re_L^{3/4} \quad \text{where} \quad Re_L = \frac{u'L}{\nu}$$

where  $u'$  is a characteristic velocity scale of the flow,  $\nu$  is the fluid molecular cinematic viscosity and  $Re_L$  is the flow Reynolds number. In three dimensions, the number of points necessary to describe all scales characteristic of turbulence varies as

$$N \propto Re_L^{9/4}$$

The number of time steps  $n_\tau$  necessary to describe the flow links the characteristic time of the flow  $t_L \sim L/u'$  to the characteristic time of turbulence  $t_\eta$ :

$$n_\tau = \frac{t_L}{t_\eta} = \frac{L}{u't_\eta}$$

Considering that the Courant number limits the time step for a stable computation as

$$CFL = \frac{c_0 \Delta t}{\Delta x} \sim \frac{c_0 t_\eta}{\eta} \sim \mathcal{O}(1),$$

the total computation cost for the turbulent region is proportional to

$$N \times n_\tau \propto \frac{Re_L^3}{M}$$

where  $M = u'/c_0$  is the characteristic flow Mach number. As the goal is not only to properly resolve the turbulent region, but also to compute the sound radiated in the far field, the characteristic acoustic length scale  $\lambda$  is introduced; at low Mach numbers, it is linked to the integral turbulence scale  $L$  as

$$\frac{\lambda}{L} \sim \frac{1}{M}$$

Thus the computation of one acoustic wavelength in three dimensions increases the estimation for total computational resources to

$$N_{\text{tot}} \sim \frac{Re_L^3}{M^4} \tag{1.1}$$

It is clear from Equation (1.1) that flows at high Reynolds number and/or low Mach number are almost not reachable by DNS. As an illustration, consider that the computing power available in the mid-80's allowed to compute turbulent flows with a Reynolds number of order  $10^3$  in the case of channel flow. Nowadays, the computable Reynolds numbers approach  $10^4$ . However, flows of interest for aeroacoustic problems have Reynolds numbers

of at least  $10^6$  and will therefore not be affordable before long. For these reasons, Direct Numerical Simulation of noise is mainly applied on model problems aiming at addressing fundamental issues of aeroacoustic theory or providing benchmark solutions (study of co-rotating vortices<sup>74</sup>, vortex pairing in mixing layer<sup>14</sup>).

Among recent attempts to the DNS of sound on real flows, the works of Freund<sup>47;48;50</sup> are remarkable, with successful computations of low Reynolds number jets and their radiated noise by DNS; the analysis of the computed acoustic field provided constitute a valuable insight into the physics involved in jet acoustic radiation.

### 1.3.1.2 Large Eddy Simulation (LES)

Large Eddy Simulation is a macrosimulation in which only the largest structures of the flow are calculated, the effect of the smallest scales being modeled. A spatial filter allows the separation of scales. It is generally considered that the behavior of filtered small scales is close to isotropy, which justifies the use of a subgrid-scale model. In most cases, a functional modeling is used where the role of missing scales is modeled (dissipation of the small structures energy); a structural modeling can also be employed, where the missing terms are modeled<sup>91</sup>.

The cost of this method is, as well as for Direct Numerical Simulation, linked to the smallest resolved scale, which is here the Taylor scale  $\lambda_g$ . According to Bailly *et al.*<sup>7</sup>, the number of points necessary to describe the Taylor scale is

$$\frac{L}{\lambda_g} \sim Re_L^{1/2}$$

In three dimensions, the number of mesh points then varies as

$$N \propto Re_L^{3/2}$$

After introducing the time, the computing cost is proportional to  $Re_L^2/M$ . Considering the resolution of one acoustic wave length by Large Eddy Simulation, a dimensional analysis similar to the DNS case leads to a total number of operations proportional to  $Re_L^2/M^4$ .

The direct computation of noise using LES is thus more tractable than using DNS, but the propagation of sound up to the far field is still barely achievable in practical applications. The elaboration of high-order, low dispersive and low dissipative numerical schemes<sup>8</sup> makes reliable Direct Noise Computations possible, but still at a high cost. The analysis of these direct computations of sound with causality methods<sup>13</sup> provides a valuable insight into the noise generation mechanisms. Recent developments include the implementation and validation of solvers in curvilinear coordinates<sup>69;70</sup> together with high order numerical schemes, enabling the handling of more complex geometries such as cylinders and airfoils. Besides, domain decomposition methods are developed<sup>107</sup> in order to decrease

the computational cost of direct aeroacoustic computations; indeed, the equations, grids, numerical schemes and time steps are adapted to each subregion of interest to meet local physical requirements.

An important issue linked to the use of LES for aeroacoustic computations is the subgrid scale modeling and its effect on the radiated noise; in particular, the subgrid scale model should not produce spurious acoustic radiation by itself (Piomelli *et al.*<sup>83</sup>, S  ror *et al.*<sup>94;95</sup>). Some studies aim at quantifying and modeling the contribution of the modeled subgrid scales to the radiated noise (Rubinstein and Zhou<sup>90</sup>, He *et al.*<sup>58</sup>). Bogey and Bailly<sup>10-12</sup> chose to explicitly filter the subgrid scales, without any additional turbulent viscosity based subgrid modeling: a filtering operation applied to fluctuating quantities removes the high wave numbers close to the grid cutoff.

### 1.3.2 Hybrid methods of noise computation

Hybrid approaches constitute an alternative to the direct computation of noise; they consist in two-steps calculations, where the determination of the aerodynamic velocity and pressure fields is decoupled from the computation of the acoustic waves. It is then possible to adapt the numerical techniques to the constraints of each computational step. These hybrid approaches still can lack information on the interactions between the aerodynamic and acoustic fields; in particular, refraction effects by the mean flow are incompletely, or even not at all, computed, as well as potential couplings between the aerodynamic and the acoustic fields. However, these methods are more affordable in terms of computing power and time. Moreover, they are often the only methods applicable in complex configurations.

The first step is to determine a space-time evolution of a turbulent aerodynamic field from a solution of Navier-Stokes equations, either by direct calculation, Large Eddy Simulation or unsteady Reynolds Averaged Navier-Stokes. Pressure and/or velocity fluctuations are used to build the acoustic source terms, which are integrated into a propagation model, leading to the radiated noise in the far field.

In the following, we give a presentation of some hybrid methods, with examples of applications and particular features.

#### 1.3.2.1 Lighthill's Acoustic Analogy

##### Derivation of Lighthill's equation

In 1952, Lighthill<sup>64</sup> writes his famous paper in which he shows that the two conservation equations of the flow can be combined to give rise to a conventional wave equation of the form:

$$\text{acoustic wave operator} = \text{source term}.$$

From the full Navier-Stokes mass and momentum conservation equations

$$\frac{\partial \rho}{\partial t} + \frac{\partial(\rho u_i)}{\partial x_i} = 0 \quad (1.2)$$

$$\frac{\partial(\rho u_i)}{\partial t} + \frac{\partial(\rho u_i u_j)}{\partial x_j} = -\frac{\partial p}{\partial x_i} + \frac{\partial \tau_{ij}}{\partial x_j} \quad (1.3)$$

we perform the operation  $\frac{\partial(1.2)}{\partial t} - \frac{\partial(1.3)}{\partial x_i}$  to obtain the equation:

$$\frac{\partial^2 \rho}{\partial t^2} = \frac{\partial^2}{\partial x_i \partial x_j} (\rho u_i u_j + p \delta_{ij} - \tau_{ij})$$

Subtracting  $c_0^2 \nabla^2 \rho$  on both sides of previous equation, where  $c_0$  is the mean sound velocity, we obtain Lighthill's equation:

$$\frac{\partial^2 \rho}{\partial t^2} - c_0^2 \nabla^2 \rho = \frac{\partial^2 T_{ij}}{\partial x_i \partial x_j} \quad (1.4)$$

where Lighthill's tensor  $T_{ij}$  is defined as

$$T_{ij} = \rho u_i u_j + (p - c_0^2 \rho) \delta_{ij} - \tau_{ij} \quad (1.5)$$

If density  $\rho_0$  is uniform and constant, we can re-write Lighthill's equation in the following way:

$$\begin{cases} \frac{\partial^2 \rho_a}{\partial t^2} - c_0^2 \nabla^2 \rho_a = \frac{\partial^2 T_{ij}}{\partial x_i \partial x_j} \\ T_{ij} = \rho u_i u_j + ((p - p_0) - c_0^2 (\rho - \rho_0)) \delta_{ij} - \tau_{ij} \end{cases} \quad (1.6)$$

with  $\rho_a = \rho - \rho_0$  outside the source region. This formulation allows to show that, outside the aerodynamic field, Lighthill's tensor is null: indeed, the fluid velocity  $u_i$  is then null, and taken that the fluctuating acoustic density  $\rho - \rho_0 = \rho'$  is also  $\rho' = p'/c_0^2$ , Lighthill's tensor cancels:  $T_{ij} = 0$ .

In numerous cases, Lighthill's tensor's expression can be simplified:

- ★ when Reynolds number is high, the viscous stress tensor  $\tau_{ij}$  is negligible behind  $\rho u_i u_j$ <sup>1</sup>;
- ★ when the gas is perfect, then  $p' = c_0^2 \rho' + \frac{p_0}{c_v} s'$ ;

---

<sup>1</sup>This is shown by a dimensional analysis:  $\tau_{ij} \propto \frac{\mu U}{D}$ , thus  $\frac{\rho u_i u_j}{\tau_{ij}} \propto \frac{\rho U^2}{\frac{\mu U}{D}} \propto \frac{UD}{\nu} = Re \gg 1$ .

★ when entropy fluctuations can be neglected,  $s' = 0$  and  $p' = c_0^2 \rho'$ .

Lighthill's tensor is eventually reduced to:

$$T_{ij} = \rho u_i u_j. \quad (1.7)$$

### Interpretation

Since it is exactly built on the full fluid mechanics equations without assumptions, Equation (1.4) is exact. Lighthill gives the following interpretation: it is

*the equation of propagation of sound in a uniform medium at rest due to externally applied fluctuating stresses*<sup>64</sup>.

Lighthill's tensor  $T_{ij}$  constitutes the external stresses in the form of a quadrupolar source term. In this brilliant interpretation, two distinct regions are considered: the *source region* where sound is generated from the complex and non linear flow field, and the *observer region*, which is a uniform medium at rest where the linear density fluctuations constitute the acoustic field.

The source term contains not only the sound produced by turbulence, but also all sound–flow interactions, provided that these interactions occur in the source domain. However, no interactions between the radiated noise (in far field) and the aerodynamic field can be taken into account. Indeed, density fluctuations in left- and right-hand-side of Equation (1.6) are supposed independent; in the propagation operator, the acoustic density fluctuation  $\rho_a$  is considered, while in the source term, density  $\rho$  contains both acoustic and turbulent fluctuations. If the flow Mach number is low, it is relevant to consider an incompressible source region with constant density  $\rho_0$ , which simplifies the aerodynamic problem; in this case, no sound–flow interaction is computed, even in the source region, but such effects are supposed to be negligible at low Mach numbers.

A number of papers published recently (cf. for instance Tam<sup>100;101</sup> or Fedorchenko<sup>43</sup>) introduced some confusion regarding the use of Lighthill's Acoustic Analogy and its efficiency to properly catch effective noise sources. In particular, it was argued that, *as turbulence plays no role in the formulation of the analogy*<sup>100;101</sup>, this theory can not give reliable results. On the contrary, Peake<sup>78</sup> and Bogey *et al.*<sup>16</sup> state that turbulence is accounted for implicitly in the description of the source term, which has to be accurately computed to provide consistent results. In the present study, with low velocities and internal flow, the acoustic prediction performed with such an analogy should produce consistent results. Indeed, as shown in Bogey *et al.*<sup>16</sup>, even sound–flow interaction effects can be accounted for and computed by Lighthill's Acoustic Analogy provided that the source term contains these effects; in the case of a low Mach number flow with small sound–flow interaction effects, a compressible computation of the Lighthill's tensor on a region including all sound sources and all sound–flow interactions can give accurate results.

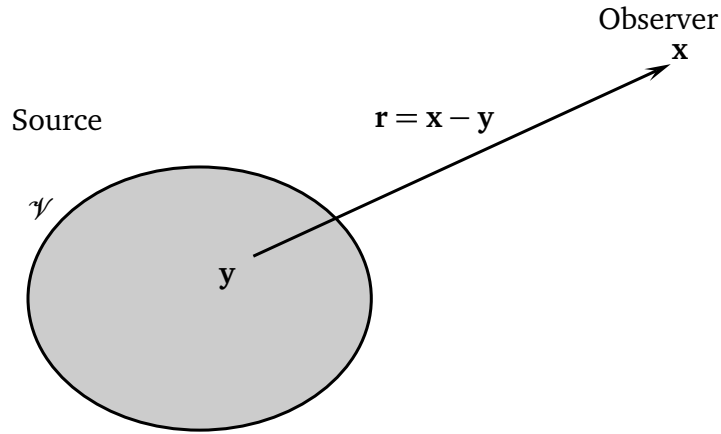


Figure 1.3 – Notations used for Lighthill's Acoustic Analogy analogy.

### Solution of Lighthill's equation

The analytical solution of Lighthill's equation is obtained by using Green's functions, allowing to express the solution of an inhomogeneous wave equation as an integral equation. This formalism leads to different formulations of Lighthill's solution, depending on the dimension of the problem (two or three dimensions) and solution domain required (time or spectral). Moreover, the solution can express time or spatial derivatives of the source term  $T_{ij}$  or of the Green's function. An exhaustive review of these formulations in free space is given in Gloerfelt<sup>53</sup>. We give here the solution given by Lighthill<sup>64</sup> (in chapter 2, the spectral two-dimensional formulation used in this study is also presented):

$$\rho_a(\mathbf{x}) = \frac{1}{4\pi c_0^2} \frac{\partial^2}{\partial x_i \partial x_j} \iiint_{\mathcal{V}} T_{ij} \left( \mathbf{y}, t - \frac{|\mathbf{x} - \mathbf{y}|}{c_0} \right) \frac{d\mathbf{y}}{|\mathbf{x} - \mathbf{y}|} \quad (1.8)$$

where  $\mathbf{x}$  is the observer's location and  $T_{ij}$  is taken at the retarded time  $t - \frac{|\mathbf{x} - \mathbf{y}|}{c_0}$ ;  $\mathcal{V}$  denotes the volume of the source region (see Figure 1.3 for notations).

Although these analytical solutions are exact, they are of utility only in free space or in particular configurations where the Green's function is exactly known; moreover, Lighthill's tensor space-time fluctuations have to be described in the volume containing the sources. In the absence of computational fluid dynamics results, this is merely impossible. That is why Lighthill's analogy has been firstly extensively used to get magnitude orders for the acoustic power. In his early paper in 1952<sup>64</sup>, Lighthill expresses the first intensity scaling law for an observer located at the distance  $x$  as

$$\overline{\rho'^2} \simeq \left( \frac{\rho_0 \ell}{4\pi x} \right)^2 M_0^8$$

where  $M_0 = U_0/c_0$  is the Mach number of the flow and  $U_0$ ,  $\ell$  are the typical velocity and length scale of the flow. This is the so-called 8<sup>th</sup> power law of Lighthill.

### 1.3.2.2 Addition of a mean flow

One flaw of Lighthill's analogy is that the observer is located in a uniform medium at rest. Therefore, if a mean flow is present in the observer domain, mean flow effects on the acoustic propagation, such as convection, refraction, diffusion and diffraction of acoustic waves, are missed by previous model. Lighthill's analogy can be re-formulated in order to bring to light a more general wave operator containing all mean flow effects on the acoustic propagation. In the consequent equation, mean flow effects in the source region will be contained in the source term as before, whereas mean flow effects in the observer region will be accounted for by the propagation operator.

#### Phillips' extension to a unidirectional shear flow

Phillips<sup>80</sup> proposes in 1960 to take into account a moving medium with a modification of the propagation operator; he introduces the variable  $\pi = \ln(p/p_0)$ , pressure logarithm, and writes the following equation for a moving medium:

$$\frac{d^2\pi}{dt^2} - \frac{\partial}{\partial x_i} \left( c^2 \frac{\partial \pi}{\partial x_i} \right) = \gamma \frac{\partial u_i}{\partial x_j} \frac{\partial u_j}{\partial x_i} \quad (1.9)$$

where it is assumed that the flow is cold and that Reynolds number is high enough to neglect viscous stresses effects.

Considering a two-dimensional unidirectional shear mean flow  $U(x_2)$ , we write

$$u_i = U(x_2)\delta_{1i} + u'_i$$

and Equation (1.9) writes:

$$\frac{D^2\pi'}{Dt^2} - \frac{\partial}{\partial x_i} \left( c_0^2 \frac{\partial \pi'}{\partial x_i} \right) = 2\gamma \frac{\partial u'_2}{\partial x_1} \frac{dU}{dx_2} + \left\{ \gamma \frac{\partial u'_i}{\partial x_j} \frac{\partial u'_j}{\partial x_i} - \overline{\gamma \frac{\partial u'_i}{\partial x_j} \frac{\partial u'_j}{\partial x_i}} \right\} \quad (1.10)$$

where  $D/Dt$  is the derivation operator following the mean flow:

$$\frac{D}{Dt} = \frac{\partial}{\partial t} + U \frac{\partial}{\partial x_1}$$

Equation (1.10) presents the advantage that density  $\rho$  is taken out from the source term. However, the propagation operator does not contain all the interactions of the mean flow with the acoustic field; indeed, the acoustic source term proportional to the shear  $dU/dx_2$  is linear in fluctuations and thus is associated to the refraction of acoustic waves.

### Lilley's formulation

Lilley<sup>66</sup> (1972) has proposed to derive Equation (1.10) with respect to time, and he has obtained the following third order differential equation:

$$\frac{d}{dt} \left\{ \frac{d^2 \pi}{dt^2} - \frac{\partial}{\partial x_i} \left( c^2 \frac{\partial \pi}{\partial x_i} \right) \right\} + 2 \frac{\partial u_i}{\partial x_j} \frac{\partial}{\partial x_i} \left( c^2 \frac{\partial \pi}{\partial x_i} \right) = -2\gamma \frac{\partial u_i}{\partial x_j} \frac{\partial u_j}{\partial x_k} \frac{\partial u_k}{\partial x_i}$$

In the case of the two-dimensional unidirectional shear mean flow, simplifications lead to the total propagation operator:

$$\frac{D}{Dt} \left\{ \frac{D^2 \pi'}{Dt^2} - c_0^2 \left( \frac{\partial^2 \pi'}{\partial x_i \partial x_j} \right) \right\} + 2c_0^2 \frac{dU}{dx_2} \frac{\partial^2 \pi'}{\partial x_1 \partial x_2} = \mathcal{Q}(\mathbf{x}, t) \quad (1.11)$$

The source term  $\mathcal{Q}(\mathbf{x}, t)$  in the right-hand-side contains no term linear in fluctuations, thus all mean flow effects on acoustic waves are included in the left-hand-side propagation operator. Besides, the third order propagation operator of Lilley's equation contains not only acoustic pressure fluctuations, but also pressure fluctuations linked to the aerodynamic instabilities of the flow. Solving this differential equation is non trivial, because the Green's function in free field is only known for asymptotic developments at high or low frequencies. Moreover, it is impossible to derive a generalization to any mean flow, making this analogy useful in a very limited number of cases.

### Goldstein: use of a convected wave equation

After Phillips and Lilley, Goldstein<sup>55</sup> has written his own theory consisting in a wave equation convected in the observer medium:

$$\nabla^2 p' - \frac{1}{c_0^2} \frac{D_\infty^2 p'}{Dt^2} = \frac{\partial^2 \tilde{T}_{ij}}{\partial x_i \partial x_j} \quad (1.12)$$

where  $D_\infty/Dt$  is the derivative operator following the mean flow defined as

$$\frac{D_\infty}{Dt} = \frac{\partial}{\partial t} + U_\infty \frac{\partial}{\partial x_1} \quad (1.13)$$

if we consider a mean flow with a constant component  $U_\infty$  in the first direction  $x_1$ . Note that the mean flow is here constant and spatially uniform (it is the mean flow present in the observer region). The source term  $\tilde{T}_{ij}$  is now defined as

$$\tilde{T}_{ij} = \rho \tilde{u}_i \tilde{u}_j + (p' - c_0^2 \rho') \delta_{ij} - \tau_{ij} \quad \text{and} \quad \tilde{u}_i = u_i - \delta_{i1} U_\infty$$

Although this equation is similar to Lighthill's Equation (1.6), it differs from it in two respects. First, it involves a moving-medium wave equation instead of a stationary medium

wave equation, with the use of time derivative of Equation (1.13) following the mean flow instead of  $\partial/\partial t$ . Second, Lighthill's stress tensor is expressed in terms of the relative velocity  $\tilde{u}_i = u_i - \delta_{i1}U_\infty$  instead of the total velocity  $u_i$ . The recent analogy proposed by Goldstein<sup>56</sup> aims at providing a generalized framework for noise prediction methods in the form of linearized inhomogeneous Euler equations.

### 1.3.2.3 Extension to solid surfaces: Curle and Ffowcs Williams & Hawkings developments

#### Curle's analogy

In his second paper in 1954<sup>65</sup>, Lighthill mentions the importance of solid surface on the generation of sound and suggests that they should be taken into account by a *surface integral, whose physical interpretation is easily verified to be the dipole radiation associated with the force between the solid boundary and the fluid*<sup>65</sup>. In 1955, Curle<sup>30</sup> brings some formalism to these assumptions by including solid surfaces in the formulation.

Indeed, Curle<sup>30</sup>, in reference to Stratton<sup>99</sup>, gives the following solution to the inhomogeneous wave Equation (1.6):

$$\rho - \rho_0 = \frac{1}{4\pi c_0^2} \iiint_{\mathcal{V}} \frac{\partial^2 T_{ij}}{\partial y_i \partial y_j} \frac{d\mathbf{y}}{|\mathbf{x} - \mathbf{y}|} + \frac{1}{4\pi} \iint_{\mathcal{S}} \left\{ \frac{1}{r} \frac{\partial \rho}{\partial n} + \frac{1}{r^2} \frac{\partial r}{\partial n} \rho + \frac{1}{c_0 r} \frac{\partial r}{\partial n} \frac{\partial \rho}{\partial t} \right\} dS(\mathbf{y}) \quad (1.14)$$

In this equation, all quantities  $\frac{\partial^2 T_{ij}}{\partial y_i \partial y_j}$ ,  $\frac{\partial \rho}{\partial n}$ ,  $\rho$  and  $\frac{\partial \rho}{\partial t}$  are taken at the retarded time  $t - r/c_0$  where  $r = |\mathbf{x} - \mathbf{y}|$  and  $\mathbf{n}$  is the normal pointing outward from the fluid. The first integral is taken over the total volume  $\mathcal{V}$  external to solid boundaries, and the second integral is taken over the surface  $\mathcal{S}$  of the solid boundaries; this last integral represents *the effect upon the hydrodynamic flow itself of the solid boundaries*<sup>30</sup>.

After applying the divergence theorem twice, it appears that Equation (1.14) can be rewritten in a form similar to the original Lighthill's solution (1.8):

$$\rho - \rho_0 = \frac{1}{4\pi c_0^2} \frac{\partial^2}{\partial x_i \partial x_j} \iiint_{\mathcal{V}} \frac{T_{ij}(\mathbf{y}, t - r/c_0)}{r} d\mathbf{y} - \frac{1}{4\pi c_0^2} \frac{\partial}{\partial x_i} \iint_{\mathcal{S}} \frac{P_i(\mathbf{y}, t - r/c_0)}{r} dS(\mathbf{y}) \quad (1.15)$$

where  $P_i = -n_j p_{ij} = -n_j(p\delta_{ij} - \tau_{ij})$ .

In Equation (1.15), the surface integral, representing the modification to Lighthill's theory, is exactly equivalent to the sound generated in a medium at rest by a distribution of dipoles of strength  $P_i$  per unit area,  $P_i$  being the force per unit area exerted on the fluid by the solid boundaries in the  $x_i$  direction. Therefore, *one can look upon the sound field as the sum of that generated by a volume distribution of quadrupoles and by a surface distribution of dipoles*.

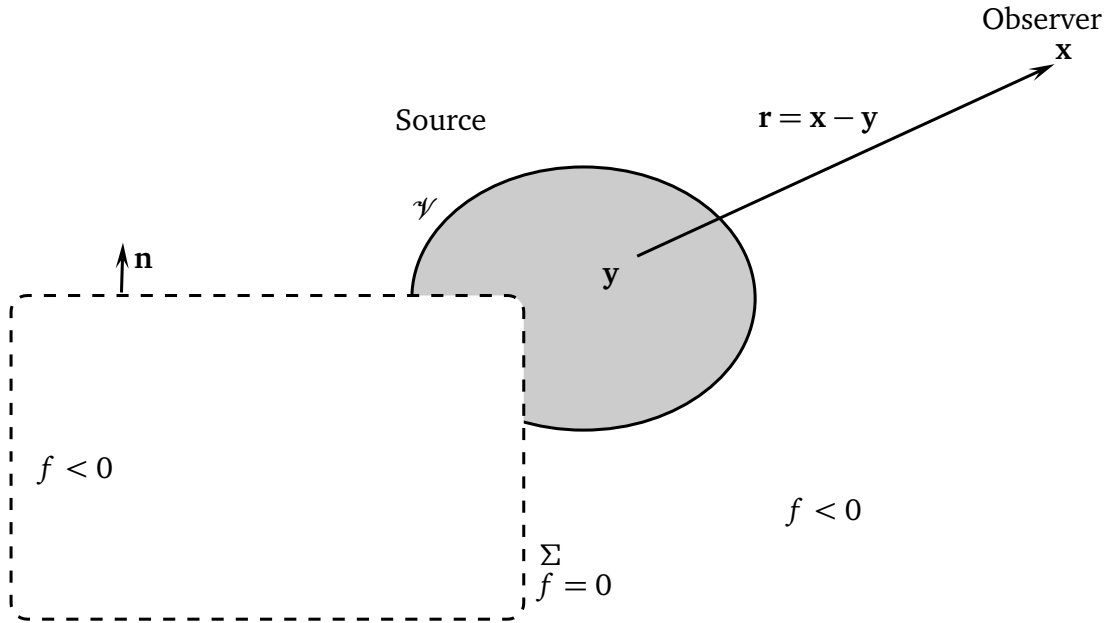


Figure 1.4 – Notations used for Ffowcs Williams & Hawkings analogy.

### Ffowcs Williams & Hawkings' analogy

In 1969, Ffowcs Williams & Hawkings<sup>44</sup> bring a mathematical correction to previous Lighthill and Curle formulations thanks to the introduction of generalized functions. Indeed, they notice that the equations of mass and momentum conservation of fluid, and thus Equation (1.4) which is a recombination of the previous ones, are valid in the region exterior to any closed internal surface that may be present; these equations are therefore valid in the volume outside the surfaces, but are meaningless elsewhere: this is an inhomogeneous situation in space. The introduction of generalized functions<sup>40</sup> can restore spatial homogeneity.

In the generalized functions formalism, we can replace the physical surface by a mathematical closed surface  $\Sigma$ , partially included in the source volume  $\mathcal{V}$ ; in order to get the most general results, we consider a not impenetrable surface  $\Sigma$ . Notations are displayed in Figure 1.4. By definition,  $f(\mathbf{x}, t) = 0$  on the surface,  $f$  is positive in the fluid surrounding the surface and  $f$  is negative inside  $\Sigma$ . Moreover,  $\Sigma$  is moving at the velocity  $\mathbf{u}^\Sigma$ . Thus the evolution of the surface is given by

$$\frac{\partial f}{\partial t} + \mathbf{u}^\Sigma \cdot \nabla f = 0$$

and the unit normal outward to surface  $\Sigma$  is defined as

$$\frac{\nabla f}{|\nabla f|} = \mathbf{n}$$

The discontinuous variable  $\rho H(f)$  is introduced, where  $H$  is the Heaviside function

defined as

$$H(f) = \begin{cases} 1 & \text{if } f > 0 \\ 0 & \text{if } f < 0 \end{cases}$$

With this definition, the variable  $\rho H(f)$  exists in the whole space, and the discontinuity previously present on the variable  $\rho$  is now contained in the function  $H(f)$ . This function, existing only in the framework of generalized functions<sup>17;40;41</sup>, has the following properties:

$$\begin{cases} \nabla H(f) = \delta(f) \nabla f \\ \frac{\partial H(f)}{\partial t} = \delta(f) \frac{\partial f}{\partial t} = -\delta(f) u_j^\Sigma \frac{\partial f}{\partial x_j} \end{cases}$$

The conservation equations can then be multiplied by  $H(f)$  in order to build Lighthill's equation based on the generalized fluctuations  $\rho H(f)$ . For the mass conservation equation it yields

$$\begin{aligned} \frac{\partial}{\partial t} [\rho H(f)] + \frac{\partial}{\partial x_j} [\rho u_j H(f)] &= (\rho - \rho_0) \frac{\partial f}{\partial t} \delta(f) + \rho u_j \frac{\partial f}{\partial x_j} \delta(f) \\ &= [\rho(u_j - u_j^\Sigma) + \rho_0 u_j^\Sigma] \frac{\partial f}{\partial x_j} \delta(f) \\ &= [\rho(u_n - u_n^\Sigma) + \rho_0 u_n^\Sigma] \delta(f) \end{aligned} \quad (1.16)$$

where normal velocities are defined as

$$\begin{cases} u_n = u_j \frac{\partial f}{\partial x_j} \\ u_n^\Sigma = u_j^\Sigma \frac{\partial f}{\partial x_j} \end{cases}$$

as respectively the local fluid velocity in the direction normal to the surface, and the local normal velocity of surface  $\Sigma$ . The momentum conservation equation is rewritten as:

$$\begin{aligned} \frac{\partial}{\partial t} [\rho u_i H(f)] + \frac{\partial}{\partial x_j} [(\rho u_i u_j + (p - p_0) \delta_{ij} - \tau_{ij}) H(f)] \\ &= \rho u_j \frac{\partial f}{\partial t} \delta(f) + ((p - p_0) \delta_{ij} - \tau_{ij} + \rho u_i u_j) \frac{\partial f}{\partial x_j} \delta(f) \\ &= [(p - p_0) \delta_{ij} - \tau_{ij} + \rho u_i (u_j - u_j^\Sigma)] \frac{\partial f}{\partial x_j} \delta(f) \\ &= [(p - p_0) \delta_{ij} - \tau_{ij} + \rho u_i (u_n - u_n^\Sigma)] \delta(f) \end{aligned} \quad (1.17)$$

Ffowcs Williams & Hawkings equation is then obtained by forming the equation

$$\frac{\partial(1.16)}{\partial t} - \frac{\partial(1.17)}{\partial x_i} - c_0^2 \frac{\partial^2}{\partial x_i \partial x_j} [(\rho - \rho_0) H(f)] \quad :$$

$$\left\{ \frac{\partial^2}{\partial t^2} - c_0^2 \frac{\partial^2}{\partial x_i \partial x_j} \right\} [(\rho - \rho_0)H(f)] = \frac{\partial}{\partial t} [Q\delta(f)] - \frac{\partial}{\partial x_i} [F_i\delta(f)] + \frac{\partial^2}{\partial x_i \partial x_j} [T_{ij}H(f)] \quad (1.18)$$

$$\text{with } \begin{cases} Q &= \rho(u_n - u_n^\Sigma) + \rho_0 u_n^\Sigma \\ F_i &= (p - p_0)\delta_{ij} - \tau_{ij} + \rho u_i(u_n - u_n^\Sigma) \\ T_{ij} &= \rho u_i u_j + (p - p_0)\delta_{ij} - c_0^2(\rho - \rho_0) - \tau_{ij} \end{cases} \quad (1.19)$$

The first source term  $Q$  is a monopole and the second term  $F_i$  is a dipole. Both are surface sources: they only act on the surface  $\Sigma$  as indicated by the Dirac delta function  $\delta(f)$ ;  $Q$  corresponds to the thickness noise, while  $F_i$  corresponds to the loading noise.  $T_{ij}$  is the quadrupolar Lighthill's stress tensor, as defined previously in (1.5), and the Heaviside function  $H(f)$  indicates that  $T_{ij}$  only acts throughout the volume outside the surface  $f = 0$ . This last source term is responsible of the flow self noise. Note that in absence of surface, Equation (1.18) exactly reduces to Lighthill's Equation (1.4).

Ffowcs Williams & Hawkings equation is often used for complex problems involving rotating surfaces, such as helicopter rotors. Although there is no doubt about the importance of the quadrupolar source term, this term is often neglected because of the computational resources necessary to accurately resolve the near field of the blades of a rotating machinery; indeed, it is far more easy to have a description of  $\rho$ ,  $\rho u_i$  and  $p$  on a surface than of  $T_{ij}$  in the whole volume exterior to the surface. Therefore, one can make use of a fictitious permeable surface in order to include most of the energetic volume source inside the surface, avoiding the costly computation of the volume integral. Such approaches require a great understanding of the flow field in the vicinity of the solid surface(s) in order to define the permeable surface and make sure that the volume sources left outside the surface play a minor role.

A study made by Casper *et al.*<sup>23</sup> shows, using a spectral formulation of Ffowcs Williams & Hawkings equation applied on a high-lift wing configuration, that the contribution of volume sources to the total noise is non negligible, and that the only contribution of the solid surfaces is not enough to predict the far-field radiated noise.

### 1.3.2.4 Linearized Euler Equations

In most applications, mean flows are more complex than those prescribed in Lilley's or Goldstein's analogies; it is then necessary to define a propagation operator exact for all kinds of flows. It is the case of Linearized Euler Equations (LEE), that account for all kinds

of linear interactions between acoustic fluctuations and any aerodynamic mean flow field. They can be applied in the frame of complex geometries, particularly in the case of internal flows, because the associated Green's function does not need to be known. Finally, they are easy to solve since the differential system is of first order only. As Linearized Euler Equations support acoustic fluctuations as well as aerodynamic fluctuations originating from vorticity or entropy. Therefore, instabilities may develop especially in shear zones. The control of these instabilities is still an open subject.

The derivation of Linearized Euler Equations describe the behavior of small perturbations around a steady mean flow; for this reason, each variable  $\phi$  is decomposed into a mean  $\phi_0$  and a fluctuating quantity  $\phi'$ . For a perfect gas, these equations write:

$$\left\{ \begin{array}{l} \frac{\partial \rho'}{\partial t} + \frac{\partial}{\partial x_j} (\rho' \bar{u}_j + \bar{\rho} u'_j) = 0 \\ \frac{\partial (\bar{\rho} u'_i)}{\partial t} + \frac{\partial \bar{\rho} \bar{u}_j u'_i}{\partial x_j} + \frac{\partial p'}{\partial x_i} + (\bar{\rho} u'_j + \rho' \bar{u}_j) \frac{\partial \bar{u}_i}{\partial x_j} = 0 \\ \frac{\partial p'}{\partial t} + \frac{\partial}{\partial x_j} (p' \bar{u}_j + \gamma \bar{p} u'_j) + (\gamma - 1) \left[ p' \frac{\partial \bar{u}_j}{\partial x_j} - u'_j \frac{\partial \bar{p}}{\partial x_j} \right] = 0 \end{array} \right. \quad (1.20)$$

In order to assume noise generation in the equations, and considering isentropic flows, it is necessary to introduce source terms; moreover, as the noise is exclusively generated aerodynamically, only the source term associated to the momentum equations is non-zero in the system (1.20). As shown by Bogey *et al.*<sup>15</sup>, in the case of a parallel mean flow  $u_{01} = u_{01}(x_2)$ ,  $u_{02} = 0$ , it can be written by analogy with Lilley's equation, exclusively from the terms nonlinear in turbulent velocity fluctuations:

$$S_i = -\rho_0 \left[ \frac{\partial u'_i u'_j}{\partial x_j} - \overline{\frac{\partial u'_i u'_j}{\partial x_j}} \right] \quad (1.21)$$

Thus, the source terms are only terms of turbulence noise, all the interactions between the mean aerodynamic field and acoustic waves being contained in the propagation operator. This method is used the same way as Lighthill's analogy: the source terms are provided by a separate CFD computation (either DNS or LES) on a source region, then propagated with the system of equations (1.20) on the acoustic domain enclosing the source region. Such computations are presented in Bogey<sup>9</sup>, applied successively to a mixing layer and to a high Reynolds number jet ( $M = 0.9$ ,  $Re = 6.5 \times 10^4$ ). However, the generalization to an arbitrary mean flow is still to be established.

### 1.3.2.5 Wave extrapolation methods

This class of methods does not rely on an acoustic analogy, like the hybrid methods presented previously, but rather on an extension of the near-field data to the far field. In practice, these methods are often used when an accurate compressible aerodynamic flow field description, obtained with DNS or LES, is available in the acoustic near field. A wave extrapolation method can then be applied to propagate the acoustic waves from the near field to the far field.

Integral formulations using the Green's functions formalism take the form of Kirchhoff's or Ffowcs Williams & Hawkings' methods. In Kirchhoff's method, a control surface enclosing all acoustic sources is defined; inside this surface, the noise sources and the acoustic near field is computed with CFD, and outside the surface, the acoustic pressure field is simply described by a wave equation, solved with the use of Green's functions. The wave extrapolation method based on Ffowcs Williams & Hawkings' analogy assumes a porous surface  $\Sigma$  in the analogy containing all noise sources; this leads to the suppression of the volume integral, and is very similar to Kirchhoff's method (see Gloerfelt<sup>53</sup> for details on these methods). Both formulations present a difficulty in the definition of the control (or porous) surface, the solution being sensitive to the location of this integration surface; this issue is discussed in Brentner & Farassat<sup>17</sup> and in Prieur and Rahier<sup>86</sup> for instance. In order to propagate only the acoustic fluctuations from the Kirchhoff's surface, De Roeck *et al.*<sup>32</sup> also propose an aerodynamic/acoustic splitting technique to discard aerodynamic fluctuations.

Another approach is proposed by Freund *et al.*<sup>49</sup>, with the resolution of a convected wave equation outside the aerodynamic region:

$$\Delta p - \frac{1}{c_0^2} \frac{D^2 p}{Dt^2} = 0 \quad \text{where} \quad \frac{D}{Dt} = \frac{\partial}{\partial t} + U_i \frac{\partial}{\partial x_i}$$

This method presents the advantage of discarding the problem of the integration surface; moreover, any mean flow field  $U_i$  can be considered in the propagation region. However, its application requires specific boundary conditions, and the compatibility between both computations, namely the CFD and the convected wave equation computations, has to be taken with great care. Finally, the interface between both domains and meshes can create spurious disturbances.

Linearized Euler Equations can also be applied to propagate the acoustic radiation in the far field. The same difficulty of domains linking as for the convected wave equation appears. As all fluctuating quantities are propagated, and not only the pressure, non linear problems of acoustic propagation are achievable with this method. This strength is however costly in computing time compared to previous methods of acoustic waves extrapolation.

### 1.3.3 Using CAA in complex configurations of internal flows

In complex configurations of internal flows, the first class of methods, namely Direct Noise Computation, is clearly not applicable, even when choosing a Large Eddy Simulation. Indeed, in addition to their prohibitive computational cost, the optimized high order finite differences discretization schemes (Bogey *et al.*<sup>10</sup>) and boundary conditions (Tam & Dong<sup>102</sup>) usually required are not currently developed for complex geometries; these schemes are designed for cartesian meshes. Recently, extensions have been made to fit more complex shapes, such as cylinders or airfoils, using curvilinear coordinates (see Marsden<sup>68</sup>), while preserving the accuracy of the schemes. However, these codes are currently not able to tackle complex geometries of industrial interest. Besides, wave extrapolation methods are not appropriate for internal acoustic propagation for evident reasons: the computing time required for free field wave radiation will be lost when surfaces are to be accounted for; moreover, the development of Green's function tailored to complex geometries is almost impossible.

Besides, some of the hybrid methods described in previous sections are either not applicable, or not appropriate for the present study of aeroacoustic noise radiation of internal low Mach number flows. Indeed, Phillips' and Lilley's analogies are defined for particular unidirectional uniform and shear flows, no expression being derived or even derivable for ordinary flows. Although Goldstein's analogy could be consistent, we stress here that in the context of low Mach number flows, the mean flow effects on the acoustic propagation, radiation and scattering can be neglected and will be in the remaining of this study.

Lighthill's equation, where no assumption has been raised, can be implemented in a finite element framework in order to conform to any geometric complexity, the source term being described thanks to Computational Fluid Dynamics. We give in chapter 2 the formalism used in this study, where a variational formulation of Lighthill's equation, originally written by Oberai *et al.*<sup>76</sup>, is derived. This implementation presents the advantage of being applicable in an industrial context using free or commercial computing codes; indeed, the only requirement for CFD is to perform a Large Eddy Simulation accurately in any geometry, which is achieved by almost all finite volumes codes having central differencing schemes for spatial discretization; for the acoustic computational step, Free Field Technologies<sup>46</sup> have implemented a variational formulation of Lighthill's Acoustic Analogy in its spectral finite elements code Actran/LA<sup>20;21;46</sup>, see Sandbodge *et al.*<sup>92</sup> for instance regarding recent applications. Moreover, Lighthill's Acoustic Analogy only requires an incompressible definition of the Lighthill's source term for low Mach number flows, which reduces the simulation time.

Another method of practical interest has been recently proposed by Schram *et al.*<sup>93</sup>, combining Curle's analogy with a Boundary Element Method. This method is similarly applicable in complex geometries, and noise sources are provided by an incompressible

Large Eddy Simulation of the low Mach number flow field. We refer the reader to Schram *et al.*<sup>93</sup> and Martínez-Lera *et al.*<sup>71</sup> for details on this method.

## 1.4 Organization of the manuscript

The manuscript is organized so as to reflect the general progression of the work, from the study of academic cases to validate the methodology to the application to a slice, then three-dimensional geometry, the main developments of this work being spread in Chapters 3 and 4.

The second chapter handles the theoretical aspects of this work, with detailed developments of the spectral variational formulation of Lighthill's Acoustic Analogy. Practical aspects of the implementation in the finite elements framework are firstly addressed, with the discretization and boundary conditions problems; the infinite elements, necessary for free far field radiation in the finite elements context, are in particular specified. In a second section, the requirements for noise sources description are focused at; Large Eddy Simulation principles are reminded, and some discretization, boundary conditions and solver specificities in CFD code Fluent are given. In the last section of this chapter, the practical application of the method is examined, with a detailed description of the steps involved when applying the method. The potential issues associated with the method are finally given, and some hints from the literature enable to consider applicable solutions.

The third chapter presents the validation of the method thanks to academic studies. In particular, the source term definition is studied, in a will to clarify the role of the linear source terms in Lighthill's tensor; to this purpose, the system of two corotating vortices evolving in a medium at rest is studied. The variational formulation of Lighthill's Acoustic Analogy is applied, considering two source terms: a first term obtained using the total velocities, and the second using the fluctuating velocities; results are validated by comparison to a Direct Numerical Simulation and an analytical resolution of Lighthill's Acoustic Analogy. The addition of a mean shear layer enables moreover to study the effects of a mean flow on the acoustic radiation. The issue of turbulent structures leaving the domain, creating spurious noise at the boundary, is then considered with the convection of a perfect vortex crossing a virtual boundary; spatial filters are developed to alter the spurious dipolar radiation created at the boundary. Finally, the mesh interpolation, which is a challenging and crucial issue when applying hybrid methods combining several computational domains and meshes, is tackled; while a complete study has not been performed, general rules are developed, which help designing the acoustic mesh knowing the CFD mesh and the corresponding turbulent aerodynamic flow field.

The last chapter presents the application of the hybrid noise prediction method to a real case consisting of a straight rectangular duct obstructed by a diaphragm. This case presents the advantage of being simple to handle numerically, as a cartesian mesh is straightforward,

but the aerodynamic features are complex enough to consider it as a challenging validation case. The turbulence and noise are solely created by the geometry changes, namely successive sharp restriction and expansion, which allows to discard the tricky problems of turbulent inlet boundary conditions and transition to turbulence at the wall. The study of a low Mach number flow, with an inlet velocity of 6 m/s, enables to use the conventional approximation for Lighthill's tensor  $T_{ij} \simeq \rho_0 u_i u_j$ . The diaphragm model is firstly reduced in the spanwise direction to a slice of 10% of the total span, corresponding to an extrusion of the two-dimensional model over ten cells. A Large Eddy Simulation is performed and aerodynamic results are compared to reference results. The limitations of this case are shown to be linked to the geometry restriction in the third direction, where turbulent structures do not have enough space to develop. Therefore, the complete three-dimensional flow field is computed and the hybrid noise prediction method is applied. The aerodynamic flow features are consistent with those found in similar studies; the acoustic radiation, computed with Actran/LA, is also found to be consistent with both numerical and experimental reference results.

Conclusions and prospects are drawn in chapter 5. Two annexes close this document; the first one is dedicated to a two dimensional Large Eddy Simulation on the diaphragm geometry, showing the inconsistency of such an approach; the second one deals with spatial filters used to remove grid-to-grid oscillations from the full scale diaphragm computation.

## 2.

# Theoretical foundations of the computational method

---

*T*HIS CHAPTER is dedicated to the detailed presentation of the Computational AeroAcoustics method used in this work and its implementation. It is a two steps hybrid approach relying on Lighthill's Acoustic Analogy<sup>64</sup>, assuming the decoupling of noise generation and propagation. The first step consists of an incompressible Large Eddy Simulation of the turbulent flow field, during which a source term is recorded on a given time interval. In the second step, a variational formulation of Lighthill's Acoustic Analogy discretized in the finite element framework is solved in the Fourier space, providing the radiated noise up to the free field thanks to the use of infinite elements<sup>46</sup>. The finite element implementation allows complex geometries to be studied, and the spectral formulation presents the advantage of discarding the problem of retarded times, always present when working with Lighthill's Acoustic Analogy in time formulations.

A detailed description of Lighthill's Acoustic Analogy implementation in a spectral finite element framework is firstly presented; acoustic propagation is also explained in this particular discretization space, as well as acoustic boundary conditions used in this work, namely infinite elements and modal duct bases. Then, acoustic sources modeling is introduced with the use of Computational Fluid Dynamics; Large Eddy Simulation is discussed along with discretization in space and time, boundary conditions and initial conditions. Finally, an overview of the method is outlined, with a description of all steps involved in the practical application of Fluent-Actran/LA coupling. Potential issues associated to the computational method are dealt with at the end of the chapter, and some hints being proposed to overcome the difficulties.

## 2.1 Lighthill's Acoustic Analogy applied in a spectral finite element framework

### 2.1.1 Variational formulation of Lighthill's Acoustic Analogy

The implementation of Lighthill's Acoustic Analogy was firstly derived by Oberai *et al.*<sup>76</sup>, and further developed and implemented in the finite/infinite elements framework by Caro *et al.*<sup>20;21</sup>; refer also to Actran User's Guide<sup>46</sup> for details on implementation and discretization. The starting point is Lighthill's equation:

$$\frac{\partial^2}{\partial t^2}(\rho - \rho_0) - c_0^2 \frac{\partial^2}{\partial x_i \partial x_i}(\rho - \rho_0) = \frac{\partial^2 T_{ij}}{\partial x_i \partial x_j} \quad (2.1)$$

with

$$T_{ij} = \rho u_i u_j + \delta_{ij}((p - p_0) - c_0^2(\rho - \rho_0)) - \tau_{ij} \quad (2.2)$$

where  $\rho$  is the density and  $\rho_0$  its reference value in a medium at rest,  $c_0$  is the reference sound velocity,  $T_{ij}$  is Lighthill's tensor,  $u_i$  are the components of the fluid velocity,  $p$  is the pressure and  $\tau_{ij}$  is the viscous stress tensor. The strong variational statement associated to Equation (2.1) is written as:

$$\int_{\Omega} \left( \frac{\partial^2}{\partial t^2}(\rho - \rho_0) - c_0^2 \frac{\partial^2}{\partial x_i \partial x_i}(\rho - \rho_0) - \frac{\partial^2 T_{ij}}{\partial x_i \partial x_j} \right) \delta \rho \, d\mathbf{x} = 0 \quad \forall \delta \rho \quad (2.3)$$

where  $\delta \rho$  is a test function and  $\Omega$  designates the computational domain. Following Green's theorem, the previous equation is integrated by parts along space derivatives:

$$\begin{aligned} \int_{\Omega} \left( \frac{\partial^2}{\partial t^2}(\rho - \rho_0) \delta \rho + c_0^2 \frac{\partial}{\partial x_i}(\rho - \rho_0) \frac{\partial \delta \rho}{\partial x_i} + \frac{\partial T_{ij}}{\partial x_j} \frac{\partial \delta \rho}{\partial x_i} \right) d\mathbf{x} = \\ \int_{\partial\Omega=\Gamma} \left( c_0^2 \frac{\partial}{\partial x_i}(\rho - \rho_0) n_i + \frac{\partial T_{ij}}{\partial x_j} n_i \right) \delta \rho \, d\Gamma(\mathbf{x}) \quad \forall \delta \rho \end{aligned} \quad (2.4)$$

with  $n_i$  the normal pointing outward of  $\Omega$ . Replacement of  $T_{ij}$  by its definition using Equation (2.2) leads to:

$$\begin{aligned} \int_{\Omega} \left( \frac{\partial^2}{\partial t^2}(\rho - \rho_0) \delta \rho + c_0^2 \frac{\partial}{\partial x_i}(\rho - \rho_0) \frac{\partial \delta \rho}{\partial x_i} + \frac{\partial T_{ij}}{\partial x_j} \frac{\partial \delta \rho}{\partial x_i} \right) d\mathbf{x} = \\ \int_{\Gamma} \frac{\partial}{\partial x_j} (\rho u_i u_j + (p - p_0) \delta_{ij} - \tau_{ij}) n_i \delta \rho \, d\Gamma(\mathbf{x}) \quad \forall \delta \rho \end{aligned} \quad (2.5)$$

After having defined  $\Sigma_{ij}$  as

$$\Sigma_{ij} = \rho u_i u_j + (p - p_0) \delta_{ij} - \tau_{ij}, \quad (2.6)$$

the equation on the acoustic density fluctuations  $\rho_a = \rho - \rho_0$  is finally derived:

$$\int_{\Omega} \left( \frac{\partial^2 \rho_a}{\partial t^2} \delta \rho + c_0^2 \frac{\partial \rho_a}{\partial x_i} \frac{\partial \delta \rho}{\partial x_i} \right) d\mathbf{x} = - \int_{\Omega} \frac{\partial T_{ij}}{\partial x_j} \frac{\partial \delta \rho}{\partial x_i} d\mathbf{x} + \int_{\Gamma} \frac{\partial \Sigma_{ij}}{\partial x_j} n_i \delta \rho d\Gamma(\mathbf{x}) \quad \forall \delta \rho \quad (2.7)$$

In this formulation, called the variational formulation of Lighthill's analogy, we gave rise to two source terms: a volume term and a surface term. Similarly to Ffowcs Williams & Hawkings' equation for the terminology, the volume source term is associated to flow self noise, while the surface source term corresponds to loading noise. Recalling the momentum equation

$$\frac{\partial \rho u_i}{\partial t} + \frac{\partial \rho u_i u_j}{\partial x_j} = - \frac{\partial}{\partial x_j} (p \delta_{ij} - \tau_{ij})$$

we can write

$$n_i \frac{\partial \Sigma_{ij}}{\partial x_j} = n_i \frac{\partial}{\partial x_j} (\rho u_i u_j + (p - p_0) \delta_{ij} - \tau_{ij}) = -n_i \frac{\partial}{\partial t} (\rho u_i) \quad (2.8)$$

As a result, if the surface  $\Gamma$  is fixed or vibrating in its own plane, the expression (2.8) reduces to zero.

In practice, the surface source term can be used in only one circumstance: when the surface is a fixed virtual surface. Indeed, the spectral formulation is unable to take into account the displacement of solid surfaces. Besides, in the case of a rotating machine, where the rotating part is enclosed in a fixed volume, a control surface, also called porous surface, can be defined, and the source term  $\partial \Sigma_{ij} / \partial x_j$  accounts for the effect of the flow enclosed inside the control surface on noise generation. In the following of this study, we only consider fixed solid surfaces without rotating parts, and no porous surface is defined; the surface source term thus vanishes. Moreover, we adopt the following vector notation for the volume source term:

$$S_i = \frac{\partial T_{ij}}{\partial x_j}. \quad (2.9)$$

### 2.1.2 Spectral formulation

As Actran/LA is written in the frequency domain, Equation (2.7) is transformed to the spectral space thanks to a conventional Fourier transform. The time Fourier transform of a signal  $\phi(\mathbf{x}, t)$  is defined as

$$\mathcal{F}[\phi(\mathbf{x}, t)] = \hat{\phi}(\mathbf{x}, \omega) = \int_{-\infty}^{\infty} \phi(\mathbf{x}, t) e^{-i\omega t} dt \quad (2.10)$$

where  $\omega = 2\pi f$  is the angular pulsation. Adopting the following notations for harmonic perturbations of any quantity  $\phi$

$$\phi(\mathbf{x}, t) = \tilde{\phi}(\mathbf{x})e^{i\omega t}$$

the spectral equation is written as:

$$\int_{\Omega} \left( -\omega^2 \tilde{\rho}_a \delta\rho + c_0^2 \frac{\partial \tilde{\rho}_a}{\partial x_i} \frac{\partial \delta\rho}{\partial x_i} \right) d\mathbf{x} = - \int_{\Omega} \frac{\partial \tilde{T}_{ij}}{\partial x_j} \frac{\partial \delta\rho}{\partial x_i} d\mathbf{x} + \int_{\Gamma} \frac{\partial \tilde{\Sigma}_{ij}}{\partial x_j} n_i \delta\rho d\Gamma(\mathbf{x}) \quad \forall \delta\rho \quad (2.11)$$

As Actran/LA is part of a large family of Actran products, a certain consistency is required to share common features, such as boundary conditions for instance. In the original and widely spread Actran software, which is designed to solve acoustic and vibration problems, a convected wave equation is implemented to enable the resolution of generation and propagation of acoustic disturbances within a flow; a continuous flow potential model is derived assuming a non-viscous fluid and a reversible, adiabatic and irrotational flow field. In this model, flow irrotationality enables to express that the velocity vector  $\mathbf{v}$  derives from a potential  $\phi$ :  $\mathbf{v} = \nabla\phi$ . The substitution of this expression into the mass and momentum conservation equations, and the decomposition of the flow variables into mean (subscript 0) and acoustic variables (subscript  $a$ ), finally leads to the convected wave equation for the acoustic velocity potential  $\phi_a$ :

$$\frac{\partial}{\partial t} \left( -\frac{\rho_0}{c_0^2} \frac{D\phi_a}{Dt} \right) + \nabla \cdot \left( \rho_0 \nabla\phi_a - \frac{\rho_0}{c_0^2} \frac{D\phi_a}{Dt} \mathbf{v}_0 \right) = 0 \quad (2.12)$$

In absence of mean flow,  $\mathbf{v}_0 = 0$  and previous equation reduces to a conventional wave equation for the acoustic velocity potential, equivalent to an acoustic pressure or density wave equation. Similarly, a convected formulation is written for most boundary conditions, using also the velocity potential  $\phi$ . In the following, the mean flow is always zero and only the non convected formulations are considered. Note that the variable change, from  $\rho_a$  to  $\phi$  or  $\tilde{\rho}_a$  to  $\tilde{\phi}$  does not mean that an hypothesis has been made on the acoustic variables.

Therefore, the variable of resolution within Actran is the transformed potential  $\tilde{\psi}$  defined as

$$\tilde{\rho}_a = -\frac{i\omega\tilde{\psi}}{c_0^2} \quad \text{and} \quad \tilde{\psi} = \rho_0\tilde{\phi}$$

As a result, the test function is now associated to the variable  $\tilde{\psi}$  and is noted  $\delta\psi$ . Making the appropriated changes in Equation (2.11) and dividing by  $\rho_0 i\omega$  leads to:

$$\int_{\Omega} \frac{1}{\rho_0} \left( k^2 \tilde{\psi} \delta\psi - \frac{\partial \tilde{\psi}}{\partial x_i} \frac{\partial \delta\psi}{\partial x_i} \right) d\mathbf{x} = \frac{i}{\rho_0 \omega} \int_{\Omega} \frac{\partial \tilde{T}_{ij}}{\partial x_j} \frac{\partial \delta\psi}{\partial x_i} d\mathbf{x} - \frac{i}{\rho_0 \omega} \int_{\Gamma} \frac{\partial \tilde{\Sigma}_{ij}}{\partial x_j} n_i \delta\psi d\Gamma(\mathbf{x}) \quad \forall \delta\psi \quad (2.13)$$

### 2.1.3 Discretization

In this section we first remind the basic equations of a finite/infinite elements discretization<sup>46</sup>. The computational acoustic domain  $\Omega$  is split into an inner domain,  $\Omega_i$ , and an outer domain,  $\Omega_o$ , with

$$\Omega = \Omega_i \cup \Omega_o$$

Conventional Galerkin finite elements are used to discretize the inner domain, and infinite elements are selected for the outer domain, if present; the solving method in this latter domain is detailed in § 2.1.4.2. In the inner domain, the discretization involves  $N_e$  finite elements noted  $\Omega^e$ :

$$\Omega_i = \bigcup_{e=1}^{N_e} \Omega^e$$

A set of interpolation functions  $\lambda_i(\xi)$ , defined in terms of local coordinates  $\xi$ , is used to interpolate locally any variable  $\tilde{\psi}$  based on its nodal values  $(\tilde{\psi}_n)_{1 \leq n \leq N_n}$ :

$$\tilde{\psi}(\mathbf{x}) = \sum_{n=1}^{N_n} \lambda_n(\xi) \tilde{\psi}_n \quad (2.14)$$

where  $N_n$  is the number of nodes and  $\lambda_n$  is the  $n$ -th shape function. Note that each shape function  $\lambda_n$  is associated to a particular node  $n$ , and satisfies  $\lambda_n(\xi_m) = \delta_{nm}$ ; the shape functions exist globally in the finite elements model, but are defined locally within each finite element. Similarly, the gradient of  $\tilde{\psi}$  can be written using the derivatives of the shape functions:

$$\nabla \tilde{\psi}(\mathbf{x}) = \sum_{n=1}^{N_n} \nabla \lambda_n(\xi) \tilde{\psi}_n \quad (2.15)$$

In matrix form, Equations (2.14) and (2.15) write

$$\tilde{\psi}(\mathbf{x}) = \mathbf{\Lambda}(\xi) \tilde{\Psi} \quad (2.16)$$

$$\nabla \tilde{\psi}(\mathbf{x}) = \mathbf{B}(\xi) \tilde{\Psi} \quad (2.17)$$

where  $\mathbf{\Lambda}$  and  $\mathbf{B}$  are matrices of size  $1 \times N_n$  and  $N_{\text{dim}} \times N_n$  respectively,  $N_{\text{dim}}$  being the problem dimension;  $\tilde{\Psi}$  is the vector of the unknown nodal values of  $\tilde{\psi}$ . In Galerkin's approach, test functions in Equation (2.13) are chosen in the functional space of shape functions and coincide with  $(\lambda_n)_{1 \leq n \leq N_n}$  at the nodes. Using Equations (2.14) and (2.15),

the discretization of (2.13) can thus be written as a system of  $N_n$  equations:

$$\begin{aligned} \sum_e \int_{\Omega^e} \frac{k^2}{\rho_0} \left( \sum_{n=1}^{N_n} \lambda_n \tilde{\psi}_n \right) \lambda_p \, d\Omega^e - \sum_e \int_{\Omega^e} \frac{1}{\rho_0} \left( \sum_{n=1}^{N_n} \nabla \lambda_n \tilde{\psi}_n \right) \cdot \nabla \lambda_p \, d\Omega^e \\ = \sum_e \frac{i}{\rho_0 \omega} \int_{\Omega^e} \nabla \tilde{T}_{ij} \cdot \nabla \lambda_p \, d\Omega^e - \sum_e \frac{i}{\rho_0 \omega} \int_{\Gamma^{e'}} \nabla \tilde{\Sigma}_{ij} \cdot \mathbf{n} \lambda_p \, d\Gamma^{e'} \end{aligned} \quad (2.18)$$

where  $1 \leq p \leq N_n$ . Exchanging the summation on  $N_n$  nodes with the integral on each finite element  $\Omega^e$  brings to:

$$\begin{aligned} \sum_e \sum_{n=1}^{N_n} \left( \frac{k^2}{\rho_0} \int_{\Omega^e} \lambda_n \lambda_p \, d\Omega^e \right) \tilde{\psi}_n - \sum_e \sum_{n=1}^{N_n} \left( \frac{1}{\rho_0} \int_{\Omega^e} \nabla \lambda_n \cdot \nabla \lambda_p \, d\Omega^e \right) \tilde{\psi}_n \\ = \sum_e \frac{i}{\rho_0 \omega} \int_{\Omega^e} \nabla \tilde{T}_{ij} \cdot \nabla \lambda_p \, d\Omega^e - \sum_e \frac{i}{\rho_0 \omega} \int_{\Gamma^{e'}} \nabla \tilde{\Sigma}_{ij} \cdot \mathbf{n} \lambda_p \, d\Gamma^{e'} \end{aligned} \quad (2.19)$$

These  $N_n$  equations on the  $N_n$  unknown values  $\tilde{\psi}_n$  are finally written in matrix form, best suited for the finite element resolution:

$$(-\mathbf{K} + \omega^2 \mathbf{M}) \tilde{\Psi} = \mathbf{F} \quad (2.20)$$

where the stiffness and mass matrices  $\mathbf{K}$  and  $\mathbf{M}$  are defined as the assembly of corresponding element matrices:

$$\mathbf{K} = \sum_e \mathbf{K}^e \quad \text{where} \quad \mathbf{K}^e = \frac{1}{\rho_0} \int_{\Omega^e} \mathbf{B}^T \mathbf{B} \, d\Omega_e \quad (2.21)$$

$$\mathbf{M} = \sum_e \mathbf{M}^e \quad \text{where} \quad \mathbf{M}^e = \frac{1}{\rho_0 c_0^2} \int_{\Omega^e} \mathbf{\Lambda}^T \mathbf{\Lambda} \, d\Omega_e \quad (2.22)$$

The vector source term  $\mathbf{F}$  on the right-hand-side of Equation (2.20) is obtained by assembling the contributions on all finite elements, separating contributions on the volume (index  $e$ ) from the contributions on the control surface (index  $e'$ ):

$$\mathbf{F} = \sum_e \mathbf{F}^e + \sum_{e'} \mathbf{F}^{e'} \quad (2.23)$$

Element matrices of source terms are given by

$$\mathbf{F}_i^e = \frac{i}{\rho_0 \omega} \int_{\Omega^e} \frac{\partial \tilde{T}_{ij}}{\partial x_j} \cdot \nabla \lambda_i \, d\Omega_e \quad (2.24)$$

$$\mathbf{F}_i^{e'} = -\frac{i}{\rho_0 \omega} \int_{\Gamma^{e'}} \frac{\partial \tilde{\Sigma}_{ij}}{\partial x_j} \cdot \mathbf{n} \lambda_i \, d\Gamma_{e'} \quad (2.25)$$

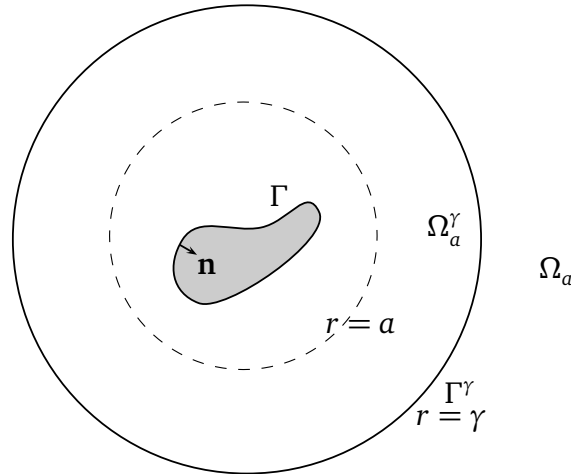


Figure 2.1 – Notations for the derivation of the finite/infinite variational formulation.

## 2.1.4 Boundary conditions

In this section, all variables are supposed to be expressed in the frequency domain; therefore, the  $\tilde{\cdot}$  notation will be omitted to lighten the equations.

### 2.1.4.1 Natural boundary condition

In presence of a solid boundary  $\Gamma$ , the surface source term in the variational formulation (2.7) vanishes, according to Equation (2.8). The appropriate boundary condition which must be satisfied on  $\Gamma$  is

$$\frac{\partial p}{\partial x_i} n_i = -\rho a_n \quad (2.26)$$

where  $a_n(\mathbf{x}, \omega)$  is the prescribed normal surface acceleration on  $\Gamma$ . This corresponds to the natural boundary condition associated with the weak variational problem.

### 2.1.4.2 Infinite elements

The use of infinite elements, refer to the works of Astley & Coyette<sup>4;5</sup>, Van den Nieuwenhof & Coyette<sup>108;109</sup>, and of Astley<sup>3</sup> for a recent review on infinite elements, allows to compute the far field acoustic radiation outside the physical domain, by enforcing the Sommerfeld radiation condition at large distances from the aeroacoustic sources. Infinite elements are based on the multipole expansion of the wave equation's solution; the expansion's order directly governs the accuracy of the boundary condition. The infinite element method implemented in Actran is an extension of a variable order Legendre polynomial formulation whose numerical performance has been extensively studied and assessed<sup>4;5</sup>.

### Derivation of the variational statement

The free field radiation problem can be described as follows. Considering an unbounded region  $\Omega_a = \{r \in \mathfrak{R} : r > a\}$  enclosing an acoustic source, for instance a radiating or scattering object or aeroacoustic sources, the complex pressure amplitude  $p(\mathbf{x})$  satisfies the Helmholtz equation (see Figure 2.1 for notations):

$$\nabla^2 p + k^2 p = 0 \quad (2.27)$$

where  $k = \omega/c_0$  is the wave number. Moreover, in the far field, the Sommerfeld radiation condition requires that

$$r \left( \frac{\partial p}{\partial r} + ikp \right) \rightarrow 0 \quad \text{when } r \rightarrow \infty \quad (2.28)$$

where  $r$  is a spherical polar radius. At large distances from the source, an approximation of Equation (2.28) provides the following impedance-type boundary condition:

$$\frac{\partial p}{\partial r} = -ikp + \epsilon \quad \text{at } r = \gamma \quad (2.29)$$

where  $\gamma$  is large. A truncated exterior domain  $\Omega_a^\gamma = \Omega_a \cap \{r \in \mathfrak{R} : r < \gamma\}$ , delimited by the surface  $\Gamma^\gamma$ , is thus defined. The variational statement is obtained after multiplying Helmholtz equation (2.27) by a test function  $w$ , integrating over  $\Omega_a^\gamma$  and finally integrating by parts, following the same steps as for the derivation of the variational formulation of Lighthill's Acoustic Analogy. Taking Sommerfeld's condition (2.29) and the natural boundary condition (2.26) into account leads to

$$\int_{\Omega_a^\gamma} (\nabla p \cdot \nabla w - k^2 p w) d\Omega_a^\gamma + \int_{\Gamma^\gamma} (ikpw - \epsilon w) d\Gamma^\gamma - \int_{\Gamma} \rho a_n w d\Gamma = 0 \quad \forall w \quad (2.30)$$

As the integration is performed over the finite domain  $\Omega_a^\gamma$ , the solution  $p$  and its gradient must be square integrable over this region. In the limit  $\gamma \rightarrow \infty$ , this condition is achieved here by applying the Cauchy Principal Value method while it is also possible to weight the test functions to make them  $L^2$ -integrable<sup>51</sup>. It will be shown later that the chosen trial and test functions make the left-hand-side of Equation (2.30) well-defined in the Cauchy principal sense. In addition, for these formulations, the term

$$\int_{\Gamma^\gamma} \epsilon w d\Gamma^\gamma \quad (2.31)$$

vanishes as  $\gamma \rightarrow \infty$  and will be discarded in the following.

Note that, in the previous developments, the region  $\Omega_a$  is assumed to be a sphere for

the sake of clarity, but the infinite element methodology has been shown to apply similarly on more general shapes, such as spheroids or ellipsoids.

### Holford expansion

Considering that only outwardly propagating solutions are present in the unbounded region  $\Omega_a$ , Holford's expansion theorem<sup>114</sup> states that the complex pressure amplitude  $p(r, \theta, \phi)$ , expressed in the spherical polar coordinates  $r$ ,  $\theta$  and  $\phi$ , can be represented in this region by a uniformly convergent series of multipole terms of the form

$$p(r, \theta, \phi) = e^{-ikr} \sum_{v=1}^{\infty} \frac{G_v(\theta, \phi)}{(r/a)^v} \quad (2.32)$$

where  $G_v(\theta, \phi)$  is a directivity function. The leading term in Equation (2.32) gives the expected behavior  $p(r, \theta, \phi) \propto e^{-ikr}/r$  in the far field, while the remaining terms contribute to the near and intermediate field. In practice, the sum (2.32) is truncated; the number of retained terms, which will actually be the order of infinite elements, determines the extent to which the truncated expansion is able to resolve near field effects.

This result has been shown to hold also for spheroidal and ellipsoidal coordinates<sup>19</sup>, with substitution of spherical coordinates  $r$ ,  $\theta$  and  $\phi$  by the spheroidal coordinates  $\rho$ ,  $\vartheta$  and  $\varphi$ , and the performance of these formulations has been successfully assessed<sup>5</sup>.

### Infinite elements trial solution

The infinite element trial solution  $\tilde{p}(\mathbf{x})$  is defined similarly, taking the form

$$\tilde{p}(r, \theta, \phi) = \sum_{\mu=1}^m \sum_{v=1}^n q_{\mu v} Q_{\mu v}(r, \theta, \phi) \quad (2.33)$$

where  $q_{\mu v}$  and  $Q_{\mu v}(r, \theta, \phi)$  are respectively unknown coefficients and known interpolation functions. The interpolation functions are written as products of radial and transverse shape functions  $f_v(r/a)$  and  $g_\mu(\theta, \phi)$ :

$$Q_{\mu v}(r, \theta, \phi) = f_v(r/a) g_\mu(\theta, \phi)$$

The summations over  $v$  and  $\mu$  correspond to discretization in the radial and transverse directions, respectively. The transverse basis functions  $g_\mu(\theta, \phi)$  are defined as global shape functions of a finite element surface discretization of  $\Gamma_\gamma$ . The radial basis functions  $f_v(r/a)$  are defined as the product of an outwardly propagating wave-like term,  $e^{-ikr}$ , and a poly-

nomial of order  $n$  in inverse powers of  $r/a$ :

$$f_\nu(r/a) = e^{-ik(r-a)} \times \left(\frac{a}{r}\right) \times F_\nu(a/r) \quad (2.34)$$

where  $F_\nu(a/r)$  is the shifted Legendre polynomial of order  $\nu - 1$ .

### Test functions

Test functions  $w$  are chosen in a form similar to trial functions:

$$w(r, \theta, \phi) = \sum_{\mu=1}^m \sum_{\nu=1}^n q_{\mu\nu} \left(\frac{a}{r}\right)^2 \{Q_{\mu\nu}(r, \theta, \phi)\}^* \quad (2.35)$$

where  $*$  denotes the complex conjugate; this is the Astley-Leis formulation<sup>2</sup>.

Note that, from the expression of test and trial functions with the canceling factors  $e^{+ikr}$  and  $e^{-ikr}$ , the term (2.31) vanishes as  $\gamma \rightarrow \infty$ . Moreover, this conjugated infinite element formulation assures the well-definition of Equation (2.30) in the Cauchy principal sense as shown by Astley<sup>2</sup>.

### Matrix expression

The unknown trial coefficient  $q_{\mu\nu}$  can be renumbered using a single index and placed in the vector  $\mathbf{q}$  of length  $N = m \times n$ . The complete system of linear equations is then obtained by substituting the expression (2.33) of trial functions into the variational statement (2.30) and evaluating the resulting expression for the test functions (2.35). In the limit  $\gamma \rightarrow \infty$ , this gives

$$\mathbf{A}\mathbf{q} = \mathbf{f} \quad (2.36)$$

where the matrix components of  $\mathbf{A}$  and  $\mathbf{f}$  are given by

$$\left\{ \begin{array}{l} A_{\alpha\beta} = \lim_{\gamma \rightarrow \infty} \left\{ \int_{\Omega_a^\gamma} (\nabla w_\alpha \cdot \nabla Q_\beta - k^2 w_\alpha Q_\beta) d\Omega_a^\gamma + ik \int_{\Gamma^\gamma} w_\alpha Q_\beta d\Gamma^\gamma \right\} \\ f_\alpha = \int_{\Gamma} \rho a_n w_\alpha d\Gamma \quad \text{where} \quad 1 \leq \alpha, \beta \leq N \end{array} \right.$$

#### 2.1.4.3 Modal surfaces

In the diaphragm application case, infinite acoustic ducts have to be modeled at the upstream and downstream boundary conditions to reflect the testing conditions, namely anechoic ends. The modal behavior of rectangular hard walled ducts is therefore described in this section according to their definition and implementation in Actran<sup>46</sup>, knowing that the developments for circular, annular or arbitrary cross-sections are similar. The devel-

opments presented here apply to zero flow case in the axial direction; indeed, for the low Mach numbers considered in this study, mean flow effects are supposed negligible.

### Analytical developments

In Cartesian coordinates, the acoustic wave equation writes

$$\frac{\partial^2 \phi}{\partial x^2} + \frac{\partial^2 \phi}{\partial y^2} + \frac{\partial^2 \phi}{\partial z^2} + k^2 \phi = 0 \quad (2.37)$$

where  $\phi$  is the acoustic velocity potential. The acoustic pressure  $p$  is given by

$$p = -i\rho_0 c_0 k \phi$$

and the acoustic velocity vector  $\mathbf{v}$  is

$$\mathbf{v} = \nabla \phi.$$

A general solution of Equation (2.37) expressed in terms of duct modes is

$$\phi(x, y, z) = \sum_{s=0}^{\infty} C_s^\phi \phi_s(x, y) e^{-ik_s z} \quad (2.38)$$

where  $\phi_s(x, y)$  are the eigenfunctions of the Laplace operator in a cross-section of a duct;  $\phi_s(x, y)$  undergoes the rigid wall boundary condition, namely  $\partial \phi_s(x, y) / \partial n = 0$ . In these developments, the duct modes, orthogonal to each other, are normalized according to the following scalar product

$$\frac{1}{S} \int_S \phi_s(x, y) \phi_r^*(x, y) dS = \delta_{sr} \quad (2.39)$$

where  $S$  is the cross-sectional area of the considered duct. Equation (2.38) enables to write the following expressions for the pressure  $p_s$  associated to a given duct mode

$$p_s(x, y, z) = C_s^p \phi_s(x, y) e^{-ik_s z} \quad \text{where} \quad C_s^p = \frac{C_s^\phi}{-i\rho_0 c_0 k}$$

and for the acoustic velocity  $v_{sz}$  along the duct axis

$$v_{sz} = \frac{C_s^p k_s}{\rho_0 c_0 k} \phi_s(x, y) e^{-ik_s z}$$

For a duct of rectangular cross-section with transverse dimensions  $a$  and  $b$ , the solution of Equation (2.37) writes

$$\phi(x, y, z) = \sum_{m=0}^{\infty} \sum_{n=0}^{\infty} \cos\left(\frac{m\pi x}{a}\right) \cos\left(\frac{n\pi y}{b}\right) (a_{mn}^+ e^{-ik_{zmn}^+ z} + a_{mn}^- e^{-ik_{zmn}^- z})$$

where  $m$  and  $n$  denote the modal orders along transverse directions  $x$  and  $y$  respectively, and  $k_{zmn}^+$  and  $k_{zmn}^-$  are the longitudinal wave numbers. Each mode  $(m, n)$  can be examined through

$$\phi_{mn}(x, y, z) = A_{mn}^\phi N_{mn} \cos(k_{xm}x) \cos(k_{yn}y) e^{-ik_{zmn}z}$$

where  $N_{mn}$  is the normalization factor, and having introduced the notations  $k_{xm} = m\pi/a$  and  $k_{yn} = n\pi/b$ . Similarly, we can write

$$p_{mn}(x, y, z) = A_{mn}^p N_{mn} \cos(k_{xm}x) \cos(k_{yn}y) e^{-ik_{zmn}z} \quad \text{where} \quad A_{mn}^p = \frac{A_{mn}^\phi}{-i\rho_0 c_0 k}$$

Note that these expressions comply with the rigid wall boundary condition at  $x = 0$ ,  $x = a$ ,  $y = 0$  and  $y = b$  since

$$\left. \frac{\partial \phi}{\partial x} \right|_{x=0} = \left. \frac{\partial \phi}{\partial x} \right|_{x=a} = \left. \frac{\partial \phi}{\partial y} \right|_{y=0} = \left. \frac{\partial \phi}{\partial y} \right|_{y=b} = 0$$

The longitudinal wave numbers  $k_{zmn}^+$  and  $k_{zmn}^-$  are obtained using the dispersion relation:

$$k_{zmn}^+ = \sqrt{k^2 - (k_{xm}^2 + k_{yn}^2)} \quad \text{and} \quad k_{zmn}^- = -\sqrt{k^2 - (k_{xm}^2 + k_{yn}^2)}$$

which results in mode  $(m, n)$  cut-on frequency  $k_{co} = \sqrt{k_{xm}^2 + k_{yn}^2}$ . The normalization condition (2.39) is rewritten as

$$\frac{1}{ab} \int_0^a \int_0^b |N_{mn}|^2 \cos^2(k_x x) \cos^2(k_y y) dx dy = 1$$

yielding

$$N_{mn} = \frac{2}{\sqrt{(1 + \delta_{m0})(1 + \delta_{n0})}}.$$

### Matrix formulation

Considering that modal coupling acts on the boundary  $\Gamma_{\text{mod}}$ , a new term appears on the right-hand-side of the variational formulation (2.13):

$$-\frac{1}{\rho_0} \int_{\Gamma_{\text{mod}}} \delta\psi n_i \frac{\partial \psi}{\partial x_i} d\Gamma_{\text{mod}} \quad (2.40)$$

$N_{\text{mod}}$  selected modes  $\Phi_i$  are used to express the boundary variable  $\psi$  on  $\Gamma_{\text{mod}}$ , with

$$\psi(\mathbf{x}, \omega) = \sum_{i=1}^{N_{\text{mod}}} \Phi_i(\mathbf{x}, \omega) \alpha_i$$

where  $\alpha_i$  is the participation factor of  $i$ -th mode  $\Phi_i$ . After substitution into term (2.40) and discretization, the contribution of modal components to the discrete right-hand-side vector  $\mathbf{F}$  of Equation (2.20) is

$$\mathbf{F}^{\text{mod}} = \sum_e \mathbf{F}^{\text{mod},e} \quad \text{or} \quad \mathbf{F}^{\text{mod}} = \alpha \mathbf{D} = \alpha \sum_e \mathbf{D}^e \quad (2.41)$$

where  $\alpha$  is the vector of modal participation factors, and matrix  $\mathbf{D}$  is built by assembling the element boundary contributions; matrix components of an element contribution are expressed as

$$\mathbf{D}_{ij}^e = -\frac{1}{\rho_0} \int_{\Gamma_{\text{mod}}}^e N_i n_k \frac{\partial \Phi_j}{\partial x_k} d\Gamma_{\text{mod}}^e \quad (2.42)$$

### Procedure to solve the modal-FE coupling

The coupling between modal components and the Finite Elements (FE) system, the latter being of the form  $\mathbf{A}\Psi = \mathbf{F}$ , see Equation (2.20), is obtained by splitting the solution vector  $\Psi$  into subvectors  $\Psi_{\text{mod}}$  and  $\Psi_r$  related to the number of nodes on the modal basis and in the remaining of the model, respectively. The right-hand-side vector  $\mathbf{F}$  and matrix  $\mathbf{A}$  are split accordingly:

$$\begin{bmatrix} \mathbf{A}_{rr} & \mathbf{A}_{ri} \\ \mathbf{A}_{ir} & \mathbf{A}_{ii} \end{bmatrix} \begin{pmatrix} \Psi_r \\ \Psi_{\text{mod}} \end{pmatrix} = \begin{pmatrix} \mathbf{F}_r \\ \mathbf{F}_{\text{mod}} \end{pmatrix} \quad (2.43)$$

where  $\mathbf{F}_{\text{mod}} = \mathbf{D}\alpha$  and  $\Psi_{\text{mod}} = \Phi\alpha$ . The coupled modal-finite element system then writes

$$\begin{bmatrix} \mathbf{A}_{rr} & \mathbf{A}_{ri} & \mathbf{0} \\ \mathbf{A}_{ir} & \mathbf{A}_{ii} & \mathbf{D} \\ \mathbf{0} & \mathbf{E} & \mathbf{H} \end{bmatrix} \begin{pmatrix} \Psi_r \\ \Psi_{\text{mod}} \\ \alpha \end{pmatrix} = \begin{pmatrix} \mathbf{F}_r \\ \mathbf{0} \\ \mathbf{0} \end{pmatrix} \quad (2.44)$$

where coupling matrices  $\mathbf{E}$  and  $\mathbf{H}$  express the continuity between the modal and finite element solutions on the modal surface  $\Gamma_{\text{mod}}$ , expressed for the  $i$ -th mode as

$$\int_{\Gamma_{\text{mod}}} \Phi_i^* \left( \Psi - \sum_{j=1}^{N_{\text{mod}}} \alpha_j \Phi_j \right) d\Gamma_{\text{mod}} \quad (2.45)$$

Components of matrices  $\mathbf{E}$  and  $\mathbf{H}$  are written

$$\mathbf{E}_{ik} = \int_{\Gamma_{\text{mod}}} \Phi_i^* N_k d\Gamma_{\text{mod}}^e \quad \text{and} \quad \mathbf{H}_{ij} = - \int_{\Gamma_{\text{mod}}} \Phi_i^* \Phi_j d\Gamma_{\text{mod}}^e \quad (2.46)$$

with  $1 \leq i, j \leq N_{\text{mod}}$  and  $1 \leq k \leq N_{\psi_{\text{mod}}}$ ,  $\psi_{\text{mod}}$  being the number of nodes on the modal surface.

### 2.1.5 Solver

Matrix equations are solved by a linear algebraic solver. The matrices resulting from space discretization often have a sparse structure, meaning that most of the coefficients are zero; during a conventional matrix factorization, a large number of these zero elements become non-zero: this is called *fill-in* and it increases both memory consumption and computational time. Therefore, a more efficient solving strategy is the *LU-factorization* implemented in linear solvers, where the matrix  $\mathbf{Z}$  is factorized into the product  $\mathbf{Z} = \mathbf{L}\mathbf{U}$ ;  $\mathbf{L}$  is a lower triangular matrix with ones on the main diagonal and  $\mathbf{U}$  is upper triangular.

In this procedure, the solution  $\mathbf{x}$  of the system  $\mathbf{Z}\mathbf{x} = \mathbf{b}$  is obtained in two steps; in the first step, the system  $\mathbf{L}\mathbf{y} = \mathbf{b}$  is solved for  $\mathbf{y}$ , and in the second step, the system  $\mathbf{U}\mathbf{x} = \mathbf{y}$  is solved for  $\mathbf{x}$ .

In this work, the MUMPS (MULTifrontal Massively Parallel Solver) direct linear solver, developed by CERFACS, ENSEEIHT-IRIT and INRIA<sup>24</sup>, and implemented within Actran<sup>46</sup>, has been used for all acoustic computations.

## 2.2 Modeling the noise sources with Computational Fluid Dynamics

In the two steps hybrid method of noise computation studied in this work, choice has been made to work with commercial codes for both CFD and acoustic computations, with the additional constraint of managing a reasonable computing time. Regarding the CFD computation, this naturally leads to performing a Large Eddy Simulation, available in all commercial CFD codes nowadays. Basic principles of Large Eddy Simulation will first be described in § 2.2.1, then the numerical aspects associated to the use of Fluent v6.3.26 code are treated in § 2.2.2.

### 2.2.1 Large Eddy Simulation

Large Eddy Simulation consists in separating the large flow scales from the smaller and resolving exactly only the large, the smaller scales being modeled. Therefore, a spatial filtering is defined and applied to Navier-Stokes equations; a closing subgrid-scale modeling takes the small scales effect into account, their behavior being close to isotropic.

#### 2.2.1.1 Definition of the spatial filtering

The filtered velocity field  $\hat{u}_i$  is obtained by a convolution product in physical space of the original velocity  $u_i$  with a filter function  $G_\Delta$ :

$$\hat{u}_i(\mathbf{x}, t) = \int_{\mathcal{D}} G_\Delta(\mathbf{x}, \vec{y}) u_i(\mathbf{x} - \mathbf{y}, t) d\mathbf{y} = G_\Delta \star u_i \quad (2.47)$$

The integral runs over the whole computational domain  $\mathcal{D}$ . This filtering operation applies on all flow field variables. The filter  $G_\Delta$  is usually normalized with

$$\int G_\Delta(\mathbf{x}, \mathbf{y}) d\mathbf{y} = 1.$$

The simplest filtering consists in filtering on the mesh size  $\Delta$ . The rectangular filter, also called box-filter or top-hat, is defined as:

$$G_\Delta(\mathbf{x} - \mathbf{y}) = \begin{cases} 1/\Delta^3 & \text{if } |x_i - y_i| \leq \Delta/2, \\ 0 & \text{otherwise.} \end{cases} \quad \text{with } \Delta = (\Delta x_1 \Delta x_2 \Delta x_3)^{1/3} \quad (2.48)$$

Gaussian and Fourier are other commonly used filters. With the notations introduced above, each flow quantity can be decomposed into its filtered, resolved component and

its non resolved, high frequency component, as

$$u_i = \hat{u}_i + u'_i$$

Note that in most CFD codes, as is the case within Fluent, the filtering is not applied explicitly, meaning that there is no effective scales separation. Instead, an implicit filtering is performed through mesh projection: no structure smaller than the local mesh size can be represented by the simulation.

### 2.2.1.2 Filtered Navier-Stokes equations

For incompressible flows, as it will be the case in most applications treated here (but not necessarily with constant density), we can write the filtered Navier-Stokes momentum equation as:

$$\frac{\partial \rho \hat{u}_i}{\partial t} + \frac{\partial}{\partial x_j} (\rho \hat{u}_i \hat{u}_j) = -\frac{\partial \hat{p}}{\partial x_i} + \frac{\partial \hat{\tau}_{ij}}{\partial x_j} + \frac{\partial \hat{t}_{ij}}{\partial x_j} \quad (2.49)$$

where  $t_{ij}$  is subgrid-scale (SGS) tensor representing the effects of non resolved scales.  $t_{ij}$  is written as:

$$\begin{aligned} t_{ij} &= \rho \hat{u}_i \hat{u}_j - \rho \widehat{\hat{u}_i \hat{u}_j} = \rho \hat{u}_i \hat{u}_j - \rho (\widehat{\hat{u}_i + u'_i})(\widehat{\hat{u}_j + u'_j}) \\ &= \underbrace{\rho \hat{u}_i \hat{u}_j - \rho \widehat{\hat{u}_j \hat{u}_i}}_{(1)} - \underbrace{\rho \widehat{u'_i \hat{u}_j} - \rho \widehat{\hat{u}_i u'_j}}_{(2)} - \underbrace{\rho \widehat{u'_i u'_j}}_{(3)} \end{aligned} \quad (2.50)$$

Term (1) is Leonard tensor and is noted  $L_{ij}$ ; term (2) is the cross-terms tensor, noted  $C_{ij}$ , and term (3) is the real subgrid constraint.  $t_{ij}$  tensor is at this stage considered as an unknown in Equation (2.49); the closing problem then consists in approaching  $t_{ij}$  by a function of the only resolved, filtered quantities, i.e., a function of the large scales field.

Note that  $t_{ij}$  tensor has no physical meaning, and that it is not related to the mesh, as no discretization of equations has already been done. Besides, as some authors define the tensor with an opposite sign (like in Fluent<sup>45</sup>), it is important to be watchful about this sign.

In the following, we will only deal with the real subgrid constraint, then:

$$t_{ij} = \rho \widehat{u'_i u'_j} \quad (2.51)$$

### 2.2.1.3 Closing with a subgrid-scale turbulent viscosity model

In order to solve filtered equations (2.49), it is necessary to define a closing for the subgrid-scale tensor  $t_{ij}$ . In a general way, most subgrid-scale models are built on the evaluation of a turbulent viscosity  $\nu_t \sim \ell \times u$ . The only choice of velocity scale  $u$  differentiates

the models, as  $\ell$  is only linked to the filter width  $\Delta$ . The purpose of this subgrid model is to dissipate turbulent kinetic energy, as we do not solve the small scales in the calculation; the use of a statistic modeling is justified by the quasi-isotropic behavior of the small scales of motion.

In this modeling, the principle is to express the subgrid-scale tensor  $t_{ij}$  with gradients of the filtered velocity, i.e., with directly solved components of velocity. Thus,  $t_{ij}$  is split into the sum of its deviatoric and its spherical or isotropic part:

$$t_{ij} = t_{ij}^D + t_{ij}^I \quad \text{with} \quad \begin{cases} t_{ij}^D = -\rho \widehat{u'_i u'_j} + \frac{1}{3} \rho \widehat{u'_k u'_k} \delta_{ij} \\ t_{ij}^I = -\frac{1}{3} \rho \widehat{u'_k u'_k} \delta_{ij} = -\frac{2}{3} \rho \widehat{k}_{sgs} \delta_{ij} \end{cases}$$

with, in the incompressible case,

$$t_{ij}^D = 2\mu_t \widehat{s}_{ij}^D \quad \text{where} \quad \widehat{s}_{ij} = \widehat{s}_{ij}^D = \frac{1}{2} \left( \frac{\partial \widehat{u}_i}{\partial x_j} + \frac{\partial \widehat{u}_j}{\partial x_i} \right) \quad (2.52)$$

where  $\widehat{s}_{ij}$  is the rate-of-strain tensor for the resolved scale.  $t_{ij}^I$  represents the opposite of the residual energy, or subgrid-scale energy  $\widehat{k}_{sgs}$ ; it is the part of turbulent kinetic energy which is not solved by the mesh. This term is present in order to assure that the relation is valid when indexes are contracted:

$$t_{ij} = 2\mu_t \widehat{s}_{ij} - \frac{2}{3} \rho \widehat{k}_{sgs} \delta_{ij} \quad \text{with} \quad \rho \widehat{k}_{sgs} = -\frac{1}{2} t_{kk} \quad (2.53)$$

The filtered Navier-Stokes equation then writes:

$$\frac{\partial \rho \widehat{u}_i}{\partial t} + \frac{\partial}{\partial x_j} (\rho \widehat{u}_i \widehat{u}_j) = -\frac{\partial \widehat{p}^*}{\partial x_i} + \frac{\partial}{\partial x_j} \left[ (\mu + \mu_t) \frac{\partial \widehat{u}_i}{\partial x_j} \right] \quad (2.54)$$

where the pressure term  $\widehat{p}^*$  now contains the isotropic part  $t_{ij}^I$  of the subgrid-scale stress tensor  $t_{ij}$ :

$$\widehat{p}^* = \widehat{p} - \frac{1}{3} t_{kk} = \widehat{p} + \frac{2}{3} \rho \widehat{k}_{sgs}$$

#### 2.2.1.4 Smagorinsky subgrid-scale model

Smagorinsky subgrid-scale model<sup>96</sup> is the most widely used. A dimensional analysis is the base of the subgrid-scale turbulent viscosity construction:

$$\nu_t \sim \ell \times u \sim \ell \times \ell \left| \frac{\partial \widehat{u}_1}{\partial x_2} \right| \sim \ell^2 \left| \frac{\partial \widehat{u}_1}{\partial x_2} \right|$$

By choosing  $\ell = C_s \Delta$  for the length and  $\hat{s} = \sqrt{2\hat{s}_{ij}\hat{s}_{ij}}$  for the gradients of solved velocity, the following expression can be derived:

$$\nu_t = (C_s \Delta)^2 \sqrt{2\hat{s}_{ij}\hat{s}_{ij}} \quad \text{where} \quad \hat{s}_{ij} = \frac{1}{2} \left( \frac{\partial \hat{u}_i}{\partial x_j} + \frac{\partial \hat{u}_j}{\partial x_i} \right) \quad (2.55)$$

$C_s$  is the Smagorinsky constant and  $\Delta$  is the characteristic subgrid length. The usual evaluation of Smagorinsky constant is  $C_s \simeq 0.18$ , but most computations are now performed with  $C_s \simeq 0.10$  that provides best results. A dynamic procedure was later proposed by Germano *et al.*<sup>52</sup>, where the  $C_s$  is a space-time function. The presence of walls can be taken into account with a modification of the constant  $C_s$ , thanks to a van Driest damping function for instance or a two-layers modeling.

A slightly modified version of the Smagorinsky model is applied within Fluent<sup>45</sup>, with the Smagorinsky-Lilly subgrid-scale model where the constant is modified in the vicinity of walls:

$$\nu_t = L_s^2 \sqrt{2\hat{s}_{ij}\hat{s}_{ij}} \quad \text{where} \quad L_s = \min(\kappa d, C_s \Delta)$$

with  $\kappa$  the von Kármán constant and  $d$  the distance to the closest wall. This model was found to yield best results with the constant  $C_s \simeq 0.10$ .

## 2.2.2 Numeric aspects within Fluent

### 2.2.2.1 Finite volume approach

Fluent<sup>45</sup> uses a control-volume-based technique to convert a general scalar transport equation to an algebraic equation. This control volume technique consists of integrating the transport equation about each control volume, yielding a discrete equation that expresses the conservation law on a control-volume basis.

#### 2.2.2.2 Solver formulation

Two solver formulations are available within Fluent v6.3.26<sup>45</sup>: the pressure-based and the density-based formulation. The pressure-based approach was initially developed for low Mach number incompressible flows, while the density-based approach was designed for high speed compressible flows. In both methods the velocity field is obtained from the momentum equations. In the density-based solver, density is obtained from the continuity equation while pressure is computed from the equation of state, and continuity, momentum and energy equations are solved simultaneously. In the pressure-based solver, pressure is obtained by solving a Laplace-like equation, which is derived by manipulation of continuity and momentum equations; the momentum, pressure and scalar equations are solved sequentially in that order.

In this work, the explicit version of the density-based solver has been chosen for simulating the problems developed in Chapter 3 and involving the direct computation of aerodynamic noise. This corresponds to a full compressible approach.

For all computations on the diaphragm geometry reported in Chapter 4, the implicit pressure-based solver has been used. This implicit algorithm used by the pressure-based solver belongs to the class of projection methods, where the constraint of mass conservation, described in the continuity equation, is achieved by solving a pressure correction equation. The pressure correction equation is derived from the continuity and momentum equations in such a way that the velocity field, corrected by the pressure, satisfies the continuity. Since the governing equations are nonlinear, coupled to one another, and solved sequentially, several iterations are performed until the solution converges, with the resolution of all equations at each iteration.

### 2.2.2.3 Space discretization

#### Second-order upwind scheme

For Direct Numerical Simulation considered in Chapter 3, turbulence modeling is turned off, and the most accurate space discretization scheme available in Fluent is the second-order upwind scheme. This scheme is chosen by default for the space discretization of all flow equations. Second-order upwinding consists in computing the cell faces quantities using a multidimensional reconstruction approach. A Taylor series expansion of the cell-centered solution about the cell centroid ensures high order accuracy. With this scheme, the face value  $\phi_f$  is computed using the following expression:

$$\phi_f = \phi + \nabla\phi \cdot \mathbf{r}$$

where  $\phi$  and  $\nabla\phi$  are the cell-centered value and its gradient in the upstream cell, and  $\mathbf{r}$  is the displacement vector from the upstream cell centroid to the face centroid.

#### Central differencing scheme

For the Large Eddy Simulations, high order accurate space discretization is desired. The highest central differencing available in Fluent is of second order to comply with any unstructured mesh. The central differencing scheme is applied to the momentum equations and calculates the face value for a variable  $\phi_f$  as follows:

$$\phi_f = \frac{1}{2} (\phi_0 + \phi_1) + \frac{1}{2} (\nabla\phi_0 \cdot \mathbf{r}_0 + \nabla\phi_1 \cdot \mathbf{r}_1)$$

where indices 0 and 1 refer to the cells that share face  $f$ ,  $\nabla\phi_0$  and  $\nabla\phi_1$  are the gradients in cells 0 and 1, respectively, and  $\mathbf{r}$  is the vector directed from the cell centroid toward

the face centroid. The numerical procedure stability is ensured by the use of a deferred approach:

$$\phi_f = \underbrace{\phi_{f,UP}}_{\text{implicit part}} + \underbrace{(\phi_{f,CD} - \phi_{f,UP})}_{\text{explicit part}}$$

Here, subscripts UP and CD stand for upwind and central differencing schemes, respectively. As indicated, the upwind part is treated implicitly while the difference between the central-difference and upwind values is treated explicitly. Provided that the numerical solution converges, this approach leads to pure second-order differencing.

Note that a bounded version of central differencing is available, designed to discard numeric instability by limiting the diffusion; this scheme is actually a blending between the pure central differencing scheme described previously and a first order upwind scheme. However, the damping introduced can entail physical problems when the erased wiggles have a physical origin, and are not just spurious numerical errors. A best practice is to resort to this bounded scheme only when central differencing leads to unphysical instabilities.

#### 2.2.2.4 Time discretization and advancement scheme

Time discretization involves the integration of each term of the differential equations on a time step  $\Delta t$ . For any given scalar quantity  $\phi$ , the equation of time advancement is written in the following form:

$$\frac{\partial \phi}{\partial t} = F(\phi)$$

where the left-hand-side is relative to time evolution, and the right-hand-side function  $F$  contains space evolution. Time integration of left-hand-side transient term is straightforward, and, at the first order using a backward differencing scheme, is written:

$$\frac{\phi^{n+1} - \phi^n}{\Delta t} = F(\phi)$$

A second order discretization is written as follows:

$$\frac{3\phi^{n+1} - 4\phi^n + \phi^{n-1}}{2\Delta t} = F(\phi)$$

where subscripts  $n - 1$ ,  $n$  and  $n + 1$  refer to the values of  $\phi$  at, respectively, the previous, the current, and the next time step.

Once the time derivative has been evaluated, the time at which  $F(\phi)$  is evaluated in the right hand side have to be chosen. The implicit approach involves evaluating  $F(\phi)$  at the future time level, yielding, for the first order integration:

$$\frac{\phi^{n+1} - \phi^n}{\Delta t} = F(\phi^{n+1})$$

This involves that  $\phi^{n+1}$  in a given cell is related to  $\phi^{n+1}$  in the neighboring cells through  $F(\phi^{n+1})$ :

$$\phi^{n+1} = \phi^n + \Delta t F(\phi^{n+1})$$

The resolution of this implicit equation requires an iterative scheme before moving to the next time step. This implicit, iterative, time advancement is unconditionally stable and convergence is reached at each time step. A non-iterative time advancement scheme also exists, in which the division error is made the same order of magnitude as the truncation error, instead of reducing it to zero. This scheme is computationally less expensive and allows to keep a good time precision in only one iteration per time step, speeding up the simulation by up to 200-400 %. Implicit time-stepping at second order has been used for all diaphragm calculations, see Chapter 4, in conjunction with the implicit pressure-based solver.

The explicit approach consists in expressing  $F(\phi)$  at the current time step,

$$\frac{\phi^{n+1} - \phi^n}{\Delta t} = F(\phi^n)$$

allowing to make  $\phi^{n+1}$  explicitly only dependent of the existing solution values  $\phi^n$ :

$$\phi^{n+1} = \phi^n + \Delta t F(\phi^n)$$

With explicit time-stepping, the time step is driven by the CFL condition and is constant throughout the domain (global time-stepping), equal to the minimum of all local time steps in the domain. A 4-step Runge-Kutta scheme is chosen to express the time derivative. In this work, explicit time-stepping is used in conjunction with the density-based solver for the validation studies.

### 2.2.2.5 Outlet boundary conditions

For all direct noise computations, Non Reflecting Boundary Conditions (NRBC) are applied at the domain boundaries, allowing the pressure waves leaving the computational domain without creating spurious waves that would disturb the acoustic pressure field. In addition to the application of NRBC, the mesh is stretched toward the boundaries in order to dissipate the outgoing waves before they reach the boundaries. The NRBC implemented within Fluent are based on the characteristic wave relations derived from the Euler equations, and applied only on pressure-outlet boundary conditions, see Thompson<sup>104;105</sup>. As their formulation is one dimensional, they require that the outgoing waves are incident nearly normally on the border. Moreover, though no warning has been raised regarding this topic, investigations undertaken in the frame of this study have shown that the junction of two Non Reflecting Boundary Conditions at corners or discontinuities is highly sensitive,

as high amplitude pressure waves propagating inside the domain are created at the corner as soon as it is attained by an outgoing wave. For all these reasons, the use of characteristic Non Reflecting Boundary Conditions has to be taken with great care. In Chapter 3, where direct noise computations are undertaken, NRBC are applied on the left and right boundaries of the square domain, while a symmetry is set at top and bottom; this avoids the corner reflections. Note that the domain could be made circular with a unique continuous NRBC without problems, although this prevents the possibility to build a cartesian mesh in the whole domain.

The development of more efficient radiation and outflow boundary conditions by Tam & Webb<sup>103</sup>, further developed by Tam & Dong<sup>102</sup>, has enabled the resolution of problems involving outgoing waves not perpendicular to the boundary, and where non-uniform mean flows are present. However, these schemes are mainly developed for high order finite differences codes for direct noise computation, and fall out of the scope of the present study.

#### **2.2.2.6 Initial conditions**

The initial conditions applied at the beginning of an unsteady CFD computation must, in the best case, represent a guessed solution of the mean flow field. However, it is common practice, when dealing with jet flows in free field, to initialize the flow field at zero velocity and ambient pressure/density; indeed, a more advanced initial solution would not gain computing time, since the turbulent perturbations, generated with the unsteadiness of the flow, have to cross the whole computational domain before a converged flow field solution can be found. In confined flow problems though, starting from such a "zero" solution causes stability and convergence problems: in these problems, the pressure drop between the inlet and outlet plays a crucial role and must be steadily converged before starting the unsteady simulation. Therefore, for all computations presented here on the diaphragm geometry, a first Reynolds Averaged Navier-Stokes  $k - \epsilon$  computation has been converged to second order and is used as an initial condition for the Large Eddy Simulation.

## 2.3 Practical application of the method

### 2.3.1 General overview

The method consists of coupling a CFD code with a finite element acoustic software where the variational formulation of Lighthill's Acoustic Analogy is implemented. Here follow the different steps of a practical computation, provided that a transient solution of the flow field has already been obtained:

1. An analysis of the flow field allows to determine in which region(s) of the flow acoustic source terms will be considered; an acoustic mesh is built on the whole region of interest for acoustics, with fine elements in the region(s) of source terms and bigger elements elsewhere;
2. A mesh file containing the coordinates of the nodes where source terms are to be considered is created;
3. This mesh file is read by the CFD code, presently Fluent v6.3.26<sup>45</sup>, and the acoustic nodes are localized in the CFD domain;
4. A database containing the time history of the source term vector  $\mathbf{S} = [S_1 \ S_2 \ S_3]^t$  in three dimensions at each node of the acoustic mesh is created; if the acoustic nodes are not located at the cell centers of the CFD mesh, where  $\mathbf{S}$  is actually computed, then an interpolation is performed to get  $\mathbf{S}$  at the correct acoustic node locations;
5. A utility program reads the data and transforms the source terms from time to spectral domain; these spectral data, written as the vector

$$\tilde{\mathbf{S}} = \left[ \Re(\tilde{S}_1) \ \Im(\tilde{S}_1) \ \Re(\tilde{S}_2) \ \Im(\tilde{S}_2) \ \Re(\tilde{S}_3) \ \Im(\tilde{S}_3) \right]^t$$

are stored in a specific exchange format;

6. The acoustic computation is performed within Actran/LA<sup>46</sup>, with reading of the spectral source terms.

Items 4 and 5, dealing with mesh interpolation and Fourier transform respectively, are particularly sensitive and are developed in the following sections.

### 2.3.2 Source interpolation: from the CFD mesh to the acoustic mesh

When applying a hybrid CAA method, the source term information coming from the CFD code have to be passed to the acoustic code in order to perform the final acoustic propagation. In addition, the CFD and the acoustic codes do not require the same mesh

refinement to reach accuracy: usually, one order of magnitude separates both mesh sizes, the CFD being the finer mesh due to the requirements for accurate turbulence modeling. While it is not absurd to use all the information available on the source terms for the acoustic propagation, this results in a much too big acoustic finite element model for the current computing resources. Therefore, one has to resort to interpolating the finely defined source terms on the coarser acoustic mesh. Kaltenbacher *et al.*<sup>62</sup> recently proposed a conservative interpolation where the source terms are firstly integrated over the whole source region; after a bilinear interpolation of each CFD source term in the acoustic finite elements using their shape functions, the result is added to the nodes of the acoustic grid, preserving the overall sum of the acoustic sources; unfortunately, no validation of this method was presented.

While a systematic study of interpolation schemes and methods is beyond the scope of this work, this subject is of primary importance and has to be considered. In academic studies considered in Chapter 3, as the meshes are quite small, no interpolation is done between CFD and acoustic meshes: the acoustic nodes are located exactly at the CFD mesh cell centers. However, this strategy is not achievable in the three-dimensional diaphragm study of Chapter 4 since it would lead to a finite element model of around 5 millions nodes. Therefore, a high order non conservative interpolation is applied and described in § 4.3.4.2.

### 2.3.3 Transformation in the spectral domain

The transformation from time to domain to spectral domain of a signal  $\phi(t)$  is performed thanks to a Fourier transform, as defined in Equation (2.10) and expressed here in terms of frequency  $f$ :

$$\hat{\phi}(f) = \mathcal{F}[\phi(t)] = \int_{-\infty}^{+\infty} \phi(t)e^{-i2\pi ft} dt \quad (2.56)$$

Numerical signals are discretized, and a sampling of time signal  $\phi(t)$  at the time step  $\Delta t$  is given by:

$$\phi(t_k) = \phi_k \quad \text{with} \quad t_k = k\Delta t \quad \text{and} \quad 1 \leq k \leq N$$

$N$  consecutive independent samples are obtained at the sampling frequency  $f_s = 1/\Delta t$ ;  $N$  is supposed even. The discrete Fourier transform associated to expression (2.56) writes

$$\hat{\phi}(f_n) = \hat{\phi}_n = \Delta t \sum_{k=1}^N \phi_k e^{-i2\pi f_n t_k} \quad (2.57)$$

$$\text{with} \quad f_n = n\Delta f, \quad \Delta f = \frac{1}{N\Delta t} \quad \text{and} \quad -N/2 \leq n \leq N/2$$

where  $N\Delta t = T$  is the total sampling time. In addition,  $\hat{\phi}_{-N/2} = \hat{\phi}_{N/2}$  so that the discrete Fourier transform maps  $N$  complex values  $\phi_k$  to  $\hat{\phi}_n$ . The Nyquist-Shannon theorem, also called sampling theorem, assures a complete representation of the signal if the signal is band limited and the sampling frequency greater than twice the signal bandwidth; the critical frequency associated to the signal bandwidth is the Nyquist frequency, given by  $f_c = 1/(2\Delta t)$ .

According to Parseval theorem, the total power of the signal is the same in the time and in the frequency domain, which yields, for continuous signals

$$\int_{-\infty}^{+\infty} |\phi(t)|^2 dt = \int_{-\infty}^{+\infty} |\hat{\phi}(f)|^2 df$$

The Power Spectral Density  $S_{\phi\phi}$  is then obtained from an estimation of the signal mean squared amplitude for a stationary random evolution:

$$|u^2| = \frac{1}{T} \int_{-\infty}^{+\infty} \phi(t)^2 dt = \frac{1}{T} \int_0^T |\hat{\phi}(f)|^2 df = \int_{-\infty}^{+\infty} S_{\phi\phi}(f) df$$

In discrete form, this is written

$$\int_{-\infty}^{+\infty} S_{\phi\phi}(f) df \simeq \frac{\Delta f}{T} \sum_{n=-N/2}^{N/2} |\hat{\phi}_n|^2 \quad \text{yielding} \quad S_{\phi\phi}(f_n) = \frac{1}{T} |\hat{\phi}_n|^2$$

When working with real signals, as is the case with aerodynamic signals of pressure or velocity for instance, a one-sided spectrum is defined for positive frequencies, and the Power Spectral Density (PSD) is given by

$$S_{\phi\phi}(f_n) = \frac{2}{T} |\hat{\phi}_n|^2 \quad \text{with} \quad 0 \leq n \leq N/2$$

Actran/LA provides a script called iLA to compute the Fourier transform. In iLA, the Fourier transform for a real signal is defined using a different convention:

$$\hat{\phi}_{n,iLA} = \frac{2}{N} \sum_{k=1}^N \phi_k e^{-i2\pi f_n t_k} = \frac{1}{T} \times \hat{\phi}_n$$

Therefore, the PSD of the signal is related to  $\hat{\phi}_{n,iLA}$  by

$$S_{\phi\phi}(f_n) = T |\hat{\phi}_{n,iLA}|^2$$

Before computing the Fourier transform, the mean value is removed from time signal  $\phi_k$  for detrending, and a Hanning windowing is applied in order to assure that both ends

of the signal are zero. The final time signal is written

$$\phi_{k,final} = \left( \phi_k - \frac{1}{N} \sum_{j=1}^N \phi_k \right) \times w_k \quad \text{with} \quad w_k = \frac{1}{2} \left( 1 - \cos \left( \frac{2\pi k}{N} \right) \right) \quad (2.58)$$

where  $w_k$  is the Hanning window. Note that iLA allows to use other types of windowing, like the triangular or Gaussian windows. Moreover, it is possible to average the transforms of individual (overlapping) segments of the total signal to increase the accuracy of the power spectrum.

## 2.4 Potential issues associated with the method

### 2.4.1 Accuracy of the computed noise sources

The sensibility of the radiated sound to errors in the source term computation is not well understood; in particular, errors made due to the subgrid-scale modeling in the evaluation of Lighthill's tensor may be non negligible<sup>112</sup>. The simplified Lighthill's tensor, with constant density, is decomposed for better understanding of this issue:

$$T_{ij} = \rho_0 u_i u_j = \underbrace{\rho_0 \hat{u}_i \hat{u}_j}_{T_{ij}^{LES}} + \underbrace{\rho_0 (\widehat{u_i u_j} - \hat{u}_i \hat{u}_j)}_{T_{ij}^{SGS}} + \underbrace{\rho_0 (u_i u_j - \widehat{u_i u_j})}_{T_{ij}^{MSG}} \quad (2.59)$$

where the  $\widehat{\cdot}$  denotes spatial filtering of Large Eddy Simulation. In the above expression, the first term  $T_{ij}^{LES}$  corresponds to the resolved part of Lighthill's tensor, while the second term  $T_{ij}^{SGS}$  is actually the opposite of the subgrid-scale tensor  $t_{ij}$  defined in Equation (2.50). The last term,  $T_{ij}^{MSG}$ , is the high-frequency part of Lighthill's tensor not resolved by the LES, and is thus its missing part. Only the first term  $T_{ij}^{LES}$  in Equation (2.59) is directly available from a Large Eddy Simulation; an evaluation of  $T_{ij}^{SGS}$  is possible only when the subgrid-scale term is explicitly available from the CFD code. When a high-order selective filtering is applied<sup>10-12</sup>, the larger structures well computed by LES are not affected by the subgrid-scale modeling, and the subgrid term  $T_{ij}^{SGS}$  plays a negligible role. S  ror *et al.*<sup>95</sup> performed *a posteriori* tests on decaying isotropic turbulence and showed that the contribution to the radiated sound of the missing part is negligible, while *a priori* tests proved the importance of the subgrid-scale contribution.

### 2.4.2 Spatial truncation of convected noise sources

It is a well-known observation that the spatial truncation of volume source terms in Lighthill's analogy, or in Ffowcs Williams & Hawkings' analogy, creates spurious noise of dipolar nature. Recently, Casper *et al.*<sup>23</sup> showed that with the study of a vortex convection.

Several authors then have proposed different strategies to overcome this difficulty, intrinsically linked to the application of a hybrid method of noise computation using volume source terms slowly decaying.

In the case of vortex pairing in an axisymmetric jet having an extended source region, Mitchell *et al.*<sup>74</sup> propose an original way of avoiding the generation of spurious sound waves at the truncation boundary. Having noticed that downstream of vortex pairing, for  $x > x_m$ , the source terms can be modeled in the spectral space based on their form at  $x = x_m$ , they model the behavior of the source terms downstream for  $x > x_m$  while keeping the computed source terms for  $x \leq x_m$ . However, this artifice is only possible when the source term is very simple.

Spatial filters have been applied by Oberai *et al.*<sup>76</sup>, Pérot<sup>79</sup> and more recently by Obrist *et al.*<sup>77</sup>, toward the downstream boundary in order to remove spurious noise, under the form of linear, exponential and cosine functions, respectively, with a certain success. Wang *et al.*<sup>113</sup>, after showing that the spurious boundary noise is due to the time variation of Lighthill stress fluxes across the boundary, propose a different approach based on the frozen eddy assumption. In this correction method, a surface integral is added to the truncated volume integral; this new surface source term takes into account the Lighthill stress fluxes, carried by the convecting eddies at a convection velocity  $U_c$ , across the outlet boundary. Such a solution to Lighthill equation (1.4) takes the integral form

$$\rho(\mathbf{x}, t) = \frac{x_i x_j}{4\pi c_0^4 |\mathbf{x}|^3} \left\{ \frac{\partial^2}{\partial t^2} \iiint_{\mathcal{V}} T_{ij} \left( \mathbf{y}, t - \frac{|\mathbf{x}|}{c_0} \right) d\mathbf{y} + \frac{\partial}{\partial t} \iint_{\mathcal{S}} U_c T_{ij} \left( \mathbf{y}, t - \frac{|\mathbf{x}|}{c_0} \right) d\mathbf{y} \right\}$$

This solution eliminates the spurious noise created at the truncation boundary. This applies in the limit of the frozen eddy assumption, violated in the case of turbulent flows of practical interest. Martínez-Lera *et al.*<sup>71</sup> recently proposed a correction to Wang's formulation, under the form of a Doppler amplification factor to account for convection effects at the truncation boundary  $\mathcal{S}$ .

### 2.4.3 Mesh interpolation

It has been mentioned in §2.3.1 that noise sources computed within the flow simulation on the CFD mesh have to be interpolated on the acoustic mesh to be propagated to the desired locations. Indeed, the constraints are much more severe for the design of the CFD mesh than for the acoustic mesh, and the characteristic mesh sizes of both meshes differ by at least one order of magnitude in the source regions. Therefore, in order to keep an accurate definition of the sources, it is necessary either to refine the acoustic mesh in these regions to match the CFD mesh size, or to interpolate noise sources on a coarser acoustic mesh. The first solution is only tractable on small meshes; in real cases, such as for the diaphragm presented in Chapter 4, keeping the CFD mesh accuracy for the acoustic mesh

in the source regions would lead to a considerably heavy finite element model of several millions degrees of freedom. Therefore, an interpolation has to be performed to lighten the acoustic model; note that this intermediate interpolation operation is only required due to the limited available computing resources. As the interpolation is currently only supported at the order 0 within Fluent, meaning that the closest CFD cell to each acoustic node is considered, an interpolation scheme has to be defined externally.

As shown in previous studies<sup>37;68;69</sup>, a study on interpolation schemes can be performed to determine the best scheme for a given application. As expected, high order schemes and schemes based on Lagrange polynomials give the best results with a reduced interpolation error. However, they are only useful in a fully Cartesian framework. When working on non Cartesian meshes, as is the case in the diaphragm study (see Chapter 4), even low order methods are difficult to handle. Moreover, the interpolation on arbitrary meshes (tetrahedra, polyhedra) is not much discussed in the literature. Therefore, and only for the diaphragm case study, the strategy is to record source data on a fully Cartesian mesh almost coincident with the CFD mesh to retain accuracy, allowing thus the use of high order interpolation schemes. Due to time constraints, only non conservative interpolation schemes have been developed in this work. However, conservative procedure would be more appropriate for energy conservation reasons in future studies.

## 2.5 Conclusion

In this chapter, the theoretical details of a two steps aeroacoustic calculation have been presented. The first step involves a fluid calculation performed within Fluent<sup>45</sup>; an explicit (compressible) density-based solver is used for the study of academic cases thanks to Direct Numerical Simulations, see Chapter 3, while a pressure-based, incompressible solver is used for the low Mach number "real life" application dealt with in Chapter 4, namely the diaphragm problem. The second computational step consists in applying Lighthill's Acoustic Analogy, with the propagation of the volume sources computed in the previous step; this is performed within Actran/LA<sup>46</sup>. Major issues associated with this hybrid method are also discussed.

# 3.

## Assessment of the hybrid method

---

*T*HE ASSESSMENT of the numerical strategy is a crucial point since it generally enables to highlight validity limits. Therefore, it is of major importance to choose problems as representative as possible of the real application conditions, and in the meantime to set the conditions at their extrema. In the present work, the first important issue is to validate the general approach. On the contrary to a Direct Noise Computation, in this two steps method many numerical details are involved, and working on academic cases is imperative. The study of the time evolution of two corotating vortices presents several advantages; indeed, the simplicity and compacity of this two dimensional system makes the achievement of a DNS reference solution affordable. Moreover, it is easy to discard the issues linked to the application of this hybrid method: interpolation from the CFD to the acoustic mesh, handling of outgoing structures from the acoustic domain. The fundamental analysis of the source term definition can then be led without being disturbed by other issues<sup>1</sup>.

The second phenomenon considered in this chapter is the handling of outgoing turbulent structures from the acoustic domain. In this case, a perfect vortex is convected out of the domain and the corresponding acoustic radiation is studied. Spatial filters are defined to eliminate the spurious noise emitted due to the truncation boundary and their effect is characterized.

---

<sup>1</sup>Note that parts of Chapters 3 and 4 have already been published in Piellard *et al.*<sup>81;82</sup>

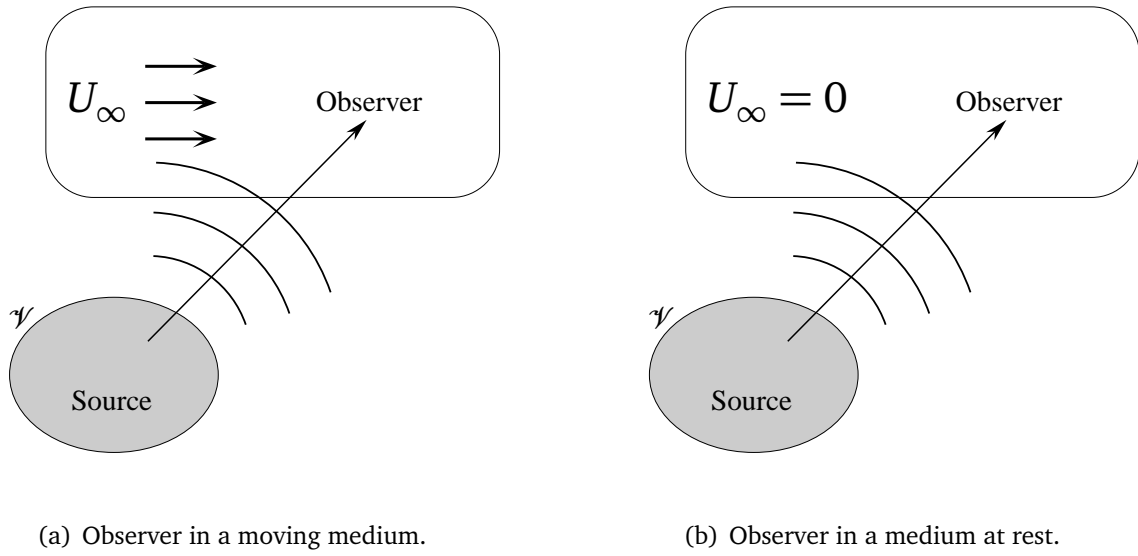


**Figure 3.1** – Two configurations for the observer: (a): the ambient medium is in movement or (b): at rest.

### 3.1 General validation: corotating vortices study

As illustrated in Figure 3.1, there are two possible configurations for the observer: either he is located in a mean flow, see Figure 3.1(a), or in a medium at rest like in Figure 3.1(b).

If the observer is in a moving medium, with the mean velocity  $U_\infty$ , then the acoustic propagation of sources must take it into account to compute the refraction of acoustic waves by the mean flow; this is achieved when choosing a convected wave operator. In the case of Linearized Euler Equations, the mean flow appears in the left-hand-side, i.e., in the propagation operator; therefore, the source term(s) must only contain non-linear source terms. Indeed, Bogey *et al.*<sup>15</sup> have shown that the non-linear source term

$$S_i^f = \frac{\partial T_{ij}^f}{\partial x_j} = \frac{\partial(\rho u'_i u'_j)}{\partial x_j} \quad \text{where} \quad u'_i = u_i - \bar{u}_i \quad (3.1)$$

must be used, while the source term containing linear effects

$$S_i^t = \frac{\partial T_{ij}^t}{\partial x_j} = \frac{\partial(\rho u_i u_j)}{\partial x_j} \quad (3.2)$$

produces erroneous results, as the linear terms are present on both sides of the propagation equation.

On the contrary, if the observer is in a medium at rest, i.e., there is no mean flow in the observer's region, the source must contain all linear terms. Moreover, discarding the mean

flow field in the source term leads to wrong results.

In order to confirm this point, the evolution of two corotating vortices is studied; vortices are firstly placed in a medium at rest, and then in a shear layer. This study presents the advantage of discarding other issues cited previously. Indeed, the system of vortices involves no convection out of the computational domain, clearing the spatial truncation issue; moreover, no interpolation is made between CFD and acoustic meshes. The objective here is to understand the physics underlying in the hybrid method of noise computation; therefore, Direct Numerical Simulation and Direct Noise Computation will be used, by means of Fluent, to minimize numerical errors, while incompressible Large Eddy Simulation is the targeted CFD modeling for real applications.

### 3.1.1 Analytical resolution of Lighthill's Acoustic Analogy

A two-dimensional spectral solution of Lighthill's equation has also been developed for validation. Green's functions are used to solve Lighthill's equation, which allows to express the solution of an inhomogeneous wave equation as an integral. The free-space Green's function  $G(\mathbf{x}, t|\mathbf{y}, \tau)$  is the response, at position  $\mathbf{x}$  and time  $t$ , to an impulse signal from  $\mathbf{y}$  emitted at time  $\tau$ . It is defined as the physical solution of the inhomogeneous wave equation

$$\frac{\partial^2 G(\mathbf{x}, t|\mathbf{y}, \tau)}{\partial x_i^2} - \frac{1}{c_0^2} \frac{\partial^2 G(\mathbf{x}, t|\mathbf{y}, \tau)}{\partial t^2} = \delta(\mathbf{x} - \mathbf{y}) \delta(t - \tau) \quad (3.3)$$

where  $\delta$  is the Dirac generalized function. In the spectral domain, using the convention defined in Equation (2.10), wave Equation (3.3) becomes the Helmholtz equation

$$(\nabla^2 + k^2) \hat{G}(\mathbf{x}|\mathbf{y}, \omega) = \delta(\mathbf{x} - \mathbf{y}) \quad (3.4)$$

where  $k = \omega/c_0$  is the wavenumber, and the two-dimensional solution of Equation (3.4) writes

$$\hat{G}(\mathbf{x}|\mathbf{y}, \omega) = \frac{i}{4} H_0^{(2)}(kr) \quad (3.5)$$

where  $H_0^{(2)}$  is the Hankel function of second kind and order 0, and  $r = |\mathbf{x} - \mathbf{y}|$ . Lighthill's Equation (2.1) can be written on acoustic pressure fluctuations  $p_a = p - p_0$  instead of density fluctuations  $\rho_a = \rho - \rho_0$ , yielding

$$\nabla^2 p_a - \frac{1}{c_0^2} \frac{\partial^2 p_a}{\partial t^2} = -\frac{\partial^2 T_{ij}}{\partial x_i \partial x_j} \quad (3.6)$$

In the spectral domain, the inhomogeneous wave Equation (3.6) is transformed into an inhomogeneous Helmholtz equation:

$$(\nabla^2 + k^2)\hat{p}_a(\mathbf{x}, \omega) = -\frac{\partial^2 \hat{T}_{ij}(\mathbf{x}, \omega)}{\partial x_i \partial x_j} \quad (3.7)$$

The solutions of Lighthill's equation expressed as integral formulations are obtained by convoluting the Green's function with the source term of Equation (3.6):

$$p_a = c_0^2 \rho_a = -G \star \frac{\partial^2 T_{ij}}{\partial x_i \partial x_j}$$

Using the two-dimensional spectral expression (3.5) leads to the following solution:

$$p_a(\mathbf{x}, \omega) = -\frac{i}{4} \iint_{S_0(\mathbf{y})} H_0^{(2)}(kr) \frac{\partial^2 T_{ij}(\mathbf{x}, \omega)}{\partial y_i \partial y_j} d\mathbf{y} = -\frac{i}{4} \iint_{S_0(\mathbf{y})} \frac{\partial^2 H_0^{(2)}(kr)}{\partial y_i \partial y_j} T_{ij}(\mathbf{x}, \omega) d\mathbf{y}$$

in free space. Analytical developments using the properties of Hankel functions lead eventually to the two-dimensional spectral solution of Lighthill's equation:

$$p_a(\mathbf{x}, \omega) = -\frac{i}{4} \iint_{S_0(\mathbf{y})} \left[ k^2 \frac{r_i r_j}{r^2} H_0^{(2)}(kr) - k \left( \frac{2r_i r_j}{r^3} - \frac{\delta_{ij}}{r} \right) H_1^{(2)}(kr) \right] T_{ij}(\mathbf{x}, \omega) d\mathbf{y} \quad (3.8)$$

Equation (3.8) will be used in the following to confirm results obtained with the variational formulation of Lighthill's analogy.

### 3.1.2 Two corotating vortices in a medium at rest

Vorticity acceleration produces an acoustic radiation, as investigated by Powell<sup>85</sup>. This mechanism is highlighted in the particular two-dimensional case of two corotating vortices; the vortices turn around each other before merging, and then form a solely eddy structure. The scheme on Figure 3.2(a) presents the vortices system<sup>9</sup>: two identical corotating vortices, clockwise rotating are considered; they are separated by the distance  $2r_0$ . The pair formed by both vortices also rotates clockwise. Each vortex is initialized by its tangential velocity  $V_\theta$ , using Scully's vortex model in order to avoid any velocity discontinuity at the vortex center:

$$V_\theta(r) = -\frac{\Gamma r}{2\pi(r_c^2 + r^2)}$$

where  $r$  is the current distance from the vortex center,  $\Gamma$  the vortex circulation;  $r_c$  is the distance at which the vortices tangential velocity is maximal,  $V_{max} = \Gamma/4\pi r_c$ .

The radii ratio  $r_c/r_0$  is fixed to 0.22, and the rotation Mach number  $M_r = V_{max}/c_0$  is 0.5. According to Powell<sup>85</sup>, in such a configuration, the rotation velocity on the circle of

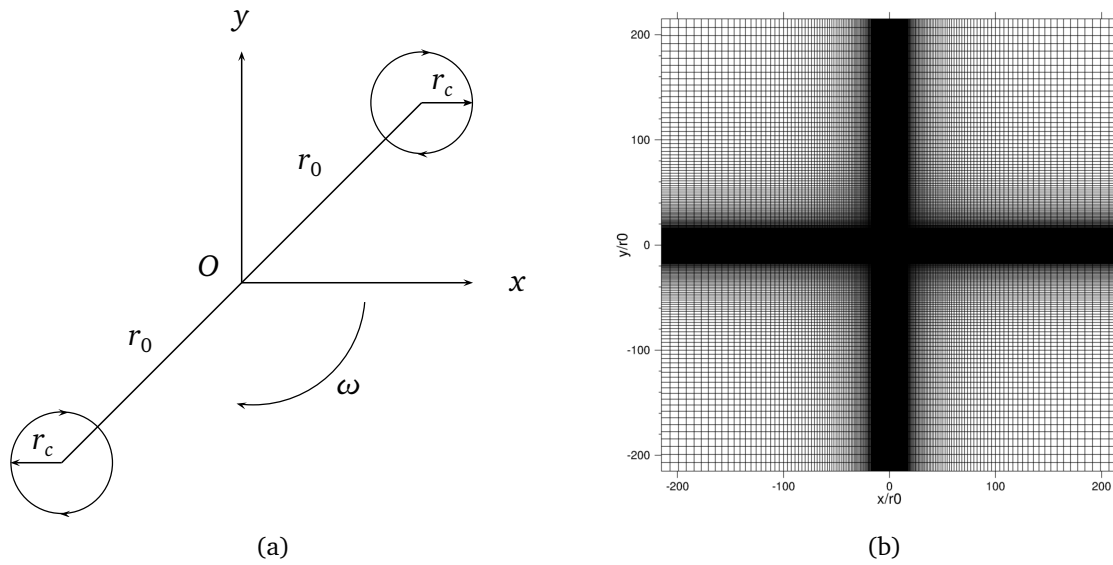


**Figure 3.2** – Two corotating vortices in a medium at rest. (a): Scheme of the vortices system. (b): CFD mesh.

radius  $r_0$  is given by  $\omega = \Gamma/4\pi r_0^2$ ; thus the rotation period is  $T = 8\pi^2 r_0^2/\Gamma$  and the rotation Mach number is  $M_r = \Gamma/4\pi r_0 c_0$ .

A compressible direct numerical simulation, namely without modeling, is performed using the density-based solver of Fluent, see § 2.2.2.2. Time discretization is explicit with a 4-step Runge-Kutta algorithm, and for spatial discretization a second-order upwind scheme is considered. Results are processed as follows: the acoustic pressure directly computed by CFD in the far field is considered as the reference result; the variational formulation of Lighthill is then carried out, with propagation of the source terms as computed by CFD; finally, the application of Lighthill's equation's analytical solution, as defined in § 3.1.1, serves as an ultimate verification.

### 3.1.2.1 Direct Noise Computation

The computational domain extends from  $-215 r_0$  to  $215 r_0$  in each direction and is meshed with  $489 \times 489$  points, identically in both  $x$  and  $y$  directions. The mesh size is constant on the first 100 points from the center, with  $\Delta = r_0/36 = 1 \times 10^{-4}$  m, and a stretching rate of 4% is applied on the 144 following points. Non Reflecting Boundary Conditions are applied on lateral sides of the computational in order to let the pressure waves leave the domain without disturbances; symmetry boundary conditions are applied on top and bottom boundaries.

At  $t = 0$ , both vortices are introduced at  $(r_0, 0)$  and  $(-r_0, 0)$  in a medium at rest (uniform density  $\rho_0$  and pressure  $p_0$ ). The time step computed by the solver as  $\text{CFL} = (c_0 + V_{\max})\Delta t/\Delta$  is fixed at 0.5, leading to a theoretical rotation period of approximately

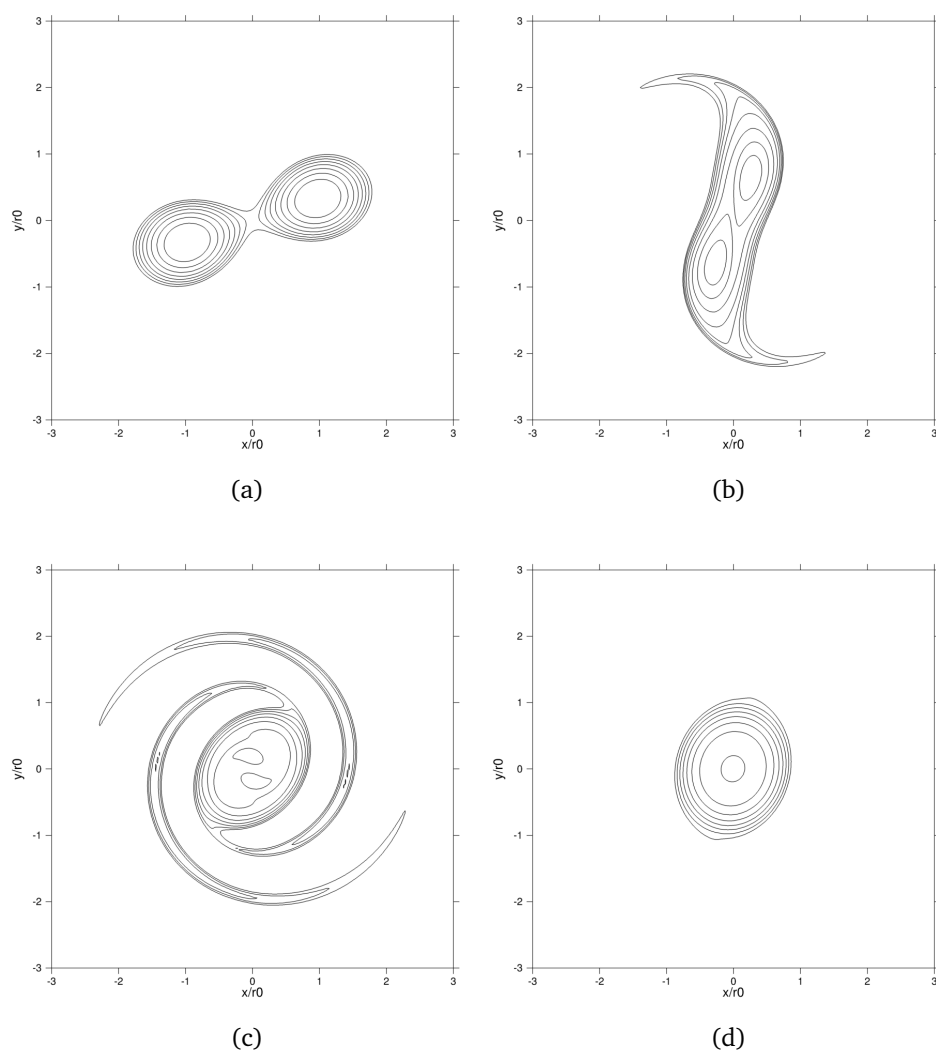


**Figure 3.3** – Two corotating vortices in a medium at rest. Vorticity field obtained after (a): 50000, (b): 106000, (c): 108500 and (d): 120000 time steps. Vorticity isocontours from  $10^4$  to  $1.22 \times 10^5$   $s^{-1}$ .

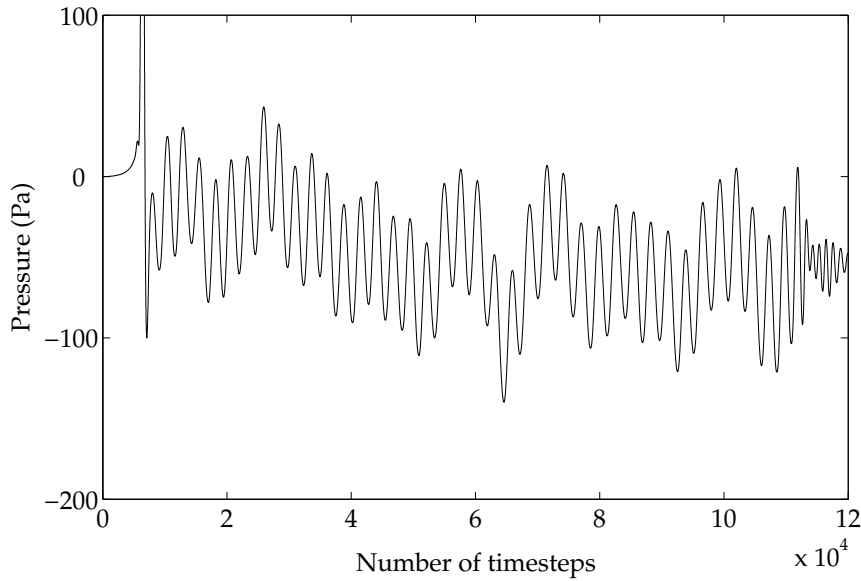


**Figure 3.4** – *Two corotating vortices in a medium at rest. Static pressure fluctuations  $p - p_0$  at point  $(50 r_0, 50 r_0)$  as a function of the number of time steps. Levels in Pa.*

$5260 \Delta t$ . The acoustic source associated to the corotating vortices is a rotating quadrupole. The frequency  $f_a$  of the acoustic radiation is twice the rotation frequency of the vortices, due to the symmetry of the structure; the corresponding theoretical acoustic wavelength is  $\lambda_a = 29.6 r_0$ .

### 3.1.2.2 Merging mechanism

The vortices undergo the following evolution<sup>73</sup>: the vortices first perform several rotations before merging, leading to a single vortex structure. In the present case, the vortices perform 19 rotations keeping well separated from each other, the first rotation at the frequency described by Powell<sup>85</sup> ( $T \sim 5360 \Delta t$ ), the following at an ever decreasing frequency with a mean period of  $T_{\text{mean}} \sim 5440 \Delta t$ . Then, during the 20th rotation, the vortices come closer to each other while accelerating the rotation, and quickly merge. Some vorticity filaments are ejected at the fringe of the central eddy structure while both cores are merging, and eventually these filaments are integrated to the remaining big eddy structure. The latter is slightly elliptic, but recovers slowly a circular shape. This merging mechanism is shown in Figure 3.3, where the vorticity field is represented at different times of the structure evolution.

### 3.1.2.3 Acoustic radiation

The pressure signal is recorded at the point  $(50 r_0, 50 r_0)$  in order to analyze the radiating frequency; its evolution is reported in Figure 3.4. A transient signal is recognized at

the very beginning, with an amplitude higher than the physical signal's one. This transient pressure wave is created by initial conditions, and completely leaves the domain after 7000 time steps without creating spurious waves.

After the transient, three phases with different acoustic radiation are recognized on the pressure signal. Firstly, between time steps 7000 and 108500, the 19 periods of rotation at the mean period  $T_{\text{mean}} = 5440\Delta t$  produce an acoustic radiation at the frequency  $f_a \sim 2/T_{\text{mean}}$ . Then, frequency and levels increase as the vortices come closer to each other. Follows a period with an ever increased frequency, and levels equal to one fourth of levels observed during rotation; this corresponds to the detachment and reattachment of vorticity filaments. Finally, the acoustic radiation decreases while the single vortex structure becomes slowly circular.

Note that the mean of the pressure signal is not equal to the initial pressure  $p_0$ ; the disturbances are probably due to defaults in the boundary conditions. This low-frequency depression can alter the representation of acoustic pressure waves; in this case, visualizing the dilatation field  $\Theta$  is often more appropriate taken that the sound field is almost harmonic, refer to Colonius *et al.*<sup>29</sup> for instance. In the acoustic far field, dilatation is moreover proportional to the pressure time derivative:

$$\Theta = \nabla \cdot \mathbf{u} = -\frac{1}{\rho_0 c_0^2} \frac{\partial p}{\partial t}$$

The dilatation in far field during the rotation phase is shown in Figure 3.5. It presents a double spiral structure, corresponding to a rotating quadrupolar acoustic source. The wavelength associated with the acoustic radiation is  $\lambda_a = 30 r_0$ , corresponding to a frequency  $f_a = 3150\text{Hz}$ . Figure 3.6(a) reports how the quadrupole lobes are shifted by 45 degrees with respect to the principal axes of the two vortices, as illustrated in Figure 3.3(a). Figure 3.6(b) presents the dilatation in near field, showing the more complex structure composed of two face-to-face quadrupoles.

### 3.1.2.4 Application of the hybrid method

The source terms  $S_i^t = \partial T_{ij}^t / \partial x_j$  and  $S_i^f = \partial T_{ij}^f / \partial x_j$ , refer to equations (2.9) and (3.1)-(3.2), are recorded during the vortices rotations, between the time steps  $10^4$  and  $10^5$ , every 20 time steps. They are recorded on the central  $200 \times 200$  cells where the Cartesian mesh is uniform, corresponding to a square extending from  $-2.8 r_0$  to  $2.8 r_0$  in both directions. A snapshot of these source terms is given in Figure 3.7. For indication, the instantaneous, mean and fluctuating velocity fields are also given in Figure 3.8. From these figures, it is clear that the mean velocity field is localized in the vortices region and is zero in the acoustic propagation region, as expected.

The source terms are transformed to the spectral space thanks to a Fast Fourier Trans-

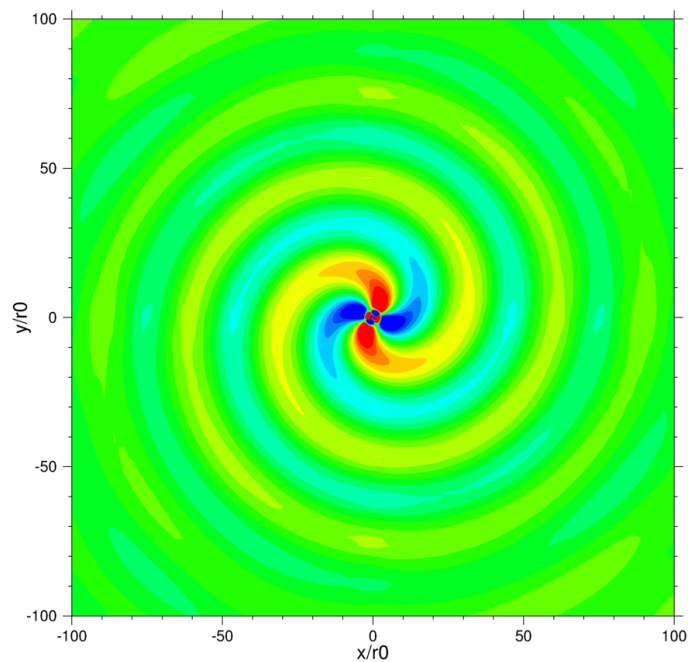


**Figure 3.5** – Two corotating vortices in a medium at rest. Dilatation field obtained after 50000 time steps. Levels from  $-15$  to  $15 \text{ s}^{-1}$ .

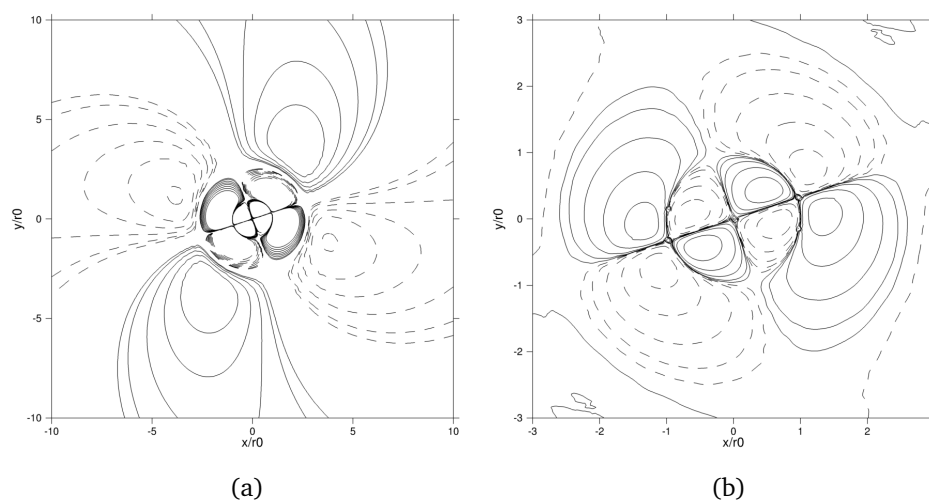


**Figure 3.6** – Two corotating vortices in a medium at rest. Dilatation field obtained after 50000 time steps. (a): 8 isocontours from  $8$  to  $56 \text{ s}^{-1}$ . (b): 5 isocontours from  $10$  to  $810 \text{ s}^{-1}$ . — : positive isocontours, - - - : negative isocontours.

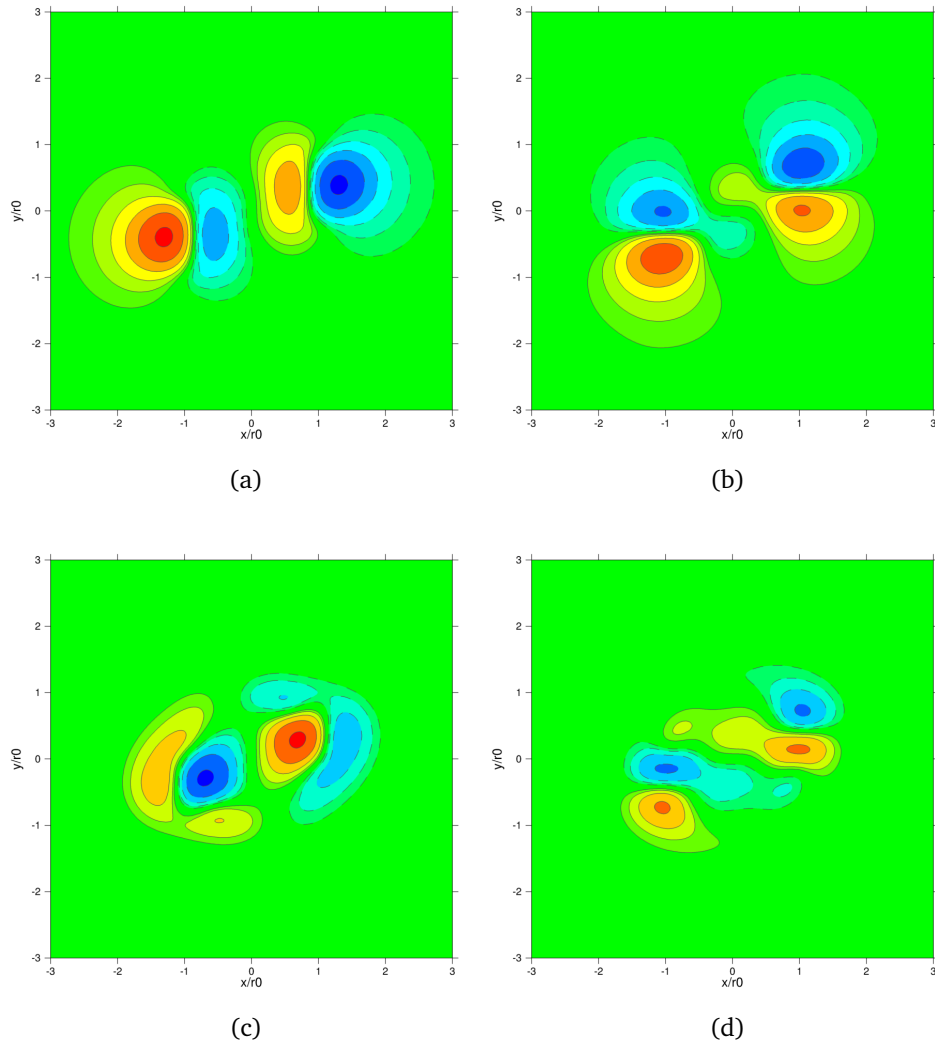


**Figure 3.7** – Two corotating vortices in a medium at rest. Instantaneous source terms obtained after 50000 time steps. (a):  $S_1^t$ , (b):  $S_2^t$ , (c):  $S_1^f$  and (d):  $S_2^f$ . 6 isocontours from  $6 \times 10^5$  to  $1.1 \times 10^7$  Pa/m. — : positive isocontours, - - - : negative isocontours.

form in order to be propagated. The time signal is centered, removing of the mean, and a Hanning filtering is applied before transformation. The acoustic propagation is realized by using these spectral source terms through the implementation (2.11) described in §1.3.2.1, with the direct solver MUMPS<sup>24</sup>. Infinite elements of order 20 placed along the circular boundary assure a free field propagation without reflection at the boundary.

The mesh used for the acoustic propagation is circular and extends from  $-104r_0$  to  $104r_0$  in both directions. It is designed so that its nodes exactly match the CFD cell centers in the region where sources are recorded in order to avoid interpolation<sup>2</sup>; in the remainder of the domain, the mesh size is constrained to  $\Delta_{ac} = 5$  mm, assuring accurate acoustic

<sup>2</sup>In a finite volume code, the velocity is computed at the cell centers; computing and exporting source terms at this location allows a more accurate gradient computation and avoids errors of interpolation from the cell center to the nodes.

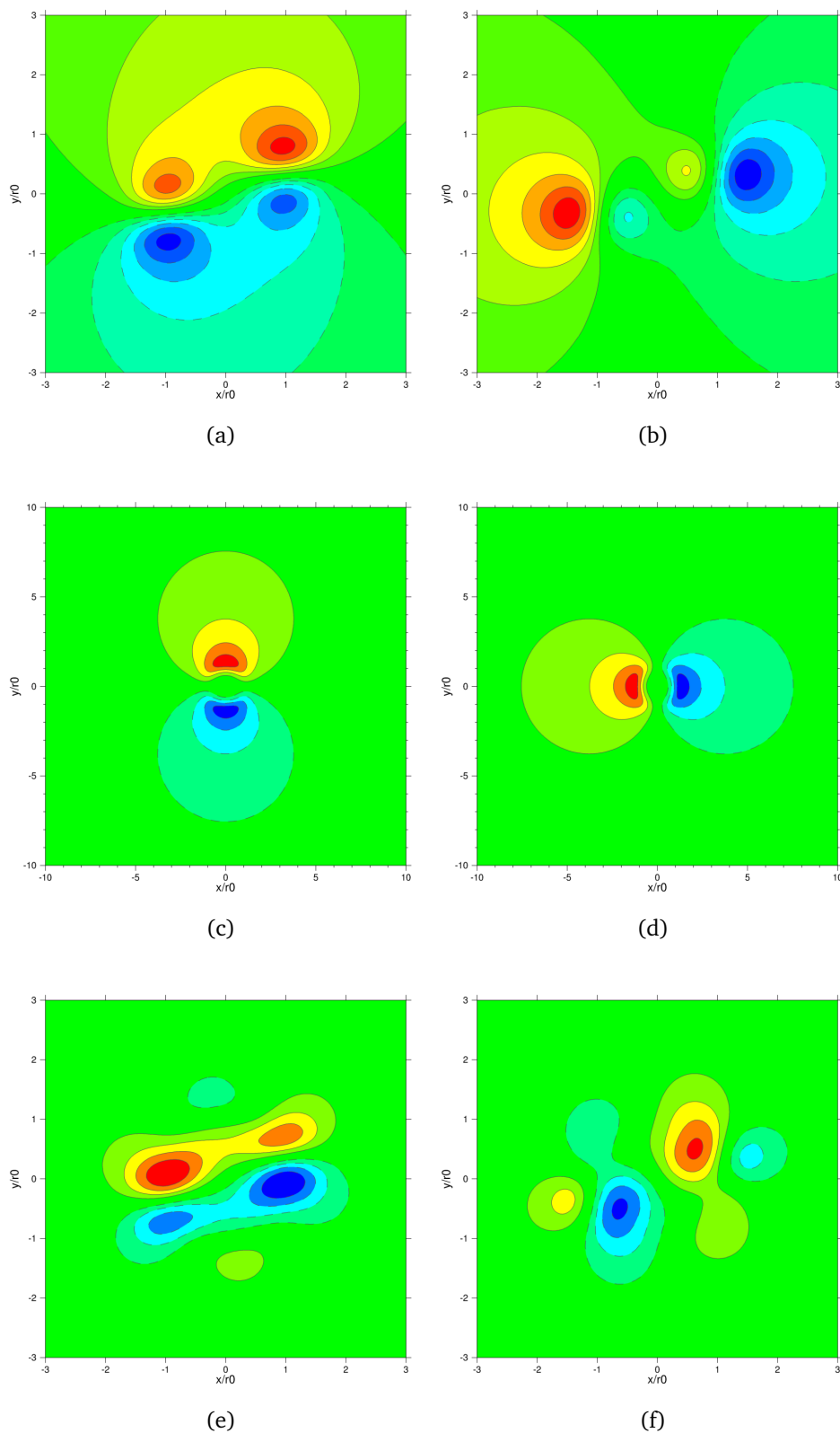


**Figure 3.8** – Two corotating vortices in a medium at rest. Instantaneous source terms obtained after 50000 time steps. (a):  $u$  and (b):  $v$ , instantaneous velocity; 6 isocontours from 20 to 120 m/s. (c):  $\bar{u}$  and (d):  $\bar{v}$ , mean velocity; 4 isocontours from 20 to 80 m/s. (e):  $u'$  and (f):  $v'$ , fluctuating velocity; 4 isocontours from 20 to 80 m/s. — : positive isocontours, - - - : negative isocontours.

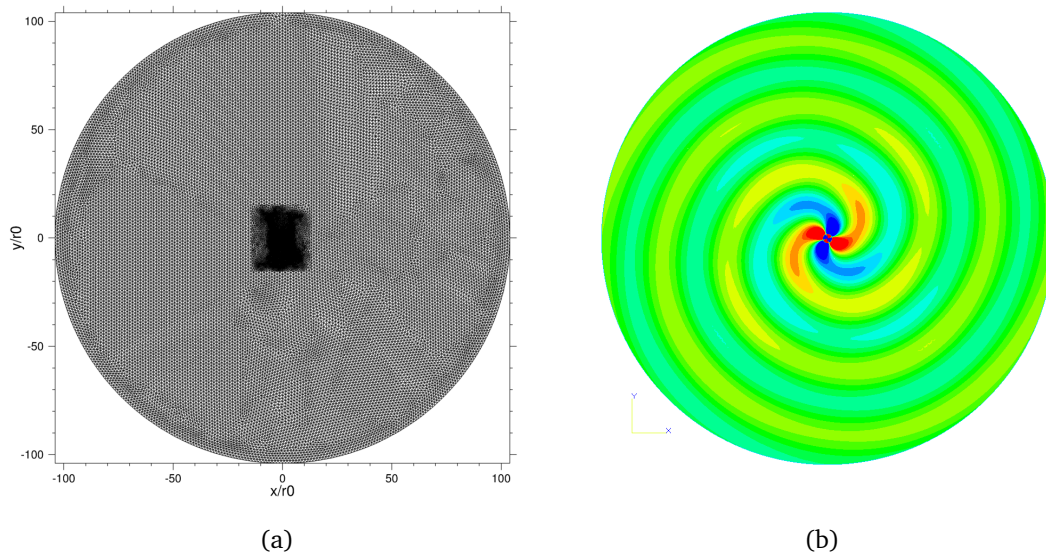


**Figure 3.9** – Two corotating vortices in a medium at rest. (a): Acoustic mesh. (b): Acoustic pressure field (real part) at the main radiation frequency  $f_a$ ; levels from  $-50$  to  $50$  Pa. The domain extends spatially from  $-104 r_0$  to  $104 r_0$  in both directions.

propagation up to 11300 Hz. The generally admitted criterion states that one acoustic wavelength has to be discretized by at least 6 elements. The acoustic mesh is displayed in Figure 3.9(a). The acoustic radiation is then computed in the whole acoustic domain.

### 3.1.2.5 Application of the analytical resolution

Similarly, in order to compute the analytical solution of Lighthill's equation, the source terms  $T_{ij}^t$  and  $T_{ij}^f$  are recorded on the same  $200 \times 200$  points in the center of the CFD mesh and at the same time steps. After the same treatment on the time signal (mean removing and Hanning filtering), the acoustic pressure radiated by these source terms at point  $(50 r_0, 50 r_0)$  is computed with equation (3.8).

### 3.1.2.6 Acoustic results

As a first validation, Figure 3.9(b) presents the acoustic radiation as computed by the variational formulation at the main frequency of radiation  $f_a = 3153$  Hz. The radiation structure is identical to the one determined by direct computation, namely a rotating quadrupole characterized by its double spiral shape. The levels correspond to the mean amplitude of the pressure signal presented in Figure 3.4.

Acoustic results are shown in Figure 3.10 in terms of sound pressure levels radiated at point  $(50 r_0, 50 r_0)$ . The three methods described above are compared: the direct computation, the variational formulation and the analytical resolution of Lighthill's Acoustic

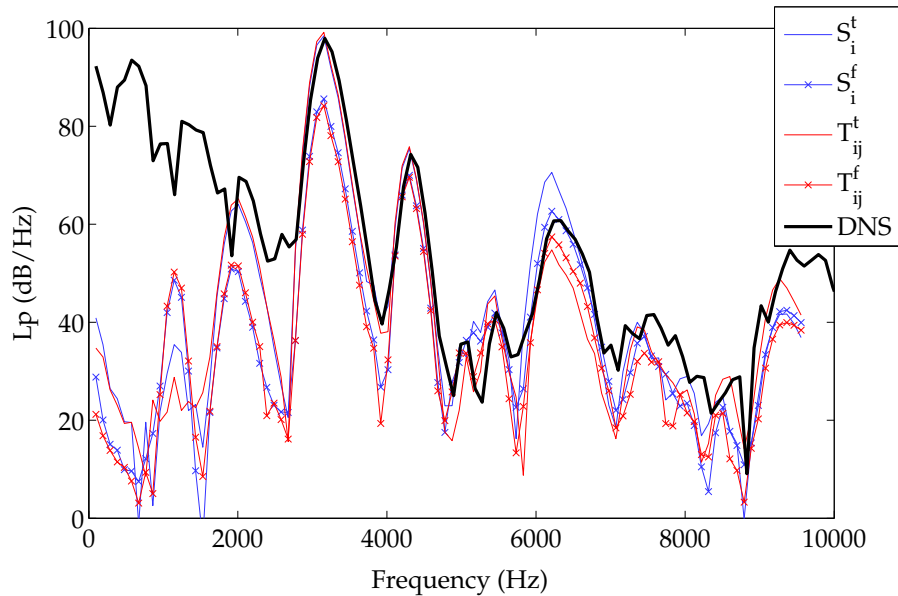


**Figure 3.10** – Two corotating vortices in a medium at rest. Sound pressure level radiated at point  $(50r_0, 50r_0)$  obtained with three different methods. Black: direct calculation; blue: variational formulation; red: analytical resolution of Lighthill’s Acoustic Analogy. Without symbols: levels obtained using the total source terms  $S_i^t$  and  $T_{ij}^t$ . With symbols: levels obtained using the fluctuating source terms  $S_i^f$  and  $T_{ij}^f$ . Levels in dB.

Analogy. Moreover, the two possible definitions of the source terms are used in both hybrid resolutions. It is found that the DNS, the variational and analytical resolutions produce the same levels provided the total source terms  $S_i^t$  and  $T_{ij}^t$  are used.

The agreement is excellent at the radiation frequency  $f_a = 3150\text{Hz}$ . In the low-frequency range, the DNS spectrum departs significantly from spectra obtained using hybrid resolutions; a possible explanation lies in the fact that the direct pressure field is slightly disturbed at low frequencies, as already observed on the time pressure signal in Figure 3.4; however, these disturbances do not alter the signal at the main radiation frequency. An important feature of the graph is the good correlation between the spectra obtained by both the variational and analytical solutions of Lighthill’s Acoustic Analogy; this allows in particular to validate its variational implementation: in absence of surfaces, both formulations are equivalent. The only disparity between both spectra is found at higher frequencies, above 6000 Hz, where the variational formulation produces higher levels; this is likely to be due to the spatial derivation in the former source term definition, where a factor proportional to  $M^2$  appears.

When using the fluctuating source terms  $S_i^f$  and  $T_{ij}^f$ , the spectra produced by both hybrid resolutions provide the same results, with levels shifted 13 dB below the DNS spectrum. In the considered case, there is no explicit mean flow in the observer region, namely in the propagation region. However the localized mean flow present inside the source re-

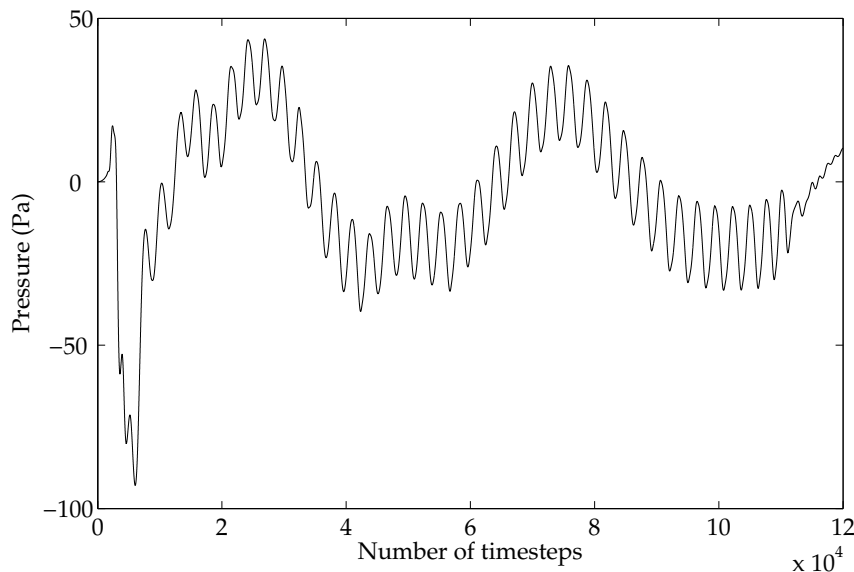


**Figure 3.11** – Two corotating vortices in a medium at rest, incompressible simulation. Static pressure evolution at point  $(50 r_0, 50 r_0)$  as a function of the number of time steps. Levels in Pa.

gion, see Figure 3.8, plays a major role in the acoustic source terms, and the source term  $S_i^t$  built on the total velocities has to be used.

### 3.1.2.7 Incompressible computation

The simulation is performed a second time, with constant density in order to assess if previous results are linked to the compressibility. The same numerical parameters are chosen: the simulation is laminar, using the density-based solver of Fluent; second order upwind spatial discretization is used for flow variables, while the time discretization is implicit of second order, with the time step  $\Delta t = 1 \times 10^{-7}$  s.

As previously, the vortices perform 19 rotations before merging. The vortices evolution is the identical to the one shown in Figure 3.3 and is not reported here. The static pressure signal is displayed in Figure 3.11; as the computation is incompressible, the levels are not representative, on the contrary of frequency content. It is observed that the vortices rotation is slightly faster than in the compressible simulation, yielding an acoustic radiation at the frequency  $f_a = 3444$  Hz. The acoustic spectra obtained using the variational and the analytical formulations of Lighthill's Acoustic Analogy at point  $(50 r_0, 50 r_0)$  are presented in Figure 3.12. These spectra exhibit nearly the same levels as for the compressible simulation for the main radiating frequency,  $f_a$ , with a shift of 11 dB when using the fluctuating source terms with respect of spectra obtained using the total source terms. This last computation allows to understand that compressibility effects play a minor role in Lighthill's source term in low Mach number conditions.

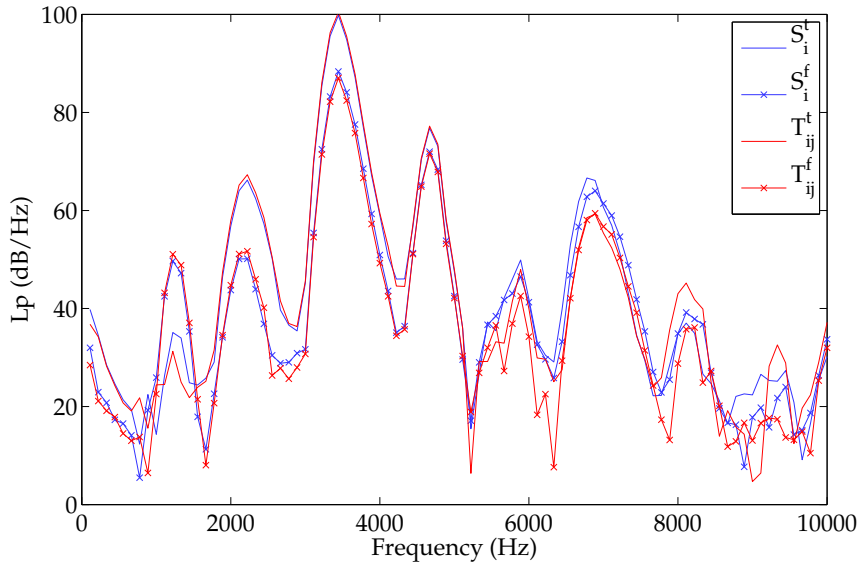


**Figure 3.12** – Two corotating vortices in a medium at rest, incompressible simulation. Sound pressure level radiated at point  $(50 r_0, 50 r_0)$  obtained with two different methods. Blue: variational formulation; red: analytical resolution of Lighthill's Acoustic Analogy. Without symbols: levels obtained using the total source terms  $S_i^t$  and  $T_{ij}^t$ . With symbols: levels obtained using the fluctuating source terms  $S_i^f$  and  $T_{ij}^f$ . Levels in dB.

### 3.1.3 Two corotating vortices placed in a shear layer

The addition of a shear layer, previously introduced by Bogey *et al.*<sup>15</sup>, allows to study the effects of a mean velocity field on the acoustic radiation. The shear layer is built between two parallel plane flows of opposite velocity  $\Delta U$  and  $-\Delta U$ , producing thus a zero mean convection velocity. With this definition, the vortices are not convected by the mean flow field and remain in the center of the computational domain. The shear profile, also shown in Figure 3.13, is defined with the following hyperbolic-tangent expression of the longitudinal mean velocity:

$$u_0(y) = \Delta U \tanh\left(\frac{u}{2r_0}\right)$$

where  $r_0$ , half distance between vortices, is also the shear layer momentum width. The mean velocity is fixed at  $\Delta U = c_0/8$ .

The same computations as in the previous case are performed: a DNS constitutes the reference results, while the variational and analytical formulations of Lighthill's Acoustic Analogy are successively applied using the complete source terms  $S_i^t$  and  $T_{ij}^t$ , and using the fluctuating source terms  $S_i^f$  and  $T_{ij}^f$  in which the mean velocity considered is only the mean shear layer. The mean local velocity due to the constant vortices rotation is no longer considered.

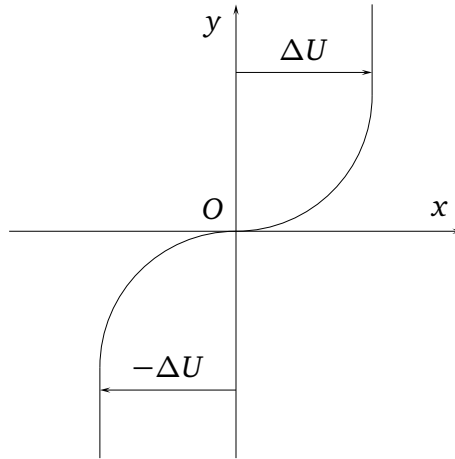


Figure 3.13 – Scheme of the shear layer used for corotating vortices.

### 3.1.3.1 Direct Noise Computation

The computational features are similar to those used before: two identical vortices are introduced at  $(r_0, 0)$  and  $(-r_0, 0)$  together with the mean shear layer velocity field. The boundary conditions are adapted to allow flow entrance without disturbances: at the upper half of left border and lower half of right border, where fluid is entering the domain, a pressure shear profile corresponding to the velocity shear profile is imposed. The remaining lower half of left border and upper half of right border keep the Non Reflecting Boundary Conditions imposed in the medium at rest; symmetry is also kept on upper and lower boundaries.

Although this is not visible on the vorticity contours of Figure 3.14, the evolution of the vortices is modified by the presence of the shear layer. Indeed, when a vortex is located in the upper half of the shear layer, its rotation is accelerated with the positive convection velocity toward the right; the inverse happens in the lower half shear layer. This is because the shear layer is added to the natural clockwise rotation of the vortices, inducing an increase of the rotation speed  $\omega$ . Besides, during the rotation phase, the vortices rotation is not constant any more and is subject to variations, depending on the position of the vortices in the shear layer.

Due to the rotation speed increase, the vortices undergo merging sooner than in a medium at rest; here, the merging happens during the 8th rotation period and the rotation period is  $3090 \Delta t$ . The pressure signal of Figure 3.15 is similar to the signal obtained in the previous case, while the disturbances of the mean pressure seem lower.

The dilatation is used once again to represent the acoustic radiation; in presence of a mean uniform unidirectional flow  $\Delta U$ , the dilatation is related to the pressure time derivative by the following expression:

$$\Theta = -\frac{1}{\rho_0 c_0^2} \left( \frac{\partial p}{\partial t} \pm \Delta U \frac{\partial p}{\partial x} \right)$$

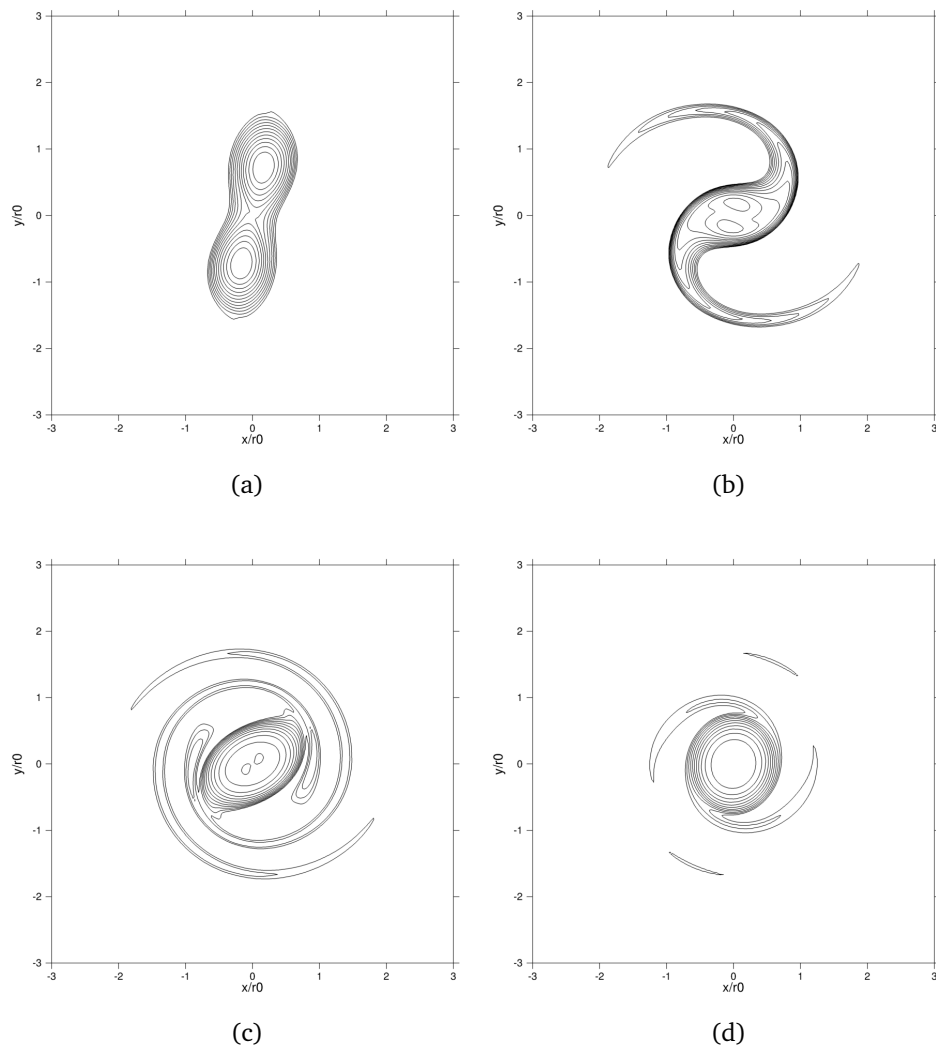


**Figure 3.14** – Two corotating vortices placed in a shear layer. Vorticity field obtained after (a): 20000, (b): 24000, (c): 26000 and (d): 28000 time steps. Vorticity isocontours from  $1.5 \times 10^4$  to  $2.2 \times 10^5 \text{ s}^{-1}$ .

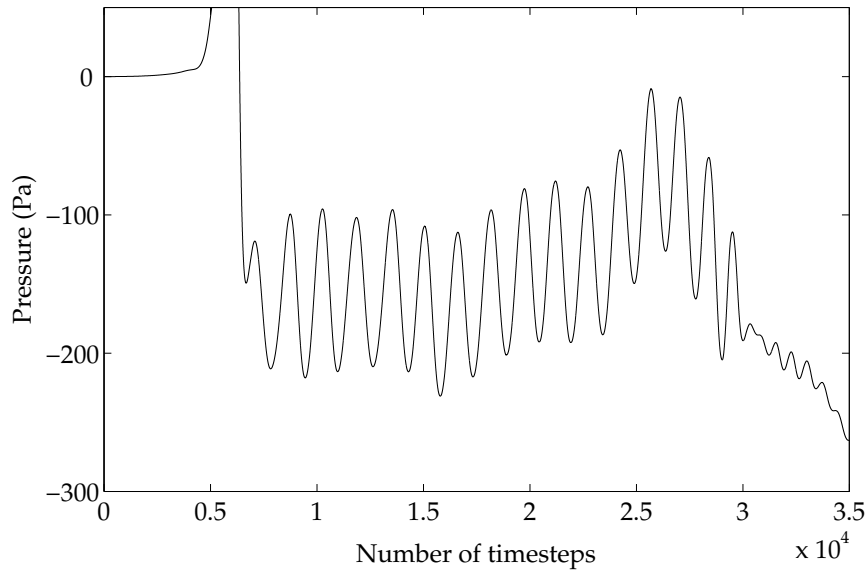


**Figure 3.15** – Two corotating vortices placed in a shear layer. Static pressure fluctuations  $p - p_0$  at point  $(50 r_0, 50 r_0)$  as a function of the number of time steps. Levels in Pa.

In Figure 3.16(a), the double spiral structure is again present, indicating a rotating quadrupole. The effects of the shear layer on the acoustic radiation are clearly visible. The wave fronts are deformed by the mean flow, having an oval shape instead of circular as in the medium at rest case. Moreover, the directivity is affected by the mean flow, with a favored radiation direction perpendicular to the mean flow, and lower levels in the main direction.

### 3.1.3.2 Acoustic results

As previously, the sound pressure level radiated at point  $(50 r_0, 50 r_0)$  is reported in Figure 3.17 for the different computations: DNS, variational formulation with use of total and fluctuating source terms, and analytical formulation with use of total and fluctuating source terms. All spectra are found to collapse, except the DNS spectrum which presents a peak at the main radiation frequency 3 dB lower than the remaining spectra. Therefore, as taking into account or not the mean flow field yields no difference in the acoustic results, it is concluded that the terms linked to pure convection in Lighthill's tensor do not contribute to the radiated sound. The small gap between the DNS and hybrid curves is explained by the fact that in both variational and analytical formulations, the source term is defined on the central portion of the CFD domain extending from  $-2.7 r_0$  to  $2.7 r_0$  in both directions. Therefore, all refraction effects computed by DNS in the whole domain are missed in hybrid formulations, leading to a slightly different result. Moreover, the propagation operator does not account for the mean flow in the observer region and is therefore not able either to catch these effects.

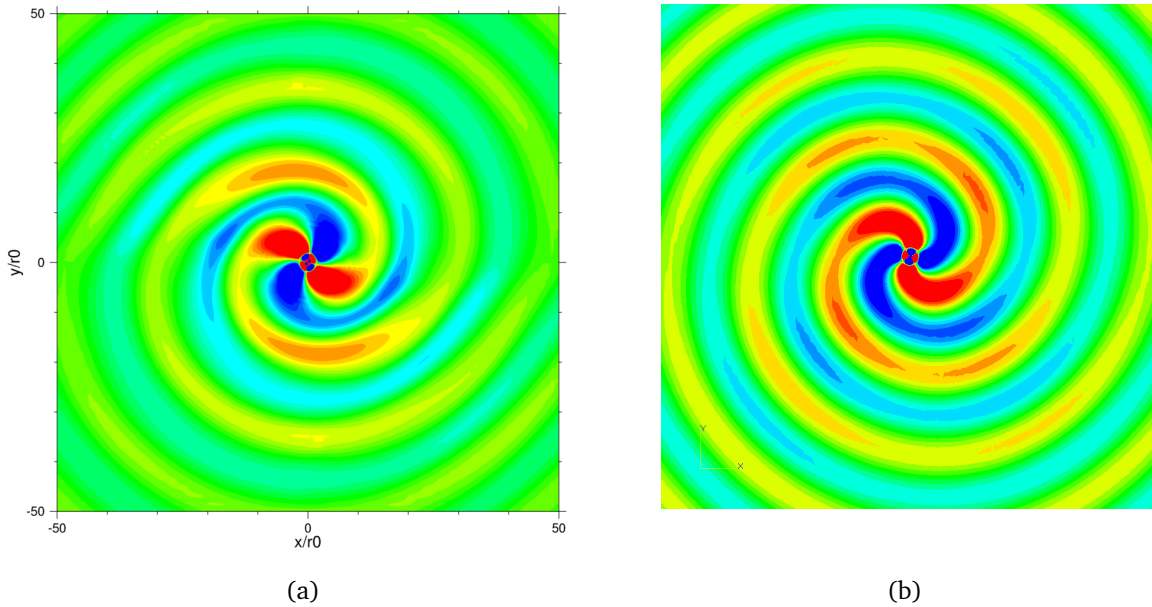


**Figure 3.16** – Two corotating vortices placed in a shear layer. (a): Dilatation field obtained after 20000 time steps. Levels from  $-50$  to  $50 \text{ s}^{-1}$ . (b): Acoustic pressure field (real part) at the main radiation frequency  $f_a$ ; levels from  $-50$  to  $50 \text{ Pa}$ . The domain extends spatially from  $-50 r_0$  to  $50 r_0$  in both directions.

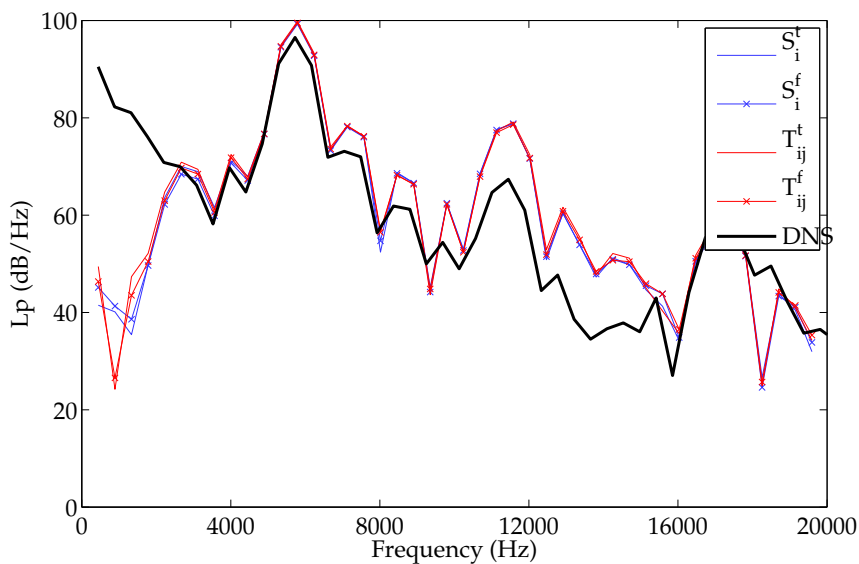


**Figure 3.17** – Two corotating vortices placed in a shear layer. Sound pressure level radiated at point  $(50 r_0, 50 r_0)$  obtained with three different methods. Black: direct calculation; blue: variational formulation; red: analytical resolution of Lighthill's Acoustic Analogy. Without symbols: levels obtained using the total source terms  $S_i^t$  and  $T_{ij}^t$ . With symbols: levels obtained using the fluctuating source terms  $S_i^f$  and  $T_{ij}^f$ . Levels in dB.

However, in terms of radiation structure, the variational formulation is consistent; the acoustic pressure field shown in Figure 3.16(b) presents a distorted double spiral structure of oval shape, less pronounced than on the dilatation field of Figure 3.16(a) but still present. The privileged radiation directions are also similar to those of the direct computation.

### 3.1.4 Conclusion

The study of corotating vortices firstly placed in a medium at rest, and then in a shear layer, has shown the correct expression of the source term in the variational formulation of Lighthill's Acoustic Analogy: the source term  $S_i^t$  build on the total velocities has to be used. Secondly, the study with the shear layer sheds some light on the convection effects in Lighthill's Acoustic Analogy: the terms linked to pure convection in Lighthill's tensor do not contribute to the radiated sound, on the contrary to the terms linked to a local mean velocity which can contribute significantly to the radiated sound. Moreover, in the variational formulation of Lighthill's Acoustic Analogy, refraction of acoustic waves by a mean flow field can only be taken into account if the source terms are computed on the whole region where acoustic mean flow interactions exist. Otherwise, as in the case of the two vortices placed in a shear layer, mean flow effects outside the source region are out of reach of the present method. The present investigation clearly supports the discussion of Bogey *et al.*<sup>15</sup>.

## 3.2 Exit of turbulent structures from the CFD domain

The spatial extent of the source term has to be treated with great care; indeed, following several authors, refer to Casper *et al.*<sup>23</sup> for instance, this study shows with the test case of a vortex convection through a virtual boundary that spatial truncation of noise sources creates spurious numerical noise of dipolar nature. While common sense would then lead to define a source region extended in the whole CFD region, the simulation time objective of the hybrid method rather leads to a selection of reduced noise source regions. In order to conciliate both aspects of the problem, a spatial filtering technique, derived from the work of Pérot<sup>79</sup>, is tested and shown to eliminate the effects of spatial truncation of noise sources.

The following study is focused on the convection of a vortex through a virtual boundary and its radiated noise. As the objective is to determine the best method to reduce spurious noise created at the boundary, and not to study the vortex evolution in the CFD code, the vortex is perfectly convected, without disturbances, within an analytical solution; the acoustic propagation is performed with the variational formulation of Lighthill's Acoustic Analogy as previously. Dissipation effects usually present in a CFD calculation are not taken into account. This is thus a very constraining test case, as in a real computation, a vortex is progressively dissipated with the convection and its energy decreases as moving toward the boundary.

### 3.2.1 Convection of a vortex through a virtual boundary: presentation

A two-dimensional vortex is initialized at the origin of the domain, whose extent is  $-50\Delta < x < 750\Delta$  in the first direction and  $-50\Delta < y < 50\Delta$  in the second direction. The mesh size  $\Delta$  is constant in both directions:  $\Delta = 5 \times 10^{-4}$  m. The vortex is initialized with the following velocity components:

$$\begin{cases} u(x, y) = U_0 + a_0 y \exp \left[ -\frac{\ln 2}{(n\Delta)^2} (x^2 + y^2) \right] \\ v(x, y) = -a_0 x \exp \left[ -\frac{\ln 2}{(n\Delta)^2} (x^2 + y^2) \right] \end{cases}$$

where  $U_0$  is the convection velocity, and the constant  $a_0 = 320 \text{ m}^2/\text{s}$  is chosen to verify that  $u_{\max} = 2 \text{ m/s}$  at a distance of  $n\Delta$  from the vortex center. With this definition, the vortex diameter is  $D = 2n\Delta$ , and  $n = 10$  and  $5$  successively in this study. The vortex is convected at velocity  $U_0$  from  $x = 0$  to  $x = 0.35$ , with the time step  $\Delta t = \Delta/U_0$ .

Regarding the acoustic propagation, the acoustic domain is a disk of radius  $800\Delta$  centered on the vortex origin at  $t = 0$  and containing the mathematical region described previously. The mathematical mesh is kept for the acoustic mesh; in the remaining of the

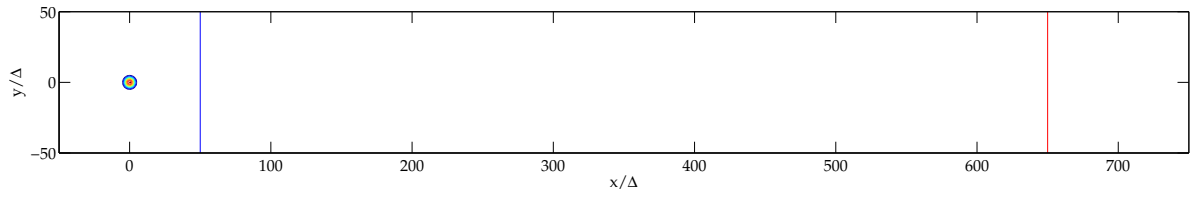


**Figure 3.18** – Initialization of the vortex. The vertical blue line indicates the location of  $x_{\min}$ , the vertical red line indicates the location of  $x_{\max}$ .

domain, the mesh is coarsened up to  $\Delta_{\max} = 10\Delta$ . Results are given in terms of acoustic power radiated by the whole domain, integrated on the circular boundary. For representation, the Strouhal number  $St = fD/U_0$  is chosen where  $f$  is the frequency.

Spatial filtering is defined as a weight applied to the source terms before Fourier transformation. This weight is applied on distance  $d = x_{\max} - x_{\min}$  (see Figure 3.18).  $x_{\min}$  is fixed at  $50\Delta$  in the whole study, while  $x_{\max}$  can vary, producing various filter lengths  $d$ . First of all, the filter length  $d$  is fixed at  $600\Delta$  and the filter shape is varied. Secondly, the best filter shape is chosen and the filter length  $d$  is adjusted.

### 3.2.2 Study on the filter shape

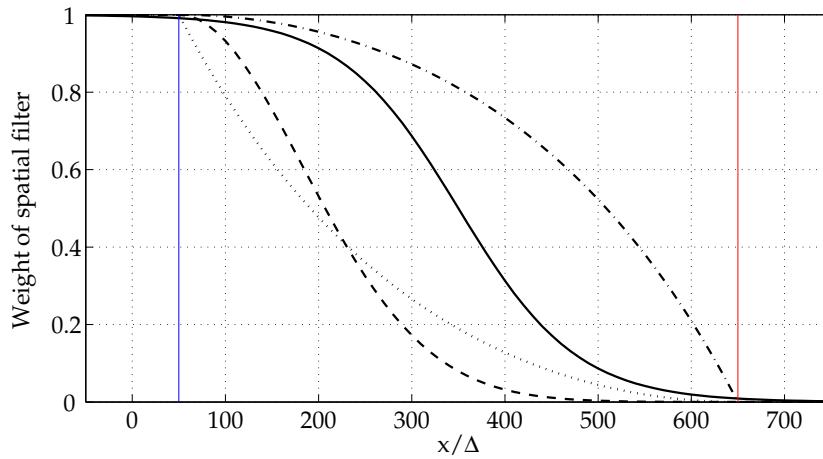


**Figure 3.19** – Spatial filters applied to the vortex convection case. The vertical blue line indicates the location of  $x_{\min}$ , the vertical red line indicates the location of  $x_{\max}$ .  $\cdots$ :  $\mathcal{W}_1$ ;  $-\cdot-\cdot-$ :  $\mathcal{W}_2$ ;  $---$ :  $\mathcal{W}_3$ ;  $—$ :  $\mathcal{W}_4$ .

The vortex diameter is fixed at  $D = 20\Delta$ , and the convection velocity is  $U_0 = 2$  m/s. The filter length is thus  $d = 600\Delta = 30D$ : the filter is applied on a distance corresponding to 30 vortex diameters. The acoustic radiation produced by a sharp truncation of the source terms at  $x = x_{\min}$ , as well as four different filter shapes are compared; the reference case is obtained by analyzing the acoustic radiation of the vortex convected without modification

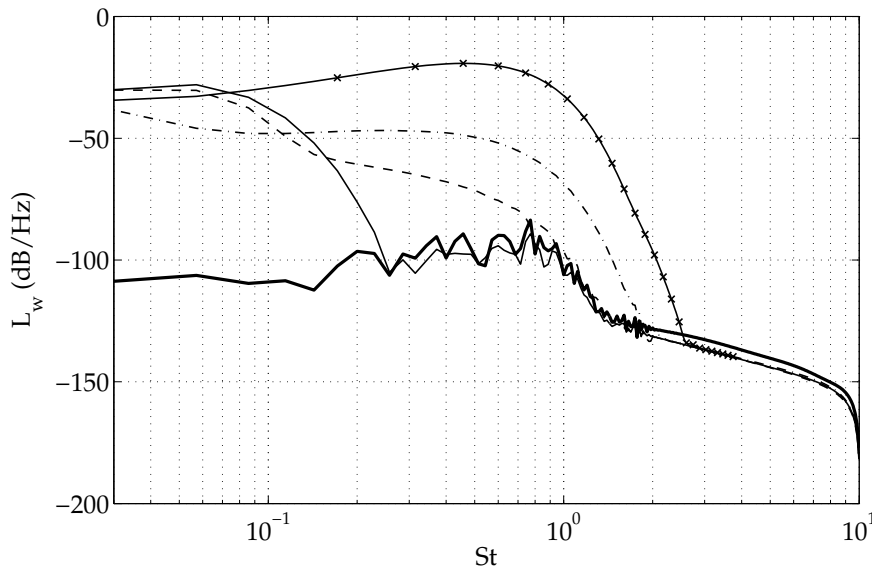


**Figure 3.20** – Acoustic power radiated by the vortex convection. Study on the filter shape. Bold solid line: reference case (no truncation, no filtering);  $-x-$ : sharp truncation at  $x_{\min}$ ;  $- \cdot - \cdot -$ :  $\mathcal{W}_2$ ;  $---$ :  $\mathcal{W}_3$ ;  $—$ :  $\mathcal{W}_4$ .

along the whole domain. The different filter weights are defined as follows:

$$\left\{ \begin{array}{l} \mathcal{W}_1(x) = -1 + \exp \left[ \frac{(x_{\max} - x)^2}{2\sigma^2} \right] \\ \mathcal{W}_2(x) = 2 - \exp \left[ \frac{(x - x_{\min})^2}{2\sigma^2} \right] \\ \mathcal{W}_3(x) = \exp \left\{ -\frac{1}{2} \left[ \frac{\alpha}{2} \frac{x - x_{\min}}{x_{\max} - x_{\min}} \right]^2 \right\} \\ \mathcal{W}_4(x) = \frac{1}{2} \left\{ 1 + \tanh \left[ -\frac{3\pi}{2d} \left( x - \frac{x_{\min} + x_{\max}}{2} \right) \right] \right\} \end{array} \right.$$

with  $\sigma = d/\sqrt{2\ln 2}$  and  $\alpha = 9$ , and are displayed in Figure 3.19. Acoustic results are presented in Figure 3.20. The sharp truncation of noise sources at  $x_{\min}$  produces a strong acoustic radiation in the low frequency range  $St < 2.6$ , with levels superior by more than 75 dB to the reference case, namely without truncation. Such a spurious acoustic radiation is often encountered when working with hybrid methods, when the acoustic terms are crossing the boundary of the region where they are considered. Casper *et al.*<sup>23</sup> have shown that the spurious radiation is of dipolar nature. Filters  $\mathcal{W}_1$  and  $\mathcal{W}_2$  are symmetric and thus produce the same acoustic radiation; therefore, only the results associated to filter  $\mathcal{W}_2$  are presented in Figure 3.20. The main observation is that all filters produce a spurious acous-

tic radiation. However, filters have a different impact on the acoustic power level. Indeed, filters  $\mathcal{W}_2$  and  $\mathcal{W}_3$ , which are sharper than filter  $\mathcal{W}_4$ , radiate in a greater range of Strouhal numbers, respectively for  $St < 1.8$  and  $St < 1.1$ , while the hyperbolic-tangent shaped filter  $\mathcal{W}_4$  radiates only for  $St < 0.26$ . This last filter is thus retained for the remaining of the study.

### 3.2.3 Study on the filter length

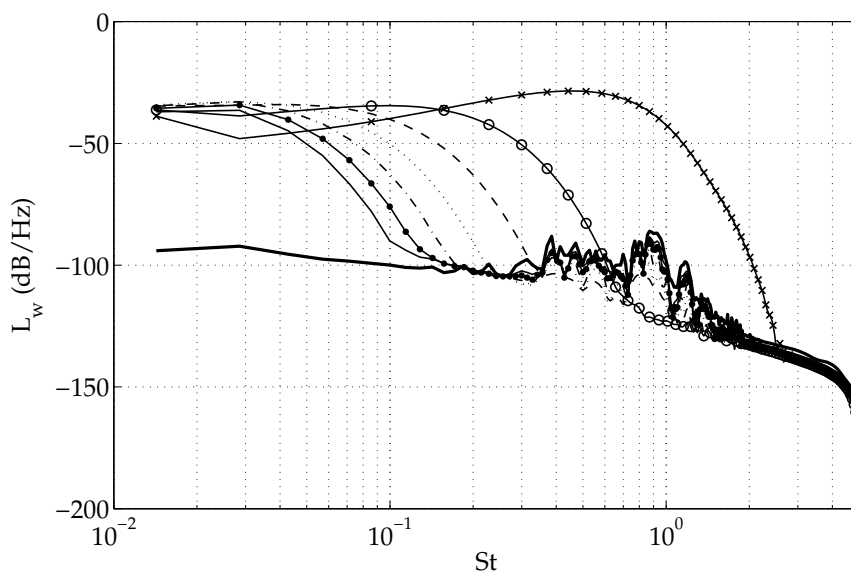


**Figure 3.21** – Acoustic power radiated by the vortex convection. Study on the filter length. Bold solid line: reference case (no truncation, no filtering);  $-x-$ : sharp truncation at  $x_{\min}$ ;  $-o-$ :  $d = 10D$ ;  $- - -$ :  $d = 20D$ ;  $\cdots\cdots$ :  $d = 30D$ ;  $- \cdot - \cdot -$ :  $d = 40D$ ;  $- \bullet -$ :  $d = 50D$ ;  $- -$ :  $d = 60D$ .

In order to minimize the length of the sponge zone that will be used for spatial filtering of acoustic source terms, a study on the filter length is performed. We chose here a convection velocity of 5 m/s and the vortex diameter is now  $D = 10\Delta$ . We apply the spatial filtering defined with the weight  $\mathcal{W}_4$ , and the filter length  $d$  is varied from  $10D$  to  $60D$ . Acoustic results are presented in Figure 3.21. The filter length directly influences the critical frequency: the critical Strouhal number decreases from 0.6 to 0.18 when the filter length varies from  $10D$  to  $40D$ . Then, a further increase of the filter length  $d$  does not seem to significantly improve spectra.

### 3.2.4 Conclusion

This study allows to state that using a  $\mathcal{W}_4$ -shaped spatial filtering on acoustic source terms on a distance of around 20 to 40 times the structure's diameter  $D$  should minimize the effects of spatial truncation above the critical Strouhal number  $St = fU_0/D$ , where  $U_0$  is the convection velocity of the structures crossing the virtual boundary.

### 3.3 Conclusion

In this chapter, the main goal was to present a general validation of the two steps hybrid method. The academic case of two corotating vortices is studied to this purpose. A compressible Direct Numerical Simulation using the density-based solver in Fluent provides reference results, as well as the database for source terms. Although incompressible source terms will be considered in the next chapter, this compressible approach is consistent, since an incompressible verification has been shown to yield similar results. This study has also assessed an important fact, namely that using an acoustic analogy where the propagation operator does not account for mean flow effects, the mean flow has to be accounted for in the source term. However, it has been also verified that mean flow effects in the observer region, outside the source region, are not computed in this way.



# 4.

## Study of a diaphragm placed in a duct at low Mach number

---

*T*HIS CHAPTER is devoted to the study of a three-dimensional internal flow in a rather simple geometry. In particular, a thorough analysis of the transient flow field and of its radiated noise is performed. Firstly, we explain the reasons for the choice of this particular geometry as a validation case for our hybrid method of aeroacoustic noise computation. Then, the experimental data obtained from a dedicated campaign in the frame of this research project are presented, constituting the base for the validation of numerical results. Two numerical studies of the diaphragm case are finally presented, the first one being applied on a periodic slice of the domain (this case will hereafter be named the diaphragm slice study); we will show that although the geometric approximation is relevant, it suffers from limitations due to the limited spanwise extent. The second numerical study applies on the complete three dimensional geometry; aerodynamic and acoustic results are compared to the reference experimental data, as well as on the Direct Noise Computation performed by Gloerfelt & Lafon<sup>54</sup>.

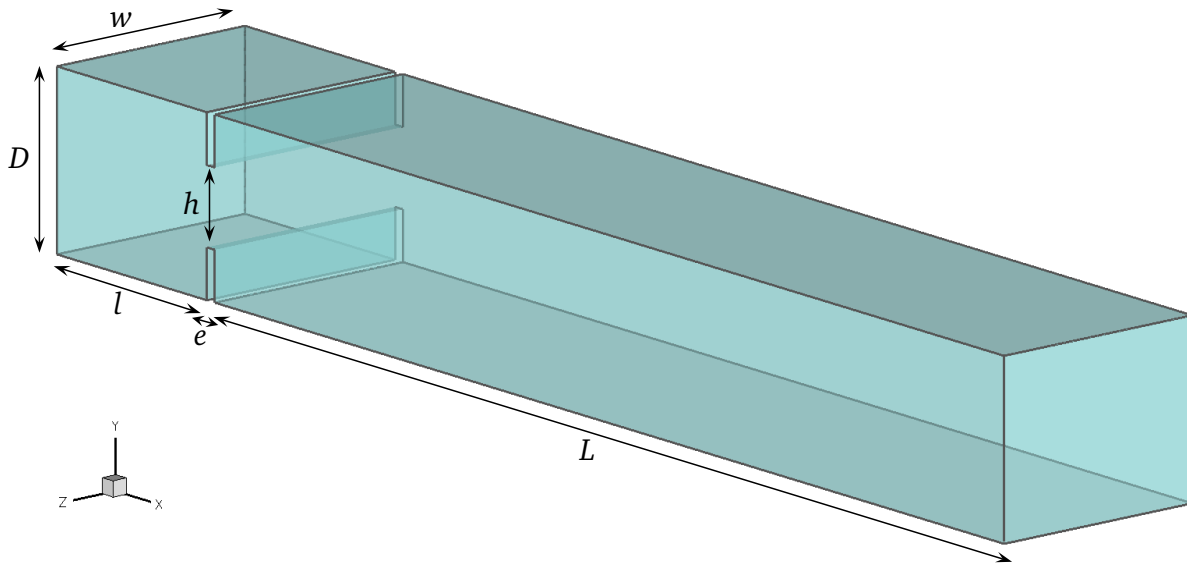


**Figure 4.1** – Diaphragm geometry. The aspect ratio is given by  $A = w/h$ , where  $w$  is the duct width and  $h$  the diaphragm opening; the expansion ratio is  $R = D/h$ , where  $D$  is the duct height. The  $x$ -axis indicates the streamwise flow direction;  $y$ - and  $z$ -axis respectively indicate the transverse and spanwise directions.

## 4.1 Introduction

### 4.1.1 Geometry

The diaphragm geometry is presented in Figure 4.1; it consists in a rectangular duct of section  $D \times w = 80 \times 100$  mm obstructed by a diaphragm whose opening is rectangular of section  $h \times w = 35 \times 100$  mm. The diaphragm extends over  $e = 5$  mm, and the inlet and outlet ducts lengths are respectively  $l = 95$  mm and  $L = 500$  mm. The aspect ratio defined as  $A = w/h$  is equal to 2.86, and the expansion ratio defined as  $D/h$  is 2.29. In this paper, we study the flow and acoustic results for a very low Mach number flow, with the mean velocity  $U_0 = 6$  m/s at the inlet, corresponding to  $M = U_0/c_0 = 0.018$ . The Reynolds number  $Re_D$  based on the inlet velocity  $U_0$  and duct height  $D$ , and the Reynolds number  $Re_h$  computed at the diaphragm, based on the maximum mean velocity  $U_m = 20$  m/s and obstruction height  $h$ , are respectively

$$Re_D = 3.3 \times 10^4 \quad \text{and} \quad Re_h = 4.8 \times 10^4$$

The flow is thus fully turbulent.

### 4.1.2 Previous studies on similar geometries

The ducted diaphragm case has generated a great interest in the aeroacoustic community. Analytical developments have also been written by Hofmans *et al.*<sup>59</sup> for the reflec-

tion and transmission coefficients of the diaphragm. Longatte<sup>67</sup> choose to apply a hybrid method consisting in propagating acoustic source terms based on mean flow quantities. The present work is based on reference results provided by Van Herpe *et al.*<sup>110;111</sup> who performed experiments in order to get the acoustic power radiated by the diaphragm, and by Glerfelt and Lafon<sup>54</sup> who performed a Direct Noise Computation.

The aerodynamic features of the flow downstream a rectangular diaphragm is very similar to that downstream a plane sudden expansion. This last geometry has been extensively studied experimentally, and many authors provide detailed descriptions of the flow characteristics for different aspect and expansion ratios. These studies mainly aim at providing a physical explanation to the symmetry breaking, pitchfork bifurcation, occurring just behind the double step in a specific range of Reynolds numbers and aspect and expansion ratios. This asymmetry causes the flow to attach to one or the other wall parallel to the expansion; this phenomenon is sometimes called the Coanda effect in the literature. The experiments of Durst *et al.*<sup>35</sup> demonstrate that the low Reynolds number flow downstream of a sudden expansion in a symmetric channel of large aspect ratio may be asymmetric and substantially three-dimensional. Cherdron *et al.*<sup>25</sup> moreover provide a map of symmetric and asymmetric flow regions, depending on Reynolds number, aspect and expansion ratios; it is found that a decrease of the aspect and expansion ratios has a stabilizing effect, which extends the range of Reynolds numbers over which symmetric flow can exist. At higher Reynolds numbers, the small disturbances generated at the lip of the sudden expansion are amplified in the shear layers, shedding patterns which alternate from one side to the other with consequent asymmetry of the mean flow. Another general conclusion of Cherdron *et al.*<sup>25</sup> is the ratio between both recirculation lengths: the smaller recirculation region length corresponds to a single wavelength of the disturbance, while the longer recirculation length is close to odd multiples of the disturbance wavelength, three in Cherdron *et al.*<sup>25</sup> experiments.

Last reviews of Escudier *et al.*<sup>38</sup> and Casarsa and Giannattasio<sup>22</sup> provide detailed experimental results for the case of turbulent flow through a plane sudden expansion (PSE) at high Reynolds numbers. In Escudier *et al.*<sup>38</sup>, aspect and expansion ratios are  $A = 5.33$  and  $R = 4$  and the Reynolds number is fixed at  $Re_h = 5.55 \times 10^4$ . In addition to the asymmetry already noticed previously, three-dimensional effects are noticed with differences along the span; this behavior is attributed to the presence of two contra-rotating vortices located downstream the expansion, near the channel side walls, seemingly resulting from the modest aspect ratio. After a detailed analysis of PIV results of the flow through a planar sudden expansion of aspect and expansion ratios  $A = 10$  and  $R = 3$  and at a Reynolds number of  $10^4$ , Casarsa and Giannattasio<sup>22</sup> propose a three-dimensional model of the complex flow field. In this model, a spanwise mass transport of spiral motion is associated to each recirculation; the mass loop is closed thanks to the presence of corner vortices in the vicinity of lateral walls.

It is interesting to note that all numerical experiments performed on planar sudden expansions report a natural evolution of the flow toward asymmetry, even when using Reynolds Averaged Navier-Stokes simulations, provided that the geometric and flow conditions are favorable to bifurcation and that a transient computation is led. Fearn *et al.*<sup>42</sup> compute the two-dimensional flow field downstream of a plane sudden expansion ( $R = 3$ ,  $A = 8$ ) with a finite-element discretization of Navier-Stokes equations. An experimental bifurcation diagram is built; in order to reproduce the disconnection due to small imperfections in the experimental apparatus, the calculations are run with a 1% change in the geometry, grid shift with respect to the symmetry axis. Fearn *et al.*<sup>42</sup> conclude that, considering the overall agreement in resulting diagrams, the bifurcation observed is a fundamental property of the Navier-Stokes equations.

Durst *et al.*<sup>36</sup> study experimentally and numerically a plane sudden expansion of aspect and expansion ratios  $A = 2$  and  $R = 2$ , at a high Reynolds number in the fully laminar region  $Re = 610$ . Three-dimensional effects are supposed weak, therefore a 2D finite element simulation is used. While a symmetric flow configuration was always assumed, flow bifurcation occurred without geometric inlet disturbances; Durst *et al.*<sup>36</sup> attribute it to truncation errors which prevent a zero transverse velocity at the symmetry plane.

More recently, De Zilwa *et al.*<sup>33</sup> assume that the flow through a plane sudden expansion of aspect ratio  $A = 4$  and expansion ratio  $R = 2.85$  is two-dimensional; they chose a transient  $k - \epsilon$  modeling, and predicted the transition from symmetry to asymmetry at  $Re = 90$ . Detailed comparisons of velocity and r.m.s. profiles are given and compared to experimental results at low Reynolds numbers; the poor agreement is attributed to the turbulence modeling limitations, while missed three-dimensional effects could also be a source of errors.

Chiang *et al.*<sup>26</sup> report an original behavior of the flow field where, in addition to the conventional step height bifurcation, a spanwise bifurcation is observed when the channel aspect ratio exceeds a critical value; indeed, in this particular case, the step height symmetry breaking evolves with different symmetry breaking orientations on the left and right sides of the channel.

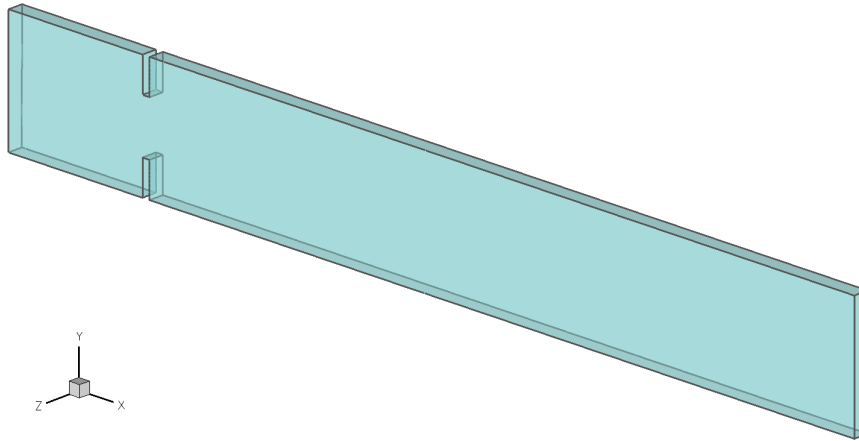


Figure 4.2 – Diaphragm slice. Sketch of the geometry.

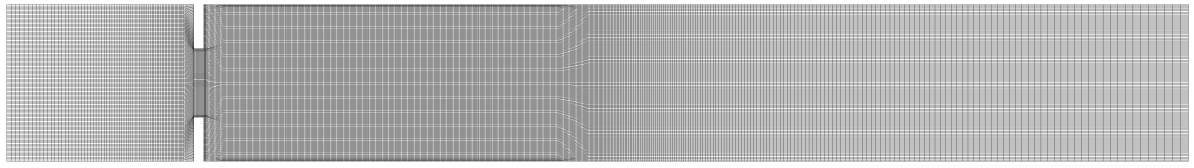
## 4.2 Numerical study on a slice of the domain

In this first numerical study, the computation is performed on a slice of the diaphragm geometry, considering that a periodicity in the  $z$ -direction is relevant;  $1/10^{\text{th}}$  of the width, i.e., 10 mm is kept, as shown in Figure 4.2. Taken the results obtained in previous studies, this domain reduction may be limiting for accuracy and in particular for the three-dimensional development of the flow, but this configuration had to be studied to stress the importance of considering the whole geometry in an (hybrid) aeroacoustic computation involving Large Eddy Simulation. Indeed, it is tempting for an industrial having little computing resources available to cut in the geometry or apply periodic or symmetry boundary conditions to reduce the computational domain, while this is not either physically consistent or representative for the actual flow field.

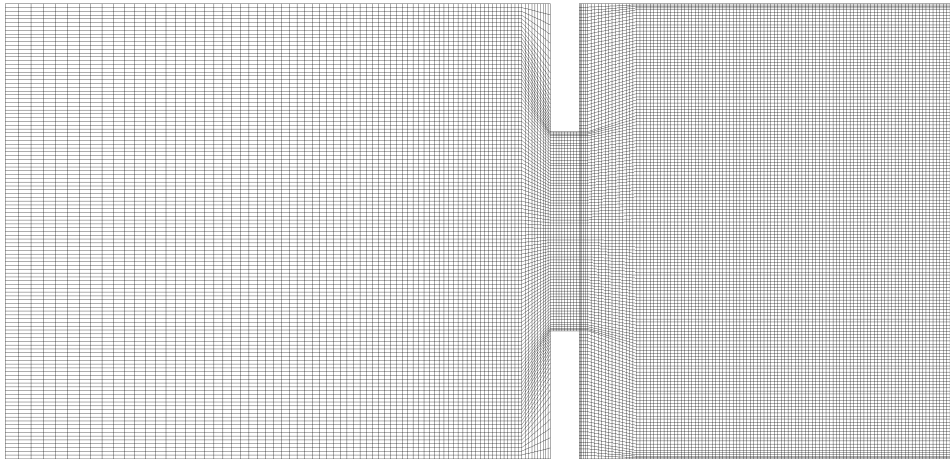
### 4.2.1 Configuration and parameters of the CFD simulation

#### 4.2.1.1 CFD mesh

The mesh is a slowly non-uniform cartesian mesh with low non-orthogonality, as visible in Figure 4.3), and composed of 843,800 cells. A first two-dimensional structured mesh is built in the XY plane with  $82 \times 120$  cells in the inlet duct,  $10 \times 74$  cells in the diaphragm aperture and  $492 \times 150$  cells in the outlet duct. In the  $x$ -direction, the mesh size is constant in the diaphragm aperture,  $\Delta x = h/70$ , and in the first half of the outlet duct,  $\Delta x = h/58$ . The mesh is then stretched to the inlet and outlet sections with the rates of 1.85% and 1.2% respectively, leading to the maximum cell size of  $h/15$  in the inlet duct and  $h/8$  in the outlet duct. In the  $y$ -direction, the mesh is constant in the diaphragm aperture,  $\Delta y = h/70$ ; in the inlet duct,  $\Delta y = h/53$ , and in the outlet duct,  $\Delta y = h/66$ . Boundary layers consisting of local refinement are also defined with the first cell of size



(a) Overall view of the mesh.



(b) Zoom on the inlet and diaphragm region.

**Figure 4.3** – *Diaphragm slice mesh. Every line mesh is shown.*

$\Delta y_{\min} = h/175$  and a stretching rate of 20 % on the upper and lower diaphragm walls and on the walls of the first part of the outlet duct, as well as on the downstream vertical walls of the diaphragm. The two-dimensional mesh is then extruded in the  $z$ -direction on 10 cells of size  $\Delta z = h/35$ .

#### 4.2.1.2 Simulation parameters

The inlet boundary condition is a uniform velocity of 6 m/s. The outlet boundary condition is an outflow condition, constraining the flow to leave the domain at the same flow-rate as at the inlet. When considering an incompressible simulation, Non Reflecting Boundary Conditions are of no use. Moreover, the association of the outflow boundary condition and the mesh growing rate toward the downstream boundary is relaxed enough to damp energetic waves downstream the region of interest and avoid reflections of pressure waves at the outlet boundary. Periodic boundary conditions are applied to the lateral sides of the model, simulating an infinite duct in the third direction. Non-slipping walls are considered for remaining surfaces.

An incompressible Large Eddy Simulation Smagorinsky–Lilly, with  $C_S = 0.1$ , is performed on the previously described mesh. Central differencing is used for the discretization of momentum equation, PRESTO! for the pressure equation, and the pressure-velocity coupling is taken into account via a PISO scheme. The time step satisfies a CFL less or

equal to 1 for the smallest cell of the domain, yielding  $\Delta t = 5 \cdot 10^{-7}$  s.

### 4.2.1.3 Initial conditions

In confined flow problems, starting from a medium at rest causes stability and convergence problems, differing from free jet flow problems. Indeed, the pressure drop between the inlet and outlet plays a crucial role and must be steadily converged before starting the unsteady simulation. Therefore, for all computations presented here on the diaphragm geometry, a first Reynolds Averaged Navier-Stokes (RANS)  $k - \epsilon$  computation has been converged to second order and is used as an initial condition for LES.

A stable transient state is reached after approximately 0.1 s of physical time, that is to say 200000 time steps; the computation is then performed for another physical period of 0.15 s for statistics and source term recordings.

## 4.2.2 Aerodynamic results

### 4.2.2.1 Mean flow analysis

The three components of the averaged velocity, presented in Figure 4.4, highlight three distinct flow regions:

1. the upstream flow, before the diaphragm, with very fine turbulent boundary layers near the walls;
2. the jet-like flow coming from the diaphragm aperture and attaching to the top wall through the Coanda effect<sup>1</sup>;
3. the quieter flow in the second part of the outlet duct, with reattachment to the bottom wall.

The remarkable behavior of attachment to the top wall just downstream of the sudden expansion has been already described by many authors from experimental measurements, see § 4.1.2, and is also present in Gloerfelt & Lafon<sup>54</sup> simulation. The Reynolds number considered in this study, of order  $10^4$ , is well above the critical Reynolds number of order  $10^2$  where transition to asymmetry was observed for large expansion ratios. In present results, the bifurcation is found to happen in favor of top wall, while other simulations performed in the same conditions showed a bifurcation toward bottom wall; truncation errors are likely to be responsible for this "choice"<sup>36</sup>.

However, the presence of a region with secondary attachment to bottom wall is more questionable. Indeed, while such a behavior was observed by some authors<sup>35;36;42</sup>, it occurred well downstream the primary attachment, typically around  $x/h = 20$ . In this slice

---

<sup>1</sup>The *Coanda effect* is the tendency for a moving fluid to attach itself to a surface and flow along it.

simulation, this secondary attachment can also be seen as a remainder of the unphysical two dimensional evolution presented in Appendix A; the reduction of the three dimensional domain may have lead to miss important three dimensional results. A dedicated experimental study would be useful to lift the veil on this uncertainty.

The levels of the mean velocity components are in good agreement with Gloerfelt & Lafon<sup>54</sup> results. The turbulent intensities reported in Figure 4.5, computed as  $u' = \sqrt{u'^2}$  for the streamwise component and normalized by  $U_m$ , present high levels in the separating shear layers, which is usually associated to a broadband acoustic radiation. Once again, discrepancies with reference results are sizable. In addition to the low levels of the spanwise turbulent intensity, expected taken that the geometry reduction in the spanwise direction prevents a correct three dimensional development, the streamwise and transverse turbulent intensity components have very high levels, in excess of  $30\%U_m$ , downstream of the attachment.

Figure 4.6 presents the path lines of the averaged flow field in the XY midplane. The large recirculation region below the jet extends over  $8.6h$ , while the smaller recirculation located above the jet, upstream attachment, is found to exist over  $2.8h$ . This last value is well below those reported by Gloerfelt & Lafon,  $5h$  and  $4.3h$  for numerical and experimental results, respectively. Two pairs of small and symmetric corner recirculation zones are present just upstream and downstream of the diaphragm, their extent being of order  $h$  and  $0.7h$ .

#### 4.2.2.2 Instantaneous flow features

Figures 4.7-4.9 present the instantaneous velocity components. The jet is finely modeled, with creation of periodic small structures shed from the downstream diaphragm lips, this being confirmed in Figure 4.10 displaying the instantaneous vorticity modulus. From these instantaneous pictures of the flow field, a strong unsteadiness is evident. Downstream vortex shedding occurring at the diaphragm lips, roll-ups are responsible for the shear layer thickening before impinging on top wall, convected by the jet-like flow.

Top and side views are added to give an indication about the three dimensional flow development. As with the turbulent intensities, the spanwise velocity component is underestimated by the slice simulation, with levels generally 3 times lower than in Gloerfelt & Lafon<sup>54</sup> simulation.

#### 4.2.2.3 Statistic analysis

##### Determination of the maximal frequency resolved by CFD

The Large Eddy Simulation cutoff frequency is determined in order to evaluate the limits of the present computation; this cutoff frequency is mainly linked to the mesh and

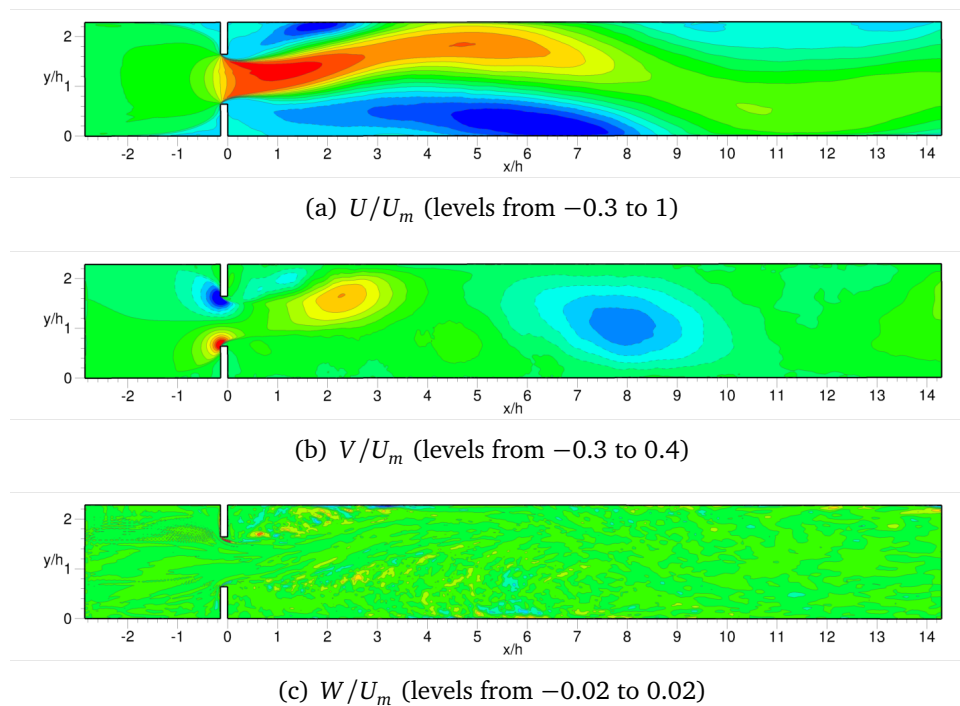


**Figure 4.4** – Diaphragm slice. Mean velocity field in the XY midplane. Solid contours have positive values, dashed contours have negative values.

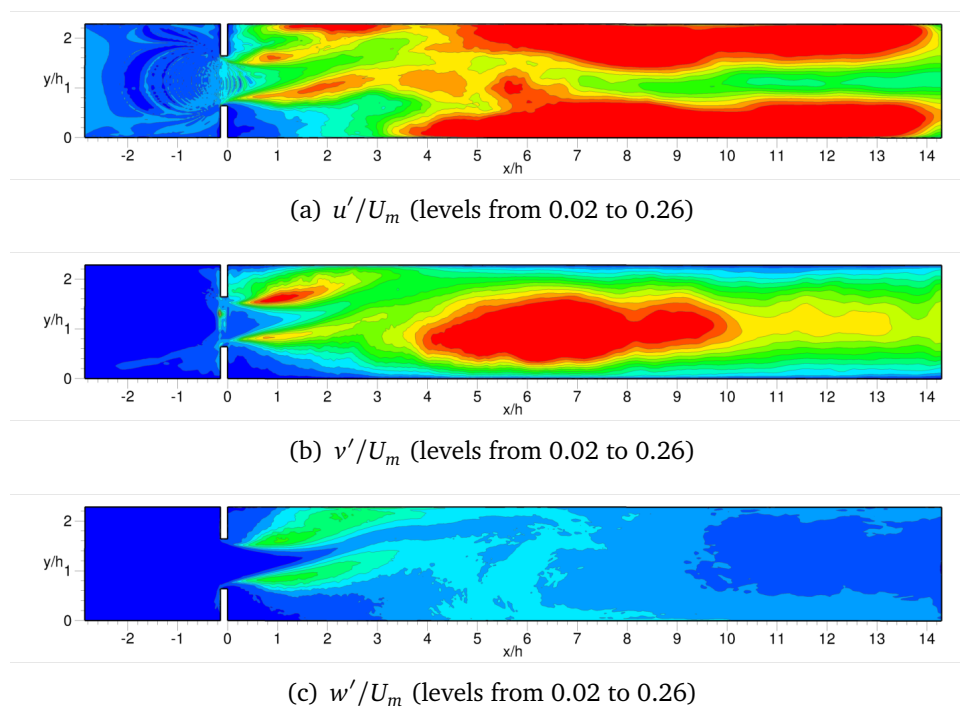


**Figure 4.5** – Diaphragm slice. Turbulence statistics in the XY midplane.

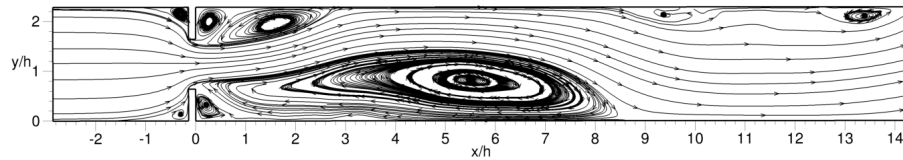


**Figure 4.6** – Diaphragm slice. Streamlines computed with the  $U$  and  $V$  components of the 3D mean velocity field in the  $XY$  midplane.

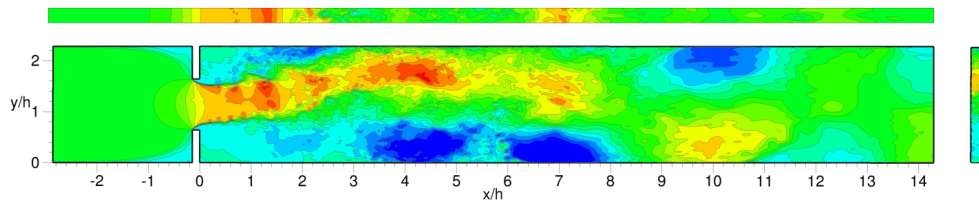


**Figure 4.7** – Diaphragm slice. Instantaneous streamwise velocity  $u$  (levels between  $-10$  and  $25$  m/s). Top, top view in the  $XZ$  midplane; bottom left, front view in the  $XY$  midplane; bottom right, cross section at  $x/h = 2.8$ .

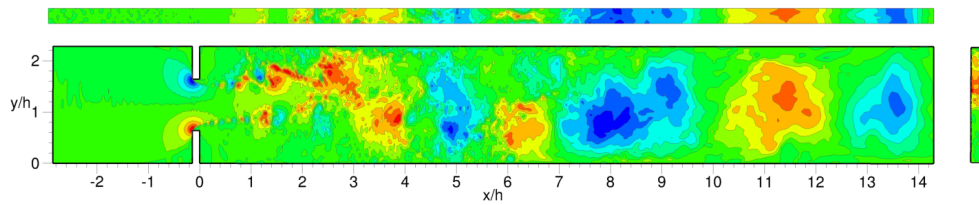


**Figure 4.8** – Diaphragm slice. Instantaneous transverse velocity  $v$  (levels between  $-10$  and  $10$  m/s). Top, top view in the  $XZ$  midplane; bottom left, front view in the  $XY$  midplane; bottom right, cross section at  $x/h = 2.8$ .

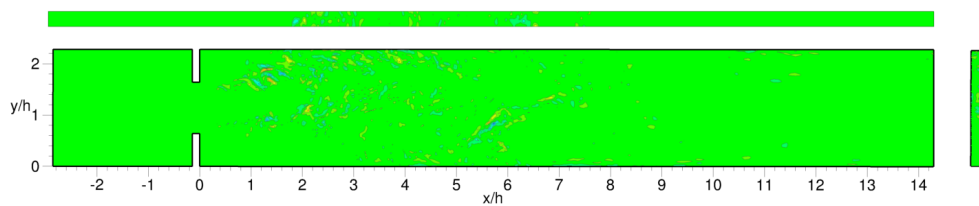


**Figure 4.9** – Diaphragm slice. Instantaneous spanwise velocity  $w$  (levels between  $-10$  and  $10$  m/s). Top, top view in the  $XZ$  midplane; bottom left, front view in the  $XY$  midplane; bottom right, cross section at  $x/h = 2.8$ .

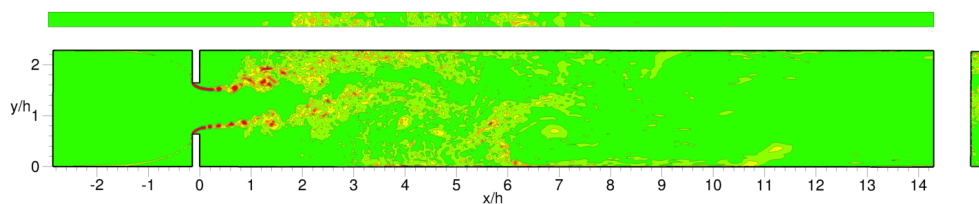


**Figure 4.10** – Diaphragm slice. Instantaneous vorticity magnitude  $\|\omega\|$  (levels between  $-1$  and  $1 \cdot 10^4$  s $^{-1}$ ). Top, top view in the  $XZ$  midplane; bottom left, front view in the  $XY$  midplane; bottom right, cross section at  $x/h = 2.8$ .

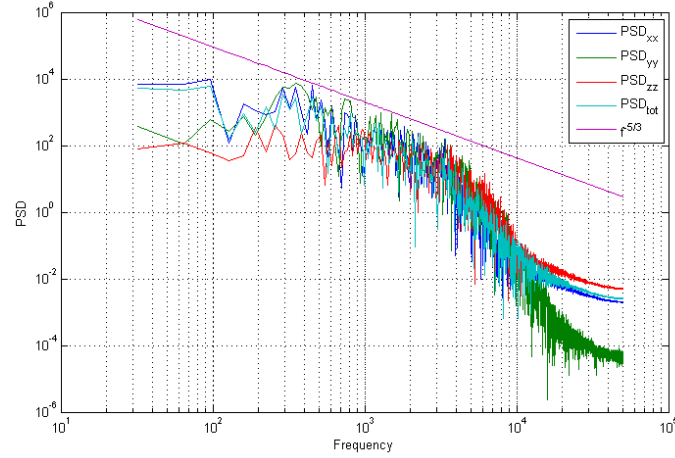


**Figure 4.11** – Diaphragm slice. Power Spectral Density of velocity components and velocity magnitude at point  $(1.81; 1.16) \times h$  in the  $XY$  midplane, and  $f^{-5/3}$  slope.

discretization schemes used. Velocity component fluctuations recorded during the transient run are analyzed at a point located in a region where turbulence is almost isotropic, outside the shear layers and inside the jet-like flow. The point  $(1.81; 1.16) \times h$ , located in the central  $XY$  plane, seems well chosen. The  $f^{-5/3}$  slope and the power spectral densities of velocity components at this point are displayed in the same graph in Figure 4.11. The cutoff frequency is the maximum frequency at which the PSD follows the  $f^{-5/3}$  slope; here,  $f_{\text{cut,CFD}} \simeq 3500$  Hz. Above this frequency, acoustic and aerodynamic results will not be considered.

### Correlation lengths

The study of correlation functions allows to determine the extent of homogeneous turbulence in the flow field. The correlation coefficient  $\mathcal{R}_{ij}$  at two points  $\mathbf{x}$  and  $\mathbf{x} + d\mathbf{x}$  of two components of the fluctuating velocity field  $u'_i$  and  $u'_j$ , is defined as

$$\mathcal{R}_{ij}(\mathbf{x}, \mathbf{x} + d\mathbf{x}) = \frac{\overline{u'_i(\mathbf{x})u'_j(\mathbf{x} + d\mathbf{x})}}{\sqrt{\overline{u'^2_i(\mathbf{x})}}\sqrt{\overline{u'^2_j(\mathbf{x} + d\mathbf{x})}}}$$

Note that  $\mathcal{R}_{ij}$  is without dimension and is always included in  $[-1; 1]$ ;  $u'_i$ ,  $u'_j$  are the fluctuating velocities in the directions  $i$  and  $j$  respectively.

In order to determine the size of the largest turbulence structures, a length scale representing the distance over which the correlation function is non-zero is defined. This integral length scale  $L_{ij}^{(k)}$  in the direction  $(k)$  is defined by integrating the correlation coefficient  $\mathcal{R}_{ij}$  in the direction  $(k)$ :

$$L_{ij}^{(k)} = \int_0^\infty \mathcal{R}_{ij}(r\mathbf{x}_k) dr$$

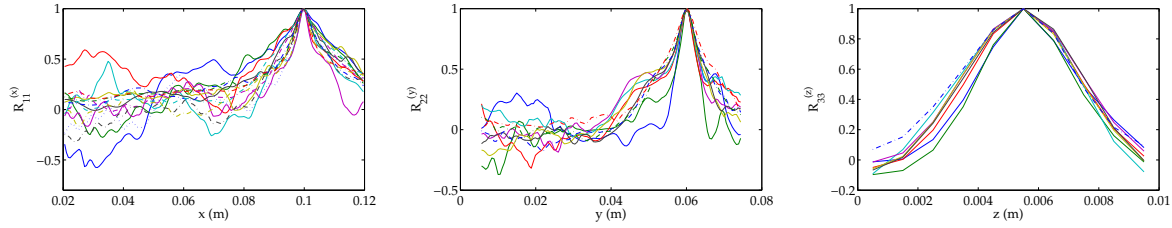


**Figure 4.12** – Correlation coefficients of fluctuating velocities. From left to right:  $\mathcal{R}_{11}(x)$ ,  $\mathcal{R}_{22}(y)$  and  $\mathcal{R}_{33}(z)$ .

The integral scales of interest in this study are the longitudinal integral scale  $L_1 = L_{11}^{(1)}$ , the transverse integral scale  $L_2 = L_{22}^{(2)}$  and the spanwise integral scale  $L_3 = L_{33}^{(3)}$ , defined as

$$\left\{ \begin{array}{l} L_1 = L_{11}^{(1)} = \frac{1}{2} \int_{-\infty}^{\infty} \mathcal{R}_{11}(x) dx \quad \text{with} \quad \mathcal{R}_{11}(x) = \frac{\overline{u'(x - dx/2)u'(x + dx/2)}}{\sqrt{\overline{u'^2(x - dx/2)}} \sqrt{\overline{u'^2(x + dx/2)}} \\ L_2 = L_{22}^{(2)} = \frac{1}{2} \int_{-\infty}^{\infty} \mathcal{R}_{22}(y) dy \quad \text{with} \quad \mathcal{R}_{22}(y) = \frac{\overline{v'(y - dy/2)v'(y + dy/2)}}{\sqrt{\overline{v'^2(y - dy/2)}} \sqrt{\overline{v'^2(y + dy/2)}} \\ L_3 = L_{33}^{(3)} = \frac{1}{2} \int_{-\infty}^{\infty} \mathcal{R}_{33}(z) dz \quad \text{with} \quad \mathcal{R}_{33}(z) = \frac{\overline{w'(z - dz/2)w'(z + dz/2)}}{\sqrt{\overline{w'^2(z - dz/2)}} \sqrt{\overline{w'^2(z + dz/2)}} \end{array} \right. \quad (4.1)$$

where centered expressions of the correlation coefficients have been used. Note that when analyzing CFD data, the integration in each direction  $+x$ ,  $-x$ , is performed until  $\mathcal{R}_{11}(x)$  crosses the  $x$  axis (and similarly for  $\mathcal{R}_{22}(y)$  and  $\mathcal{R}_{33}(z)$ ).

The correlation coefficients in the 3 directions and at different locations in the flow are displayed in Figure 4.12; their integration give the following integral scales at the point (0.1;0.06;0.055):

$$\left\{ \begin{array}{l} L_1 = 11 \text{ mm} \\ L_2 = 8 \text{ mm} \\ L_3 = 2 \text{ mm} \end{array} \right.$$

This analysis shows that the turbulence is well-developed and quasi-isotropic along directions  $x$  and  $y$ . The spanwise integral scale  $L_3$  tells us that the slice approximation may be justified, as the span extent  $L_z$  contains several spanwise integral scales  $L_3$ . However, we can state that the mesh size in the third direction is probably too coarse to resolve correctly the turbulence structures:  $L_z = 10$  mm is the model span extent and  $\Delta z = 1$  mm is the mesh size in the third direction.

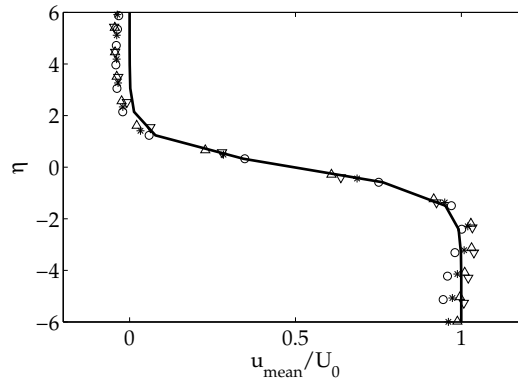


**Figure 4.13** – Mean streamwise velocity profiles for the upper shear layer versus  $\eta = (y - y_{0.5})/\delta_\theta$ , where  $y_{0.5}$  corresponds to  $\bar{u} = 0.5U_m$  and  $U_m = 20$  m/s, at different longitudinal locations.  $\circ$ :  $x = 1.2$  mm;  $*$ :  $x = 3$  mm;  $\Delta$ :  $x = 5.2$  mm;  $\nabla$ :  $x = 7.4$  mm. A hyperbolic-tangent profile  $(1 - \tanh \eta)/2$  is superimposed (—).

### Power Spectral Densities of velocity fluctuations

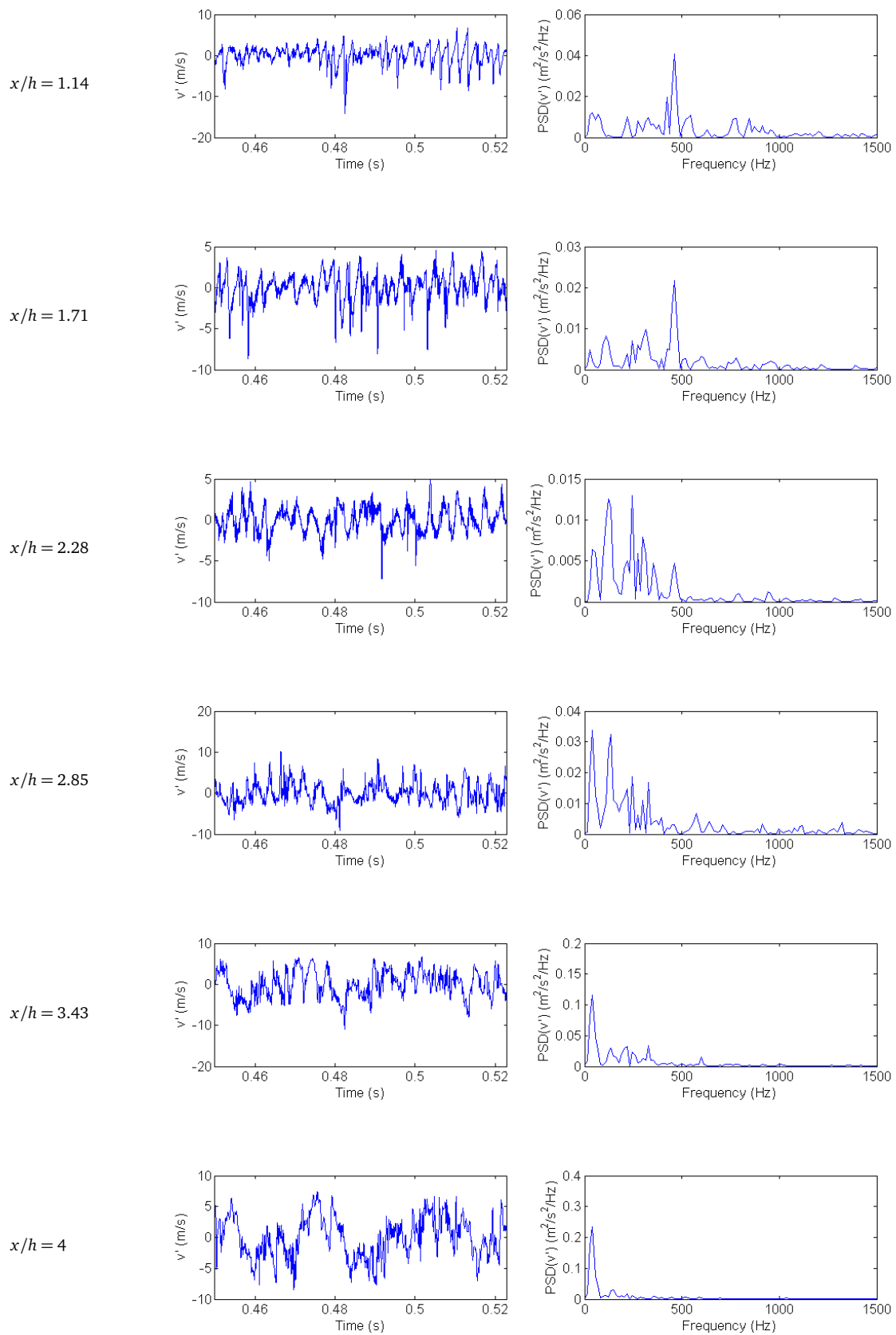
The Power Spectral Densities of vertical velocity signals are displayed in Figure 4.14 at several locations in the upper shear layer. A sharp peak centered around 460 Hz is present on the first two sensors. Similarly to Gloerfelt & Lafon<sup>54</sup>, the similarity parameter  $\eta = (y - y_{0.5})/\delta_\theta$  is defined and used to show that mean streamwise velocity profiles collapse for  $\delta_\theta = 0.55$  mm instead of 0.7 mm in the reference paper<sup>54</sup>, see Figure 4.13. This corresponds to a Strouhal number  $St_{\delta_\theta} \simeq 0.013$  for  $f = 460$  Hz and  $U_m = 20$  m/s; it is close to the most unstable frequency of a hyperbolic-tangent velocity profile. This intense peak therefore indicates the presence of primary Kelvin-Helmholtz instabilities in the jet shear layers.

The last three sensors show a very intense peak around 40 Hz. The analysis of instantaneous snapshots of velocity correlate this low-frequency with the transport of large structures by the recirculation below the jet. This frequency is not present in the reference analysis, suggesting that the recirculation below the jet is too intense due to the restriction in the third direction inherent to the slice model.

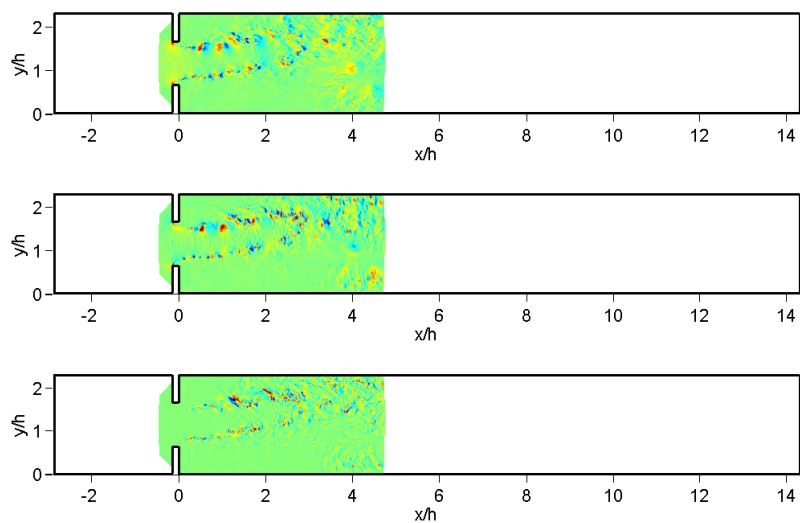
The sensors located from  $x/h = 1.71$  to 4 exhibit a more broadband content, with a peak around 130 Hz (this peak is however masked by the very intense peak at 40 Hz for the last three sensors). This frequency is linked with the periodic shedding of large-scale jet-column instabilities, as suggested by Gloerfelt & Lafon<sup>54</sup>.

#### 4.2.2.4 Analysis of the source terms

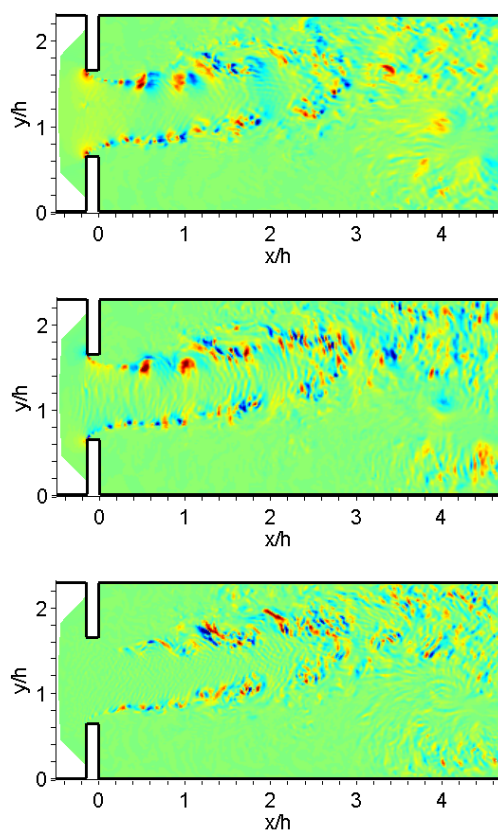
The three instantaneous components of the source term  $S_1$ ,  $S_2$  and  $S_3$  are displayed in Figure 4.15 on the region where they are recorded, for  $-0.43 \leq x/h \leq 4.7$ . The three components of the source term present well organized structures located mainly in the shear layers; vortex shedding is clearly visible on the two first components  $S_1$  and  $S_2$ ,



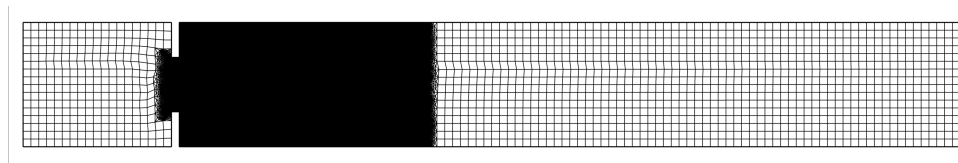
**Figure 4.14** – Left: instantaneous velocity fluctuations  $v'$ , right: power spectral densities of  $v'$ . Signals were recorded at  $y = 0.05$  m,  $z = 0.0055$  m; the  $x$  position is indicated on the left of each subfigure.



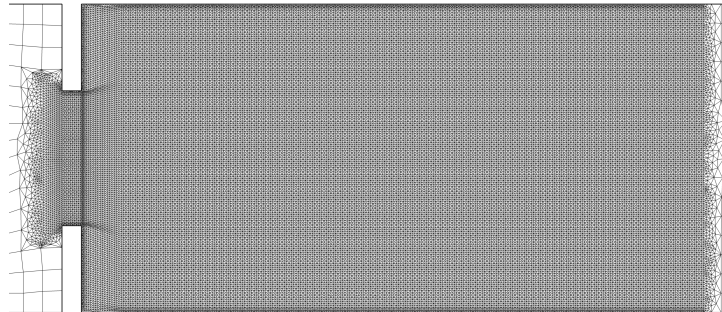
(a) General view of the source region in the diaphragm geometry.

(b) Zoom on the region where  $\mathbf{S}$  is recorded.

**Figure 4.15** – Visualization of the source term  $\mathbf{S}$  in the plane  $z = 0.0055$  m. In both figures, the 3 components of the source term  $S_1$ ,  $S_2$  and  $S_3$  are displayed from top to bottom. Levels between  $-1$  and  $1 \times 10^5$  Pa/m.



(a) Overall view of the two dimensional acoustic mesh.



(b) Zoom on the acoustic source region.

**Figure 4.16** – *Two dimensional acoustic mesh used for the diaphragm slice computation.*

from both downstream diaphragm lips. While the most intense features of the source term are well contained in the limited export region, some structures convected by the lower recirculation zone are crossing the outlet boundary, successively leaving and entering the domain at  $x/h = 4.7$ . By visualization of  $S_i$  time evolution, it is noticed that this phenomenon of acoustic sources crossing downstream boundary is not permanent, but rather occurs periodically; however, it was not possible to determine a frequency linked to this event.

### 4.2.3 Acoustic simulation

The previous diaphragm slice Large Eddy Simulation is exploited to compute the acoustic power radiated at the outlet of the duct. Like in the reference simulation<sup>54</sup> and experimental<sup>111</sup> results, the acoustic duct is supposed semi-infinite at both ends, as is the case in the fluid computation. A two dimensional acoustic computation is performed based on the acoustic sources computed in the central XY plane.

#### 4.2.3.1 Configuration and numerical parameters

##### Mesh

The mesh is built in a way to keep the CFD accuracy in the source region shown in Figure 4.15; therefore, as was the case in the validations of chapter 3, the acoustic nodes are placed at the CFD cell centers in order to avoid interpolation errors. Outside of the source region, the acoustic mesh is coarsened up to a maximum mesh size of  $h/7$ , see Figure 4.16.

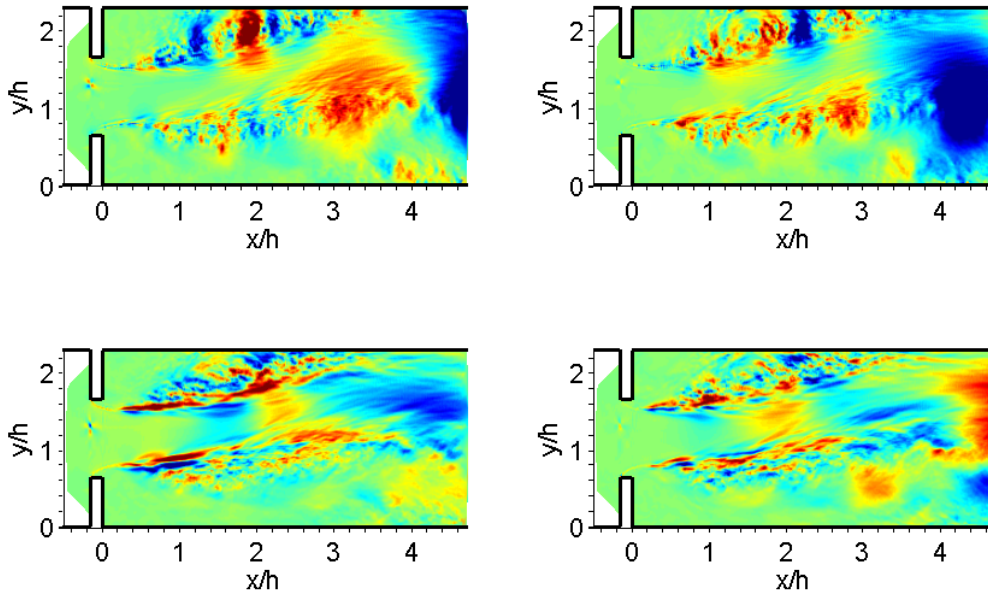


**Figure 4.17** – Diaphragm slice: two dimensional acoustic source components in the frequency domain at  $f = 30$  Hz,  $\Re(\tilde{S}_1)$ ,  $\Im(\tilde{S}_1)$ ,  $\Re(\tilde{S}_2)$  and  $\Im(\tilde{S}_2)$  from left to right and top to bottom. Levels from  $-2$  to  $2 \times 10^3$  Pa/m.

### Acoustic simulation parameters

As explained previously, acoustic sources consisting of the two-components vector  $[S_1 \ S_2]^t$  are used in the acoustic model. Note that the third component  $S_3$  of the source vector is omitted in this computation. The natural condition is used at the walls. At inlet and outlet, modal bases are defined to force acoustic waves leave the duct without reflections. Free outgoing modes are used at both ends; for the frequencies considered,  $f \leq 2000$  Hz, the only propagating mode is the plane wave as the cutting frequency for the duct is 2125 Hz, based on the duct height.

The total signal length is 100 ms, recorded at the sampling rate of  $f_s = 100$  kHz, corresponding to one sample every 20 CFD time steps. The signal is Fourier transformed after being windowed with a Hanning window. The resulting resolution frequency is 10 Hz. Figure 4.17 presents the acoustic source terms  $\tilde{S}_i$  in the frequency domain at the main radiating frequency of 30 Hz. A second processing is performed by averaging the contribution of 19 overlapping samples of 10 ms each, the samples being 50% overlapped; this last processing yields a resolution frequency of 100 Hz.

### 4.2.3.2 Spatial filtering to damp outgoing sources

Spatial filtering, as studied in § 3.2, is applied to smooth source outgoing from the source region. A cosine-type filter is applied, with a weight exactly equal to zero at the outlet boundary and to unity where the filter starts to act:

$$\mathcal{W}(x) = \frac{1}{2} \left\{ 1 + \cos \left[ \frac{(x - x_{\min})\pi}{x_{\max} - x_{\min}} \right] \right\}$$

with the same conventions as in § 3.2. Two filtering lengths  $d = x_{\max} - x_{\min}$  are fixed,  $1.14h$  and  $1.86h$ , and their effect is studied.

### 4.2.3.3 Conversion from 2D to 3D acoustic power

The present CFD computation is three dimensional (slice), and in a first approach the noise is computed with a two dimensional acoustic model, using the noise sources computed in the plane  $z = 0.0055$  m of the CFD model. The acoustic pressure obtained from a 2D acoustic computation does not depend on the dimension of the problem, while the acoustic power does; indeed, the power value is obtained on a surface of integration. Two methods are proposed to compute the acoustic power from this 2D simulation.

The plane wave assumption is valid in the present case up to 2125 Hz, which is the cutting frequency associated to the duct height  $D$ . Under this assumption, only the plane wave is propagating in the duct, and far enough from the aerodynamic sources, the acoustic pressure is only a function of the duct axial position  $x$  and is constant in duct sections. The acoustic intensity  $I$  is then expressed as

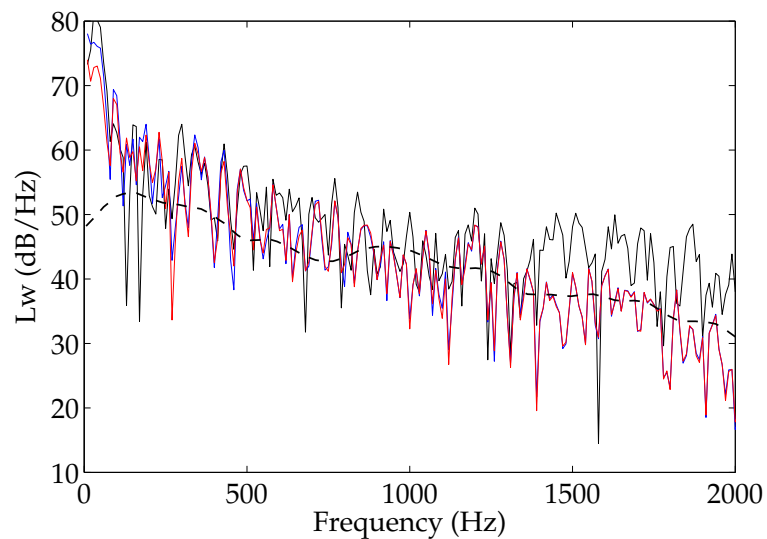
$$I = \frac{p_{\text{rms}}'^2}{\rho_0 c_0}$$

where  $p_{\text{rms}}'$  is the acoustic pressure, either provided by a two- or a three-dimensional acoustic computation. Finally, the acoustic power is obtained by multiplying the intensity by the duct section surface  $S$ :

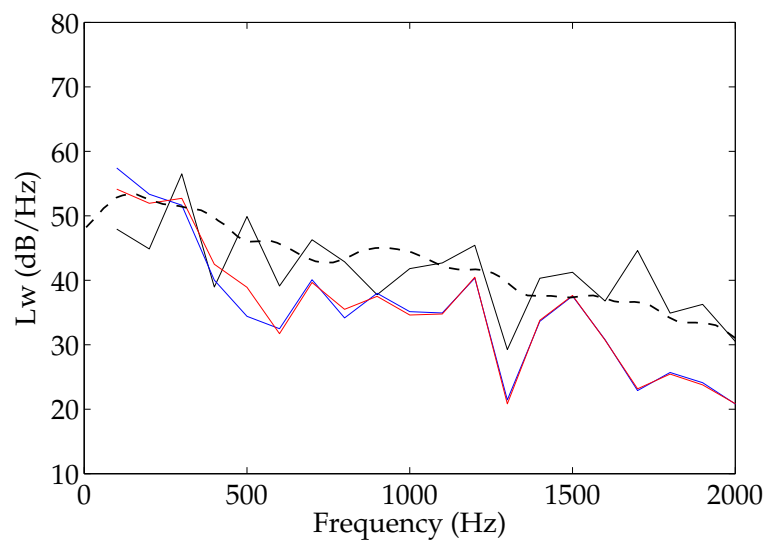
$$\mathcal{P} = I \times S \quad (4.2)$$

Actran also provides the intensity radiated by the modal bases at both ends of the duct. Under the duct cutting frequency, both methods should yield the same results:

$$\mathcal{P} = \frac{p_{\text{rms}}'^2}{\rho_0 c_0} \times S = I_{\text{modal basis}} \times S. \quad (4.3)$$



(a) no time averaging (resulting resolution frequency: 10 Hz)



(b) time averaging over 19 overlapping samples (resulting resolution frequency: 100 Hz)

**Figure 4.18** – Diaphragm slice. Acoustic power level spectra, in dB/Hz, without and with time averaging over 19 samples, for different lengths of spatial filtering. ---: reference result (see Gloerfelt & Lafon<sup>54</sup>). —: no spatial filtering; —: spatial filtering over 1.14h; —: spatial filtering over 1.86h.

	Reference results <sup>54</sup>	No averaging			Averaging over 19 samples		
		$d = 0$	$d = 40$	$d = 65$	$d = 0$	$d = 40$	$d = 65$
Inlet	69	96.3	94.4	90.9	79.0	79.5	77.9
Outlet	78.8	96.5	94.7	91.2	79.3	79.9	78.3
Total	79	99.4	97.6	94.0	82.2	82.7	81.1

**Table 4.1** – Overall acoustic power radiated by the diaphragm, in dB.  $d$ , in mm, refers to the presence of spatial filtering and specifies its application length.

#### 4.2.3.4 Acoustic results

##### Effect of spatial filtering and averaging

The effect of spatial filtering and of time averaging is presented in Figure 4.18. As was already shown in the academic case of a vortex crossing a virtual boundary, the application of spatial filtering mainly damps low frequencies, while high frequencies are smoothly attenuated. In the present case, both cosine filters yield the same acoustic power levels at frequencies higher than 500 Hz; levels obtained with filtering are very close to the levels obtained without filtering in the range 500 – 1400 Hz, while they are attenuated at higher frequencies. At frequencies lower than 500 Hz, not only the filtering but also its application length has an effect; thus, the longer filtering length of  $1.86h$  yields more attenuation on the high-energy peak of 20 – 40 Hz. Note that the difference between both filters is mainly visible on this peak. Spatial filtering has the same qualitative effect on the total signal than on the averaged signal.

Regarding the averaging, its effect is clearly to smooth the spectra; moreover, the levels are seen to be reduced after averaging. This could be due to the use of a non normalized weighting function, namely the Hanning window. Table 4.2.3.4 gathers the overall acoustic power levels, in dB, for each computed configuration. From this overall power values, the configuration with 19 averaged samples and spatial filtering applied on  $1.86h$  yields the closest result at the outlet, compared to the reference. In addition, note that in all acoustic computations detailed here, the acoustic power at the inlet is of the same order as at the outlet, while Gloerfelt & Lafon<sup>54</sup> found a much lower value at the inlet. However, the latter was obtained after linear detrending of the directly obtained pressure, because a relatively intense continuous component was present close to the diaphragm, polluting the solution; this is a source of approximation. In present computations though, the acoustic pressure maps of Figure 4.20, see below, show that the inlet duct is long enough and that the pressure is already established 0.095 m upstream from the diaphragm, at the inlet location.

Note finally that the comparison of overall noise levels in Table 4.2.3.4 takes the low

frequencies into account, while averaged and non averaged signals do not have the same lowest frequency. For the non averaged signals, the lowest frequency is 10 Hz, while it is 100 Hz for averaged signals. Therefore, the continuous component is more present in non averaged signals, which makes the comparison of overall levels more difficult. A more relevant overall noise levels comparison should be done over the same frequency range, for instance [100–2000] Hz.

### Results' consistency

Acoustic results after propagation within Actran are examined in Figure 4.19. The spectrum of the acoustic power radiated at the outlet of the duct, obtained by averaging over 19 samples and using the  $1.86h$  cosine spatial filtering, is compared with the reference results of Gloerfelt & Lafon<sup>54</sup>. The acoustic power is computed by the two methods described previously, namely using the intensity radiated by modal basis, as computed by Actran, and by integrating the acoustic pressure at one point over the outlet and inlet sections of the duct, and closer to the acoustic source region.

At the outlet, it is shown that, computing the power using the modal basis intensity or the acoustic pressure yield the exactly same results. Besides, the acoustic pressure integrated over several sections closer to the aerodynamic region prove the consistency of the plane wave approximation from  $x = 0.3$  m; indeed, only very small deviations are observed for  $x = 0.3$  m for frequencies larger than 1950 Hz. These deviations are due to the presence of evanescent waves, since the integration section is quite close to the aerodynamic source region, the latter ending at  $x = 0.25$  m.

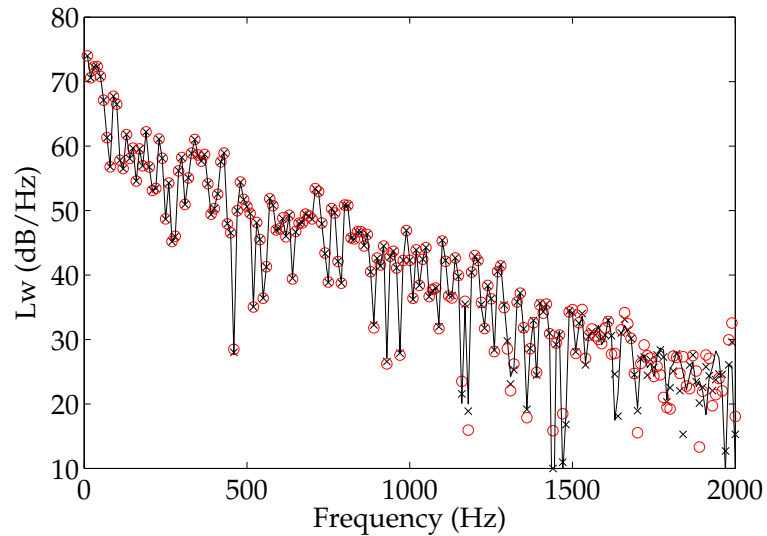
At the inlet, the agreement is not so clear, and larger deviations are observed between both power evaluation methods, even at the inlet section. In this case, differences are observed for frequencies upper than 1200 Hz. This shows that the plane wave assumption is not valid at this position, located too close from the aerodynamic source region.

The acoustic pressure maps in Figure 4.20 confirm previous results regarding the plane wave propagation assumption under the cutting frequency. Indeed, only plane wave is propagating in the duct for  $f < f_{\text{cut}}$ , while the first mode in the  $y$  direction is clearly visible for  $f = 2500$  Hz. This is valid just upstream and downstream of the aerodynamic sources. Note also that the plane wave propagation hypothesis seems to fail around 2000 Hz at the outlet, where the acoustic pressure already exhibits a  $y$ -dependency, even far from the aerodynamic sources. At the inlet, evanescent wave are seen to be important already at 1500 Hz.

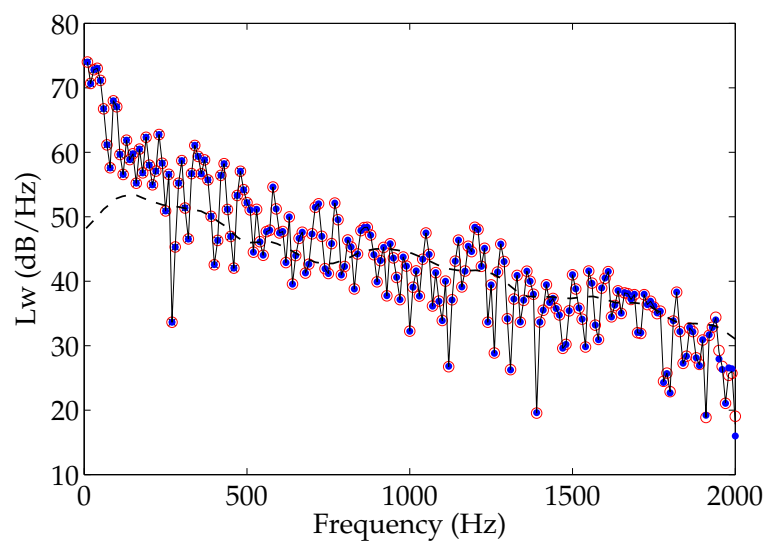
### Discussion

The present CAA approach seems to be consistent to tackle the diaphragm noise. Although in this slice configuration, turbulence levels are higher than the corresponding

levels from the reference, these differences are smoothed after the acoustic computation, except for the low-frequency peak. Spatial filtering is efficient, with, in particular, no dipolar reflections at the downstream source region boundary, as visible in Figure 4.20. Averaging the time signal smooths even more the low-frequency peak so as overall levels are closer to the reference, though overall levels are difficult to compare.

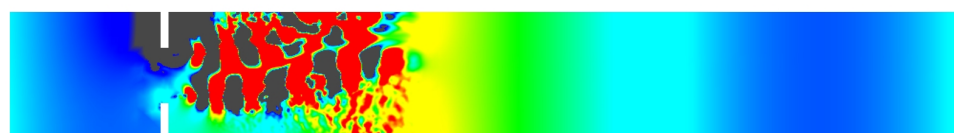


(a) Acoustic power at inlet. Acoustic power obtained by integrating the pressure at  $\times$ :  $x = -0.1$  m (inlet),  $\circ$ :  $x = -0.075$  m.

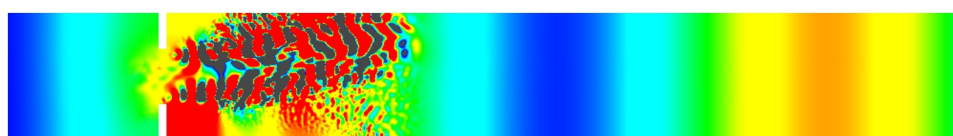


(b) Acoustic power at outlet. Acoustic power obtained by integrating the pressure at  $\times$ :  $x = 0.5$  m (outlet),  $\circ$ :  $x = 0.4$  m,  $\bullet$ :  $x = 0.3$  m.

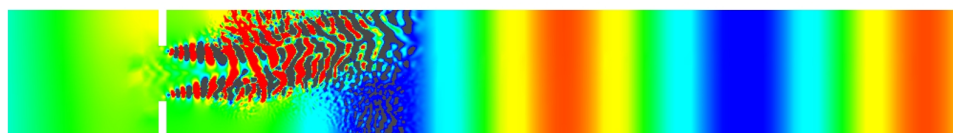
**Figure 4.19** – Diaphragm slice. Acoustic power radiated at the inlet and outlet of the duct, taken from the 10 Hz resolution computation without averaging and with spatial filtering on 1.86 h. ---: reference results of Gloerfelt & Lafon<sup>54</sup>. —: acoustic power obtained using the intensity radiated by the inlet or outlet modal basis. Symbols: see appropriate legend.



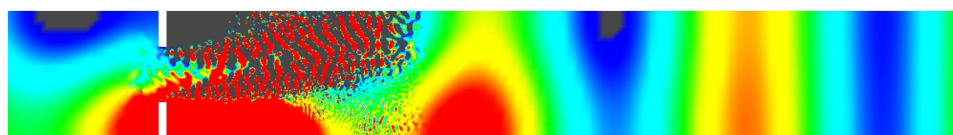
(a)  $f = 500$  Hz (levels:  $\pm 0.35$  Pa)



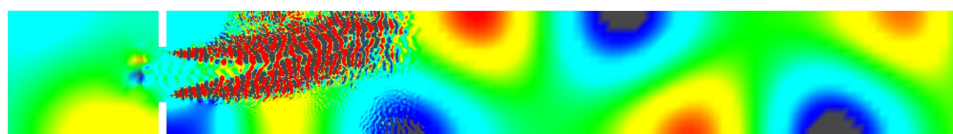
(b)  $f = 1000$  Hz (levels:  $\pm 0.2$  Pa)



(c)  $f = 1500$  Hz (levels:  $\pm 0.25$  Pa)

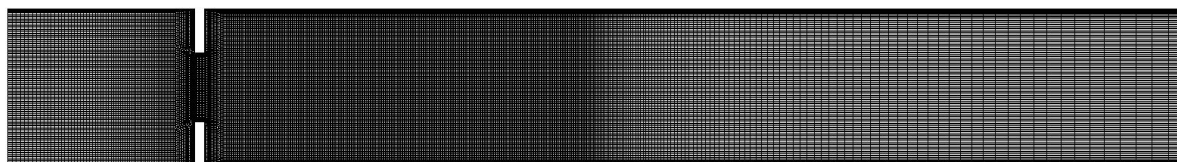


(d)  $f = 2000$  Hz (levels:  $\pm 0.04$  Pa)

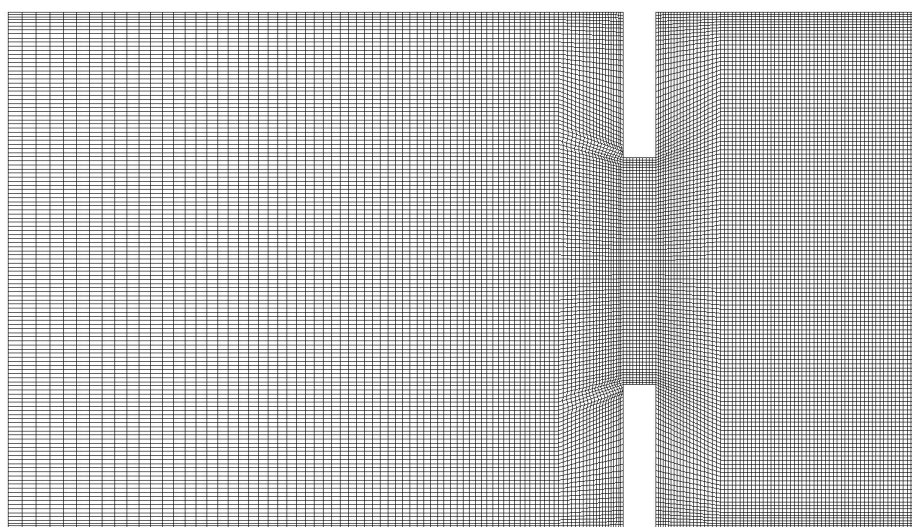


(e)  $f = 2500$  Hz (levels:  $\pm 0.08$  Pa)

**Figure 4.20** – Diaphragm slice. Acoustic pressure maps for different frequencies, taken from the 100 Hz resolution computation with 19 averages and spatial filtering on 1.86 h.



(a) Overall view of the mesh.



(b) Zoom on the inlet and diaphragm region.

**Figure 4.21** – *Diaphragm mesh. Every line mesh is shown.*

## 4.3 Numerical study on the complete 3D domain

A second computation on the total geometry is then carried out in order to overcome the limitations of the slice simulation. Results are in better agreement with experimental data regarding the flow field. Interpolation is used to define an acoustic mesh coarser than the CFD mesh, and a spatial filtering technique similar to the one described in § 3.2 is applied. Acoustic propagation is performed up to the duct inlet and outlet section planes where acoustic power is computed.

### 4.3.1 Mesh and numerical parameters for CFD

#### 4.3.1.1 Mesh

The geometry is shown in Figure 4.1. The mesh used for the CFD computation, reported in Figure 4.21, is composed of 8 millions cells. A first two-dimensional structured mesh in the XY plane is built with  $82 \times 120$  cells in the inlet duct,  $10 \times 66$  cells in the diaphragm aperture and  $428 \times 130$  cells in the outlet duct. In the  $x$ -direction, the mesh size is constant

in the diaphragm aperture,  $\Delta x = h/70$ , and in the first half of the outlet duct,  $\Delta x = h/58$ . The mesh is then stretched to the inlet and outlet sections with the rates of 1.7% and 2.75% respectively, leading to the maximum cell size of  $h/16$  in the inlet duct and  $h/4$  in the outlet duct. In the  $y$ -direction, the mesh is constant in the diaphragm aperture,  $\Delta y = h/64$ , in the inlet duct,  $\Delta y = h/54$ , and in the outlet duct,  $\Delta y = h/55$ . Boundary layers consisting of local refinement are also defined near lower and upper walls with the first cell of size  $\Delta y_{\min} = h/100$  and a stretching rate of 5% on diaphragm walls and outlet duct walls, and 10% on the inlet duct walls. The two-dimensional mesh is then extruded in the  $z$ -direction on 120 cells of size  $\Delta z = h/35$  in the central region, with a local 5% refinement near the lateral walls, with the minimum cell size  $\Delta z_{\min} = h/88$ .

#### 4.3.1.2 Numerical simulation parameters

An incompressible Large Eddy Simulation is performed on the previously described finite volume mesh. The Smagorinsky–Lilly subgrid-scale modeling is used with the constant value  $C_S = 0.1$ . Spatial discretization is central differencing of second order, and the time discretization is implicit of second order with the use of a Non Iterative Time Advancement (NITA) scheme. The time step is  $\Delta t = 10^{-5}$  s, corresponding to a maximum Courant number of 0.78. A uniform constant velocity  $U_0 = 6$  m/s is imposed at the inlet boundary, and an outflow condition at the outlet boundary.

#### 4.3.1.3 Initial conditions

A first Reynolds Averaged Navier-Stokes  $k - \epsilon$  computation has been converged to second order and is used as an initial condition for LES. A stable transient state is reached after approximately 0.2 s of physical time, that is to say 20,000 time steps; the computation is then performed for another physical period of 0.1 s for statistics and source term recordings.

### 4.3.2 Aerodynamic results

#### 4.3.2.1 Mean flow analysis

##### Upstream flow conditions

The check of inlet conditions allows to determine if the flow is fully developed and symmetric before the contraction; Figure 4.22(a) presents the streamwise velocity profiles upstream of the diaphragm in the XY midplane, normalized with the inlet velocity. The profiles are symmetric as expected, but characterize a non fully developed flow. The streamwise turbulent fluctuations in the XY midplane show to be of order 1% of  $U_0$ , with peaks on both sides of the channel centerline reaching 2.5%.

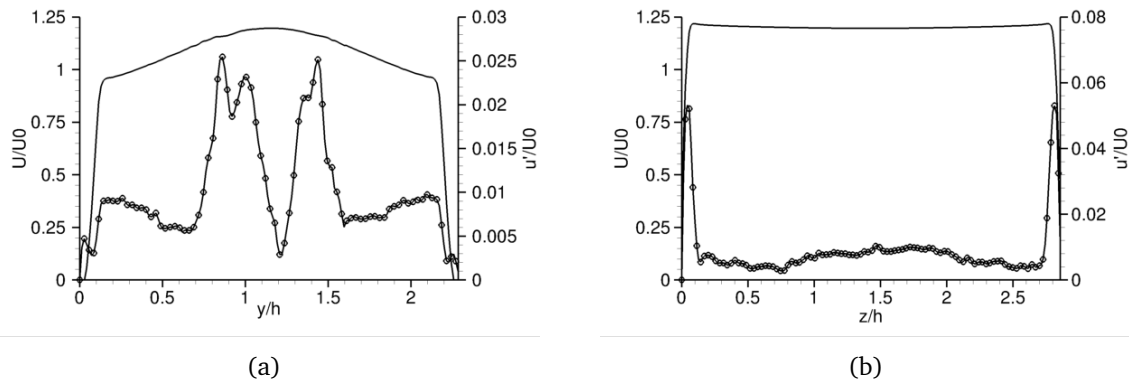


**Figure 4.22 – Diaphragm.** Profiles of mean (solid) and rms (symbols) streamwise velocity components in the (a): XY midplane and (b): XZ midplane at  $x/h = -1$ .

In the XZ midplane, the flow appears to be more developed as shown in Figure 4.22(b) by the profiles of mean and rms streamwise velocity profiles normalized by  $U_0$ . The mean velocity profile exhibits a plateau in the range  $0.3 < z/h < 2.6$ , which shows the uniformity of the inlet flow in the  $z$ -direction. Both profiles are again symmetric.

### Mean flow in the XY midplane

As the averaged components of velocity illustrate it in Figure 4.23, the flow field can be divided in three regions. Upstream of the diaphragm, the flow is uniformly sucked by the contraction, producing very fine turbulent boundary layers near the walls. The jet-like flow emanating from the diaphragm then attaches to the top wall as observed in the case of plane sudden expansions, with the formation of two recirculation regions on both sides of the core flow. Each recirculation zone is composed of one primary large structure and one corner vortex near the diaphragm walls. Finally, in the second half of the outlet duct, the flow becomes more quiet with progressive detachment from the top wall and tends to become symmetric again. Note that the probability for the flow to exhibit one or the other stable solution is the same; in a previous calculations, the flow was found to attach to the bottom wall. No secondary attachment to the opposite wall is observed, as noticed for instance by Durst *et al.*<sup>35;36</sup> or Fearn *et al.*<sup>42</sup> in the case of PSE in the laminar flow regime. However, such a secondary attachment may be absent or masked by the too short length of the outlet duct, since the experimental results show it to appear around  $x/h = 20$ .

As already discussed, the mechanism of symmetry breaking leading to asymmetry results from a fundamental instability in Navier-Stokes equations when exceeding a critical Reynolds number, depending on the expansion geometry; this instability has two stable asymmetric solutions, with attachment to one or the other wall, and one unstable symmetric solution. It is clear that in the fully turbulent regime of the diaphragm, the critical Reynolds number is exceeded, and the large enough expansion ratio  $R = 2.28$  allows the

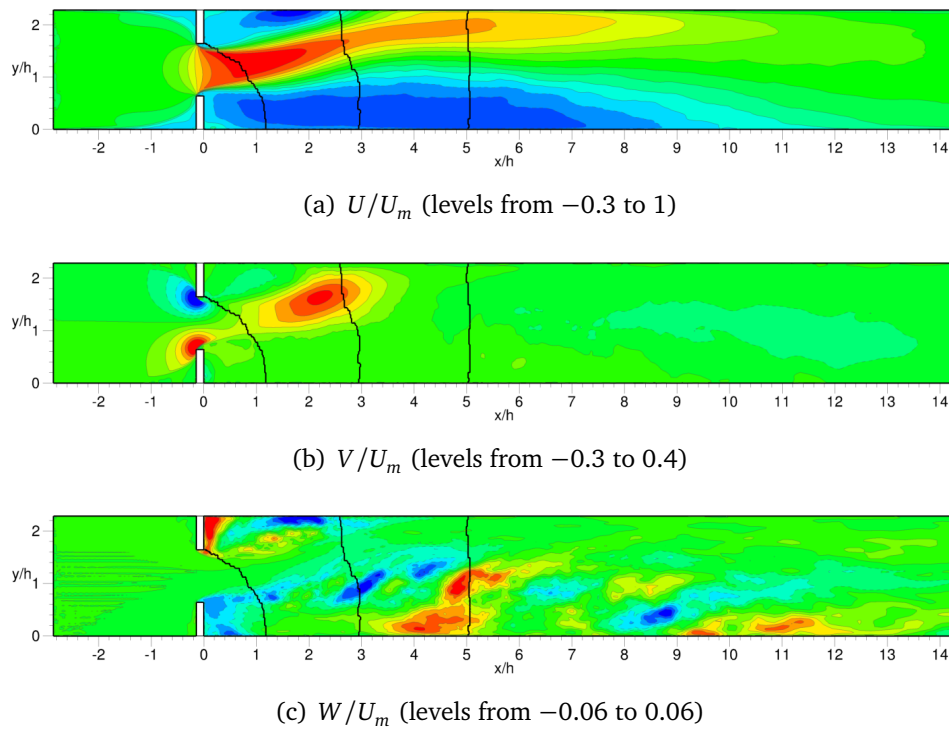


**Figure 4.23** – Diaphragm. Mean velocity field in the XY midplane. Solid contours have positive values, dashed contours have negative values. Bold black lines indicate the position of partitions for the parallel computation (4 partitions).

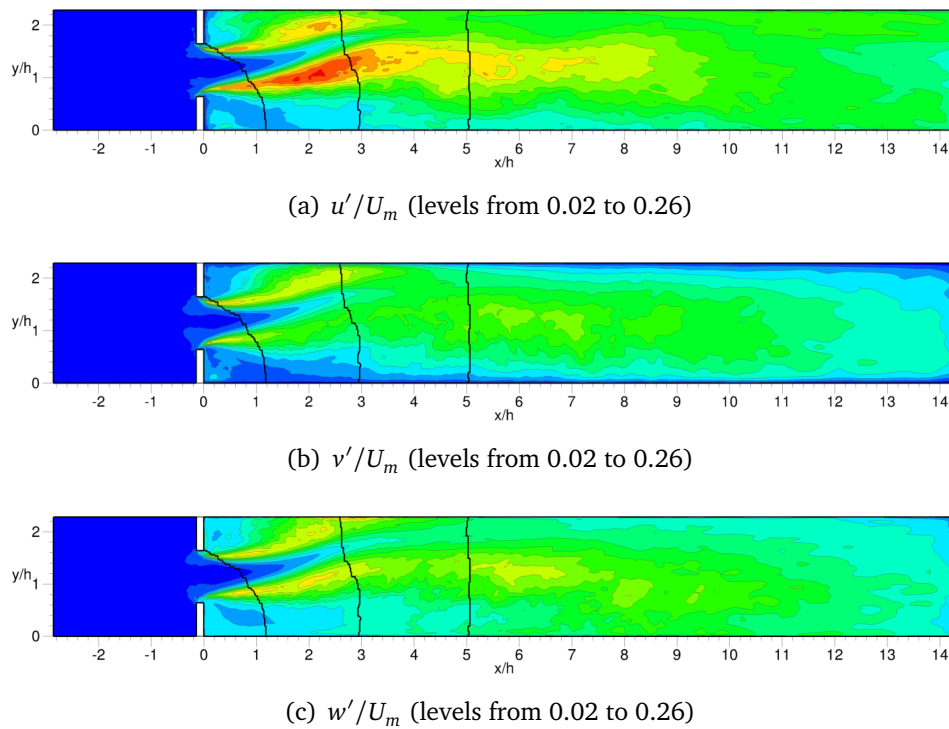


**Figure 4.24** – Diaphragm. Turbulence statistics in the XY midplane.

pitchfork bifurcation to occur. A smoother expansion can lead to a symmetric flow field even at a high Reynolds number, as shown experimentally by Smyth<sup>97</sup>, who found a symmetric field downstream of a double backward facing step of expansion ratio  $R = 1.5$  and Reynolds number  $Re_h = 2 \times 10^4$ .

The overall agreement for mean and r.m.s. velocity contours with Gloerfelt & Lafon<sup>54</sup> is satisfactory, in terms of levels as well as regarding the position and extent of recirculation zones and boundary layers. The contours of mean streamwise velocity in Figure 4.23(a) shows that the maximum values of  $U/U_m$  follow the general direction of the flow toward the top wall. The largest back flow is located in the core of the large recirculation zone, near the walls, and reaches a value of 20%  $U_m$  as noticed in previous studies<sup>22;33;36;38</sup>. Local minima and maxima of transverse mean velocity  $V$  are found at the upstream diaphragm lips, where the flow is accelerated through the contraction; in the outlet duct, a maximum is located in the lower shear layer just before the jet flow attaches the top wall.

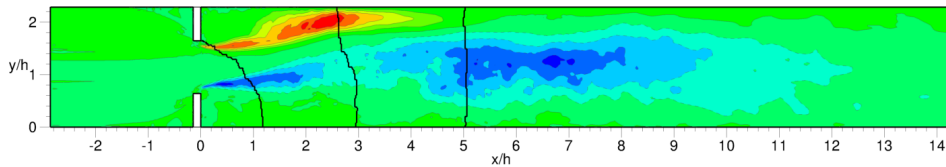


**Figure 4.25** – Diaphragm. Reynolds shear stress  $\overline{u'v'}/U_m^2$  (levels from  $-0.02$  to  $0.025$ ) in the  $XY$  midplane.

Moreover, the r.m.s. turbulent velocities normalized by the bulk velocity  $U_m$  displayed in Figure 4.24 show a significant anisotropy with streamwise intensity levels in general higher than the transverse and spanwise ones. Local maxima are found in the shear layers before the attachment. The maximum value of the r.m.s. axial turbulence intensity is  $u'/U_m|_{\max} \simeq 0.26$ , consistent with that reported by Casarsa & Giannattasio<sup>22</sup> and Escudier *et al.*<sup>38</sup>; resulting axial turbulence in the second half of the duct has a 15% mean intensity, also consistent with previous studies. The transverse turbulence intensity reaches a maximum of 18%  $U_m$  in the upper shear layer, consistent with Escudier *et al.*<sup>38</sup> and slightly higher than that of Casarsa & Giannattasio<sup>22</sup>; far downstream, the mean transverse turbulence intensity is still 10% of  $U_m$ . The Reynolds shear stress  $\overline{u'v'}$  presented in Figure 4.25 is consistent with the contours of  $U$  since its sign inversion occurs where the mean streamwise velocity is maximum. Maximum values about 2.5%  $U_m^2$  are reached in the upper shear layer at the same downstream location as the peak of axial turbulence intensity; minima of  $-2\%U_m^2$  occur in the lower shear layer just downstream of the diaphragm.

The lengths of the primary recirculations  $L_1$  and  $L_3$  and of the secondary structures  $L_2$  and  $L_4$ , as labeled in Figure 4.26, are defined as the positions where the mean streamwise velocity component changes sign. They are reported in Table 4.2 in the  $XY$  midplane. While the absolute values can hardly be compared to the values published previously, due to the wide range of PSE geometries and Reynolds numbers investigated, some tendencies

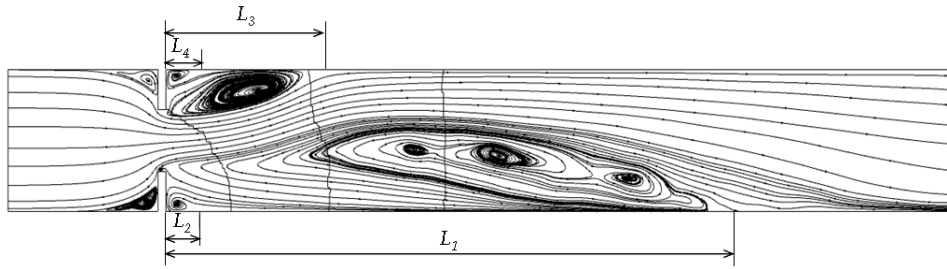


Figure 4.26 – Diaphragm. Labels of the different recirculations.

$L_1/h$	$L_2/h$	$L_3/h$	$L_4/h$
9.83	0.57	2.6	0.46

Table 4.2 – Diaphragm. Normalized lengths of the primary and secondary recirculations in the XY midplane.

can still be drawn. As reported by Casarsa & Giannattasio<sup>22</sup>, the reattachment lengths are mainly a function of the expansion ratio; for the case  $R = 3$ , the ranges provided by Abbott & Kline<sup>1</sup> are  $L_1/h = 11 - 15$  and  $L_3/h = 3.5 - 4$ ; the values reported here are substantially below these ranges, but considering the lower expansion ratio of this work, namely  $R = 2.29$ , the values found are consistent. Regarding the secondary recirculation lengths, the only reported values are from Casarsa & Giannattasio<sup>22</sup> and Spazzini *et al.*<sup>98</sup>, with  $L_2$  and  $L_4$  of the order of one; it is twice the values found here, but no conclusion can be drawn taken the disparity in the considered geometries. Note also the presence of two corner vortices, just upstream of the diaphragm; their extent is also of order  $h$ .

### Mean flow evolution along the span

As shown in Figure 4.27, where the mean path lines computed with the  $U$  and  $V$  components of the mean velocity field are drawn for three XY planes, the flow is not uniform along the span. Figure 4.28 also reports the evolution of the recirculation lengths along the span  $z/h$ . While the shorter recirculation  $L_3$  remains almost constant, the longer recirculation  $L_1$  undergoes great variations, with in particular a nearly uniform increase of  $2h$  in the right channel half from the center to the wall. Regarding the secondary corner structures, their extent is almost uniform in the central portion of the channel, and opposite behaviors are found near the lateral walls: the lower recirculation zone extent is doubled near the left wall, while the upper one is nearly doubled in the vicinity of the right wall.

The three-dimensionality of the flow field can also be investigated by visualization of the flow paths in the XZ planes, as presented in Figure 4.29 for four  $y/h$  locations: in the lower recirculation region close to the wall ( $y/h = 0.28$ ) and a bit upper ( $y/h = 0.57$ ), in the midplane ( $y/h = 1.1$ ), and in the upper recirculation, where the flow impinges the top wall ( $y/h = 1.7$ ). In the lower recirculation, just above the channel floor, see

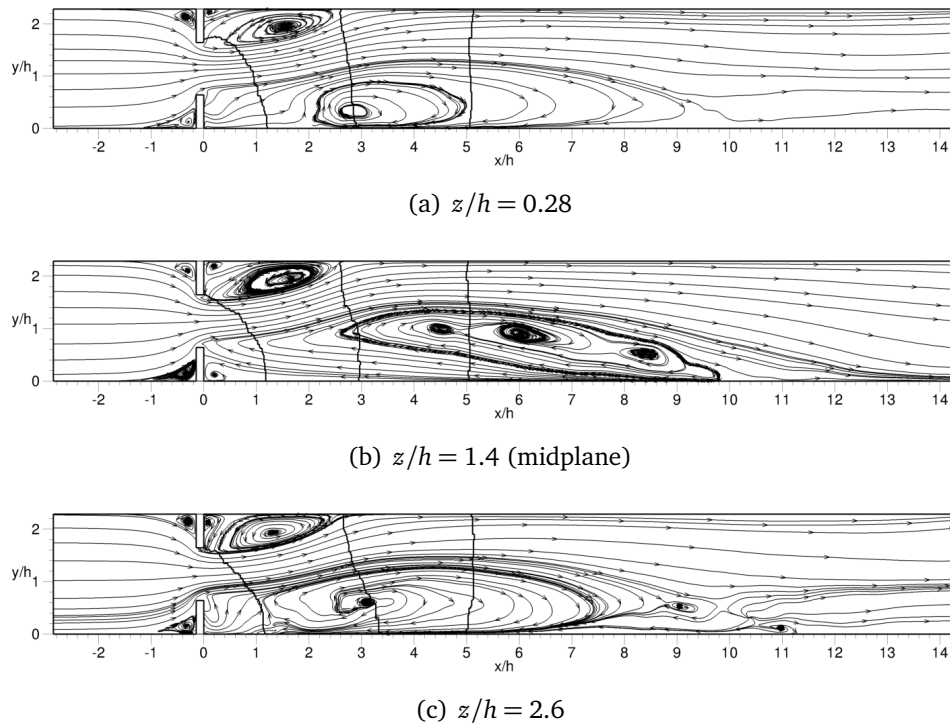


**Figure 4.27 – Diaphragm.** Streamlines in  $XY$  planes computed with the  $U$  and  $V$  components of the 3D mean velocity field at different spanwise locations.

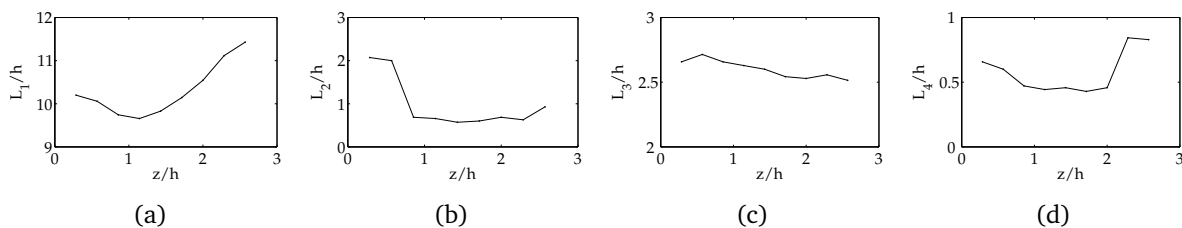


**Figure 4.28 – Diaphragm.** Recirculation lengths evolution, normalized by  $h$ , with respect to the position along the span.

Figure 4.29(a), two counter-rotating vortices are found, resulting from the impingement of the big recirculation on the lower vertical diaphragm wall; the presence of these vortices was already proposed by Abbott & Kline<sup>1</sup> and confirmed by Casarsa & Giannattasio<sup>22</sup>. These vortices are still present at  $y/h = 0.57$ , see Figure 4.29(b), but the flow exhibits a much more complex behavior with several vortex structures counter rotating at the right and left of the channel centerline. In the midplane, see Figure 4.29(c), path lines are almost parallel since the jet-like flow is dominant in this plane. Upper at  $y/h = 1.7$ , see Figure 4.29(d), the location of flow separation is recognized, with the flow directed toward the diaphragm for  $x/h < 0.6$  and toward the channel exit for  $x/h > 0.6$ .

In the light of figures 4.30 and 4.31, which present the mean axial and spanwise velocity contours at respectively  $y/h = 0.57$  and  $y/h = 1.7$ , it is noticeable that, in the upper plane at  $y/h = 1.7$ , the axial mean velocity  $U$  is not constant along the span and has its minimum

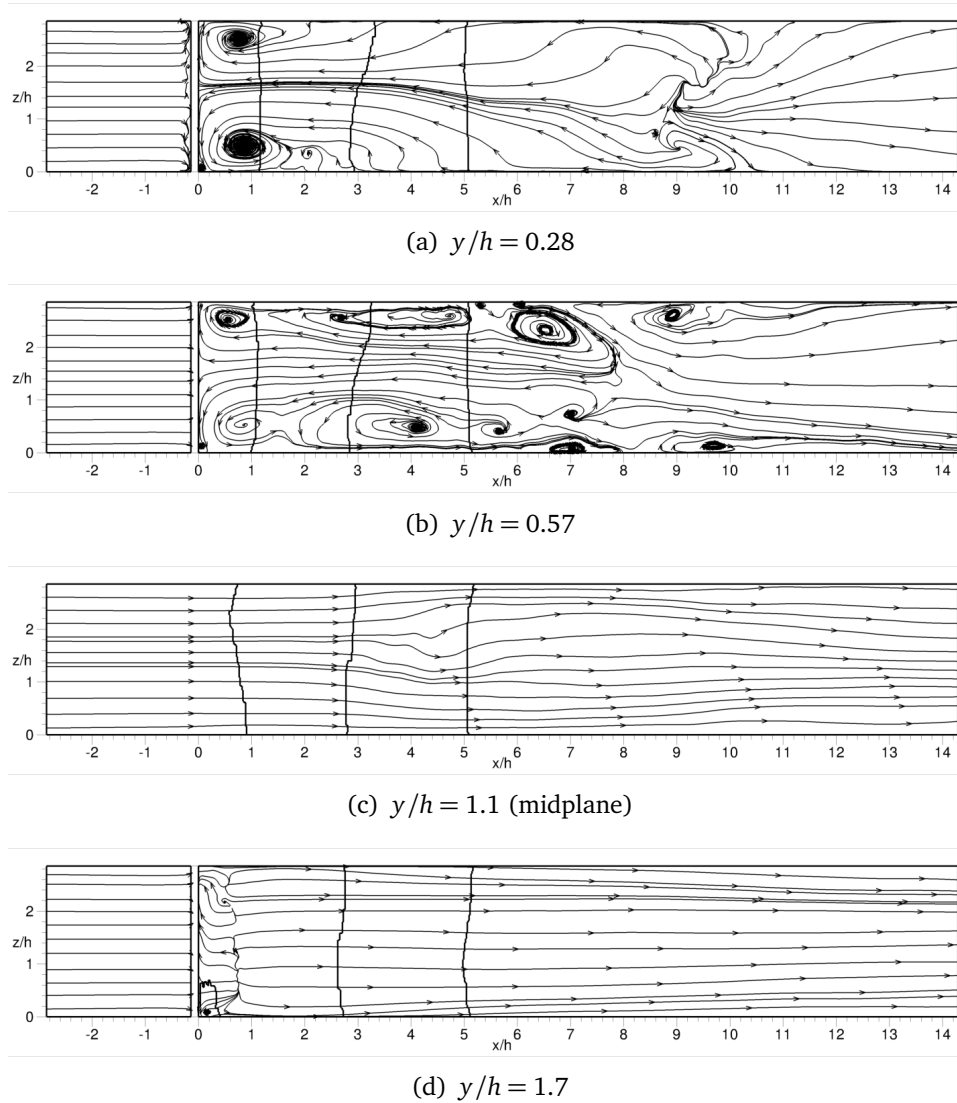


**Figure 4.29 – Diaphragm.** Streamlines in  $XZ$  planes computed with the  $U$  and  $W$  components of the 3D mean velocity field at different height locations.

values of  $-0.3U_m$  around the channel centerline. The spanwise mean flow  $W$  presents significant values only close to the diaphragm walls for  $x/h < 0.2$ , where the ground counter rotating vortices are present. In the upper plane at  $y/h = 1.7$ , the mean axial velocity contours are almost uniform along the span for  $x/h < 2.2$ , with the separation line between negative and positive velocities located at  $x/h \sim 0.6$  as noticed in Figure 4.29(d). Around  $x/h = 3$ , two symmetrical maxima of  $U$  are found around  $z/h = 0.4$  and  $2.4$ . The levels of spanwise velocity  $W$  in this plane are low, as indicated by the almost parallel path lines.

Finally, the flow paths in section cuts as shown in Figure 4.32 allow to complete the understanding of this complex flow structure. In the first planes of figures 4.32(a)-(c), the flow paths are vertical for  $0.8 < y/h < 1.5$ , which corresponds to the core flow and shear layers. However, this behavior is perturbed near the walls for  $z/h < 0.3$  and  $z/h > 2.5$ ,

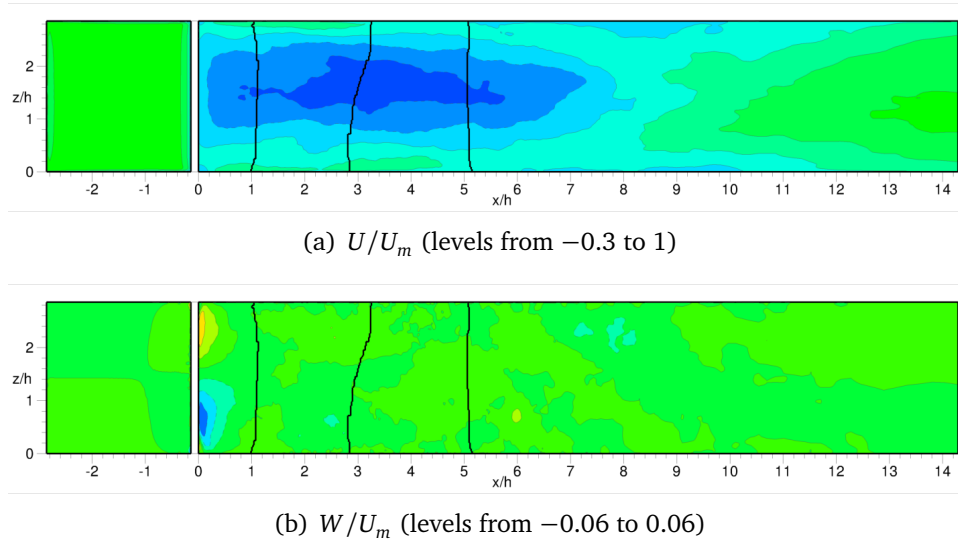


**Figure 4.30** – Diaphragm. Mean velocity field in the XZ plane located at  $y/h = 0.57$ .

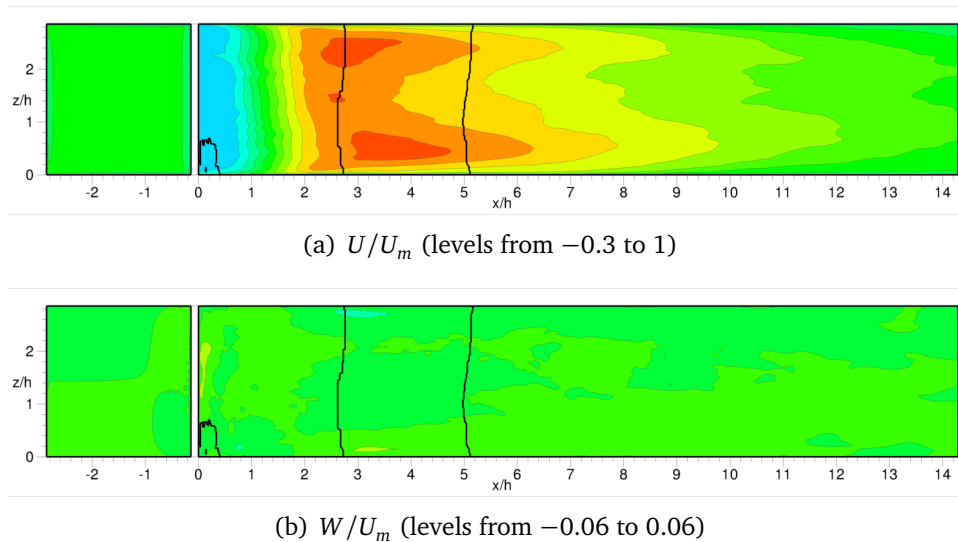


**Figure 4.31** – Diaphragm. Mean velocity field in the XZ plane located at  $y/h = 1.7$ .

where the interaction between the primary recirculations and corner vortices produce a complex flow. From  $x/h = 2$ , two counter-rotating structures develop in the lower corners; these structures are created just downstream of the ground counter-rotating vortices noticed in Figure 4.29(a) and extend over the whole longer recirculation zone.

#### 4.3.2.2 Instantaneous flow features

In Figures 4.33, 4.34, 4.35 and 4.36 are presented the instantaneous contours of, respectively, streamwise, transverse and spanwise velocity and vorticity magnitude, in the XY and XZ center planes and one YZ view. The jet unsteadiness is clearly visible, with the periodic shedding of structures from the lips of the diaphragm. The three-dimensional development is representative of the computational level of refinement. The levels and

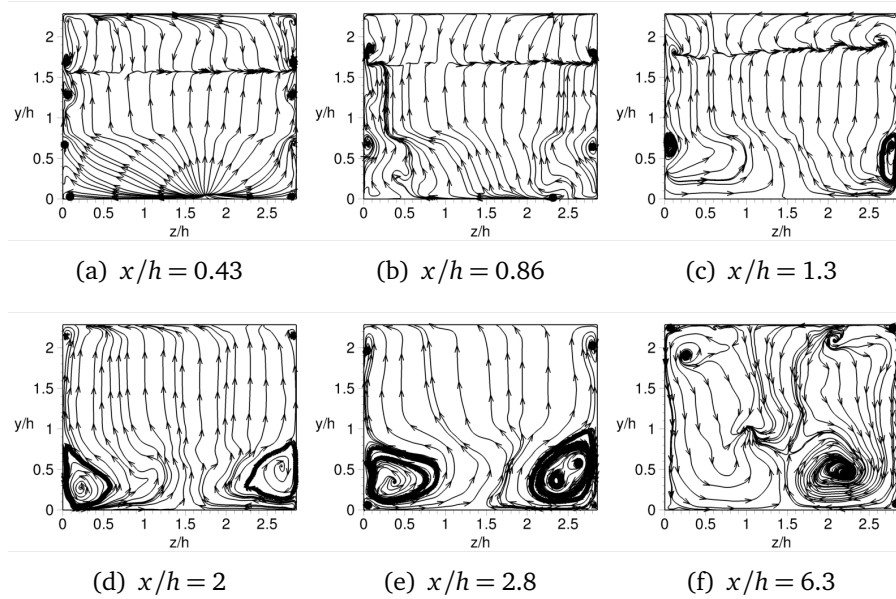


**Figure 4.32 – Diaphragm.** Streamlines in  $YZ$  planes computed with the  $V$  and  $W$  components of the 3D mean velocity field at different longitudinal locations.

the general aspect of this instantaneous flow field are conform to that shown in Gloerfelt & Lafon<sup>54</sup>.

An alternative way of representing turbulence structures is obtained by visualizing the positive  $\mathcal{Q}$  criterion, defined as the second invariant of velocity gradient tensor  $\nabla\mathbf{u}$ , Hunt *et al.*<sup>61</sup>:

$$\mathcal{Q} = \frac{1}{2}(\|\mathbf{\Omega}\| - \|\mathbf{S}\|)$$

where  $\mathbf{\Omega}$  and  $\mathbf{S}$  are the antisymmetric and symmetric parts of the velocity gradients  $\nabla\mathbf{u}$ . Figure 4.37 represents three views of the  $\mathcal{Q}$  criterion normalized with  $(U_m/h)^2$ . The identified coherent structures are located in the shear layers. Close to the diaphragm, in the thin shear layers, the structures are well organized; the first series of structures generated by a Kelvin-Helmholtz instability are almost parallel to the  $z$ -axis with a nearly cylindrical shape. Further downstream, their orientation changes, and the structures are progressively split and turn in the main flow direction as the shear layers thicken. After the flow impinges on top wall, the structures rapidly disappear.

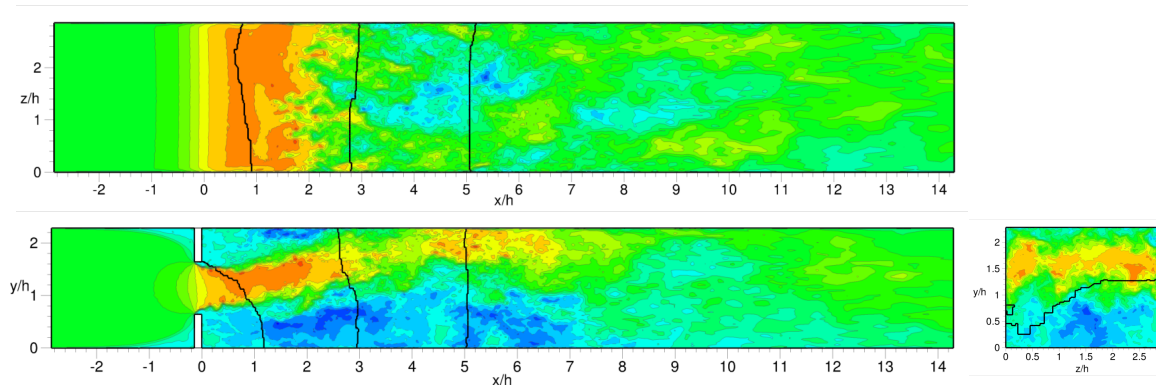


**Figure 4.33** – Diaphragm. Instantaneous longitudinal velocity  $u$  (levels between  $-10$  and  $25$  m/s). Top, top view in the XZ midplane; bottom left, front view in the XY midplane; bottom right, cross section at  $x/h = 2.8$ .

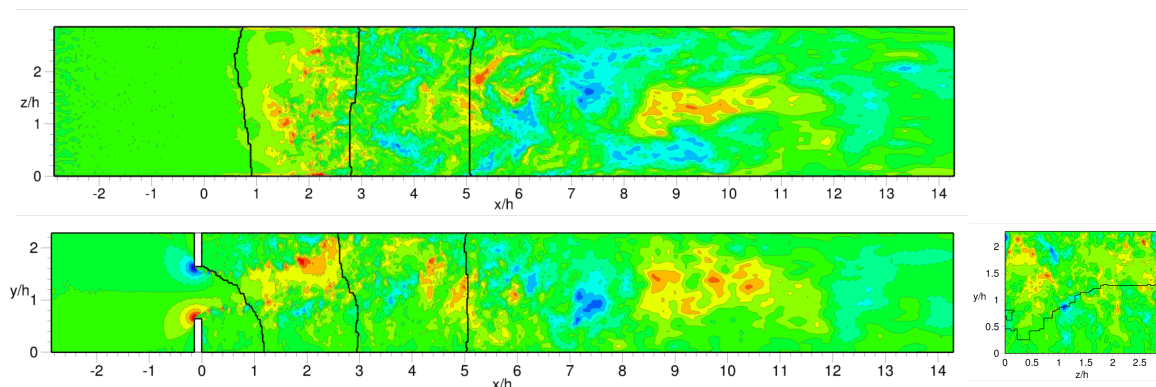


**Figure 4.34** – Diaphragm. Instantaneous crossflow velocity  $v$  (levels between  $-10$  and  $10$  m/s). Top, top view in the XZ midplane; bottom left, front view in the XY midplane; bottom right, cross section at  $x/h = 2.8$ .

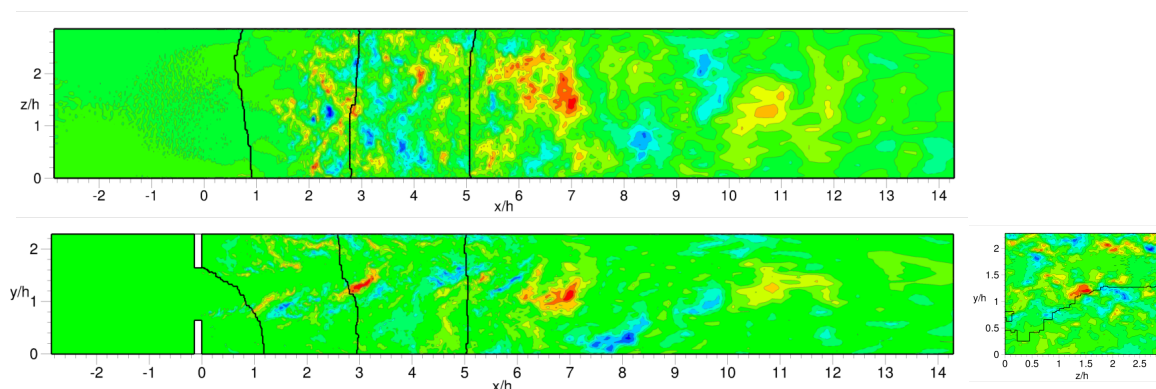


**Figure 4.35** – Diaphragm. Instantaneous spanwise velocity  $w$  (levels between  $-10$  and  $10$  m/s). Top, top view in the XZ midplane; bottom left, front view in the XY midplane; bottom right, cross section at  $x/h = 2.8$ .

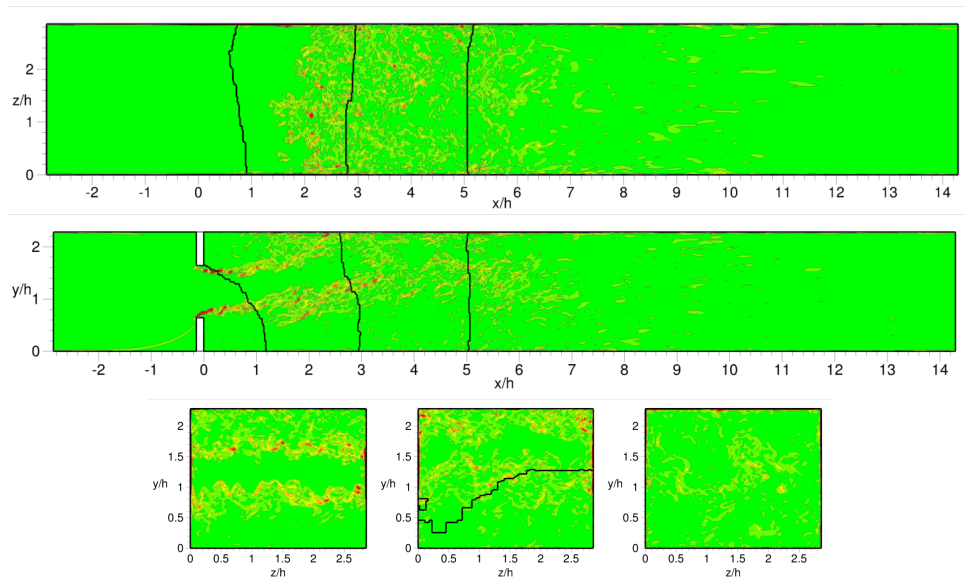


**Figure 4.36** – Diaphragm. Instantaneous vorticity magnitude  $\|\omega\|$  (levels between  $-1$  and  $1 \cdot 10^4 \text{ s}^{-1}$ ). Top, top view in the XZ midplane; middle, front view in the XY midplane; bottom, cross sections at  $x/h = 1.3, 2.8$  and  $6.3$ .

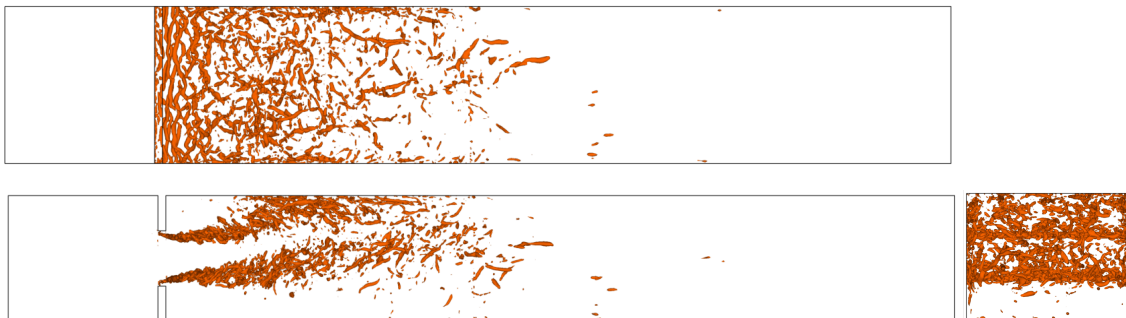


**Figure 4.37** – Diaphragm. 3d isosurfaces of  $\mathcal{Q}/(U_m/h)^2 = 10$ . Top, top view; bottom left, front view; bottom right, side view.

### 4.3.2.3 Statistic analysis

#### Correlation lengths

Correlation lengths in the three directions, defined by expressions 4.1, are computed and displayed in Figures 4.38-4.40; these integral flow scales are useful to understand the spatial structure of the flow. The evolution of streamwise correlation lengths of Figure 4.38 thus enlightens that the largest turbulence structures are located in the shear layers and are fed by the streamwise and spanwise velocity fluctuations; indeed,  $L_{11}(x)$  and  $L_{33}(x)$  are always of the same order and larger than  $L_{22}(x)$ , reaching up to 20 mm in the shear layers, while  $L_{22}(x)$  stays below 5 mm almost everywhere. More surprisingly, high values of  $L_{11}(x)$  and  $L_{33}(x)$  in the recirculation zones indicate the possible presence of large coherent structures that were not detected by the  $\mathcal{Q}$ -criterion. Finally, the three-dimensional complexity is once again evident taken the differences between the correlation lengths in several XY planes.

The transverse,  $L_{ii}(y)$ , and spanwise,  $L_{ii}(z)$ , correlation lengths evolution along  $x$  reported in Figures 4.39 and 4.40 have a different behavior. Indeed, the three are now of the same order, proving that the three velocity components of the flow field contribute equally to the existence of coherent structures. Note that the evolution of  $L_{11}(y, z)$  and  $L_{33}(y, z)$  have a very similar behavior, with a difference in length of a few millimeters in favor of  $L_{33}(y, z)$ .

It is worth noting that at this point, no universal integral length scales can be deduced from the previous analysis. In particular, the spanwise integral scale  $L_{33}(z)$  undergoes great variations along the streamwise direction; the choice for an integral scale usable for a two-dimensional acoustic simulation is therefore almost impossible.

#### Spectral content of the velocity field

An analysis similar to the one led in § 4.2.2.3 using the similarity parameter  $\eta = (y - y_{0.5})/\delta_\theta$  enables determining the width of the upper and lower shear layers; as is reported in Figure 4.41, the velocity profiles are seen to collapse for respectively  $\delta_{\theta, \text{up}} \simeq 0.8$  mm and  $\delta_{\theta, \text{down}} \simeq 0.9$  mm. Considering that a Strouhal number of  $\simeq 0.017$  corresponds to the most unstable frequency for a hyperbolic-tangent velocity profile, the excited frequencies should lie around 425 Hz and 378 Hz for the upper and lower shear layers, respectively. Note that, in Figure 4.41, the simulated profiles do not exactly coincide with the hyperbolic-tangent profile outside of the jet, for  $\eta > 2$  in Figure 4.41(a) and  $\eta < -2$  in Figure 4.41(b); indeed, in the diaphragm simulation, there are recirculations above and below the jet, which appear as negative values of  $u_{\text{mean}}/U_0$  in the profiles.

However, the Power Spectral Densities reported in Figure 4.42 do not exhibit the 425 Hz peak for the upper shear layer. Instead, a rather broadband content is found for the first

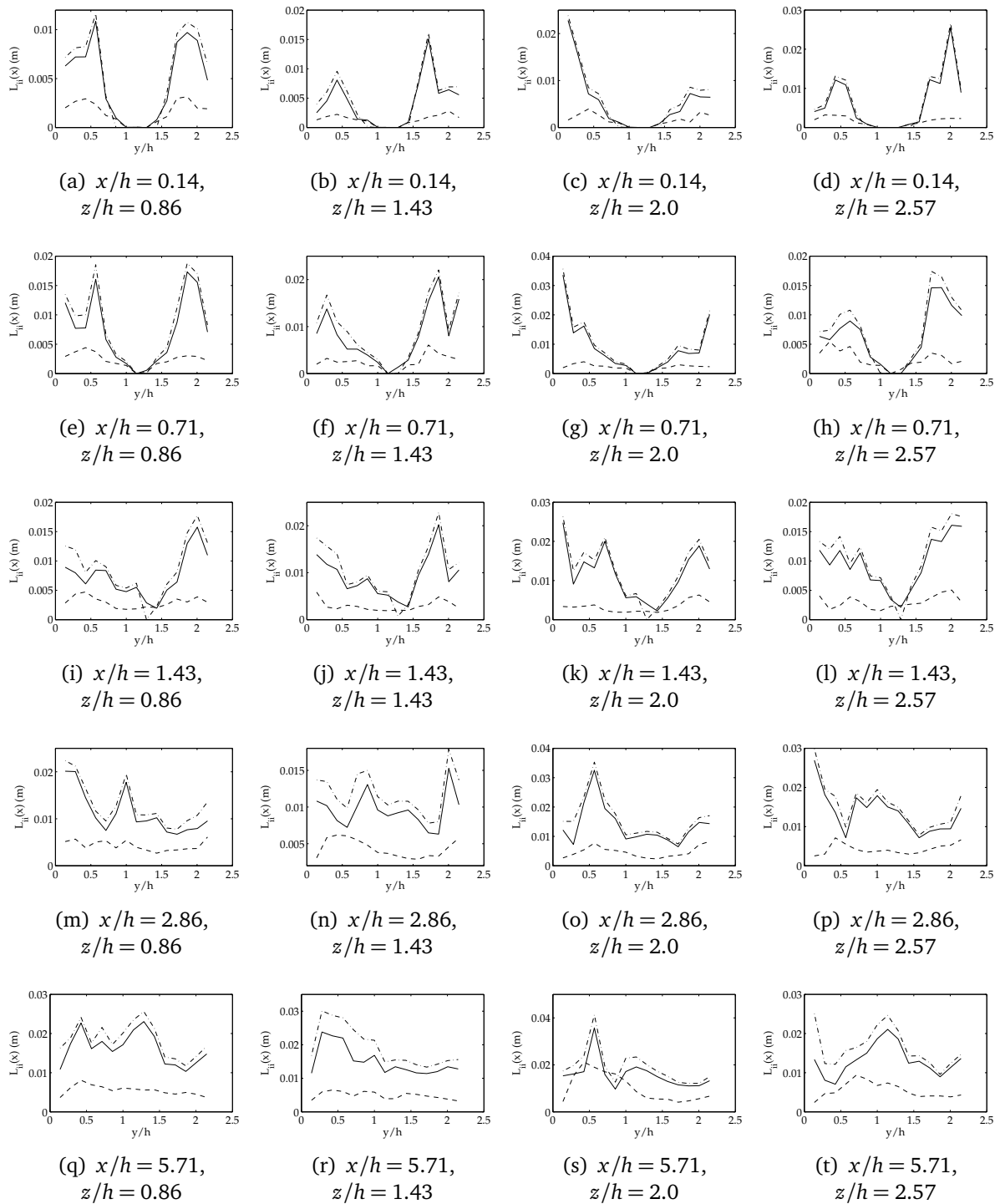


**Figure 4.38 – Diaphragm.** Correlation lengths  $L_{ii}(x)$  along the transverse direction  $y$  for different locations  $x, z$ . —:  $L_{11}(x)$ , ---:  $L_{22}(x)$ , - · -:  $L_{33}(x)$ . Note that  $L_{ii}(x) \equiv L_{ii}^{(1)}$  with the notations of expressions 4.1.

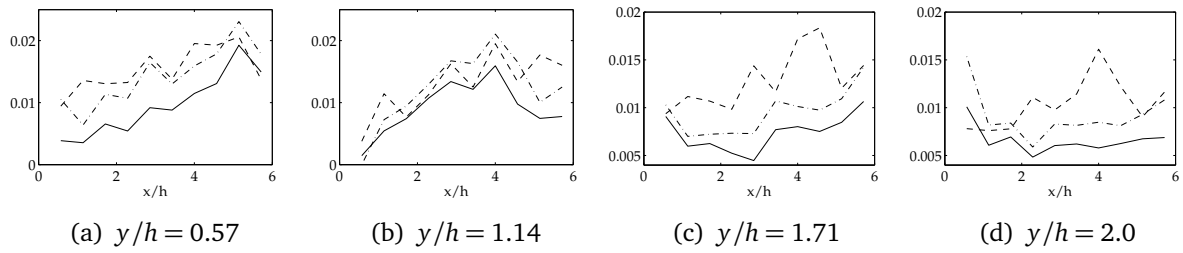


**Figure 4.39 – Diaphragm.** Correlation lengths  $L_{ii}^{(2)}$ , in m, along the streamwise direction  $x$  for different  $y$  locations, at  $z/h = 1.43$ . —:  $L_{11}^{(2)}$ , ---:  $L_{22}^{(2)}$ , -·-:  $L_{33}^{(2)}$ .

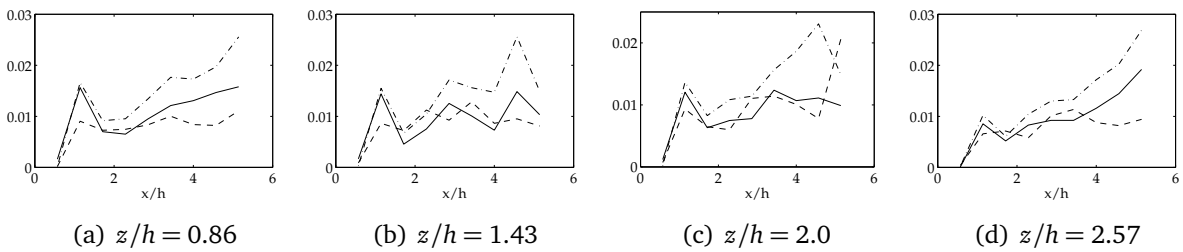


**Figure 4.40 – Diaphragm.** Correlation lengths  $L_{ii}^{(3)}$ , in m, along the streamwise direction  $x$  for different  $z$  locations, at  $y/h = 1.71$ . —:  $L_{11}^{(3)}$ , ---:  $L_{22}^{(3)}$ , -·-:  $L_{33}^{(3)}$ .

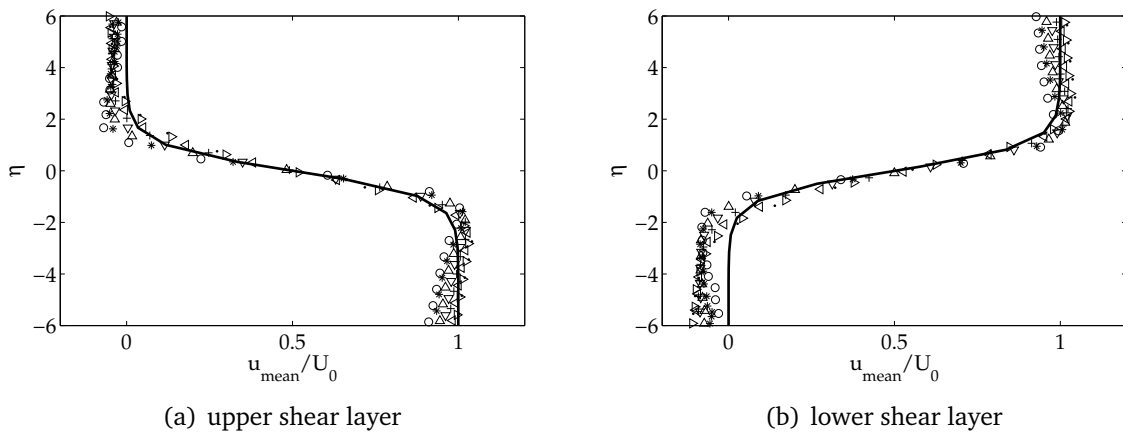


**Figure 4.41 – Diaphragm.** Mean streamwise velocity profiles for the upper and lower shear layer versus  $\eta = (y - y_{0.5})/\delta_\theta$ , where  $y_{0.5}$  corresponds to  $\bar{u} = 0.5U_m$  and  $U_m = 20$  m/s, at different longitudinal locations.  $\circ$ :  $x = 1$  mm;  $*$ :  $x = 2$  mm;  $\Delta$ :  $x = 3$  mm;  $\nabla$ :  $x = 4$  mm;  $+$ :  $x = 5$  mm;  $\triangleleft$ :  $x = 6$  mm;  $\triangleright$ :  $x = 7$  mm;  $\bullet$ :  $x = 8$  mm. A hyperbolic-tangent profile  $(1 - \tanh \eta)/2$  is superimposed on the left,  $(1 + \tanh \eta)/2$  on the right (—).

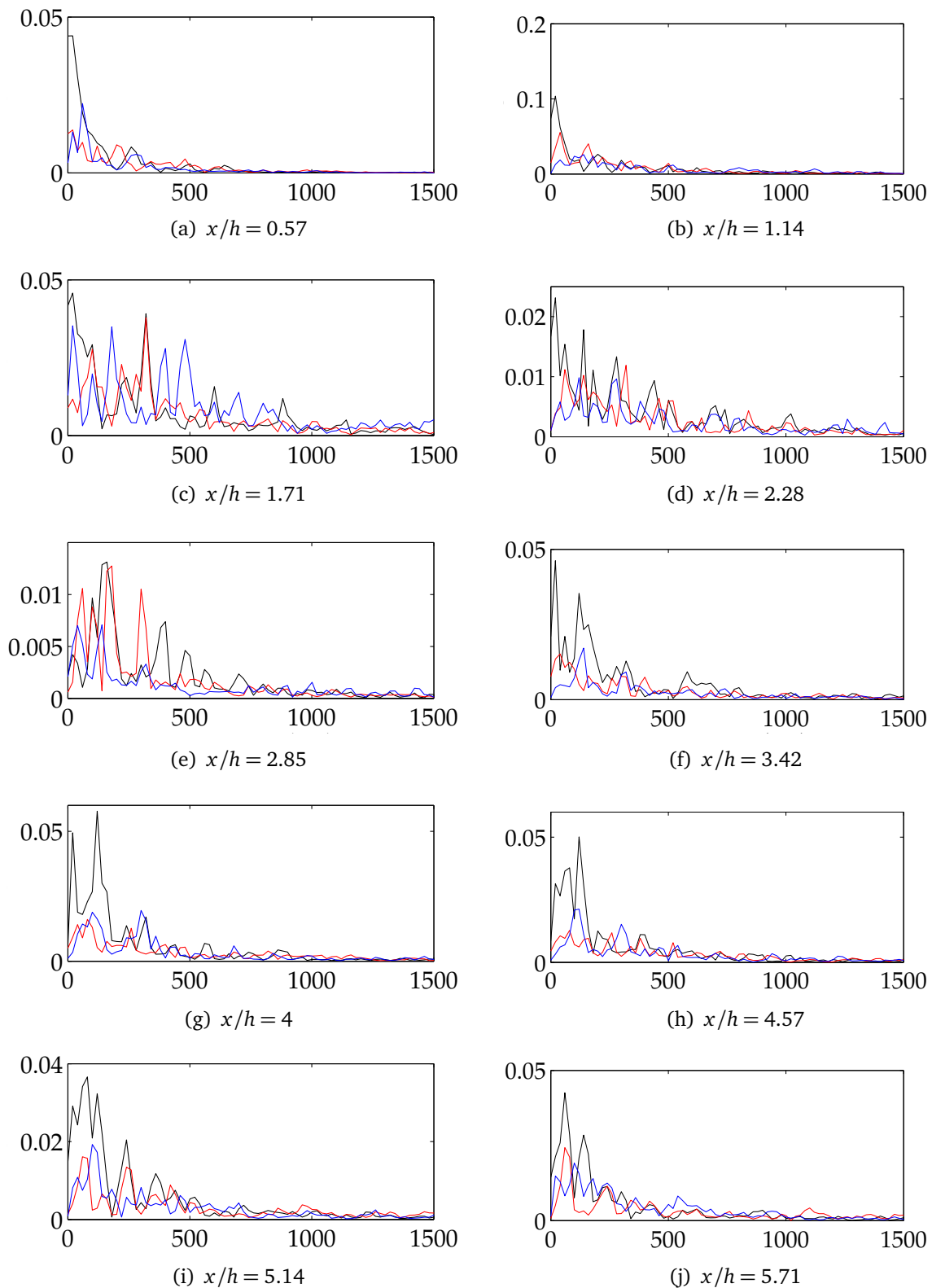


**Figure 4.42** – Diaphragm. Power Spectral Densities (PSD), in  $\text{m}^2/\text{s}^2/\text{Hz}$ , of velocity fluctuations, as a function of frequency; linear scale. Signals are recorded at  $y/h = 1.14$  (upper shear layer) and  $z/h = 1.43$  at different  $x$  positions. —: PSD of  $u'$ ; —: PSD of  $v'$ ; —: PSD of  $w'$ .

five sensors, for  $x/h \leq 2.85$ ; from then on, a well-defined peak centered at 120 Hz is dominant; Gloerfelt & Lafon<sup>54</sup> suggest that this low frequency is correlated with the periodic shedding and collapse of large scale jet-column instabilities, and is responsible for most of the radiated noise. Indeed, it was observed that this peak is dominant in the shear layers, before the impingement of the jet on top wall.

In addition, an intense and sharp low frequency peak at 20 Hz is present for almost all sensors. The visualization of PSD levels in the whole flow field shows that this peak is mainly located at the outline of recirculation regions.

### 4.3.3 Analysis and filtering of the source terms $S_i$

It is tempting to look for the most energetic source terms in the domain, and suppose that these terms are the most important contributors for far field acoustic radiation. However, according to Colonius *et al.*<sup>29</sup> and Bogey<sup>9</sup> analyses in the academic case of a mixing layer, the source term fluctuations and amplitude do not necessarily reflect the actual contributions to the radiated noise; indeed, only a small part of the source term is efficient in the far field radiation. Freund<sup>48</sup> performs a Direct Numerical Simulation of a more realistic jet flow case where the Lighthill source term is confronted with direct acoustic results; this study shows that the radiating component of the source does not coincide with peak source levels nor with peak turbulence levels. Moreover, in the ducted diaphragm case, the confining walls act as secondary noise sources in terms of reflectors, and this adds a level of complexity in the analysis. Therefore, all source terms have to be accounted for.

#### 4.3.3.1 Raw data smoothing

An intermediate fully Cartesian mesh, more tractable for post-processing than the CFD mesh and truncated at  $x/h = 7.1$ , is built to record the source term components  $S_i$ . This mesh is designed to be as close as possible to the CFD mesh to retain its accuracy, and is composed of  $397 \times 130 \times 120$  points; the  $x$ ,  $y$  and  $z$ -spacings are conform to the CFD mesh, and the mesh points are located at the CFD cells centers. After locating these points in its own domain, the CFD code performs a zero order interpolation of the source terms: at each point, the interpolated quantity is the quantity at the closest CFD cell center. This "raw" data is plotted in Figure 4.43.

A post treatment is necessary to smooth the data, similarly to Fluent's procedure for graphics display. To do this, the dual mesh of this fine Cartesian mesh is computed, so as to reflect its cell centers. The values at the nodes of the dual mesh are obtained by doing a weighted average of the surrounding node values of the original; the weights are defined as the inverse of the distance between the current node in the dual mesh and its neighbor nodes in the original mesh. This mesh change is illustrated in Figure 4.44 for a two-dimensional uniform mesh; considering the original blue cell with nodes  $n_1$ ,  $n_2$ ,  $n_3$

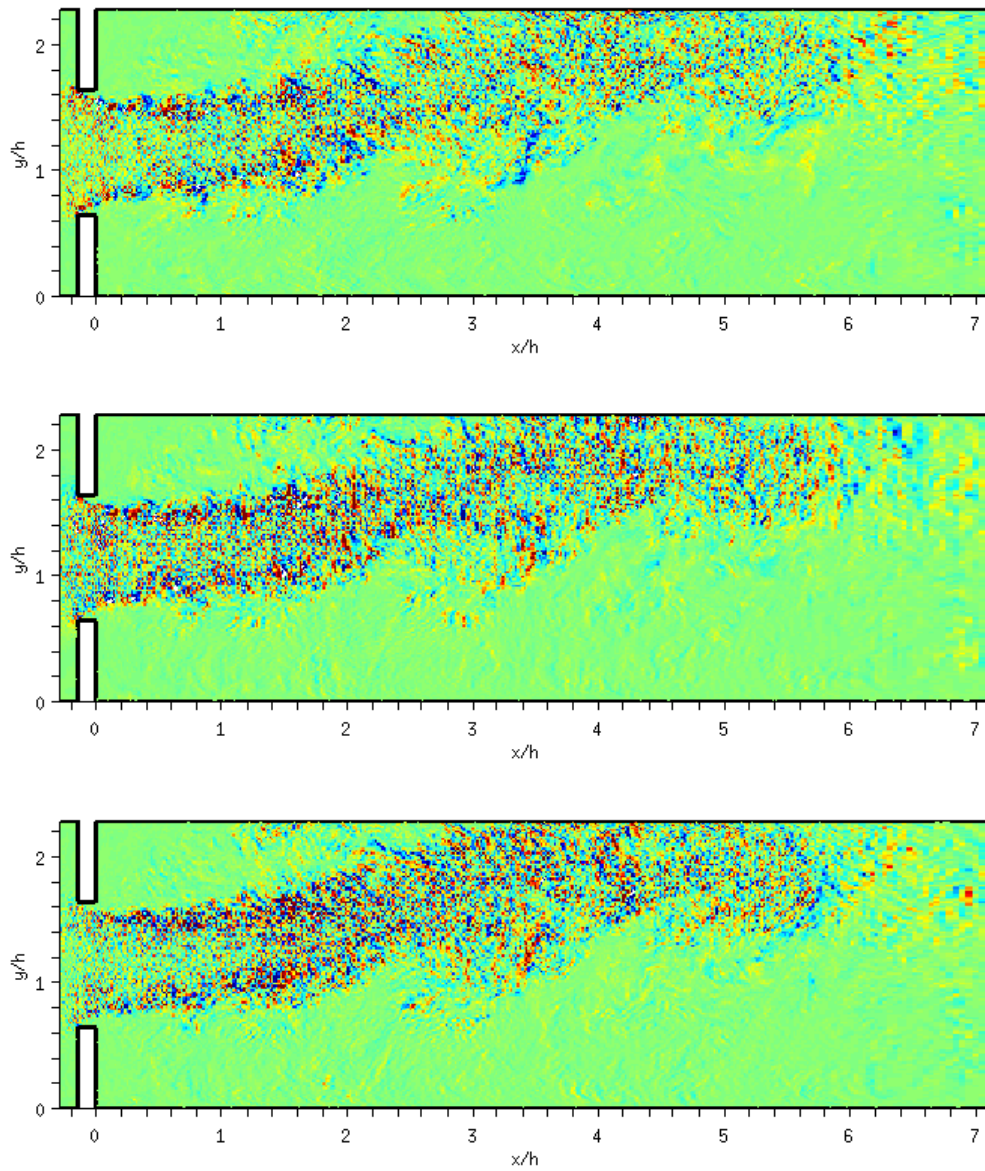


**Figure 4.43** – Diaphragm. Raw source term components in the XY midplane. From top to bottom:  $S_1$ ,  $S_2$  and  $S_3$ ; levels:  $\pm 1 \times 10^5$  Pa/m.

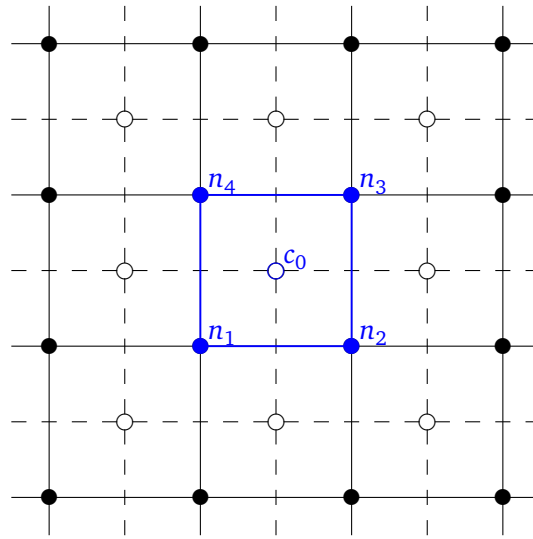


**Figure 4.44** – Illustration of original and dual mesh. In solid line: original mesh, with filled circles representing the nodes. In dashed line: dual mesh with its nodes (empty circles) located at the cell centers of original mesh.

and  $n_4$ , the dual mesh is built with one node located at the cell center  $c_0$ . Then, the value of the smoothed quantity at  $c_0$  is obtained with

$$\phi'_{c_0} = \frac{\sum_{i=1}^4 \frac{1}{d_{c_0 \rightarrow n_i}} \phi_{n_i}}{\sum_{i=1}^4 \frac{1}{d_{c_0 \rightarrow n_i}}}$$

where  $\phi_{n_i}$  is the original quantity at node  $n_i$  and  $\phi'_{c_0}$  its smooth value at cell center  $c_0$ , and  $d_{c_0 \rightarrow n_i}$  is the distance between  $c_0$  and the node  $n_i$ . The smoothed data is plotted in Figure 4.45, with a very visible improvement on the data definition.

#### 4.3.3.2 Filtering to remove grid-to-grid oscillations

The isosurfaces of the second component  $S_2$  of the smoothed source term are displayed in Figure 4.46, where grid-to-grid oscillations are evident; these non physical waves are also visible in Figure 4.45, more particularly on the second and third components of  $S_i$  since their levels are lower. These high frequencies appear during the spatial derivation of Lighthill's tensor, and must be removed since they are not supported by the mesh. A spatial filtering is required to remove those spurious waves. It is chosen here to apply a selective filtering directly on the source term components  $S_i$  and remove all wave numbers larger than the cut-off wave number. Filters are designed according to the procedure described in Bogey & Bailly<sup>10</sup>. Filters are centered on 9 points, and the cut-off wave number is  $2\pi/3$ ,

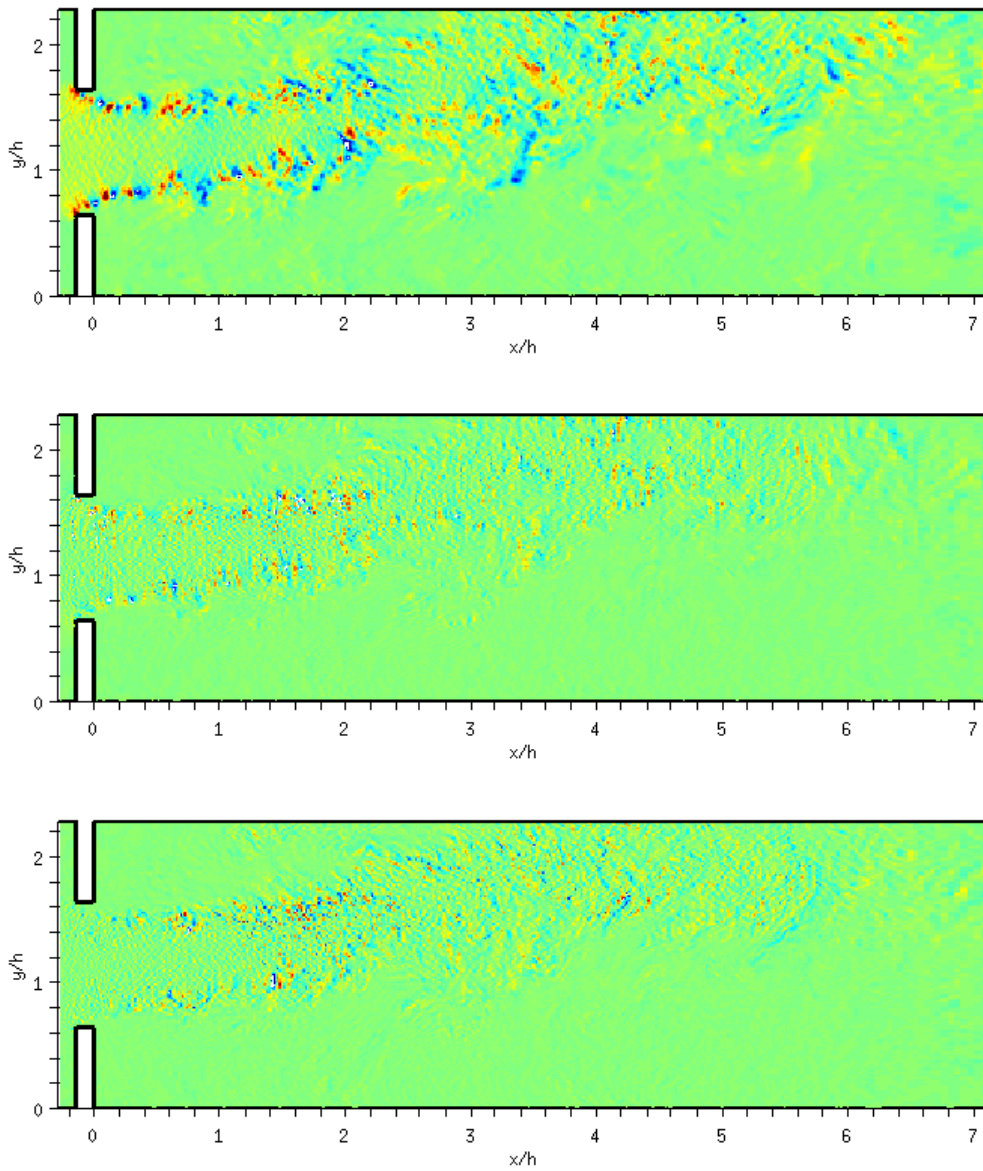


**Figure 4.45** – Diaphragm. Smoothed source term components in the XY midplane. From top to bottom:  $S_1$  ( $\pm 1 \times 10^5$  Pa/m),  $S_2$  ( $\pm 4 \times 10^4$  Pa/m) and  $S_3$  ( $\pm 4 \times 10^4$  Pa/m).

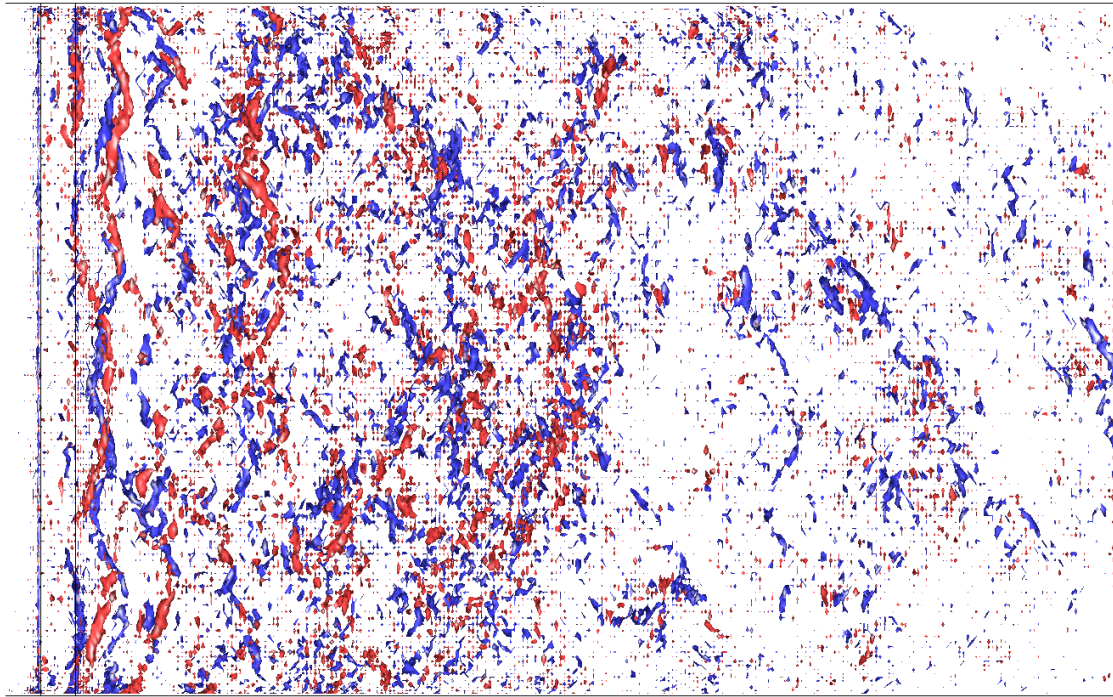


**Figure 4.46** – Diaphragm. Isosurfaces of  $S_2$  smoothed source term, top view. Blue isosurfaces: negative levels, red isosurfaces: positive levels ( $\pm 1.5 \times 10^4$  Pa/m).

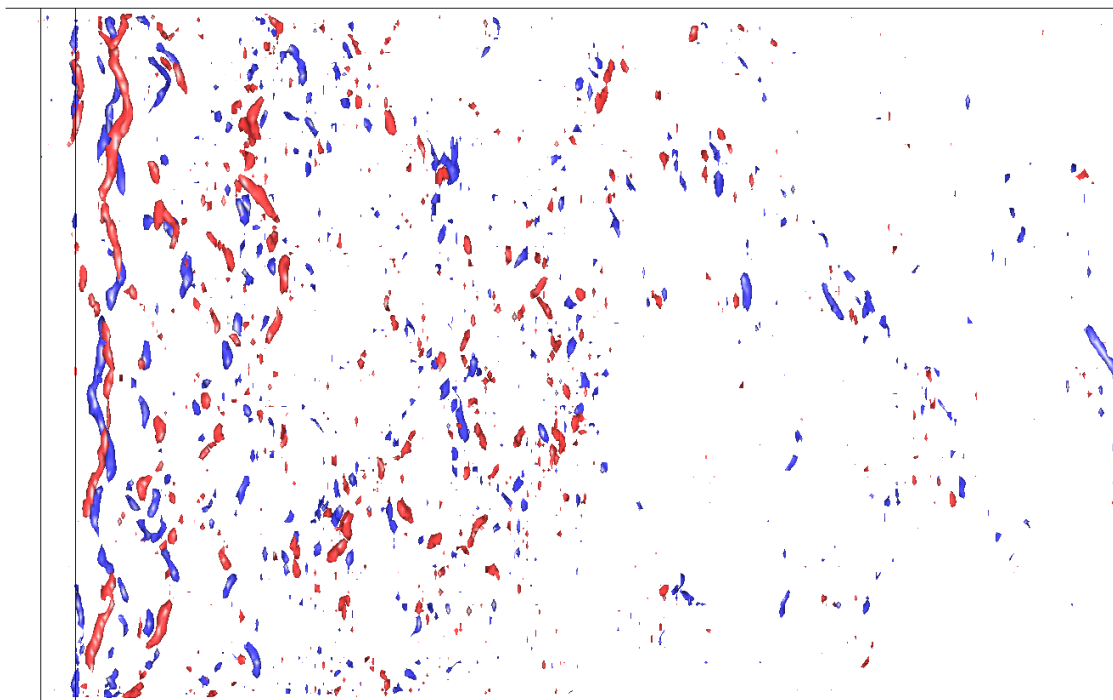


**Figure 4.47** – Diaphragm. Isosurfaces of  $S_2$  smoothed and filtered source term, top view. Blue isosurfaces: negative levels, red isosurfaces: positive levels ( $\pm 1.5 \times 10^4$  Pa/m).

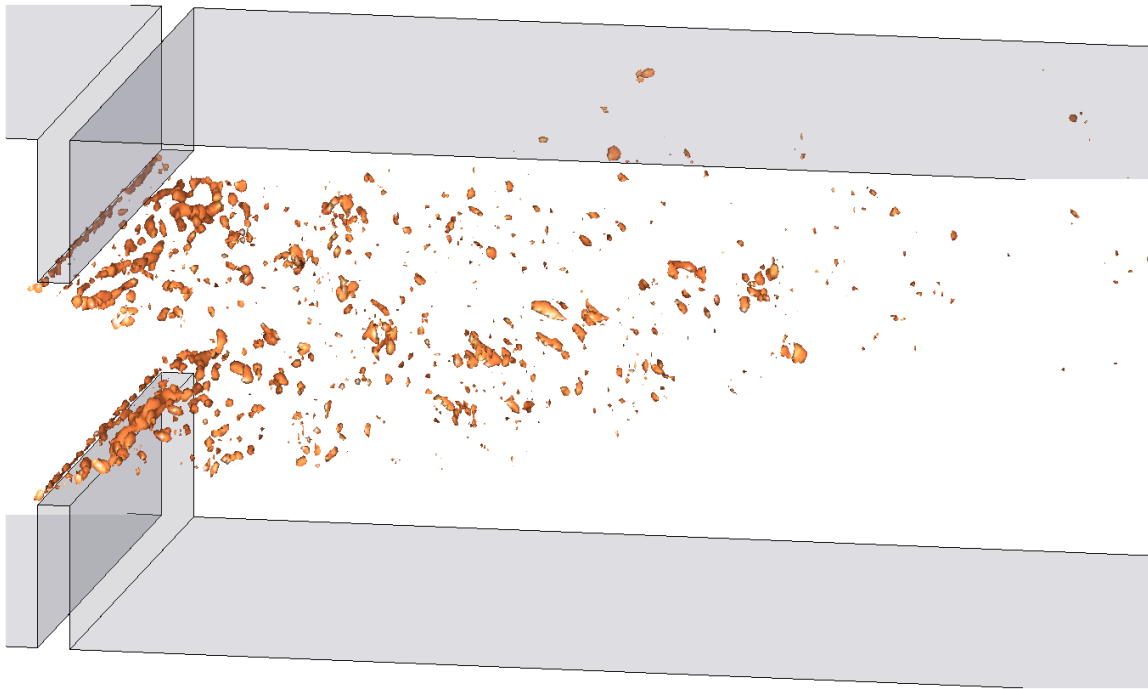
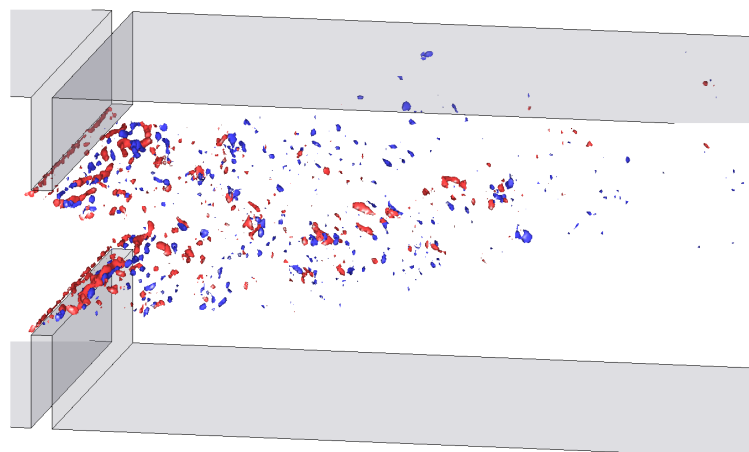


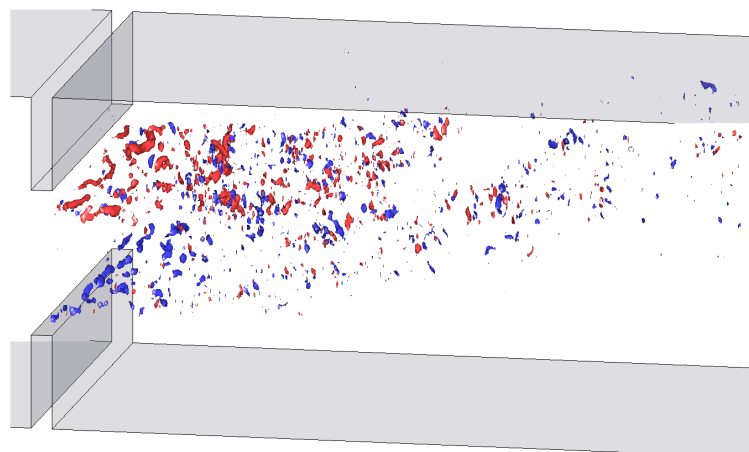
**Figure 4.48** – Diaphragm. Isosurfaces of  $\mathbf{S}$  smoothed and filtered source term, top view. Blue isosurfaces: negative levels, red isosurfaces: positive levels ( $\pm 8 \times 10^4 \text{ Pa/m}$ ).

which allows to remove all oscillations occurring on less than 1.5 grid points. Toward the domain boundaries, centered filters on 7, 5, 3 points are successively applied while the last boundary point is discarded. After filtering, all grid-to-grid oscillations are removed while preserving the essential nature of the source terms, as can be seen in Figure 4.47, as compared to Figure 4.46.

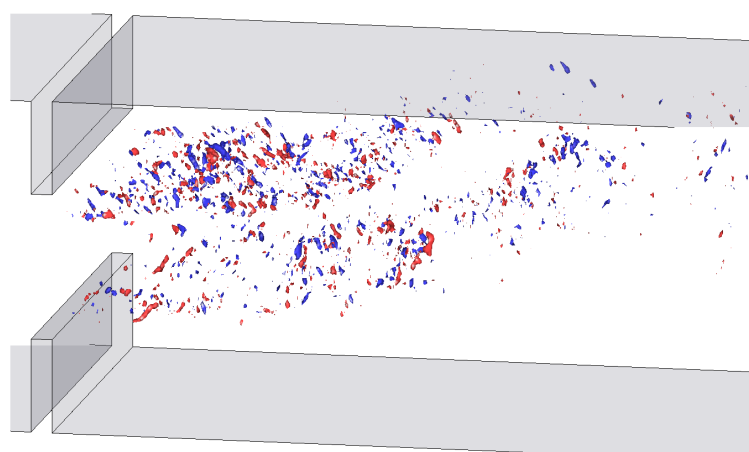
Perspective views of the three source term components are displayed in Figure 4.49; in addition, a view of the source term magnitude is presented in Figure 4.48. From this figure and according to the levels, it is clear that the main contribution to  $\mathbf{S}$  comes from its first component  $S_1$ . On the source term components visualization, source terms are identified as the juxtaposition of positive and negative isosurfaces. The analysis of their time evolution shows no particular merging event, as could be expected downstream vortex shedding from the diaphragm lips.



(a)  $S_1$  (levels at  $\pm 8 \times 10^4$  Pa/m)



(b)  $S_2$  (levels at  $\pm 1.5 \times 10^4$  Pa/m)



(c)  $S_3$  (levels at  $\pm 1.5 \times 10^4$  Pa/m)

**Figure 4.49** – Diaphragm. Isosurfaces of the three source term components, perspective view. Blue isosurfaces: negative levels, red isosurfaces: positive levels.

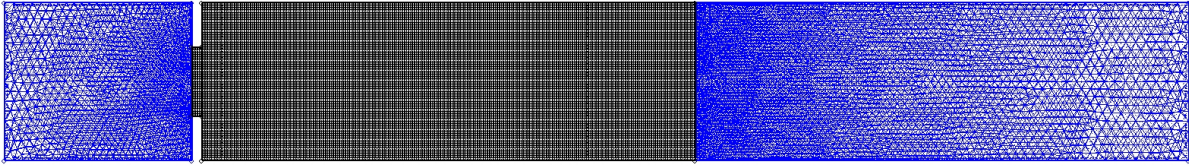


Figure 4.50 – Diaphragm. Acoustic mesh used for the three-dimensional acoustic computation.

## 4.3.4 Acoustic simulation

### 4.3.4.1 Configuration and numerical parameters

#### Transformation to the spectral domain

As in the case of corotating vortices, a Fast Fourier Transform is performed on the transient signals after detrending and application of a Hanning filtering. The acoustic time step  $\Delta t_{ac} = 10 \times \Delta t_{CFD} = 10^{-4}$  s allows reaching the maximal frequency  $f_{max} = 5000$  Hz. The total recorded physical time  $T = 100$  ms drives the frequency resolution  $f_r$  with  $f_r = 1/T = 10$  Hz if no averaging is done. Acoustic computations have also been performed using averaged source terms, the signal being averaged on 19 overlapping samples of 10 ms each, leading to a frequency resolution of 100 Hz.

#### Creation of the acoustic mesh and acoustic model parameters

The acoustic mesh, displayed in Figure 4.50, is built to retain maximum accuracy in the source term description in the region  $-0.29 < x/h < 0.7$  where most sources are located; in this region, the mesh size is uniform:  $\Delta x = \Delta y = h/28$  and  $\Delta z = h/18$  and the finite elements are wedges with triangular basis extruded along the  $x$ -direction. In the remaining of the domain, for  $x/h < -0.14$  and  $x/h > 0.7$ , tetrahedral cells are used with a maximum size of 10 mm to accurately propagate acoustic waves up to  $f_{max} = 5600$  Hz, using the criterion of 6 elements per acoustic wavelength stated in § 3.1.2.4. The total mesh is composed of 700,000 nodes and  $1.5 \times 10^6$  elements.

On the inlet and outlet faces, acoustic duct modes are imposed, such that only outgoing free modes can exist; therefore, free modes in the  $-x$ -direction are imposed at inlet, and free modes in the  $+x$ -direction are imposed at outlet. The duct modes corresponding the present geometry are gathered in Table 4.3.4.1.

The MUMPS<sup>24</sup> solver is chosen for the resolution.

#### 4.3.4.2 Interpolation from the CFD mesh to the acoustic mesh

As explained in § 2.4.3, the strategy for interpolation in the diaphragm case is to define an intermediate Cartesian mesh as fine as the CFD mesh where source terms are recorded: this is the original export mesh; the dual mesh, defined in § 4.3.3.1 and on which the

Inlet		Outlet	
mode	cut frequency (Hz)	mode	cut frequency (Hz)
(-1 0 0)	plane wave	(+1 0 0)	plane wave
(-1 0 1)	1700	(+1 0 1)	1700
(-1 1 0)	2125	(+1 1 0)	2125
(-1 1 1)	2721	(+1 1 1)	2721
(-1 0 2)	3400	(+1 0 2)	3400
(-1 1 2)	4009	(+1 1 2)	4009
(-1 2 0)	4250	(+1 2 0)	4250
(-1 2 1)	4577	(+1 2 1)	4577

**Table 4.3** – Modes considered for the inlet and outlet boundary acoustic conditions.

data is successively smoothed and filtered, is also Cartesian. High order interpolation is then possible from this dual mesh to the final acoustic mesh of Figure 4.50. Thus, a 4th order Lagrange polynomial interpolation is performed in the  $z$ -direction, followed by a two-dimensional second order linear interpolation in each XY plane. Indeed, performing the interpolation successively on different directions has been shown more efficient and less subject to errors than interpolating in all directions at the same time. Space interpolation is applied to frequency data as a last processing operation.

#### 4.3.4.3 Acoustic results

##### Analysis of source terms in the frequency domain

The six frequency components of the source term, at the frequencies of 20 and 1000 Hz, are displayed in Figures 4.51-4.52. The isosurfaces show large and organized structures at the low frequency of 20 Hz for the  $\tilde{S}_1$  component, as can be expected after the Fourier transform; these high energy structures are located well downstream of the diaphragm, in the upper and lower shear layers; the attachment to top wall seems to kill the upper structures, while the lower ones survive farer downstream. Small scales are also present at 20 Hz for the  $\tilde{S}_2$  and  $\tilde{S}_3$  components, in particular just downstream of the diaphragm where the shedding produces elongated structures in the streamwise direction, with small diameter. At 1000 Hz and the same source levels, the source field is very different, without clear topological distinction between the streamwise component and the other ones; it is composed of alternately positive and negative spots very close from each other, organized in rows parallel to the diaphragm lips. No extinction is noticed after attachment to top wall.

After interpolation onto the acoustic mesh, part of the accuracy preserved up to this point is lost, as Figures 4.53-4.56 attest. However, the overall coherence of the source terms seems to be retained.

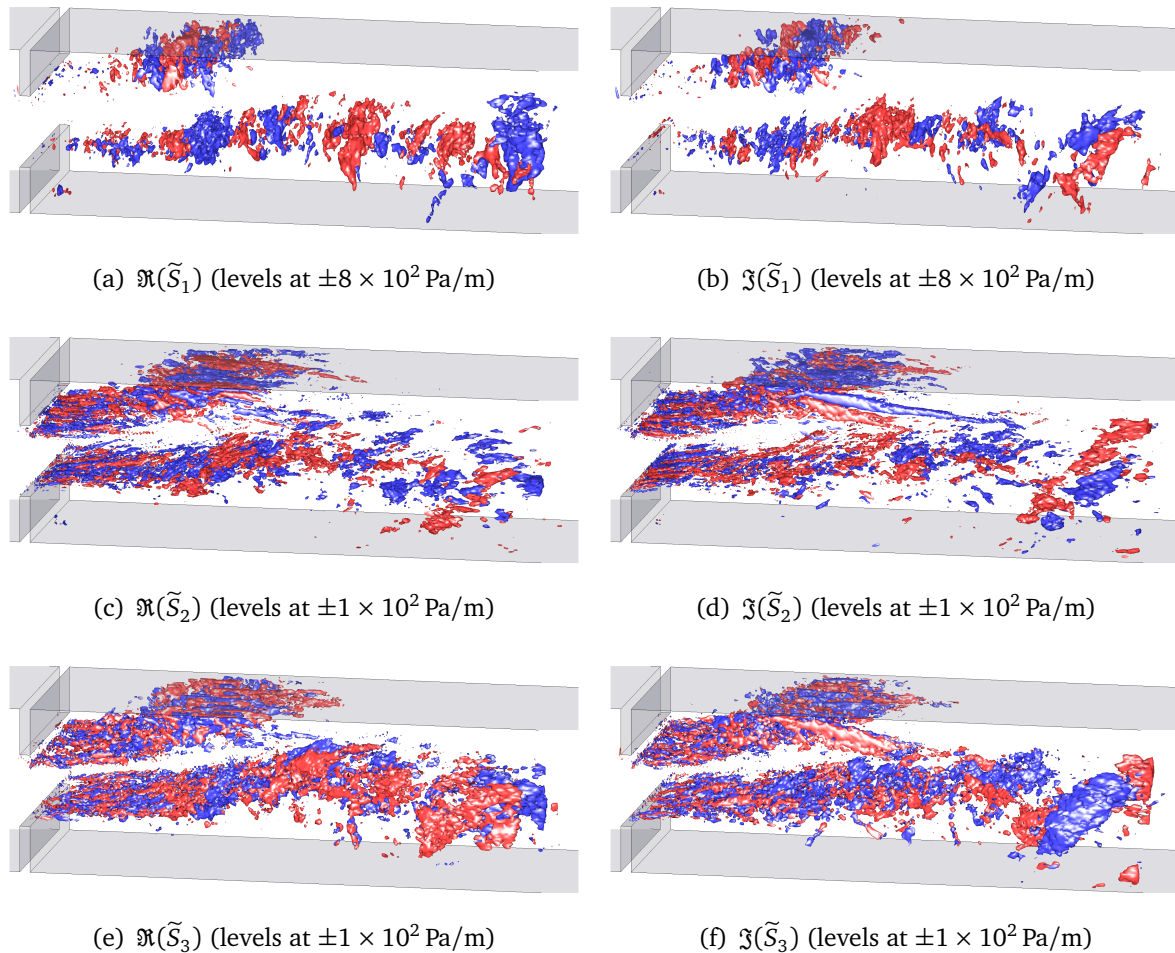


**Figure 4.51** – Diaphragm. Isosurfaces of the six frequency source term components (real and imaginary parts are displayed separately) at 20 Hz, perspective view. Blue isosurfaces: negative levels, red isosurfaces: positive levels.

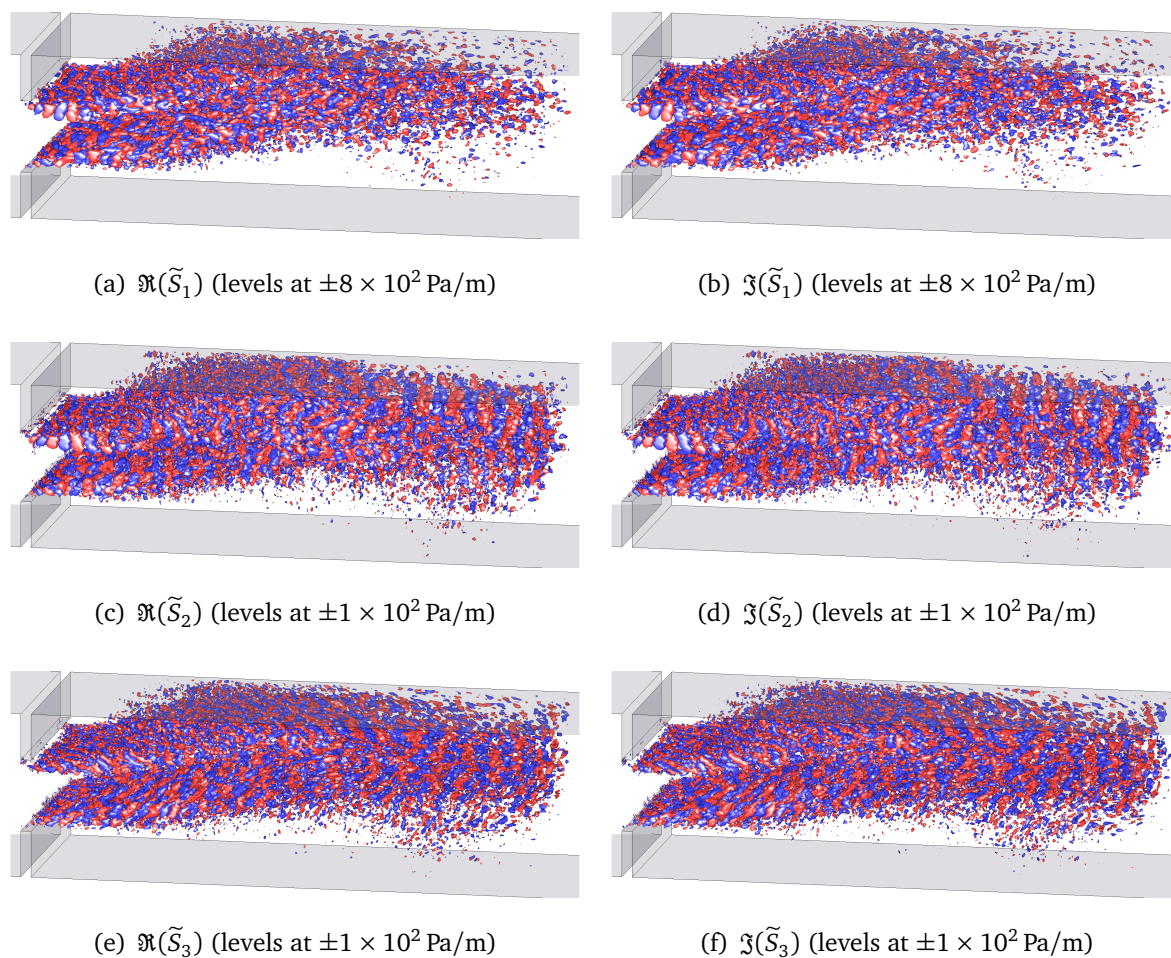


**Figure 4.52** – Diaphragm. Isosurfaces of the six frequency source term components (real and imaginary parts are displayed separately) at 1000 Hz, perspective view. Blue isosurfaces: negative levels, red isosurfaces: positive levels.

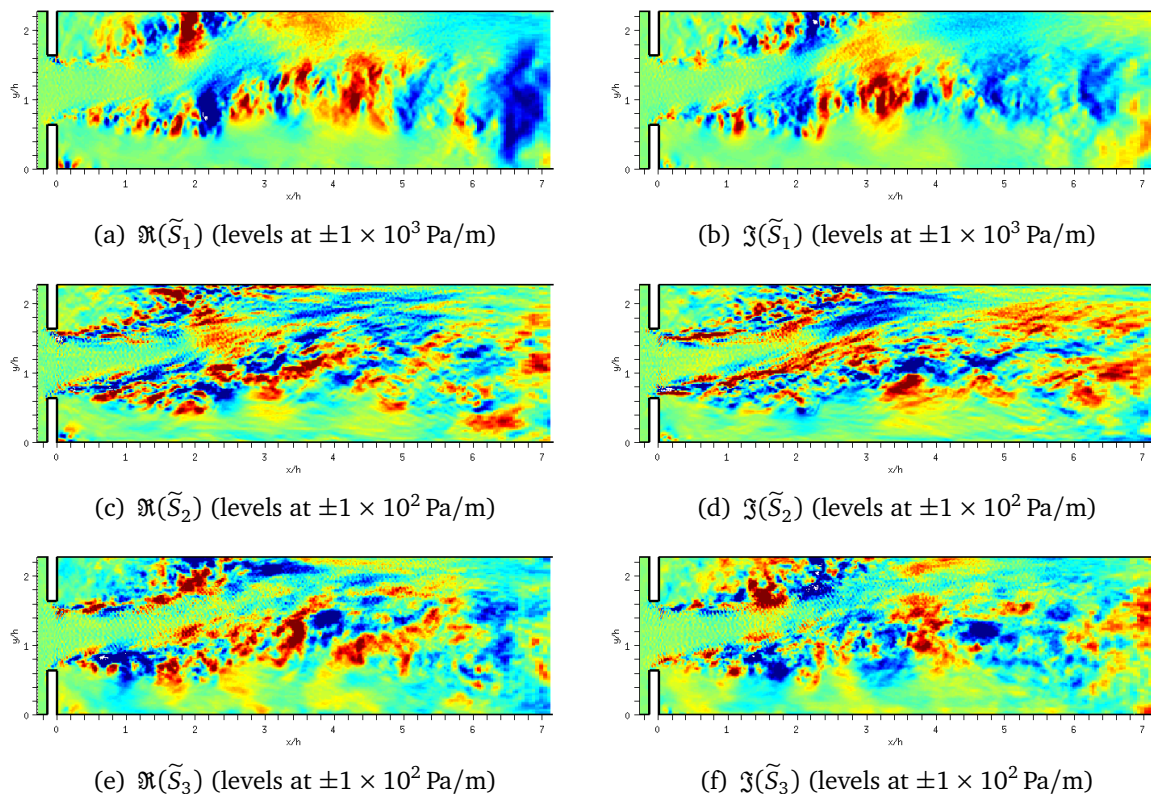


**Figure 4.53** – Diaphragm. Six frequency source term components in the XY midplane at 20 Hz before interpolation onto the acoustic mesh; real and imaginary parts are displayed separately.

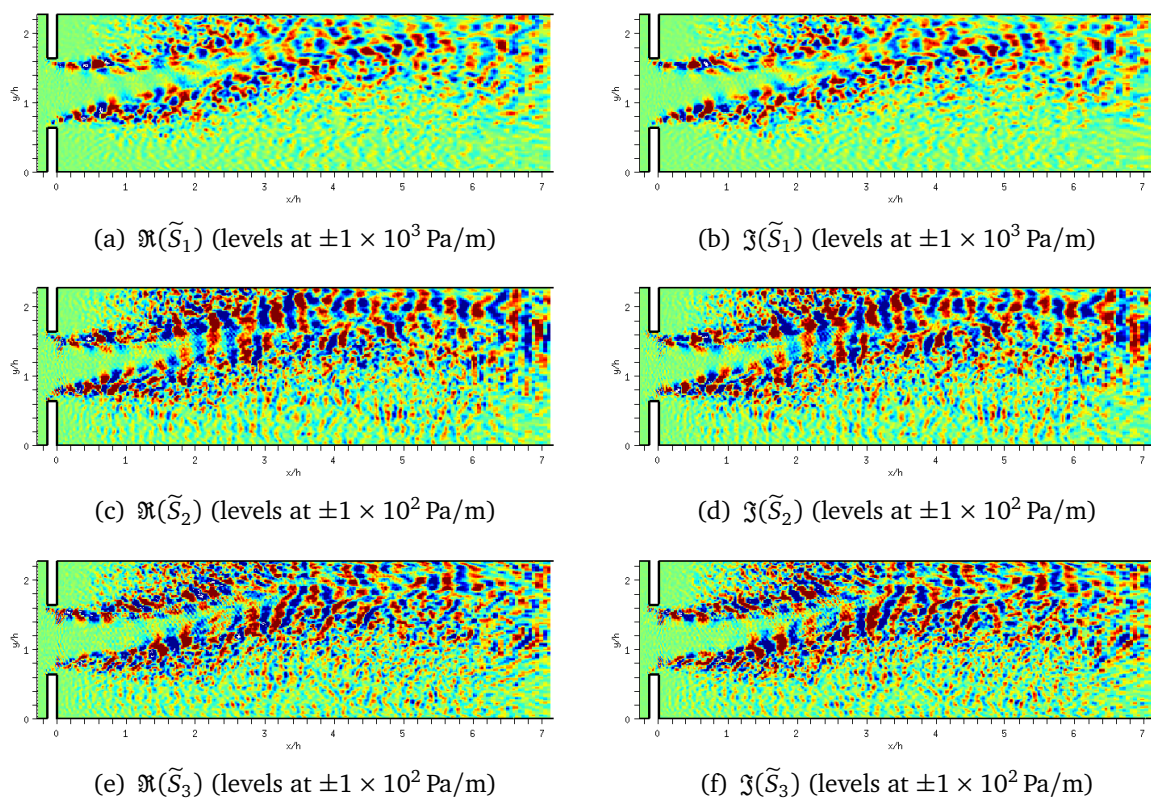


**Figure 4.54** – Diaphragm. Six frequency source term components in the XY midplane at 1000 Hz before interpolation onto the acoustic mesh; real and imaginary parts are displayed separately.

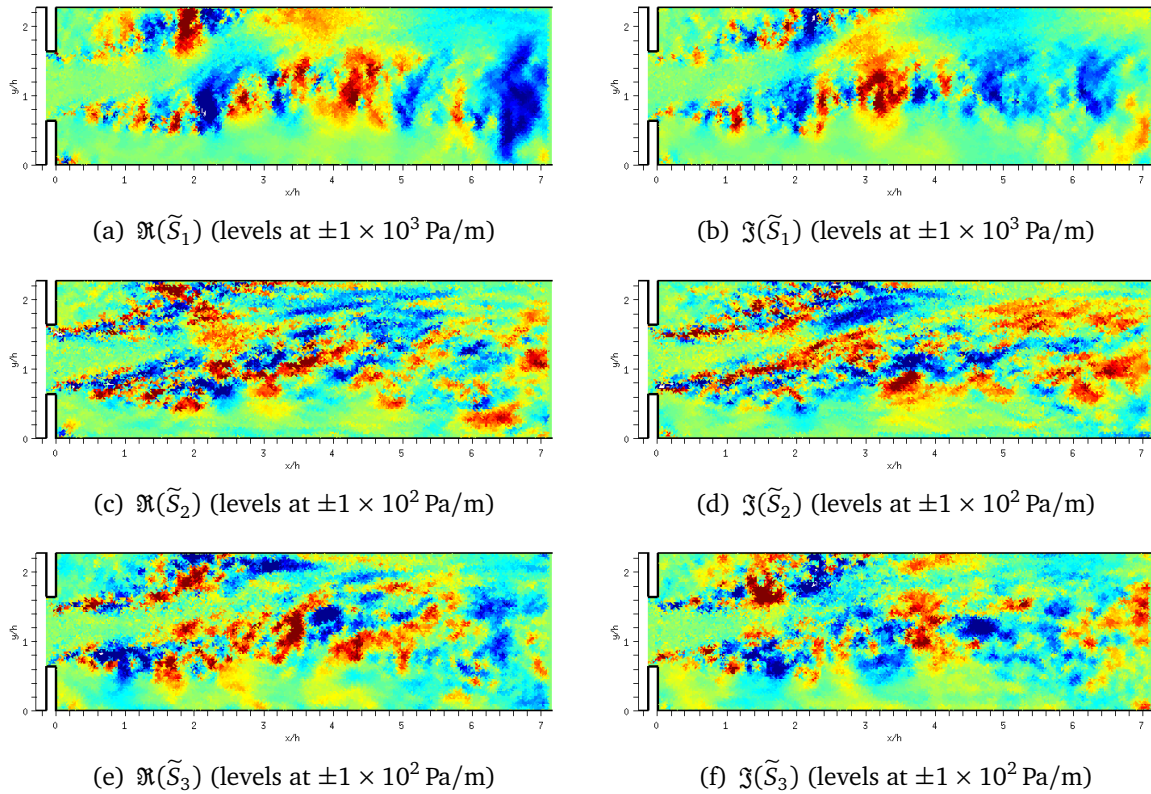


**Figure 4.55 – Diaphragm.** Six frequency source term components in the XY midplane at 20 Hz after interpolation onto the acoustic mesh; real and imaginary parts are displayed separately.

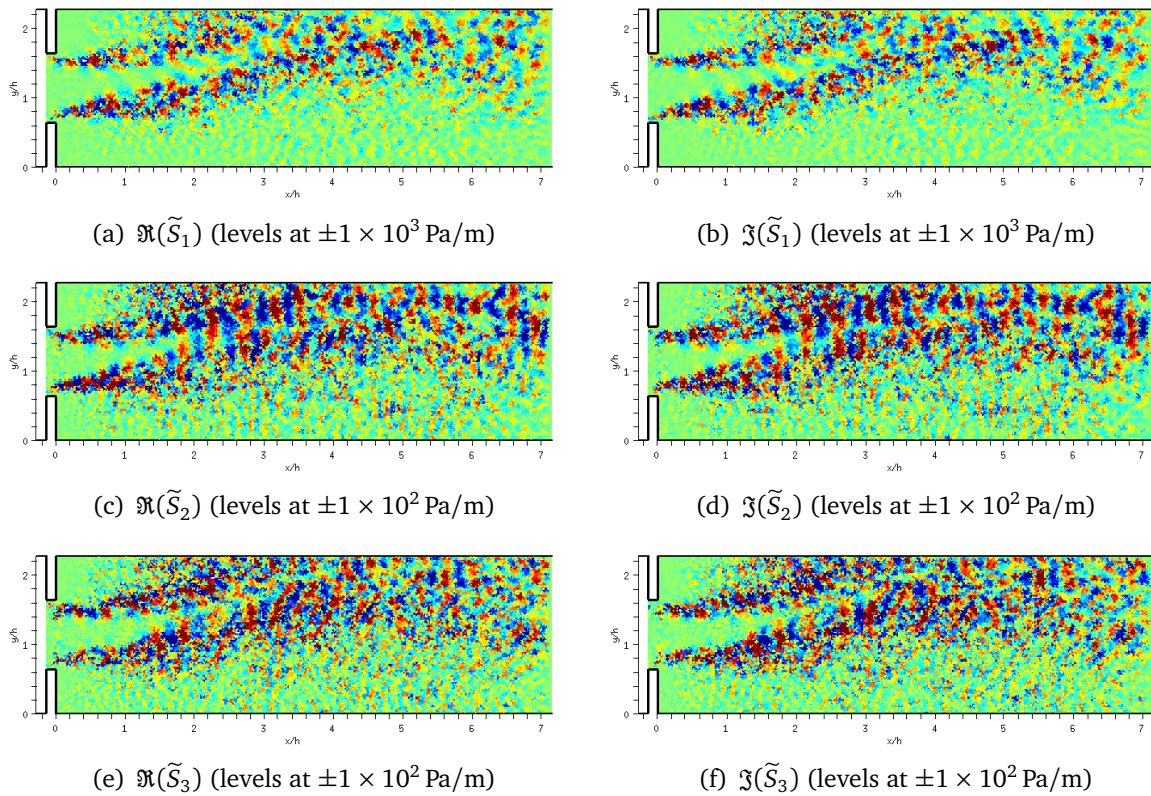


**Figure 4.56 – Diaphragm.** Six frequency source term components in the XY midplane at 1000 Hz after interpolation onto the acoustic mesh; real and imaginary parts are displayed separately.

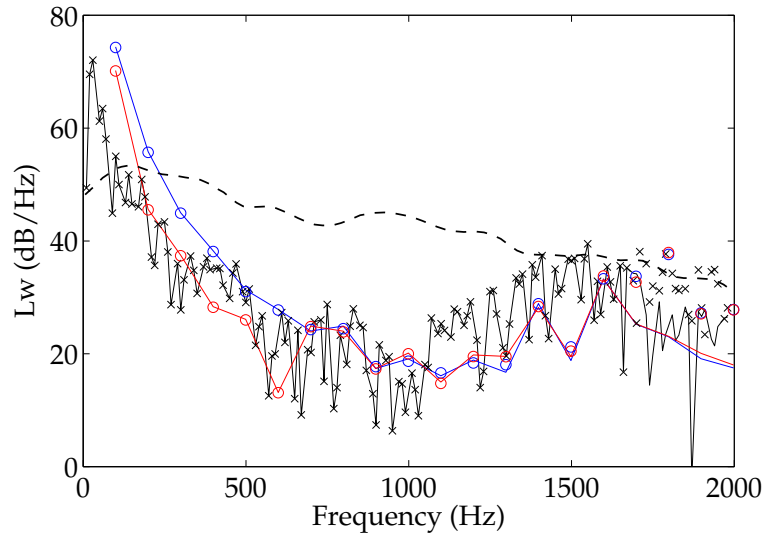


**Figure 4.57** – Diaphragm. Acoustic power radiated at the outlet of the duct. ---: reference results of Gloorfelt & Lafon<sup>54</sup>. Acoustic power obtained using the intensity, for —: the non-averaged signal without spatial filtering, —: the averaged signal without spatial filtering, —: the averaged signal with spatial filtering. Acoustic power obtained by integrating the pressure at the duct outlet for ×: the non-averaged signal without spatial filtering, ○: the averaged signal without spatial filtering, ○: the averaged signal with spatial filtering.

	Reference results <sup>54</sup>	Averaging over 19 samples		
		No averaging $d = 0$	$d = 0$	$d = 50$
Inlet	69	84.5	94.7	90.4
Outlet	78.8	84.8	94.4	90.2
Total	79	87.7	97.6	93.3

**Table 4.4** – Overall acoustic power radiated by the diaphragm, in dB.  $d$ , in mm, refers to the presence of spatial filtering and specifies its application length.

### Analysis of acoustic results

The acoustic propagation is performed within Actran using these interpolated three dimensional frequency source terms; two type of signal processing are applied, as specified previously, namely the Fourier transform of the total signal and the Fourier transform of an averaged signal. Spatial filtering is finally applied on  $1.43h$  to the averaged source terms. The acoustic power spectra computed at the outlet of the duct are displayed in Figure 4.57 together with reference results<sup>54</sup>. As for the diaphragm slice computation, a sharp peak centered around 30 Hz is present at a high level on the 10 Hz-resolution spectrum, and this low-frequency peak is still present in the averaged spectra at a lower level. In addition, the broadband shape of the spectrum is different from the reference, with a downward level slope until 1000 Hz, followed by a rise up to 1500 Hz. From then on, the spectrum shows

a tendency to follow the reference solution.

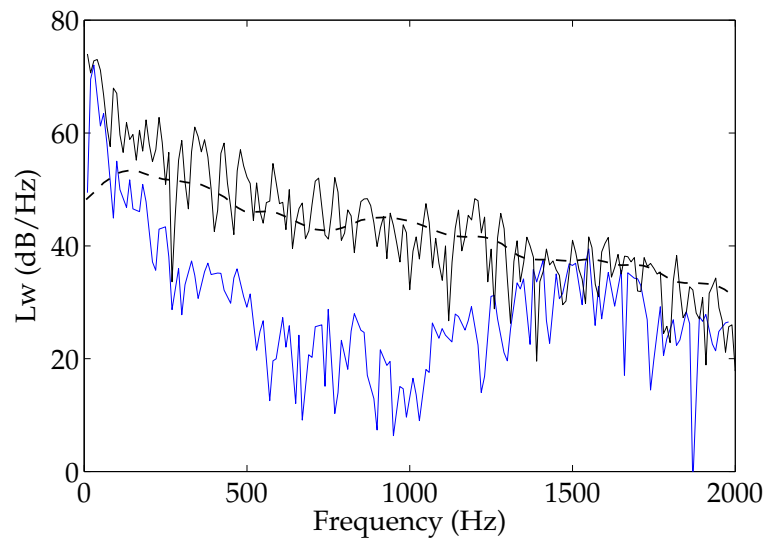
The results' consistency regarding the plane wave propagation assumption under the first duct mode at 1700 Hz is proved in Figure 4.57. Indeed, the acoustic power obtained by integrating the pressure at one point over the duct outlet section is equal to the acoustic power obtained using the modal basis intensity. The acoustic pressure maps in Figure 4.59 confirm this, with constant pressure in duct sections up to 1500 Hz; the first duct mode appears in the 2000 Hz pressure map. Spatial filtering is efficient to remove spurious scattering from the downstream source region boundary, as no dipolar radiation from this location is observed on the maps; only the plane wave propagates.

Once again, as Table 4.3.4.3 attests it, the overall power levels at the inlet are of the same order as at the outlet, which is consistent with the two-dimensional acoustic results. As noticed in § 4.2.3.4, overall levels between averaged and non averaged signals should be compared with caution because of the different lowest frequency in both spectra.

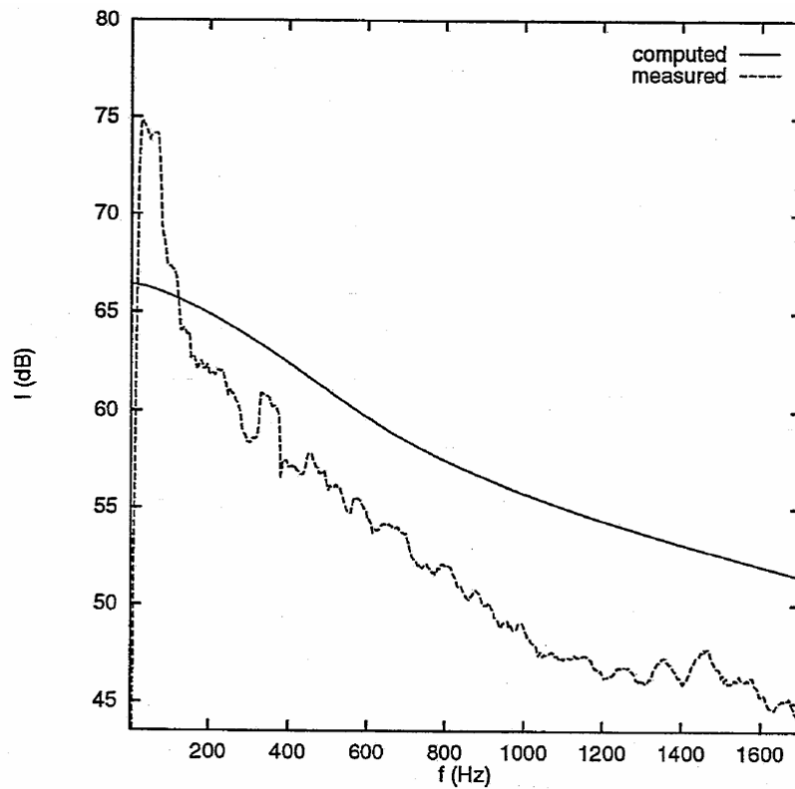
On all spectra obtained using the present method, high levels are obtained in the low frequency range, below 100 Hz. This kind of peak is not present at all in the reference spectrum, the Direct Noise Computation performed by Gloerfelt & Lafon<sup>54</sup>. In order to understand its origin, an experimental spectrum obtained by Van Herpe<sup>110</sup> is plotted in Figure 4.58. In this experiment, the domain is the same (same diaphragm and duct sections), but the inlet velocity is 14 m/s instead of 6 m/s in the present study. This experimental acoustic power spectrum also exhibits strong low frequency levels below 100 Hz. Even if the absolute levels cannot be compared because of the mass flow difference, this comparison shows the physical origin of the low frequency peak.

### Discussion and comparison with 2D results

As was already noticed, the turbulence levels obtained in the 3D computation are quantitatively very consistent with reference results of Gloerfelt & Lafon<sup>54</sup>, while the results on the slice model are globally overestimated. Acoustic results are consistent with this last remark, since the noise levels obtained on the slice model with the 2D acoustic computation are higher than the 3D acoustic results. Though, the 2D levels are closer to the reference than 3D levels. This is partly due to the sources decimation performed by interpolating data on the 3D case, the main consequence being the loss of the correct broadband shape on the spectra.

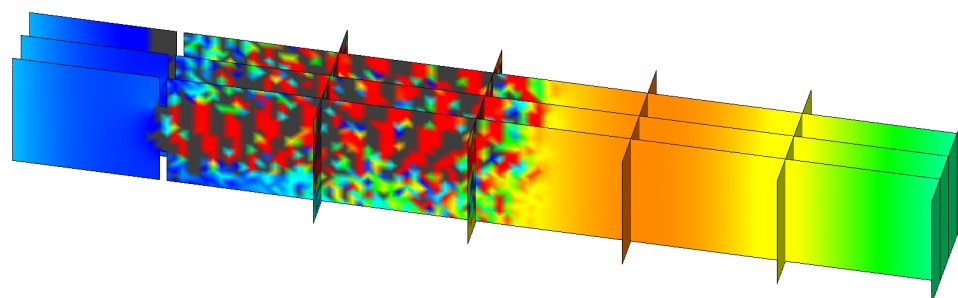


(a) Results of present work. —: 3D acoustic computation without spatial filtering and time averaging; —: 2D acoustic computation with spatial filtering and time averaging; ---: reference results of Gloerfelt & Lafon<sup>54</sup>.

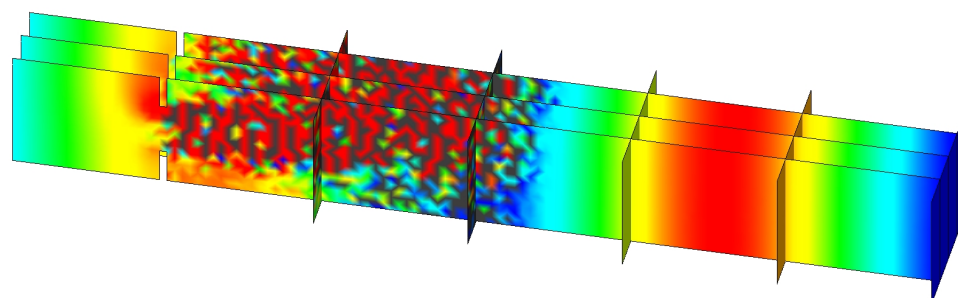


(b) Results obtained by van Herpe<sup>110</sup> for an inlet velocity of 14 m/s in the same geometry. ---: measurements, —: calculation.

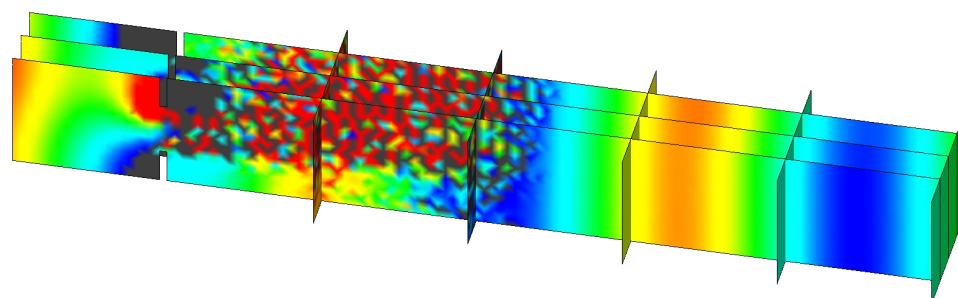
**Figure 4.58 – Diaphragm. Acoustic power radiated at the outlet of the duct.**



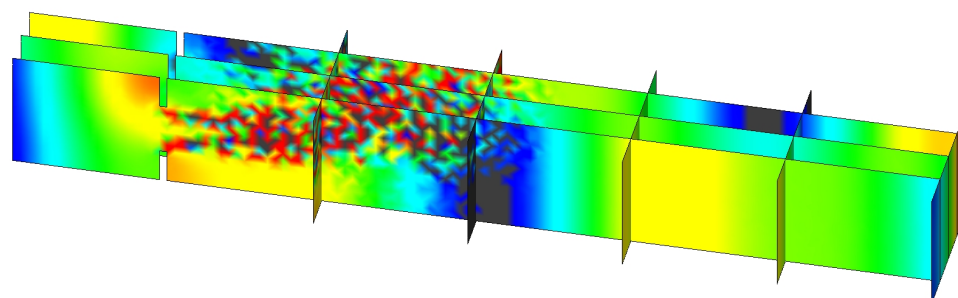
(a)  $f = 500$  Hz (levels:  $\pm 0.045$  Pa)



(b)  $f = 1000$  Hz (levels:  $\pm 0.03$  Pa)



(c)  $f = 1500$  Hz (levels:  $\pm 0.035$  Pa)



(d)  $f = 2000$  Hz (levels:  $\pm 0.08$  Pa)

**Figure 4.59** – Diaphragm. 3D acoustic pressure maps for different frequencies, taken from the 100 Hz resolution computation with 19 averages and spatial filtering on 1.43 h.

## 4.4 Conclusion

This chapter is devoted to the application of the hybrid aeroacoustic method to a real life configuration, namely a ducted diaphragm at a low Mach number. This study has enabled to assess the quality of the simulation in terms of aerodynamic results, while some issues are still opened regarding the acoustic computation for large models.

Firstly, a reduced model is considered: taken the extrusion in the spanwise direction, only 10% of the total width is retained. A Large Eddy Simulation is performed; the mean aerodynamic features are consistent with the Direct Noise Computation of Gloerfelt & Lafon<sup>54</sup>. A two-dimensional acoustic computation is performed, retaining all CFD accuracy for the definition of the source terms. Despite the absence of the third dimension, the acoustic power spectrum at the duct outlet, which is obtained using the integral spanwise length scale, is in quite good agreement with reference results. In particular, the broadband slope is accurately computed. The major discrepancy is found at very low frequencies, below 80 Hz, where a sharp peak is obtained in present simulation; this last peak is attributed to the limitations of the slice model.

To overcome the limitations of previous simulation, the same computation is achieved on the full three dimensional geometry. Similarly, a Large Eddy Simulation is performed, revealing a very complex three dimensional flow field. In addition to the large recirculations above and below the jet, already present in the slice computation, the mean flow presents two ground contra rotating vortices of  $y$  axis just below the jet. Two large contra rotating structures develop in the streamwise direction downstream of the ground vortices. All this complex flow behavior is consistent with previous experimental studies on similar geometries; the levels of the mean velocity components and turbulence intensities are also in harmony with those experimental results. The instantaneous flow field is representative of the refinement level of the simulation. In order to perform a three-dimensional acoustic computation with the source terms extracted from the CFD, an interpolation of these source terms on a coarser mesh is required to reach an acceptable finite element model size, with regard to the available computing resources. Prior to the interpolation, a cleaning and smoothening of the data is applied to remove numerical noise. However, as the interpolation from the fine CFD to the coarser acoustic mesh is a decimating process, some level of accuracy is inevitably lost. Acoustic results attest this accuracy loss, with the broadband slope quite different from the reference one.

The development of robust and versatile interpolation schemes, as well as their validation regarding accuracy and usage is out of reach of the present work, but constitutes the natural continuation of this study. A detailed experimental campaign, providing reference for the mean, rms and statistic aerodynamic fields, as well as acoustic measurements, is also required to properly conclude this work.

# Conclusion

---

*T*HIS DOCUMENT presents the implementation of a hybrid method of aeroacoustic computation for internal, low Mach number, high Reynolds number flows. This approach consists in the coupling of a finite volume Computational Fluid Dynamics code with a spectral finite element acoustics code; Fluent and Actran/LA are used throughout this work for CFD and acoustic propagation, respectively. In such a two steps aeroacoustic procedure with very low flow velocities, the aerodynamic computation is shown to require an incompressible resolution of Large Eddy Simulation type. The variational implementation of Lighthill's Acoustic Analogy in a finite elements framework enables treating any complex geometry for the acoustic propagation, as well as taking advantage of the features already implemented within Actran, such as the hard wall, infinite elements or modal duct basis boundary conditions. Moreover, considerations related to retarded time are naturally discarded when working in the spectral space. All steps in the coupling are validated separately using academic studies, and an application to a real configuration, the ducted diaphragm, is proposed. In this work, the physics of the flow field is clearly highlighted, with an attempt to understanding noise generation mechanisms. The limits of the method are also pointed out, and solutions are proposed to overcome the difficulties.

A complete validation of this computational method is presented for the first time, where Direct Numerical Simulation is compared to the present hybrid method; an analytical solution of Lighthill's Acoustic Analogy serves as an ultimate reference. The physical issue investigated is the correct definition of the source term; to a larger extent, the goal is to assess the role of linear source terms in acoustic analogies. Indeed, while linear terms have to be discarded in the source term of acoustic analogies where convection by a mean flow is accounted for in the propagation operator, it is argued that such linear terms are required in the source term of a non convected wave equation. The academic case of two corotating vortices evolution is defined to establish this point. Firstly placed in a medium at rest, then in a shear mean flow, their evolution is shown to match in every respect with

previous simulations reported in the literature. The hybrid computational method provides excellent results and confirms the previous statement, namely that the linear terms are required in the source term definition when dealing with Lighthill's Acoustic Analogy. In addition, an incompressible computation was found to yield results very consistent with the compressible computation.

The application of the previously validated method to a "real life" flow is performed with the study of a low Mach number flow in a ducted diaphragm. An incompressible Large Eddy Simulation is firstly achieved on a slice of the model consisting of 10% of the total width. General flow features are consistent with reference results, though the flow restriction along the truncated dimension yields a quasi two dimensional mean flow evolution; instantaneous three dimensional development is still visible. The two-dimensional acoustic computation compares reasonably with the reference, considering that the real wall restriction in the width is not taken into account. In order to get more realistic and accurate results, the flow field in the full three dimensional geometry is studied. The extensive analysis of the mean flow field reveals very complex three dimensional structures, whose existence and features are very likely when compared to similar experimental studies. The instantaneous field and flow statistics are similarly in reasonable agreement with reference results.

The implementation of the hybrid noise computation is more complex for this big model than for the diaphragm "slice" or for the academic cases. Indeed, the accuracy obtained in the source term description, thanks to the CFD computation, cannot be retained for the acoustic propagation since current computational resources restrict the size of the finite elements acoustic model. It is then necessary to decimate the source terms with spatial interpolation from the fine CFD mesh to the coarser acoustic mesh. After smoothing the source terms, high order interpolation is applied to yield an acceptable resolution for the acoustic computation; acoustic results after propagation are still quite far from the reference.

## Prospects

Regarding the primary objective of total simulation time, it is clear that for the full diaphragm computation it is no less than one week, but closer to one month using the local hardware, a cluster of 8 computing nodes; it is worth mentioning here that, for the slice simulation, about 80% of the total computing time for the whole aeroacoustic simulation is spent on CFD, 15% on the acoustic computation and 5% in signal processing (Fourier transform, space smoothing and interpolation). For the complete 3D simulation, figures are closer to 50% spent on CFD, 40% on acoustics and 10% on signal processing. This rough decomposition depends strongly on the hardware and its architecture, and a decrease of the total computing time is expected when working on dedicated machines

optimized for each type of computation; the optimal requirements of a finite volume CFD code are indeed very different from those of a finite elements acoustic code. However, the figures associated to the bigger problem actually show that this kind of simulation is currently out of reach for industrial applications. Significant improvement in acoustic computing time is expected if relevant and accurate interpolation schemes are validated in order to decrease the acoustic finite element model size.

The comparison to experimental results could not be achieved in the frame of this work as reference results were not available. An experimental campaign will have to be led to confirm all aerodynamic and acoustic features observed numerically. Particle Image Velocimetry (PIV) will provide reference mean flow maps, while Laser Doppler Anemometry (LDA) will supply time-resolved statistics at specific locations. The acoustic investigation should be performed with a silent airflow generator and an anechoic outlet to reproduce the numerical conditions, namely semi infinite ducts at both inlet and outlet.

Finally, the simulation tools used throughout this study are commercial software; the CFD software, Fluent in this study, could be chosen among all available solvers, provided that the Large Eddy Simulation is implemented with accurate enough space time discretization schemes. On the contrary, Lighthill's Acoustic Analogy as implemented within Actran is unique. The present work has involved the development of many scripts for signal processing, but these are rather universal and can be easily adapted to any model, even complex. The only fine tuning resides in the interpolation procedure, developed exclusively for Cartesian meshes. The extension of the present method to more complex geometries, such as HVAC systems, will require the development of space interpolation schemes adapted to arbitrary meshes. These schemes should be integrated, either in the CFD or in the acoustic software, in order to generalize the applicability to any kind of mesh, and finally to ease the use of these tools. In particular, this would avoid painful and long intermediate processing steps, and reduce the data exchange volume between the CFD and acoustic solvers. Such an interpolation procedure will have to undergo an extensive validation, which constitutes the natural continuation of this work.



# A.

## Study of the diaphragm: two-dimensional case

---

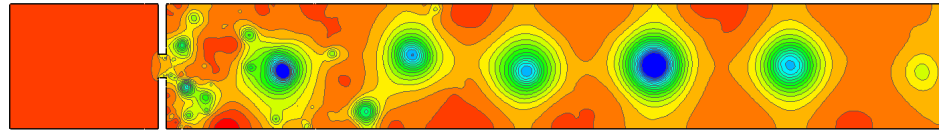
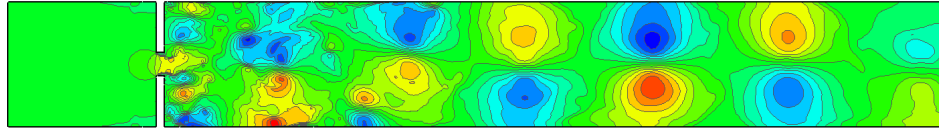
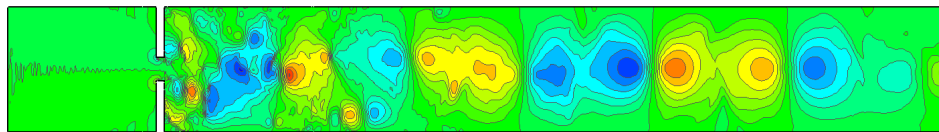
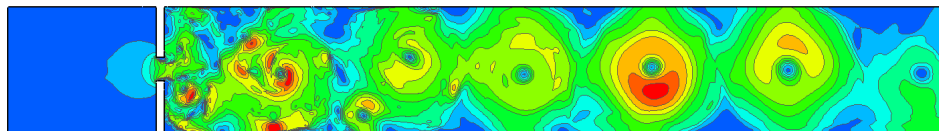
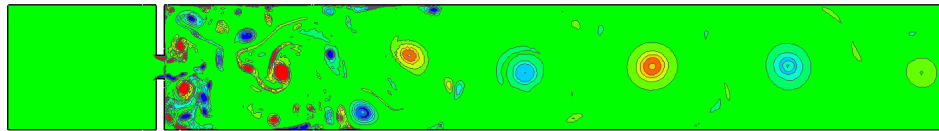
*A* TWO-DIMENSIONAL computation for the diaphragm case is performed in order to show the irrelevancy of a Large Eddy Simulation in two dimensions. The configuration here is the diaphragm with a 15 mm opening, instead of 35 mm as studied in Chapter 4, with an inlet velocity of 6 m/s. The mesh is built similarly to the three dimensional diaphragm case and contains 64,000 cells, with fine cells in the diaphragm zone ( $\Delta x = \Delta y = 0.5$  mm) and boundary layers on the diaphragm opening and downstream (5 boundary layers, the first one at 0.2 mm from the wall, with a growing rate of 20%).

A first a steady RANS  $k - \epsilon$  second-order converged calculation is performed, as an initial guess of the flow. Then transient LES is activated, using Smagorinsky–Lilly subgrid-scale model, with  $C_s = 0.1$ . A centered scheme is used for the momentum equation, PRESTO! for the pressure equation, and the pressure-velocity coupling is taken into account via a PISO scheme. The computation is incompressible, and the time step satisfies a CFL less or equal to 1 for the smallest cell of the domain:  $\Delta t = 5 \cdot 10^{-7}$ s.

### Analysis of the flow field

Results are shown in Figure A.1 at time  $t = 50$  ms. Firstly, we notice that the jet is attaching to the top wall, thanks to the Coanda effect, prior to attaching to the bottom wall later on.

Pressure, velocity and vorticity fields in Figure A.1 show eddy structures rather independent from each other; indeed, it is possible to identify some eddies in regions where

(a) static pressure (levels from  $-7000$  to  $1000$  Pa)(b) streamwise velocity  $u$  (levels from  $-60$  to  $80$  m/s)(c) transverse velocity  $v$  (levels from  $-70$  to  $80$  m/s)(d) velocity magnitude (levels from  $0$  to  $75$  m/s)(e)  $z$ -vorticity  $\omega_z$  (levels from  $-2 \times 10^4$  to  $2 \times 10^4$   $s^{-1}$ )**Figure A.1** – 2D Diaphragm, flow results at  $t=80$  ms.

there is neither flow nor recirculation zone, for instance just downstream of the diaphragm, below the jet. These eddies tend to drive each other, moving along in the same time and without mixing. They constitute vorticity clouds, also shown in Bogey<sup>7;9</sup> in the case of a two-dimensional jet. This behavior is typical of two-dimensional flows; such structures are seldom met in naturally evolving flows.

Those eddies are incoherent and are characteristic of a two dimensional calculation for a jet flow case. As the third dimension is absent, the jet cannot develop correctly, eddies can only be stretched in the  $x$  and  $y$  directions. Moreover, the energy waterfall (energy transfer from big to small eddies) does not take place in absence of the third direction, usually the preferred direction of eddies stretching.

Figure A.2 represents the streamlines at consecutive times of calculation. We notice

a flapping phenomenon; indeed, the jet successively attaches itself to the top wall, then to the bottom one, just downstream of the diaphragm. This is not observed experimentally: experiments show a definitive attachment to one wall or the other, in the case of a diaphragm with a rectangular cross-section (in the case of a diaphragm with a circular cross-section, the jet attaches itself to the wall and turns along it, and never detaches from it).

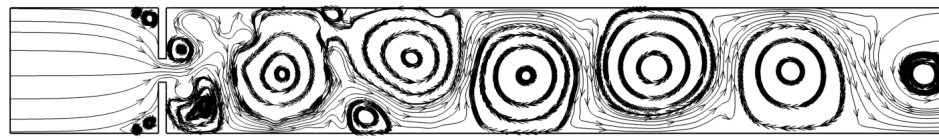
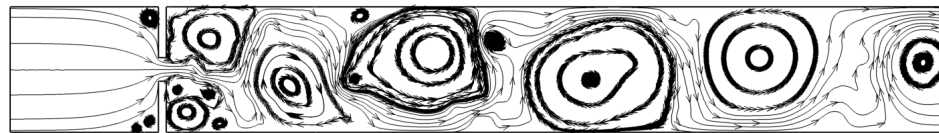
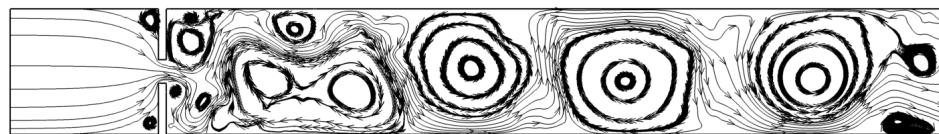
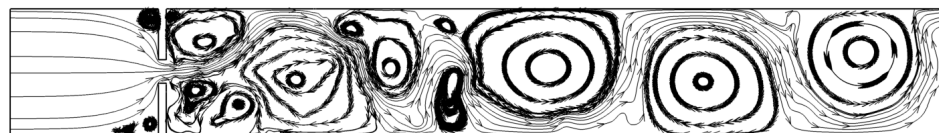
(a)  $t = 80$  ms(b)  $t = 85$  ms(c)  $t = 90$  ms(d)  $t = 95$  ms(e)  $t = 100$  ms(f)  $t = 105$  ms(g)  $t = 110$  ms

Figure A.2 – 2D Diaphragm. Streamlines colored by velocity, from  $t = 80$  ms to  $t = 110$  ms.

# Bibliography

---

- [1] ABBOTT, D. E., AND KLINE, S. J. 1962. Experimental investigation of subsonic turbulent flow over single and double backward facing steps. *Journal of Basic Engineering* **84**, 317.
- [2] ASTLEY, R. J. 1998. Mapped spheroidal elements for unbounded wave problems. *International Journal for Numerical Methods in Engineering* **41**, 1235–1254.
- [3] ASTLEY, R. J. 2008. *Computational acoustics of noise propagation in fluids - Finite and Boundary Element Methods*. Springer, ch. Infinite elements, pp. 197–230.
- [4] ASTLEY, R. J., AND COYETTE, J.-P. 2001. Conditioning of infinite element schemes for wave problems. *Communications in Numerical Methods in Engineering* **17**, 31–41.
- [5] ASTLEY, R. J., AND COYETTE, J.-P. 2001. The performance of spheroidal infinite elements. *International Journal for Numerical Methods in Engineering* **52**, 1379–1396.
- [6] AYAR, A., AMBS, R., CAPELLMANN, C., SCHILLEMET, B., AND MATTHES, M. 2005. Prediction of flow-induced noise in automotive HVAC systems using a combined CFD/CA approach. *SAE Paper 2005-01-0509*.
- [7] BAILLY, C., AND COMTE-BELLOT, G. 2003. *Turbulence*. CNRS Editions, Paris. ISBN: 2-271-06008-7.
- [8] BERLAND, J., BOGEY, C., MARSDEN, O., AND BAILLY, C. 2007. High-order, low dispersive and low dissipative explicit schemes for multiple-scale and boundary conditions. *Journal of Computational Physics* **224**, 637–662.
- [9] BOGEY, C. 2000. *Calcul direct du bruit aérodynamique et validation de modèles acoustiques hybrides*. PhD thesis, Ecole Centrale de Lyon, France. In French.

- [10] BOGEY, C., AND BAILLY, C. 2004. A family of low dispersive and low dissipative explicit schemes for noise computation. *Journal of Computational Physics* **194**, 1, 194–214.
- [11] BOGEY, C., AND BAILLY, C. 2006. Computation of a high Reynolds number jet and its radiated noise using Large Eddy Simulation based on explicit filtering. *Computers & Fluids* **35**, 1344–1358.
- [12] BOGEY, C., AND BAILLY, C. 2006. Large eddy simulations of round jets using explicit filtering with/without dynamic smagorinsky model. *International Journal of Heat and Fluid Flow* **27**, 603–610.
- [13] BOGEY, C., AND BAILLY, C. 2007. Analysis of the correlations between the turbulent flow and the sound pressure fields of subsonic jets. *Journal of Fluid Mechanics* **583**, 71–97.
- [14] BOGEY, C., BAILLY, C., AND JUVÉ, D. 2000. Numerical simulation of sound generated by vortex pairing in a mixing layer. *AIAA Journal* **38**, 12, 2210–2218.
- [15] BOGEY, C., BAILLY, C., AND JUVÉ, D. 2002. Computation of flow noise using source terms in linearized Euler equations. *AIAA Journal* **40**, 2, 235–243.
- [16] BOGEY, C., GLOERFELT, X., AND BAILLY, C. 2003. Illustration of the inclusion of sound-flow interactions in Lighthill's equation. *AIAA Journal* **41**, 8, 1604–1606.
- [17] BRENTNER, K. S., AND FARASSAT, F. 2003. Modeling aerodynamically generated sound of helicopter rotors. *Progress in Aerospace Sciences* **39**, 83–120.
- [18] BROTZ, F., WETZEL, T., SCHRUMPF, M., JUNG, M., AUGUSTIN, K., AND LANG, M. 2007. Aeroacoustic CFD simulation for automotive air conditioning applications: Behr's experience. *8th VTMS Conference and Exhibition*.
- [19] BURNETT, D. S. 1994. A three-dimensional acoustic infinite element based on a prolate spheroidal multipole expansion. *Journal of the Acoustical Society of America* **96**, 2798–2816.
- [20] CARO, S., PLOUMHANS, P., AND GALLET, X. 2004. Implementation of Lighthill's Acoustic Analogy in a finite/infinite elements framework. *AIAA Paper 2004-2891*.
- [21] CARO, S., PLOUMHANS, P., GALLET, X., SANDBODGE, R., SHAKIB, F., AND MATTHES, M. 2005. A new CAA formulation based on Lighthill's Analogy applied to an idealized automotive HVAC blower using AcuSolve and Actran/LA. *AIAA Paper 2005-3015*.
- [22] CASARSA, L., AND GIANNATTASIO, P. 2008. Three-dimensional features of the turbulent flow through a planar sudden expansion. *Physics of Fluids* **20**.

- [23] CASPER, J. H., LOCKARD, D. P., KHORRAMI, M. R., AND STREETT, C. L. 2004. Investigation of volumetric sources in airframe noise simulations. *AIAA Paper 2004-2805*.
- [24] CERFACS, ENSEEIHT-IRIT, AND INRIA. MUMPS: A multifrontal massively parallel sparse direct solver. <http://graal.ens-lyon.fr/MUMPS>.
- [25] CHERDRON, W., DURST, F., AND WHITELAW, J. H. 1978. Asymmetric flows and instabilities in symmetric ducts with sudden expansions. *Journal of Fluid Mechanics* **84**, 1, 13–31.
- [26] CHIANG, T. P., SHEU, T. W. H., HWANG, R. R., AND SAU, A. 2001. Spanwise bifurcation in plane-symmetry sudden-expansion flows. *Physical Review E* **65**.
- [27] COLONIUS, T. april 2006. Computational Aeroacoustics: overview and numerical methods. *von Karmàn Institute for Fluid Dynamics - Lecture Series 2006-05: Computational Aeroacoustics*.
- [28] COLONIUS, T., AND LELE, S. A. K. 2004. Computational aeroacoustic: progress on nonlinear problems of sound generation. *Progress in Aerospace Sciences* **40**, 345–416.
- [29] COLONIUS, T., LELE, S. A. K., AND MOIN, P. 1997. Sound generation in a mixing layer. *Journal of Fluid Mechanics* **330**, 375–409.
- [30] CURLE, N. 1955. The influence of solid boundaries upon aerodynamic sound. *Proceedings of the Royal Society of London* **231A**, 1187, 505–514.
- [31] DE GUILLEBON, H., AUGER, J.-M., DUBIEF, F., TAKLANTI, A., JOURNEAU, F., AND BLANC, P. 2003. Aeroacoustic noise induced by HVAC system: experimental and modeling analysis. *Fan Noise*.
- [32] DE ROECK, W., BAELMANS, M., AND DESMET, W. 2007. An aerodynamic/acoustic splitting technique for hybrid CAA applications. *AIAA Paper 2007-3726*.
- [33] DE ZILWA, S. R. N., KHEZZAR, L., AND WHITELAW, J. H. 2000. Flows through plane sudden-expansions. *International Journal for Numerical Methods in Fluids* **32**, 313–329.
- [34] DUBIEF, F., NAJI, SAÏD ANS LEWIS, M., AND MENDONÇA, F. 2005. Prediction of aeroacoustic noise in automotive centrifugal fans: validation of CFD and acoustic simulation techniques. *AIAA Paper 2005-2921*.
- [35] DURST, F., MELLING, A., AND WHITELAW, J. H. 1974. Low Reynolds number flow over a plane symmetric sudden expansion. *Journal of Fluid Mechanics* **64**, 1, 111–128.

- [36] DURST, F., PEREIRA, J. C. F., AND TROPEA, C. 1993. The plane symmetric sudden-expansion flow at low Reynolds numbers. *Journal of Fluid Mechanics* **248**, 567–581.
- [37] EMMERT, T., LAFON, P., AND BAILLY, C. 2007. Computation of aeroacoustic phenomena in subsonic and transonic ducted flows. *AIAA Paper 2007–3429*.
- [38] ESCUDIER, M. P., OLIVEIRA, P. J., AND POOLE, R. J. 2002. Turbulent flow through a plane sudden expansion of modest aspect ratio. *Physics of Fluids* **14**, 10, 3641–3654.
- [39] FARASSAT, F. 1980. Linear acoustic formulas for calculation of rotating blade noise. *AIAA Journal* **19**, 9, 1122–1130.
- [40] FARASSAT, F. 1994. Introduction to generalized functions with applications in aerodynamics and aeroacoustics. Technical Report 3428, NASA.
- [41] FARASSAT, F. 1996. The Kirchhoff formulas for moving surfaces in aeroacoustics - the subsonic and supersonic cases. Technical Memorandum 110285, NASA.
- [42] FEARN, R. M., MULLIN, T., AND CLIFFE, K. A. 1990. Nonlinear flow phenomena in a symmetric sudden expansion. *Journal of Fluid Mechanics* **211**, 595–608.
- [43] FEDORCHENKO, A. T. 2000. On some fundamental flaws in present aeroacoustic theory. *Journal of Sound and Vibration* **232**, 4, 719–782.
- [44] FLOWCS WILLIAMS, J. E., AND HAWKINGS, D. L. 1969. Sound generated by turbulence and surfaces in arbitrary motion. *Philosophical Transactions of the Royal Society of London* **A264**, 312–342.
- [45] FLUENT INC. Sept. 2007. *Fluent 6.3 User's Guide*.
- [46] FREE FIELD TECHNOLOGIES. 2007. *Actran/TM and Actran/LA 2007, User's Manual*.
- [47] FREUND, J. B. 1999. Direct Numerical Simulation of the noise from a Mach 0.9 jet. *3rd ASME/JSME Joint Fluids Engineering Conference*.
- [48] FREUND, J. B. 2001. Noise sources in a low-Reynolds-number turbulent jet at Mach 0.9. *Journal of Fluid Mechanics* **438**, 1, 277–305.
- [49] FREUND, J. B., LELE, S. A. K., AND MOIN, P. 1993. Matching of near/far field equation sets for direct computations of aerodynamic sound. *AIAA Paper 93–4326*.
- [50] FREUND, J. B., LELE, S. A. K., AND MOIN, P. 2000. Direct Numerical Simulation of a Mach number 1.92 turbulent jet and its sound field. *AIAA Journal* **38**, 11, 2023–2031.

- [51] GERDES, K. 2000. A review of infinite element methods for exterior Helmholtz problems. *Journal of Computational Acoustics* **8**, 1, 43–62.
- [52] GERMANO, M., PIOMELLI, U., MOIN, P., AND CABOT, W. H. 1991. A dynamic subgrid-scale eddy viscosity model. *Physics of Fluids A* **3**, 7, 1760–1765.
- [53] GLOERFELT, X. 2001. *Bruit rayonné par un écoulement affleurant une cavité: simulation aéroacoustique directe et application de méthodes intégrales*. PhD thesis, Ecole Centrale de Lyon, France. In French.
- [54] GLOERFELT, X., AND LAFON, P. 2008. Direct computation of the noise induced by a turbulent flow through a diaphragm in a duct at low Mach number. *Computers & Fluids* **37**, 4, 388–401.
- [55] GOLDSTEIN, M. E. 1976. *Aeroacoustics*. McGraw-Hill, New York.
- [56] GOLDSTEIN, M. E. 2003. A generalized acoustic analogy. *Journal of Fluid Mechanics* **488**, 315–333.
- [57] GUÉDEL, A. 1999. *Acoustique des ventilateurs - Génération du bruit et moyens de réduction*. CETIAT.
- [58] HE, G. W., WANG, M., AND LELE, S. A. K. 2004. On the computation of space-time correlations by large eddy simulation. *Physics of Fluids* **16**, 3859–3867.
- [59] HOFMANS, G. C. J., BOOT, R. J. J., DURRIEU, P. P. J. M., AURÉGAN, Y., AND HIRSCHBERG, A. 2001. Aeroacoustics response of a slit-shaped diaphragm in a pipe at low helmholtz number. 1: Quasi-steady results. *Journal of Sound and Vibration* **244**, 1, 35–56.
- [60] HOLEČEK, N., AND HOČEVAR, M. 2005. Identifying drying machine heat exchanger noise. *Facta Universitatis - Series: Working and living environment protection* **2**, 5, 431–443.
- [61] HUNT, J. C. R., WRAY, A. A., AND MOIN, P. 1988. Eddies, Streams, and Convergence zones in turbulent flows. *Center for Turbulence Research - Proceedings of the Summer Program 1988*, 193–208.
- [62] KALTENBACHER, M., ESCOBAR, M., BECKER, S., AND ALI, I. 2008. *Computational acoustics of noise propagation in fluids - Finite and Boundary Element Methods*. Springer, ch. Computational aeroacoustics based on Lighthill's acoustic analogy, pp. 115–142.
- [63] LAFON, P. 1997. Noise of confined flows. *von Karman Institute for Fluid Dynamics - Aeroacoustics and Active Noise Control, 15–18 September 1997*.

- [64] LIGHTHILL, M. 1952. On sound generated aerodynamically. part I: General theory. *Proceedings of the Royal Society of London* **A211**, 564–587.
- [65] LIGHTHILL, M. J. 1954. On sound generated aerodynamically. part II: Turbulence as a source of sound. *Proceedings of the Royal Society of London* **A222**, 564–587.
- [66] LILLEY, G. M. 1972. The generation and radiation of supersonic jet noise. In *Vol. IV - Theory of turbulence generated jet noise, noise radiation from upstream sources, and combustion noise. Part II: Generation of sound in a mixing region*, vol. AFAPL-TR-72-53. Air Force Aero Propulsion Laboratory, 1972.
- [67] LONGATTE, E. 1998. *Modélisation de la génération et de la propagation du bruit au sein des écoulements turbulents internes*. PhD thesis, Ecole Centrale des arts et manufactures, Chatenay-Malabry, France. In French.
- [68] MARSDEN, O. 2005. *Calcul direct du rayonnement acoustique de profils par une approche curviligne d'ordre élevé*. PhD thesis, Ecole Centrale de Lyon, France. In French.
- [69] MARSDEN, O., BOGEY, C., AND BAILLY, C. 2005. High-order curvilinear simulations of flows around non-Cartesian bodies. *Journal of Computational Acoustics* **13**, 4, 731–748.
- [70] MARSDEN, O., BOGEY, C., AND BAILLY, C. 2008. Direct Noise Computation of the turbulent flow around a zero-incidence airfoil. *AIAA Journal* **46**, 4, 874–883.
- [71] MARTÍNEZ-LERA, P., PRADERA, A., AND SCHRAM, C. 2007. Efficient implementation of equivalent sources from CFD data in Curle's analogy. *AIAA Paper 2007–3569*.
- [72] MENDONÇA, F., READ, A., CARO, S., DEBATIN, K., AND CARUELLE, B. 2005. Aeroacoustic simulation of double diaphragm orifices in an aircraft climate control system. *AIAA Paper 2005–2976*.
- [73] MITCHELL, B. E., LELE, S. A. K., AND MOIN, P. 1995. Direct computation of the sound from a compressible co-rotating vortex pair. *Journal of Fluid Mechanics* **285**, 181–202.
- [74] MITCHELL, B. E., LELE, S. A. K., AND MOIN, P. 1999. Direct computation of the sound generated by vortex pairing in an axisymmetric jet. *Journal of Fluid Mechanics* **383**, 113–142.
- [75] NEISE, W., AND BARSIKOW, B. 1982. Acoustic similarity laws for fans. *Journal of Engineering Industry* **104**.

- [76] OBERAI, A. A., ROKNALDIN, F., AND HUGHES, T. J. R. 2000. Computational procedures for determining structural-acoustic response due to hydrodynamic sources. *Computer Methods in Applied Mechanics and Engineering* **190**, 345–361.
- [77] OBRIST, D., AND KLEISER, L. 2007. The influence of spatial domain truncation on the prediction of acoustic far-fields. *AIAA Paper 2007-3725*.
- [78] PEAKE, N. 2004. A note on "Computational aeroacoustics examples showing the failure of the acoustic analogy theory to identify the correct noise sources by C.K.W. Tam". *Journal of Computational Acoustics* **12**, 4, 631–634.
- [79] PÉROT, F. 2004. *Calcul du rayonnement acoustique d'écoulements turbulents basé sur des analogies acoustiques couplées aux simulations aérodynamiques instationnaires*. PhD thesis, Ecole Centrale de Lyon, France. In French.
- [80] PHILLIPS, O. M. 1960. On the generation of sound by supersonic turbulent shear layers. *Journal of Fluid Mechanics* **9**, 1, 1–28.
- [81] PIELLARD, M., AND BAILLY, C. 2008. Validation of a hybrid CAA method. application to the case of a ducted diaphragm at low Mach number. *14th AIAA/CEAS Aeroacoustics Conference, May 5–7, Vancouver, Canada*, AIAA Paper 2008-2873.
- [82] PIELLARD, M., CLESSE, H., AND BAILLY, C. 2007. Vers une méthode hybride de calcul aéroacoustique appliquée à des écoulements internes: diaphragme en conduit à faible nombre de Mach. *18ème Congrès Français de Mécanique, 27–31 août, Grenoble, France*.
- [83] PIOMELLI, U., STREETT, C. L., AND SARKAR, S. 1997. On the computation of sound by large eddy simulations. *Journal of Engineering Mathematics* **32**, 217–236.
- [84] POSSON, H., AND PÉROT, F. 2006. Far-field evaluation of the noise radiated by a side mirror using LES and acoustic analogy. *AIAA Paper 2006–2719*.
- [85] POWELL, A. 1964. Theory of vortex sound. *Journal of the Acoustical Society of America* **36**, 1, 177–195.
- [86] PRIEUR, J., AND RAHIER, G. 2001. Aeroacoustic integral methods, formulation and efficient numerical implementation. *Aerospace Science and Technology* **5**, 457–468.
- [87] READ, A., MENDONÇA, F., BARONE, F., DURELLO, P., CARENA, F., GALLET, X., PLOUMHANS, P., AND CARO, S. 2004. Comparison between measured and predicted tonal noise from a subsonic fan using a coupled computational fluid dynamics and computational acoustics approach. *AIAA Paper 2004–2936*.

- [88] RICOT, D. 2002. *Simulation numérique d'un écoulement turbulent affleurant une cavité par la méthode Boltzmann sur réseau et application au toit ouvrant de véhicules automobiles*. PhD thesis, Ecole Centrale de Lyon, France. In French.
- [89] ROZENBERG, Y. 2007. *Modélisation analytique du bruit aérodynamique à large bande des machines tournantes: utilisation de calculs moyennés de mécanique des fluides*. PhD thesis, Ecole Centrale de Lyon, France. In French.
- [90] RUBINSTEIN, R., AND ZHOU, Y. 2002. Characterization of sound radiation by unresolved scales of motion in computational aeroacoustics. *European Journal of Mechanics B/Fluids* **21**, 105–111.
- [91] SAGAUT, P. 1998. *Introduction à la simulation des grandes échelles pour les écoulements de fluide incompressible*. Springer-Verlag.
- [92] SANDBODGE, R., CARO, S., PLOUMHANS, P., AMBS, R., SCHILLEMET, B., WALSHBURN, K. B., AND SHAKIB, F. 2006. Validation of a CAA formulation based on Lighthill's analogy using AcuSolve and Actran/LA on an idealized automotive HVAC blower and on an axial fan. *AIAA Paper 2006–2692*.
- [93] SCHRAM, C., MARTÍNEZ-LERA, P., AND TOURNOUR, M. 2007. Two-dimensional induct vortex leapfrogging as a validation benchmark for internal aeroacoustics. *AIAA Paper 2007–3565*.
- [94] SÉROR, C., SAGAUT, P., BAILLY, C., AND JUVÉ, D. 2000. Subgrid-scale contribution to noise production in decaying isotropic turbulence. *AIAA Journal* **38**, 10, 1795–1803.
- [95] SÉROR, C., SAGAUT, P., BAILLY, C., AND JUVÉ, D. 2001. On the radiated noise computed by large eddy simulation. *Physics of Fluids* **13**, 2, 476–487.
- [96] SMAGORINSKY, I. 1963. General circulation experiments with the primitive equations. *Monthly Weather Review* **91**, 3, 99–164.
- [97] SMYTH, R. 1979. Turbulent flow over a plane symmetric sudden expansion. *Journal of Fluids Engineering* **101**, 348–353.
- [98] SPAZZINI, P. G., IUSO, G., ONORATO, M., ZURLO, N., AND DI CICCIA, G. M. 2001. Unsteady behavior of back-facing step flow. *Experiments in Fluids* **30**, 551–561.
- [99] STRATTON, J. A. 1941. *Electromagnetic theory*. New York: McGraw Hill.
- [100] TAM, C. K. W. 2002. Computational examples showing the failure of the acoustic analogy to identify the correct noise sources. *Journal of Computational Acoustics* **10**, 4, 387–405.

- [101] TAM, C. K. W. 2002. Further consideration of the limitations and validity of the acoustic analogy theory. *AIAA Paper 2002-2425*.
- [102] TAM, C. K. W., AND DONG, Z. 1996. Radiation and outflow boundary conditions for direct computation of acoustic and flow disturbances in a nonuniform mean flow. *Journal of Computational Acoustics* **4**, 2, 175-201.
- [103] TAM, C. K. W., AND WEBB, J. C. 1993. Dispersion-Relation-Preserving finite differences schemes for computational acoustics. *Journal of Computational Physics* **107**, 262-281.
- [104] THOMPSON, K. 1987. Time dependant boundary conditions for hyperbolic systems. *Journal of Computational Physics* **68**, 1-24.
- [105] THOMPSON, K. 1990. Time dependant boundary conditions for hyperbolic systems, II. *Journal of Computational Physics* **89**, 439-461.
- [106] TOURNOUR, M., EL HACHEMI, Z., READ, A., MENDONÇA, F., BARONE, F., AND DURELLO, P. 2003. Investigation of the tonal noise radiated by subsonic fans using the aeroacoustic analogy. *Fan Noise*.
- [107] UTZMANN, J., BIRKEFELD, A., AND MUNZ, C.-D. 2008. Building blocks for direct aeroacoustic simulations based on domain decompositions. *AIAA Paper 2008-3004*.
- [108] VAN DEN NIEUWENHOF, B., AND COYETTE, J.-P. 2000. A conjugated infinte element method for half-space acoustic problems. *Journal of the Acoustical Society of America* **108**, 4, 1464-1473.
- [109] VAN DEN NIEUWENHOF, B., AND COYETTE, J.-P. 2001. Treatment of frequency-dependant admittance boundary conditions in transient acoustic finite/infinite-element models. *Journal of the Acoustical Society of America* **110**, 4, 1743-1751.
- [110] VAN HERPE, F. 1994. *Computational aeroacoustics for turbulent duct flow*. PhD thesis, Ecole Centrale de Paris.
- [111] VAN HERPE, F., CRIGHTON, D. G., AND LAFON, P. 1995. Noise generation by turbulent flow in a duct obstructed by a diaphragm. *AIAA Paper 95-035*.
- [112] WANG, M., FREUND, J. B., AND LELE, S. A. K. 2006. Computational prediction of flow-generated sound. *Annual Review of Fluid Mechanics* **38**, 483-512.
- [113] WANG, M., LELE, S. A. K., AND MOIN, P. 1996. Computation of quadrupole noise unusing acoustic analogy. *AIAA Journal* **34**, 11, 2247-2254.
- [114] WILCOX, C. H. 1956. A generalization of theorems of Rellich and Atkinson. *Proceedings of the American Mathematical Society* **7**, 271-276.